The Dissertation Committee for Dilip Rugnathbhai Maniar
certifies that this is the approved version of the following dissertation:

A Computational Procedure for Simulation of Suction Caisson Behavior Under Axial and Inclined Loads

Committee:

John L. Tassoulas, Supervisor

Lance Manuel

Mark E. Mear

Roy E. Olson

Alan F. Rauch

A Computational Procedure for Simulation of Suction Caisson Behavior Under Axial and Inclined Loads

by

Dilip Rugnathbhai Maniar, M.S., B.E., L.C.S.E.

Dissertation

Presented to the Faculty of the Graduate School of

The University of Texas at Austin

in Partial Fulfillment

of the Requirements

for the Degree of

Doctor of Philosophy

The University of Texas at Austin

August 2004

|| Shree Ganeshay Namah ||

|| Shree Krishna Sharnam Mamah ||

|| Shree Ramajee-Aata Satya chhe ||

* * *

To the loving memory of my late father Shree Rugnathbhai Narsidas Maniar.

To my loving and caring mother, Heeragauri Rugnathbhai Maniar.

To my dearest daughter, Krishna.

To my sweet and lovely wife, Jyoti.

To the lovely family of Rugnathbhai Narsidas Maniar.

To Shree Nathjee-bawa, Shree Mahaprabhujee, and Goswamijee Shree Brajeshkumarjee.

* * *

|| Jai Shree Krishna ||

Acknowledgments

I would like to express my sincere gratitude and deep appreciation to professor John L. Tassoulas for serving as advisor during my doctoral study at The University of Texas at Austin, and for his invaluable guidance on this research. He has been a constant source of knowledge, inspiration, and encouragement throughout my doctoral study. He has assisted me in a countless ways during my dark days, and I am very thankful to him for his understanding and patience. I owe him a large debt of appreciation for being my academic *guru* and accepting me as his disciple. I would like to thank professors Roy E. Olson and Alan F. Rauch for many interesting discussions regarding laboratory tests on model caissons and their behavior. I would like to thank professors L. Manuel, M.E. Mear, R.E. Olson, and A.F. Rauch, for their willingness to serve on the dissertation committee and for providing valuable comments on the manuscripts.

I am indebted to Offshore Technology Research Centers (OTRC) at The University of Texas at Austin and at Texas A&M University for providing financial support for this study. The funding was available from the U.S. Minerals Management Service and the OTRC Industry Consortium.

I am thankful to professor Victor N. Kaliakin of University of Delaware for providing bounding-surface plasticity routine used in the simulations presented in this dissertation.

I would like to express my sincere gratitude to administrative staff at the university. In particular, I thank Mmes. Kelly K. Collier, Denise D. (DeeDee) Berry, Kathleen (Kathy) M. Rose, Maria M. Castillo, and Mr. Paul J. White for handling administrative details. I would like to thank Daniel (Danny) Quiroz and Paul Ashe of Learning Resource Center (LRC) at the Department of Civil Engineering, for assisting with computer resources.

I owe an enormous debt of appreciation to number of friends and colleagues who have been generous with their technical expertise and friendship, making my seven years stay in Austin enjoyable and memorable. Although the list of these people is too long to be given in totality, I would especially like to thank Sumeet S. Panjabi, Ravishankar Shivarama, Charles M. Bowen, Jaroon Rungamornrat, and Juan F. Beltran. I look forward to our continued friendship and collaboration. I would like to thank Narendra D. Kaku and his family for providing homely environment.

I owe a great deal of thanks and respect to my parents, Rugnathbhai and Heeraguari Maniar for their unconditional love, prayers, support, patience, and encouragement throughout my life and education. I will always cherish the good traits, thoughts, and philosophy they have seeded in me. This dissertation is dedicated to them in return to countless sacrifices they have made for their children. I thank my brothers Anil and Tarun, and my sisters Indira, Bharti, and Jayshree, and their spouses for their encouragement and support. I would like to thank my nephews Viral, Harshal, Sneh, Kush, Karan, and Hemal; and my nieces Shraddha, Nishita, and Jhanvi just for being so charming and lively!

I would like to thank my wife Jyoti for her patience, understanding, and encouragement during my graduate study. Like most spouse of a graduate student, she made countless adjustments and sacrifices so that I could pursue my academic goals. I am thankful to our wonderful daughter Krishna for filling our life with so much joy and love.

Finally, I would like to express sincere respect to Goswamijee Shree Brajeshkumarjee for being my religious and spiritual guru and for showing me the *Pushti-marg* (path of grace). I am grateful to Lord Shree Nathjee-bawa for everything.

DILIP RUGNATHBHAI MANIAR

The University of Texas at Austin
August 2004

A Computational Procedure for Simulation of Suction Caisson Behavior Under Axial and Inclined Loads

Publication No. ____________________

Dilip Rugnathbhai Maniar, Ph.D.
The University of Texas at Austin, 2004

Supervisor: John L. Tassoulas

This dissertation documents the development of a computational procedure and its application to the analysis of suction caisson behavior under axial and inclined loads. The study is a part of a comprehensive research project on improving current understanding and developing effective procedures for the design of deep-water anchors.

A suction caisson is a hollow cylinder capped at the top. In deep-water applications, it is lowered and allowed to penetrate the seafloor under its self-weight, and then pushed to the required depth with suction applied by pumping water out of the caisson interior. Use of suction caissons as foundations for deep-water offshore structures and anchors for mooring lines has been increasing in the last decade.

Although researchers are attempting to understand behavior of suction caisson by means of field tests, laboratory tests, and numerical simulations, several issues and uncertainties related to capacity estimation and failure mechanisms are still not resolved. The objectives of this study are to develop a computational framework for the simulation of suction caisson behavior considering axial as well as inclined loads and including effects of both self-weight and suction installations, and verify the development by conducting simulations of laboratory tests carried out by fellow researchers on caisson models at The University of Texas at Austin.

The procedure developed in this work is applicable to the axisymmetric problems of caisson installation and pullout under axial load. Water-saturated porous finite-elements are used in the representation of the soil domain while the caisson is discretized using solid finite-elements. Nonlinear behavior of the clayey soil is described by means of a bounding-surface plasticity model. The soil-caisson interfaces are modeled with a contact algorithm based on a slide-line formulation. Various remeshing tools are developed to eliminate the need for *a priori* specification of the caisson penetration path. The developed formulation is used to obtain results for slurry consolidation, caisson installation, reconsolidation or setup of soil following installation, and caisson axial pullout.

Three-dimensional caisson models subjected to horizontal and inclined loads are analyzed using the ABAQUS/Standard computer program. The deformed geometry and state of the caisson-soil system obtained from axisymmetric simulation of the installation process are specified as initial conditions to carry out the three-dimensional analysis.

The computed behavior of the caisson is compared with laboratory observations. Computed axial as well as horizontal load capacities match well with measured capacities from the laboratory tests. The interaction between ultimate horizontal and vertical loads is computed. In general, good agreement is found between calculated and measured caisson behavior, thus verifying the validity of the procedure.

Contents

Acknowledgments **v**

Abstract **viii**

List of Tables **xviii**

List of Figures **xix**

Chapter 1 INTRODUCTION **1**

1.1 Overview 1
1.2 Literature Review 6
  1.2.1 Field Tests 7
  1.2.2 Laboratory Model Tests 9
  1.2.3 Centrifuge Testing of Suction Caissons 16
  1.2.4 Limit Analysis Using Plasticity Theory 18
  1.2.5 Numerical Analysis 19
  1.2.6 Design Issues and Uncertainties 23
  1.2.7 Applications 24
1.3 Objectives and Scope of the Study 28

Chapter 2 SOIL AS A POROUS MEDIUM: GOVERNING EQUATIONS 32
2.1 Introduction 32
2.2 Governing Differential Equations: Balance Laws 33
2.2.1 Conservation of Mixture Mass 34
2.2.2 Conservation of Linear Momentum 38
2.3 Excess Pore-Water Pressure Formulation 42
2.4 Boundary Conditions 44
2.5 Variational Statement of the Balance Laws 45
2.6 Summary 50

Chapter 3 SOIL-CAISSON SYSTEM DISCRETIZATION 51
3.1 Soil Discretization 51
3.1.1 Finite-Element Discretization 51
3.1.2 Incremental Equations 54
3.1.3 Time-Stepping 56
3.2 Caisson Modeling and Discretization 58
3.2.1 Balance Law: Linear Momentum Conservation 58
3.2.2 Variational Statement 59
3.2.3 Finite-Element Discretization 60
3.2.4 Incremental Equations 61
3.2.5 Temporal Discretization 62
3.3 Summary 62

Chapter 4 CONSTITUTIVE MODELS 63
4.1 Introduction 63
4.2 Constitutive Model for Clayey Soil 63

4.2.1 Theoretical Aspects 64
4.2.2 Three-Part Bounding-Surface 69
4.2.3 Numerical Implementation 70
4.2.4 Ageing of Clayey Soil 71
4.3 Constitutive Model for Caisson 71
4.4 Summary 72

Chapter 5 INTERFACE MODELING 73
5.1 Introduction 73
5.2 Solid Displacement Contribution 74
5.2.1 Identification of Contact Point 75
5.2.2 Evaluation of Penetration Condition 77
5.2.3 Application of Constraints 78
5.3 Darcy’s Velocity Contribution 80
5.3.1 Evaluation of Contact Condition 81
5.3.2 Application of Constraints 82
5.4 Excess Pore-Water Pressure Contribution 84
5.4.1 Evaluation of Contact Condition 85
5.4.2 Application of Constraints 85
5.5 Frictional Contact Contribution 87
5.5.1 Evaluation of Contact Condition 89
5.5.2 Stick Condition 90
5.5.3 Slip Condition 92
5.5.4 Stick-Slip Transition 93
5.6 Contribution at Release Condition 94
5.7 Summary 95

Chapter 6 REMESHING SCHEME **96**

6.1 Definition of the Penetration Path 96
6.2 Necessity of Remeshing 97
6.3 Remeshing Algorithm and Implementation 98
  6.3.1 Selection of Elements for Remeshing 98
  6.3.2 Generation of New Mesh 100
  6.3.3 Mapping of Field and State Variables 107
  6.3.4 Mesh Update 113
6.4 Another Remeshing Tool 113
6.5 Summary 113

Chapter 7 THREE-DIMENSIONAL ANALYSIS **114**

7.1 ABAQUS 114
7.2 ABAQUS Treatment of Porous Media 115
7.3 Soil Plasticity Model 116
7.4 Three-Dimensional Mesh Generation 117
7.5 Transfer of State Variables 117
7.6 Caisson-Soil Interfaces 118
7.7 Application of Inclined Load 119
7.8 Summary 120

Chapter 8 SIMULATION RESULTS AND COMPARISONS **121**

8.1 Experimental Program 121
  8.1.1 Laboratory Test Sequence 122
8.2 Soil Properties 123
  8.2.1 Bounding-Surface Plasticity Model Parameters 124
8.3 Simulation Sequence 128

8.4 Sign Conventions 129
8.5 Results: Test-Bed Preparation 129
    8.5.1 Initial Conditions 131
    8.5.2 Simulation Results 132
8.6 Results: Caisson Installation 148
    8.6.1 Self-Weight Installation Only 149
    8.6.2 Self-Weight Installation Followed by Suction Installation 162
8.7 Results: Reconsolidation or Setup 178
    8.7.1 Setup After Self-Weight Installation (SWP-Setup) . . . 178
    8.7.2 Setup After Suction Installation (SUC-Setup) 185
    8.7.3 Discussion 191
8.8 Results: Axial Pullout 191
    8.8.1 Vented Top, Rapid Axial Pullout 192
    8.8.2 Vented Top, Slow Axial Pullout 197
    8.8.3 Vented Top, Drained Axial Pullout 201
    8.8.4 Closed Top, Rapid Axial Pullout 208
    8.8.5 Summary of Axial Pullout Simulation Results 212
8.9 Results: Inclined capacity 214
    8.9.1 3D Geometry 215
    8.9.2 Horizontal Capacity 215
    8.9.3 Interaction Diagram 230
    8.9.4 Summary of Inclined Load Simulation Results 231
8.10 Summary 233

Chapter 9 SUMMARY AND CONCLUSIONS 234
9.1 Review of Project Scope and Objectives 234

9.2 Summary of Major Project Tasks and Findings 235
    9.2.1 Modeling of Saturated Soil and Caisson 236
    9.2.2 Modeling of Soil Constitutive Behavior 236
    9.2.3 Modeling of Soil-Caisson Interfaces 237
    9.2.4 Remeshing Scheme 237
    9.2.5 Three-Dimensional Analysis 238
    9.2.6 Simulation Procedure 239
    9.2.7 Simulation Results 239
9.3 Recommendations for Future Study 244
9.4 Conclusions 249

Appendix A Components of Tangent Stiffness and Residuals 250

A.1 Incremental Equation 250
A.2 Residual Vectors 251
A.3 Equivalent Mass Matrices 252
A.4 Equivalent Damping Matrices 253
A.5 Equivalent Stiffness Matrices 255

Appendix B Large-Deformation Analysis 258

Appendix C Contact Contributions 266

C.1 Solid Displacements 266
C.2 Darcy's Velocity 267
C.3 Excess Pore-Water Pressure 269
C.4 Interface Friction 270
    C.4.1 Stick Condition 270
    C.4.2 Slip Condition 272

C.5 Release Condition 273

Bibliography **275**

Vita **294**

List of Tables

8.1 Bounding-surface plasticity parameters 127
8.2 Consolidation simulation cases 133
8.3 Caisson axial pullout cases 192
8.4 Caisson axial pullout capacity 214
8.5 Caisson horizontal load capacity 216
8.6 Caisson inclined load capacity 230

List of Figures

1.1 Typical (half) geometry of a caisson anchor. 2

1.2 Caisson installation sequence. 3

1.3 Caissons used as foundations for a Tension Leg Platform (TLP). 4

1.4 Caissons used as anchors for catenary and taut mooring lines. 5

1.5 A typical caisson used for anchoring BP's Horn Mountain SPAR, Courtesy: Dr. E.C. Clukey (BP America). 27

1.6 Caisson in place (Source: Mercier, 2003). 28

4.1 Schematic illustration of bounding-surface in stress invariant space. 66

5.1 Definition of the slide-line formulation. 75

5.2 Definition of the slave node penetration into the master segment. 76

5.3 Darcy's velocity contribution. 81

5.4 Definition of the Coulomb friction law. 88

5.5 Definition of relative tangential velocity at contact. 90

6.1 Definition of the caisson penetration path. 97

6.2 Selection of finite-elements for remeshing. 99

6.3 Selected finite-element columns for remeshing (*left*), and remeshing of typical elements (*right*). 101
6.4 Number of nodes to be relocated. 102
6.5 Relocation of nodes to generate conforming mesh. 103
6.6 Node-relocation scheme for three nodes below the tip. 104
6.7 Relocation of nodes to generate non-conforming mesh. 106
6.8 Determination of the element containing the new node. 108
6.9 Mapping of state variables at integration points. 112

7.1 Application of inclined load. 119

8.1 Experimental setup. 123
8.2 Relationship between void ratio and effective pressure. 124
8.3 The axisymmetric finite-element mesh. 130
8.4 Schematic showing preparation of the normally consolidated test-bed. 131
8.5 Assumed uniform initial state of the slurry. 132
8.6 Slurry surface settlement curves obtained from one-dimensional simulations. 134
8.7 Slurry surface settlement curves obtained from axisymmetric simulations. 136
8.8 Computed and measured undisturbed undrained shear strength profiles of the slurry. 138
8.9 (a) Undeformed and (b) deformed axisymmetric configurations of the slurry. 141
8.10 Observed and computed (3D-CON) settlement curves for the kaolinitic slurry. 142

8.11 Distributions of effective vertical stress obtained from axisymmetric and 1D consolidation simulations. 143
8.12 Distribution of effective radial stress obtained from axisymmetric consolidation simulation. 144
8.13 Profiles of effective vertical and lateral stresses at the tank center. 145
8.14 Distributions of (*a*) porosity and (*b*) size of bounding-surface (see Fig. 4.1) obtained from axisymmetric consolidation simulation. 146
8.15 Isochrones of excess pore-water pressure at the tank center. . . 147
8.16 Dissipation of excess pore-water pressure with time at different depths. 148
8.17 Time history of caisson installation by self-weight. 150
8.18 (*a*) Reference and (*b*) deformed (at the end of self-weight installation) configurations. 152
8.19 Force required to install the caisson during self-weight installation. 153
8.20 Development of interfacial forces during self-weight installation. 154
8.21 Layout of pore-pressure transducers mounted on the model caisson. 155
8.22 Excess pore-water pressure at five sensor locations during self-weight installation. 156
8.23 (*a*) Path of caisson penetration and (*b*) cumulative volume of soil displaced during self-weight installation. 157
8.24 Effect of (conforming) remeshing during self-weight installation. 158
8.25 Distributions of stresses within the soil domain at the end of self-weight installation. 159

8.26 Distribution of excess pore-water pressure within the soil domain at the end of self-weight installation. 160
8.27 Distributions of (a) porosity and (b) size of bounding-surface within the soil domain at the end of self-weight installation. . 161
8.28 Time history of caisson installation by self-weight and suction. 163
8.29 (a) Reference configuration, and deformed configurations at the end of (b) self-weight installation and (c) suction installation. 164
8.30 Force required to install the caisson during initial self-weight installation. 165
8.31 Suction generation below caisson cap during suction installation. 166
8.32 Development of interfacial forces during self-weight and suction installations. 168
8.33 Measured and computed total soil resistance during initial self-weight installation. 169
8.34 Excess pore-water pressure at five sensor locations during self-weight and suction installations. 170
8.35 (a) Path of caisson penetration and (b) cumulative volume of soil displaced during self-weight and suction installations. . . . 171
8.36 Effect of (conforming) remeshing during suction installation. . 172
8.37 Distributions of effective radial stress within the soil domain at the end of self-weight and suction installations. 173
8.38 Distributions of effective vertical stress within the soil domain at the end of self-weight and suction installations. 174
8.39 Distributions of excess pore-water pressure within the soil domain at the end of self-weight and suction installations. 175

8.40 Distributions of porosity within the soil domain at the end of self-weight and suction installations. 176
8.41 Distributions of size of bounding-surface within the soil domain at the end of self-weight and suction installations. 177
8.42 Displacements of soil surface and caisson tip during setup after self-weight installation. 180
8.43 Interfacial forces during setup after self-weight installation. . . 180
8.44 Dissipation of excess pore-water pressure at sensors during setup after self-weight installation. 181
8.45 Distributions of effective radial and vertical stresses within the soil domain at the end of setup after self-weight installation. . 182
8.46 Distributions of excess pore-water pressure within the soil domain at the end of setup after self-weight installation. 183
8.47 Distribution of size of bounding-surface within the soil domain at the end of setup after self-weight installation. 184
8.48 Displacements of soil surface and caisson tip during setup after suction installation. 185
8.49 Interfacial forces during setup after suction installation. 186
8.50 Dissipation of excess pore-water pressure at sensors during setup after suction installation. 188
8.51 Distributions of effective radial and vertical stresses within the soil domain at the end of setup after suction installation. . . . 189
8.52 Distributions of excess pore-water pressure and size of bounding-surface within the soil domain at the end of setup after suction installation. 190

8.53 Vented axial capacity of caisson at 1 in/sec pullout rate after self-weight installation. 195
8.54 Components of ultimate axial capacity for SWP-VR. 195
8.55 Vented axial capacity of caisson at 1 in/sec pullout rate after suction installation. 196
8.56 Components of ultimate axial capacity for SUC-VR. 196
8.57 Vented axial capacity of caisson at 1 in per 2 days pullout rate after self-weight installation. 198
8.58 Components of ultimate axial capacity for SWP-VS. 198
8.59 Vented axial capacity of caisson at 1 in per 2 days pullout rate after suction installation. 200
8.60 Components of ultimate axial capacity for SUC-VS. 200
8.61 Vented axial capacity of caisson under drained condition after self-weight installation. 203
8.62 Components of ultimate axial capacity for SWP-VD. 204
8.63 Vented axial capacity of caisson under drained condition after suction installation. 206
8.64 Components of ultimate axial capacity for SUC-VD. 207
8.65 Closed axial capacity of caisson at 1 inch/sec pullout rate after self-weight installation. 209
8.66 Components of ultimate axial capacity for SWP-CR. 209
8.67 Closed axial capacity of caisson at 1 inch/sec pullout rate after suction installation. 211
8.68 Components of ultimate axial capacity for SUC-CR. 211
8.69 Summary of axial pullout capacity and comparison with laboratory test results (Luke, 2002). 212

8.70 Caisson-soil 3D mesh at the end of 48-hour setup following self-weight installation. 217
8.71 Caisson-soil 3D mesh at the end of 48-hour setup following suction installation. 218
8.72 Ultimate horizontal load capacity of caisson installed by self-weight. 219
8.73 Load-displacement curve for caisson installed by self-weight and subjected to horizontal load at 10 inch above caisson tip. . . . 220
8.74 Distribution of excess pore-water pressure at ultimate horizontal load acting at 10 inch above tip of the caisson installed by self-weight [−ve value indicates suction (ABAQUS sign convention for excess pore-water pressure)]. 223
8.75 Distribution of effective radial stress at ultimate horizontal load acting at 10 inch above tip of the caisson installed by self-weight (−ve value indicates compressive stress). 224
8.76 Ultimate horizontal load capacity of caisson installed by self-weight and suction. 225
8.77 Load-displacement curve for caisson installed by suction and subjected to horizontal load at 10 inch above caisson tip. . . . 226
8.78 Distribution of excess pore-water pressure at ultimate horizontal load acting at 10 inch above tip of the caisson installed by suction [−ve value indicates suction (ABAQUS sign convention for excess pore-water pressure)]. 227
8.79 Distribution of effective radial stresses at ultimate horizontal load acting at 10 inch above tip of the caisson installed by suction (−ve value indicates compressive stresses). 228

8.80 Comparison of computed horizontal capacities. 229
8.81 Ultimate horizontal and vertical loads interaction diagram for caisson subjected to inclined load at 10 inch above caisson tip. 232

Chapter 1

INTRODUCTION

1.1 Overview

Development of a computational procedure and its application to the analysis of suction caisson behavior under axial as well as inclined loads is presented in this dissertation. Depending on caisson geometry and usage, terms such as caisson pile or anchor, bucket foundation, and skirted foundation or pile are used in the literature to refer to the caisson structure. Suction caissons are hollow cylinders with the top end capped. The aspect ratio of a caisson, defined as embedded length divided by diameter, typically ranges from 4 to 12, with the outer diameter ranging from 10 to 20 feet, and the wall thickness generally between 1 to 3 inch and, in some applications, varying (in stages) along the length of the caisson. Circumferential and/or vertical stiffeners are sometimes added to provide the required stability to the caisson during installation. The geometry of a typical caisson anchor is shown in Fig. 1.1 (only half of the caisson is presented to expose the interior).

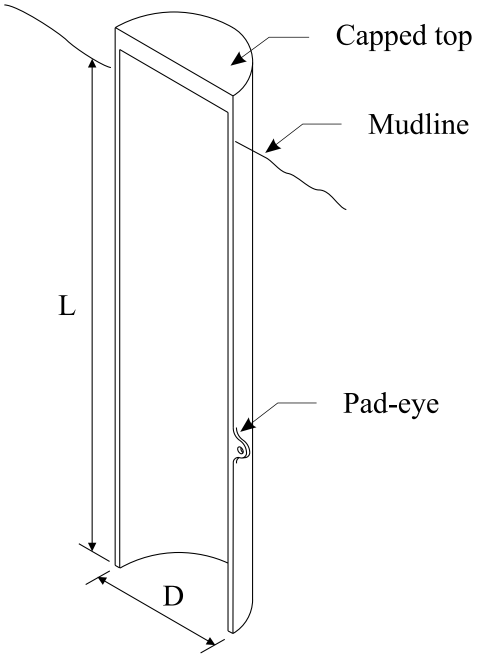

Figure 1.1: Typical (half) geometry of a caisson anchor.

During installation, the caisson is lowered to the seabed with the valves, located on the top cap, open. The caisson is first allowed to penetrate the seabed by self-weight. The butterfly valves fitted in the large holes of the top cap are designed to allow free flow of water through them without creating overpressure in the interior of the caisson during self-weight installation. When the penetration due to self-weight ceases, the valves at the top are closed. Pumps are then attached to the smaller valves located at the top to remove water trapped in the caisson interior. Underwater operations such as monitoring and controlling of valves and pumps are performed using a Remotely Operated Vehicle (ROV) at depth. Removal of water by pumping produces negative pressure in the interior of the caisson. Additional downward pressure, equal to the difference between the reduced pressure in the interior of the caisson and water pressure surrounding the caisson, acts on the caisson and drives it to required depth in the seabed. Installation of the caisson by pumping water from the interior is known as suction installation. The caisson installation sequence is shown in Fig. 1.2.

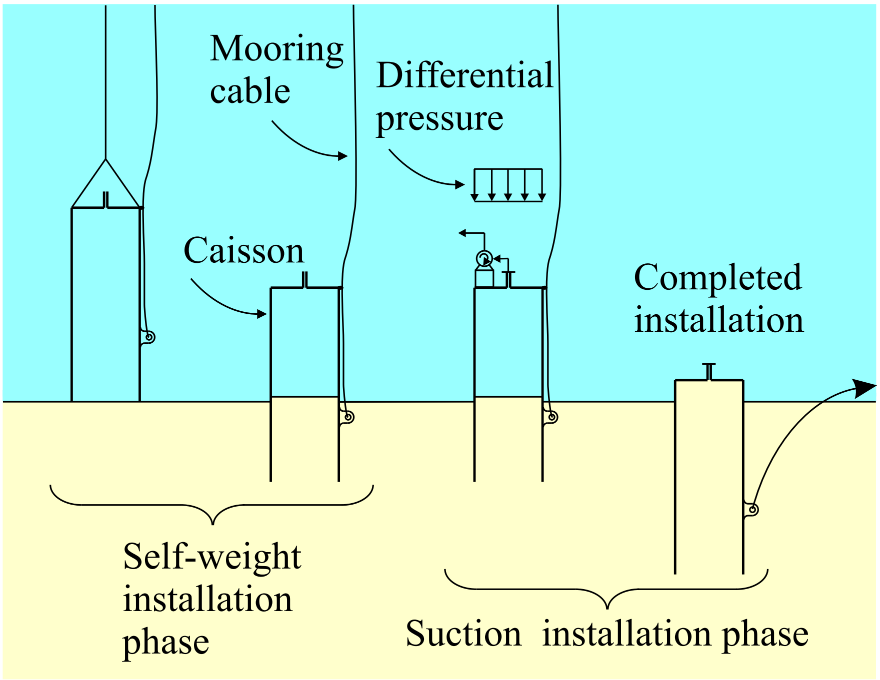

Figure 1.2: Caisson installation sequence.

The use of suction caissons as foundations for deep-water offshore structures and anchors for mooring lines has been increasing in the last decade. Caissons used as foundations for a Tension Leg Platform (TLP) are shown in Fig. 1.3 while caisson used as anchors for catenary and taut mooring lines securing an FPSO (Floating Production, Storage and Offloading) facility are depicted in Fig. 1.4. Suction caissons are an attractive option with regard to providing anchorage for floating structures in deep-water as they offer a number of advantages in that environment. They are easier to install than impact-driven piles and can be used in water depths well beyond where pile driving becomes infeasible. Suction caissons have higher load capacities than drag embedment anchors and can be inserted reliably at preselected locations and depths with minimum disturbance to the seafloor environment and adjacent facilities. Sparrevik (Sparrevik, 2001) estimates that there are as many as 300 caissons in operation around the world.

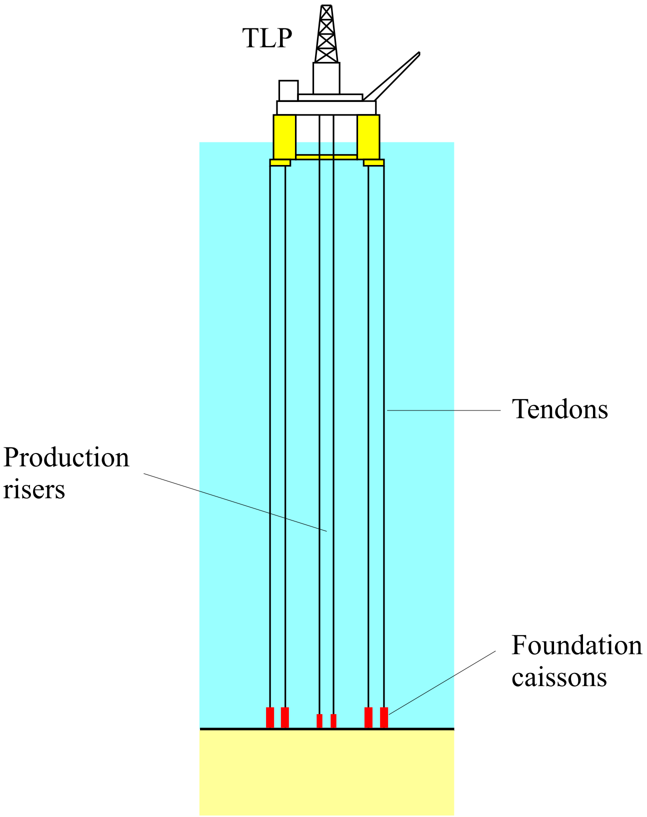

Figure 1.3: Caissons used as foundations for a Tension Leg Platform (TLP).

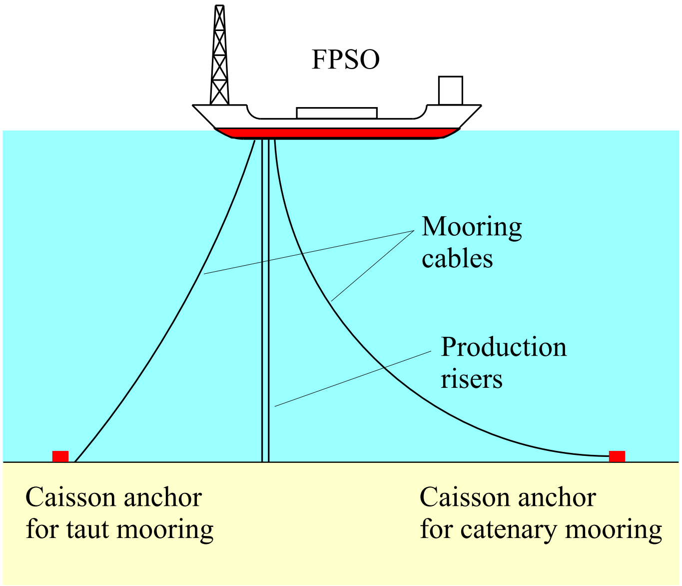

Figure 1.4: Caissons used as anchors for catenary and taut mooring lines.

Loads acting on caisson foundations and anchors are combinations of permanent (static) loads, cyclic loads at frequencies resulting from wind loading and from loop currents. For caissons used as foundations for a floating offshore facility, such as tension-leg platform (TLP), the cables or tendons extending from bottom of the facility are attached at the center of the caisson top plate and, therefore, a nearly vertical load is transmitted to the caisson. On the other hand, for caisson anchors, the mooring line is generally attached through a pad-eye which is located at about two thirds of the caisson length, thus transmitting horizontal loads (catenary mooring lines) or inclined loads (taut mooring lines) on the caisson anchor.

The capacity of suction caissons in holding tensile loads results from the combined effect of the following components (Albert *et al.*, 1987):

1. Passive suction developed under the caisson sealed cap;
2. Self-weight of the caisson, foundation template, and ballast (if any);
3. Shearing or frictional resistance along the caisson-soil interfaces;
4. Submerged weight of the soil plug inside the caisson; and
5. Reverse end bearing capacity, calculated by reversing the role of the vertical (overburden) stress in bearing capacity equations (Rauch, 2004).

Resistance against short-term axial pullout is obtained from development of the passive suction and friction along exterior interface between caisson and soil. In the longer term, dissipation of suction transfers pullout force to interior caisson-soil interface and complete dissipation of the pressure may result in complete or partial withdrawal of the caisson. Therefore, capacity of caisson under long-term axial pullout loading is governed by shearing resistance along the caisson-soil interfaces.

1.2 Literature Review

The first experimental study on suction anchors to evaluate their feasibility was reported by Goodman *et al.* (1961). Since the 1970s, several researchers have worked to obtain better understanding of suction caisson behavior by means of field tests, laboratory tests, and numerical simulations. Early full-scale tests in the field were reported by Hogervorst (1980). Soon thereafter, Senpere and Auvergne (1982) described the first commercial use of suction caissons as anchors.

In the following sections, selected field tests, laboratory tests, and numerical investigations of suction caissons that have been documented in the literature are summarized along with a review of the literature pertaining to design issues and applications of the caissons.

1.2.1 Field Tests

Extensive field tests on small-scale and full-scale caissons have been carried out by several researchers to determine installation characteristics and axial and lateral load capacities of the caissons. Although, field testing is expensive and time-consuming, it is valuable in obtaining geotechnical information relevant to the design of future caissons. The aspect ratio of the caissons tested ranges from 1 to 10 and both sandy and clayey soil conditions were examined. During the tests, the caisson behavior was recorded under various loading conditions. In the following paragraphs, a review of selected field tests is presented.

After conducting laboratory tests and a small-scale field test, Hogervorst (1980) performed three full-scale field tests on suction caisson anchors having 12.5 ft (3.8 m) diameter with length ranging from 16.4 to 32.8 ft (5 to 10 m), installed in sandy and clayey soils. The objectives of the tests were to study installation characteristics of the caissons and measure their axial as well as lateral capacities. The successful field tests provided an opportunity for systematic evaluation of the potential of caissons to anchor floating production facilities and proved the feasibility of installing caissons by the application of suction.

Tjelta *et al.* (1986) performed two large-scale field penetration tests to collect important information for the design of the CONDEEP Gullfaks C fixed concrete platform. The test structure consisted of two steel cylinders of 75 ft (23 m) height and 21 ft (6.5 m) diameter connected to each other through a concrete panel. The test assembly was installed to 72 ft (22 m) penetration in water depth of about 655 ft (200 m). The objectives of the testing program were to observe tip resistance and wall friction, confirm predictions and learn about uncertain factors related to installation and operation. The success of the tests proved the feasibility of installing long concrete skirts by suction.

Dyvik *et al.* (1993) reported four small-scale (model) field tests on a suction anchor consisting of four cylindrical cells, capped at top end, of diameter equal to 3 ft (0.87 m) and length of 2.7 ft (0.82 m), installed in soft clays at the Snorre oil and gas field in the North Sea. Both static and cyclic loading conditions were investigated. The objective of the tests was to compare measured response of the anchors to the response predicted adopting analytical foundation design procedures developed by the Norwegian Geotechnical Institute (NGI) for the design of foundations for offshore gravity platforms (Dyvik *et al.*, 1989 and Andersen *et al.*, 1989), and thus to check the validity of these procedures for design of suction anchors. Good agreement between measurements and predictions of anchor response was observed, thus demonstrating the applicability of the procedures to design such anchors (Andersen *et al.*, 1993). The investigation showed that suction anchors are viable foundations for tension leg platforms (TLPs) and permitted observation of stiffness degradation under cyclic loading at different load levels.

Keaveny *et al.* (1994) carried out five large-scale field model tests on a suction anchor installed in saturated clay and subjected to static and cyclic horizontal loads. The anchor consisted of two cylindrical cells of 2.3 ft (0.7 m) diameter and 4.6 ft (1.4 m) length. The objectives of the tests were to investigate the influence of pad-eye location and load cycles on the horizontal capacity. Approximately 100% increase in the capacity was observed by moving the pad-eye from mudline level to half-depth of the anchor and about 10% reduction in capacity was observed under cyclic loading.

Cho *et al.* (2002) conducted a series of field installation tests on steel suction caissons having inside diameter ranging from 1.65 to 8.2 ft (0.5 m to 2.5 m) and length of 16.4 (5 m), in the Onsan harbor located in Southeastern Korea. The suction caissons were installed in silty sand in water depth of about 33 ft (10 m). The objective of the tests was to validate response of the caissons observed during small-scale (model) laboratory tests (Bang *et al.*, 2000).

At present, recorded data from several field tests is available to demonstrate applicability and versatility of the caissons as foundations as well as anchors. Successful field tests proved feasibility of installing the caissons by suction and showed that they can be designed to perform efficiently in a variety of soil and loading conditions.

1.2.2 Laboratory Model Tests

Efficient and economical laboratory testing of model suction caissons can be undertaken to investigate performance of the caissons under a variety of conditions. The laboratory tests conducted on vacuum anchors and caisson anchors are summarized in the following sections.

Tests on Vacuum Anchors

Laboratory tests on vacuum anchors were conducted by Goodman *et al.* (1961), Brown and Nacci (1971), Wang *et al.* (1975), Helfrich *et al.* (1976), and Wang *et al.* (1977 and 1978). The vacuum anchors are shallow surface foundations generally used for providing temporary anchorage and require that the water be pumped out during their application to generate the required capacity (Wang *et al.*, 1975). The aspect ratio of the anchors tested ranged from 0.1 to 2.1 and different soil types were considered. In the following paragraphs a review of the laboratory tests on vacuum anchors is presented.

The first reported laboratory model tests on vacuum anchors were performed by Goodman *et al.* (1961) to determine the feasibility of anchoring mobile military field equipment. Different types of soils ranging from sand of medium fineness to highly plastic clay were used for the testing. The anchors used were of two sizes, diameter equal to 3.1 inch (79 mm) and 3.5 inch (89 mm) with length equal to 3.9 inch (99 mm) and 7.4 inch (188 mm), respectively. The study showed that the vacuum anchors in different soils are feasible for anchoring floating equipment but their response is better in clayey soils than in sandy soils.

Brown and Nacci (1971) conducted a series of laboratory tests, 14 tests in loose sand and 15 tests in dense sand, on vacuum anchors having 10 inch (254 mm) diameter and 1.75 inch (44 mm) embedded-length to study their behavior and water flow characteristics in granular soils. The tests showed that the vacuum anchors are effective for providing short-term anchorage and offer high reaction-to-weight ratio, reusability, and reversibility. The test results pointed to a linear relationship between pullout capacity and applied suction. Based on the test results, combined with observed behavior and failure mechanisms, a theory was proposed to predict pullout capacity of such anchors.

To investigate the feasibility and efficiency of the vacuum anchors, Wang *et al.* (1975) performed laboratory tests on eight model anchors installed in sandy, silty, and clayey soils. The values of the aspect ratio investigated were 0.1 and 0.5 with diameter equal to 4.5, 5.5, 7.9 and 13.25 inch. On the basis of the study, it was suspected that the anchors with lower aspect ratio would be more efficient in cohesionless soils while anchors with higher aspect ratio would be more effective in clayey soils. Linear increase in pullout capacity was observed with increasing suction, supporting earlier findings by Brown and Nacci (1971). Later, Wang *et al.* (1977) developed equations to estimate the pullout capacity of vacuum anchors based on observed failure mechanisms and adopting Mohr-Coulomb failure criteria and later, Wang *et al.* (1978) presented sample design examples to demonstrate practical applications of the anchors.

A series of 12 laboratory tests on vacuum anchors having diameter of 16 inch (406 mm) and length of 10 inch (254 mm) and installed in sand were conducted by Helfrich *et al.* (1976). The goals of the study were to generate additional test data for design purposes and to study anchor performance. As before, a linear relation between pullout capacity and suction was observed and predictions based on Mohr-Coulomb failure criteria matched well with measured capacities.

The significant findings from the laboratory tests on vacuum anchors are: for a given aspect ratio, anchor capacity increases linearly with increasing suction; the pullout capacity of vacuum anchors can be estimated reliably using available design methods; and the vacuum anchors are effective in providing short-term anchorage.

Tests on Suction Anchors

Model suction caissons have been tested under 1-g acceleration and controlled laboratory conditions by several researchers. The caissons studied were of aspect ratio in the range of 1 to 12 and were tested under various loading and soil conditions. Laboratory tests on model suction caissons conducted earlier were focused on studying efficiency and feasibility of the caissons and identifying important parameters governing their performance. Later tests were focused on improving the design methodology. In the following paragraphs, a review of selected laboratory tests on suction anchors is presented.

Larsen (1989) conducted 15 laboratory tests on model suction caissons with diameter equal to 4, 8, and 12 inch and length of 15 inch, and installed in sandy and clayey soils. The objectives of the testing program were to observe the mechanical behavior of the soil and caisson during installation and determine the lateral load capacity under static and cyclic loads. For caissons installed in sandy soil, the measured capacities under static and cyclic loads were identical but for caissons installed in normally consolidated clayey soil, the measured capacity under cyclic loading was reduced to 1/2 to 2/3 of the measured capacity under static loads. The test results demonstrated the efficiency of suction application for caisson installation.

Steensen-Bach (1992) performed 77 laboratory tests on suction caissons with aspect ratio ranging from 1.67 to 3.33 and diameter ranging from 1.9 inch (48 mm) to 3.1 inch (80 mm) installed in sandy and clayey soils. The goals of the study were to identify the contribution of suction generated during pullout to the capacity and obtain additional test data to develop design procedures.

The capacity of caissons installed in sand was found to be proportional to the generated suction. Similar observations had been made earlier by Brown and Nacci (1971) and Wang *et al.* (1975) for vacuum anchors installed in sandy soils. For caissons installed in clayey soils, the increase in pullout capacity was found to be due to a suction-induced transition in failure mechanism. Three different failure mechanisms for caissons installed in clayey soils were observed and identified at different levels of suction : local shear failure along the caisson wall; local tension failure; and general shear or reverse bearing capacity failure.

Cauble (1996) reported 14 laboratory tests on a model suction caisson installed in K_0-normally consolidated clay samples. A model caisson having both diameter and length equal to 2 inch (51 mm) was used in all the tests. The experiments were performed using an automated laboratory device which records data regarding response of the soil sample during various test stages. The tests were designed to simulate installation of caisson by suction and "pushing", reconsolidation (or setup) following installation, and subsequent undrained monotonic and sustained tensile pullout. From the laboratory results, it was concluded that wall friction contributes approximately 60% to the total capacity under monotonic pullout and that the sustained tensile load greater than the wall resistance under undrained condition leads to caisson failure. The study suggested a need for additional experimentation and analysis to clarify some of the results.

Datta and Kumar (1996) carried out 18 laboratory tests on suction caissons installed in soft clayey soils. The caissons tested were of 1.5 inch (38 mm) in diameter with aspect ratio of 2, 4, and 8, at different rates of load application. The objective of the test series was to evaluate suction force generated under the caisson during pullout. From the test results, it was observed that the suction force increases with increasing rate of load application and depth of embedment; and full suction force is developed at large displacement after mobilization of peak wall friction.

Singh *et al.* (1996) conducted eighteen laboratory tests on model suction caissons installed in soft clay. The objectives of the tests were to investigate suitability of the caissons as foundations for TLPs; to study behavior of the caissons under static axial pullout; and to evaluate the influence of pullout rate, aspect ratio, passive suction developed under the sealed cap, and water content on the pullout capacity. Caisson aspect ratio of 0.75 and 1.5 with a diameter of 4.33 inch (110 mm) were investigated. The pullout force was observed to increase with pullout displacement up to about 60% of the caisson diameter. It was also noted that the soil plug moved upwards with the caisson, and passive suction contributed significantly to the pullout resistance under short-term static loading.

Rao *et al.* (1997a) performed a series of cyclic loading tests on model suction caissons to investigate their behavior under axial pullout. The caissons tested were of aspect ratio 2 and having 3 inch (75 mm) diameter, and installed in soft marine clay. The test results showed that the capacity of caissons was unaffected at low values of the cyclic load ratio but the capacity was reduced dramatically under higher values of the ratio. In the later study by Rao *et al.* (1997b), additional laboratory tests were conducted on suction caissons. The caissons tested were of aspect ratio ranging from 1 to 2 and 3 inch (75 mm) diameter, installed in soft marine clay. For the new series of laboratory tests, the scope of the study was extended to investigate variation in suction under short-term monotonic and sustained loads. Under short-term monotonic loading, increase in suction was observed with increase in displacement while under sustained pullout, anchor failure in the form of complete removal did not occur within the observed time frame.

El-Gharbawy (1998) conducted a series of static as well as cyclic loading tests on suction caisson models to study their behavior and pullout capacity. Both vertical and inclined loading conditions were examined and different rates of load application were considered to simulate undrained and drained conditions in clayey soils. The load was applied at the center of the top cap. Caissons with aspect ratio of 2, 4, 6, and 12 were tested to investigate the effect of increasing aspect ratio on penetration resistance and pullout capacity. From the results of the experimental investigation, it was found that the rate of pullout has a significant effect on the capacity and the long-term pullout capacity is the upper limit on peak cyclic loading. Local shear failure along the caisson wall and a general shear failure (reverse bearing capacity failure) were observed to occur under drained and undrained conditions, respectively.

Byrne and Houlsby (2000 and 2002a) conducted an experimental investigation on suction caissons subjected to a variety of cyclic loads, installed in oil-saturated sandy soil. The authors did not observe any degradation of caisson capacity under cyclic loading, but did observe some effect of the rate of load application on the caisson response.

Luke (2002) reported results from 17 laboratory experiments to investigate behavior of caissons under axial pullout loads in normally consolidated clayey soils. The model suction caisson used in the experiments was constructed from an anodized aluminum tube with an outer diameter of 4 inch (100 mm) and was installed to 32 inch (800 mm) by self-weight alone, or self-weight followed by suction. After complete dissipation of excess pore-water pressure, axial pullout tests were performed rapidly as well as slowly. From the study, important conclusions related to caisson design, and recommendations for future research were made.

Coffman (2003) conducted nine laboratory tests on a model caisson installed in normally consolidated kaolin and subjected to horizontal load applied at various points along the lower half of the caisson. The objective of the testing program was to gather experimental data to support development of an improved analytical method for design of such caissons. The optimum location of horizontal load application corresponding to maximum caisson capacity was found to be at about two-thirds of the caisson depth below the mudline. The measured capacities were compared with the predictions from a simplified limit equilibrium analysis and good agreement between them was reported.

1.2.3 Centrifuge Testing of Suction Caissons

Geotechnical centrifuge tests on model suction caissons have been carried out to simulate the stress conditions and soil response at the field scale. These tests are quite costly and remain subject to various limitations. In the following paragraphs a review of selected centrifuge tests on caissons is presented.

Clukey and Morrison (1993) undertook a combined centrifuge test and analytical study to investigate the response of steel suction caisson foundations under axial pullout load and soil conditions typically encountered in the Gulf of Mexico. The centrifuge tests at 100-g acceleration were performed on a cylindrical single-cell caisson with an aspect ratio of about 2. The caisson geometry and response were scaled conforming to the laws of similitude outlined in Ko (1988). Finite-element simulation of an undrained axial pullout test was performed using 8-node quadratic axisymmetric elements available in ABAQUS/Standard program (HKS, 1998 and 2000), a commercially available general purpose finite-element analysis program. The nonlinear soil response was modeled with a tri-linear approximation of the stress-strain behavior. The finite-element study of the axial pullout case showed good agreement with the results obtained from centrifuge tests. In a later study by Clukey *et al.* (1995), the centrifuge testing program was extended to include cyclic axial and inclined loads. From the centrifuge test results, it was concluded that about 60-70 percentage of the axial pullout capacity is derived from reverse end bearing of the caisson. The combination of cyclic load ratio and the number of applied cycles that cause failure of the foundation was obtained from the cyclic load tests. Additional centrifuge tests were carried out by Clukey and Phillips (2002) to investigate the behavior of suction caissons under loading conditions for semi-taut to taut legged mooring systems.

Randolph at. al. (1998) performed centrifuge tests on suction caissons subjected to quasi-horizontal loads applied through a catenary mooring system and compared the test results with the theoretical predictions obtained using a three-dimensional upper bound analysis. The centrifuge tests were conducted under monotonic and cyclic loads on caissons installed in soils with different strength profiles. In general, a good agreement between predicted and measured capacities was observed.

House (2000) presented results from a series of geotechnical centrifuge tests conducted to study installation and response of a scaled prototype caisson. Monotonic inverse catenary loading was applied to the model caisson installed in normally consolidated kaolin clay. The objective of the testing program was to investigate the possible influence of the caisson geometry and soil characteristics on the monotonic holding capacities of the laterally loaded caissons. Measured results were compared with the predicted response adopting upper-bound plasticity analysis and good agreement between measurements and predictions was reported. It was concluded that additional data is needed to develop an optimum design methodology for the caissons.

Cao *et al.* (2001 and 2002a) presented results from eight centrifuge tests conducted on suction caissons using C-CORE's centrifuge facility (Phillips *et al.*, 1994). The tests were carried out to investigate behavior of the caissons installed in normally consolidated clay. A caisson having aspect ratio of about 3.5 was installed in-flight by self-weight, followed by suction. The caisson was then pulled out in the axial direction. The test results indicated that the penetration resistance of the caisson increased linearly with depth during both self-weight and suction installations.

Andersen *et al.* (2003) carried out three centrifuge model tests on caissons installed in normally consolidated soft clay. The objective was to investigate penetration characteristics of the caissons in soft clay. With the help of suction during installation, the caissons were installed to aspect ratio ranging from 12.4 to 14.5. It was reported that when suction was used for installation of caisson, all the displaced clay moved into the caisson interior causing considerable amount of heaving of the soil plug.

1.2.4 Limit Analysis Using Plasticity Theory

A simplified procedure based on the upper-bound method of plasticity theory was developed by Murff and Hamilton (1993) to estimate the capacity of laterally loaded piles under undrained conditions. The proposed method is an extension of the exact solution obtained by Randolph and Houslby (1984) for the limiting lateral resistance of a deeply embedded circular pile in cohesive soils. Aubeny *et al.* (2003a) adopted the proposed procedure to estimate lateral load capacity of suction caisson anchors as a function of the load attachment point location and load inclination angle, and later Aubeny *et al.* (2003b) refined the method for skin resistance coefficient α to be less than unity. The simplified plasticity procedure employed for caissons is based on an assumed kinematically admissible collapse mechanism, a flow zone around the base of the caisson and a hemispherical failure surface at the caisson tip. The validity of the simplified formulation is demonstrated through comparison with solutions obtained from rigorous three-dimensional finite-element analysis and results obtained from centrifuge tests (Clukey *et al.*, 2003).

1.2.5 Numerical Analysis

Research studies on suction caissons involving extensive axisymmetric and three-dimensional numerical simulations have been carried out in the past to determine their capacity under different loading and drainage conditions. In all cases, the stress-strain behavior of the soil was represented by means of plasticity models. The suction caisson was wished in place, with no attempt to simulate the installation process, assuming perfect interface bonding between the caisson and the surrounding soil. The initial state of stress in the soil was typically estimated in terms of the submerged unit weight and the lateral earth pressure coefficient at rest. In the following paragraphs a review of selected numerical studies is presented.

Erbrich (1994), using the ABAQUS program, conducted a series of finite-element analyses to estimate capacity of suction caissons used as foundations for fixed offshore steel platforms. Comparison between finite-element predictions and the results of a number of model tests conducted by Wang *et al.* (1978) was presented to demonstrate applicability of such analyses to estimate foundation capacity. Both standard Drucker-Prager and capped Drucker-Prager plasticity models were adopted to model nonlinear behavior of dense sand.

Sukumarn *et al.* (1999a), and Sukumaran and McCarron (1999b) documented an application of the finite-element method to estimate the capacity of suction caisson foundations installed in soft clays and subjected to axial and lateral loads under undrained conditions. Both two- and three-dimensional foundation models were analyzed using the ABAQUS program. The nonlinear behavior of the soft clay was approximated as that of an elastic-perfectly-plastic model adopting the (pressure-independent) von Mises yield criterion. The initial stresses in the soft clay were calculated assuming uniform submerged unit weight through the depth with a coefficient of lateral earth pressure equal to 0.7 to 1.0. The shear strength was assumed to be zero at the mudline level and increasing linearly with depth. The effects of load inclination, location of pad-eye, and aspect ratio on caisson response were investigated. The estimated capacities were compared with limit solutions proposed by Murff and Hamilton (1993) and Matlock (1970). The study demonstrated that finite-element analysis can be used to estimate the capacity of suction caisson foundations.

Bang and Cho (1999) conducted an analytical feasibility study to evaluate the effect of various cross-section shapes on the overall performance of suction caissons to be used for providing required mooring capacities for very large Mobile Offshore (military) Bases. The ABAQUS program was used to perform 3D finite-element analyses on axially and laterally loaded suction caissons having circular, Y-shaped and triangular cross-sections. The nonlinear behavior of seafloor sand was represented by means of a Drucker-Prager plasticity model.

Handayanu *et al.* (1999 and 2000) used a quasi-three-dimensional finite-element model to study the response of suction caissons subjected to vertical uplift and inclined loads. Axisymmetric elements with asymmetric loading available in the ABAQUS program were used to generate the finite-element model. The soil was modeled as a porous medium and its nonlinear behavior was represented by the cam-clay model. The results obtained from the finite-element analyses were verified by comparison with the laboratory results documented by Cauble (1997) and El-Gharbawy (1998).

Deng and Carter (1999a) conducted finite-element analyses on suction caissons to study the soil deformation patterns, failure mechanisms, and holding capacities developed under vertical tensile loads. The analyses were performed using a finite-element analysis program, AFENA (Carter and Balaam, 2001) developed at the Center for Geotechnical Research at the University of Sydney, Australia. The nonlinear behavior of saturated cohesive soil was simulated using the modified cam-clay model. The numerical results obtained using AFENA were compared with the experimental results documented by Singh *et al.* (1996). Deng and Carter (1999b) later extended the study to include analyses of caissons subjected to inclined uplift loads under undrained conditions. Analyses of caissons subjected to inclined loads were performed adopting a semi-analytical finite-element method (Taiebat and Carter, 2001) which is based on Fourier series approximation of field quantities in the azimuthal direction. The predictions from this analysis results were compared with the analytical solutions obtained using the plasticity limit analysis technique developed by Murff and Hamilton (1993). The numerical results obtained for the caissons installed in sand are documented by Deng and Carter (2000a). On the basis of extensive finite-element investigation, simplified expressions were developed to estimate the capacity of suction caissons taking into account the influence of the aspect ratio of the caisson, the shear strength parameters of the soil, the soil permeability, and the loading rate (Deng and Carter, 2000b and 2002).

El-Gharbawy and Olson (2000) reported a series of finite-element analyses using the PLAXIS software to verify the results obtained from laboratory tests on suction caisson foundations (El-Gharbawy, 1998). The nonlinear behavior of clayey soil was represented by an elastic-perfectly-plastic model.

Zdravkovic *et al.* (2001) conducted finite-element analyses to study effects of load inclination, caisson aspect ratio, soil adhesion, and soil anisotropy on behavior of suction caissons. The finite-element analyses were carried out using the three-dimensional Fourier series aided finite-element method in which field variables in azimuthal direction are expressed as Fourier series. Additional details about the procedure adopted for analysis are outlined in Potts and Zdravkovic (1999). Isotropic behavior of soft clay was represented using modified cam-clay soil model and anisotropic behavior was simulated using the MIT-E3 anisotropic soil model (Whittle and Kavvadas, 1994).

Cao *et al.* (2002b and 2003) carried out finite-element analyses to investigate behavior of suction caissons subjected to axial loads under the conditions of centrifuge tests carried out at C-CORE (Cao *et al.*, 2001 and 2002a). The constitutive behavior of fully saturated porous soil media was modeled using the modified cam-clay model. Appropriate contact surfaces between soil and caisson wall were defined using the contact-surface option available in the ABAQUS/Standard program. The water in the interior of the caisson was modeled with a very soft porous material to simulate development of suction by tensile strains. The computed response of the caissons agreed well with the measured response from the centrifuge tests.

1.2.6 Design Issues and Uncertainties

In contrast to driven piles, the offshore industry has not reached consensus on guidelines for design of suction caissons as several issues and uncertainties related to capacity estimation and failure mechanisms are involved. Important design issues such as design factor of safety, deep-water site characterization, and capacity estimation are identified and discussed in detail by Clukey (2001), Gilbert and Murff (2001), and Huang *et al.* (2003). Other important issues such as setup time, cyclic loading, misalignment of the caisson, skin friction, optimum location of pad-eye, horizontal and vertical load capacity interaction, reverse end bearing, and effect of disturbed soil zone resulting from plowing of the pad-eye during installation need to be addressed properly for successful design of suction caissons.

Clukey (2001) suggested a need for additional model tests to further investigate and understand issues related to caisson capacity and also recommended development of a database of deep-water soil to reduce uncertainties involving soil properties. In view of differences in caisson design relative to conventional pile design, Gilbert and Murff (2001) identified a need for additional insight for quantifying reverse end bearing, lateral-axial interaction, and lateral capacity to reduce magnitude of uncertainties. Considering limited experimental test data and field experience, Huang *et al.* (2003) indicated a need for a research study involving field load tests combined with rigorous finite-element analysis to understand behavior of suction caissons under various loading conditions.

Another important design issue related to stability of caissons against buckling during installation was addressed by Burgess and Hird (1983) and Pinna *et al.* (2001). A preliminary investigation of reliability-based design of suction caisson foundations for deep-water applications was presented by Clukey *et al.* (2000).

1.2.7 Applications

The use of suction caissons as foundations and anchors for floating offshore facilities has increased since 1990's. The caissons have been installed in water depths ranging from about 131 ft (40 m) in the North Sea to 8400 ft (2560 m) in the Mississippi Canyon of the Gulf of Mexico (Sparrevik, 2001). In the following paragraphs selected applications of suction caissons documented in the literature are presented.

Senpere and Auvergne (1982) reported the first commercial application of suction caissons used for Catenary Anchor Leg Moorings (CALM) and presented the design and installation of twelve caissons for the Gorm field in the Danish sector of the North Sea. The caissons were designed by Single Buoy Moorings, Inc. and were installed during the summer of 1980, in 131 ft (40 m) water depth and designed to sustain a maximum horizontal force of 440 kips (200 T) acting at mudline, with a diameter of 11.5 ft (3.5 m) and length of

27.9 to 29.5 ft (8.5 to 9 m). The soil profile encountered at the site consists of 20 ft (6 m) sand layer underlain by 3.3 to 6.6 ft (1 to 2 m) of soft clay then by stiff clay. Laboratory and theoretical studies during design phase and field testing, and monitoring during and after caisson installation were carried out. The successful installation and higher reliability demonstrated through field testing underscored the appeal of the caissons for anchoring mooring systems.

Albert *et al.* (1987) conducted an investigation to study the feasibility of using large-diameter suction caissons as foundations for a tension-leg platform at a site located in the Southern Adriatic Sea, in water depth of 2713 ft (827 m). Problems related to installation and stability of the caisson, and foundation capacity were examined based on principles of soil mechanics. It was concluded that the foundation system is feasible for deep-water application and the need for experimental research was suggested to optimize its potential.

Tjelta (1994) presented geotechnical aspects related to design of caisson foundation for the Europipe 16/11-E jacket platform (now known as Draupner E jacket platform) that is located in the North Sea at a site where dense sand and 230 ft (70 m) of water depth are encountered. The permanent foundation consists of a 39.4 ft (12 m) diameter and 19.7 ft (6 m) long caisson at each of the corner legs of the jacket. In order to verify the penetrability of 19.7 ft long caissons in dense sand and check the development of required capacity, comprehensive model testing at the site and in the laboratory was conducted. On the basis of the tests, it was concluded that caisson installation in dense sand is feasible with the help of suction, and it is possible to generate the required capacity in sand. Details regarding the structural design of the caisson foundation are documented by Baerheim (1994).

Colliat *et al.* (1995) carried out comparative studies to determine a suitable mooring alternative for a process barge located at NKossa site in the Gulf of Guinea having a water depth of 558 ft (170 m) and soft normally consolidated clayey soil profile. The study showed that caisson foundations represent the most suitable option, both technically and economically. The use of 16.4 ft (5 m) diameter and 39.4 ft (12 m) long steel caissons for anchoring mooring lines at the site was reported by Colliat *et al.* (1996). Details regarding the design of the anchoring system and installation of the caissons are documented by Colliat *et al.* (1998).

Audibert *et al.* (2003) have reported application of suction caissons for anchoring BP's Horn Mountain SPAR in the Mississippi canyon area of the Gulf of Mexico. The SPAR is held in position in 5500 ft (1676 m) water depth by nine caissons. Six caissons with 18 ft (5.5 m) diameter with an embedment depth of 86 ft (26.2 m) were used for the least heavily loaded anchors and three caissons with 18 ft (5.5 m) diameter with an embedment depth of 91 ft (27.7 m) were used for the most heavily loaded anchors. A picture of a caisson before installation is presented in Fig. 1.5. Two 36 inch diameter butterfly valves provided at the top of the caisson are visible in the picture. The paper documents results obtained from geotechnical monitoring during installation of the nine caissons. Rendering of a caisson installed in place is shown in Fig. 1.6.

Recently, suction caissons were considered as foundations for an offshore wind turbine mast. The wind loads acting on the turbine produce a large time-varying horizontal load and overturning moment on its foundation that must, therefore, be designed to resist such loads. A single caisson foundation or a tripod foundation can be employed for supporting offshore wind turbine mast (Byrne, 2000). Feld *et al.* (1999) have reported development of tripod

Figure 1.5: A typical caisson used for anchoring BP's Horn Mountain SPAR, Courtesy: Dr. E.C. Clukey (BP America).

foundation concept with suction caisson in order to reduce the foundation cost for the offshore wind turbines. Houlsby and Byrne (2000) have documented challenges faced by the designers of the foundation system for the turbines, and suction caissons are proposed as a viable and economic option. In Byrne *et al.* (2002b), details regarding a research project undertaken at Oxford University (UK) to determine a design framework for shallow caisson foundations for the turbine masts is presented.

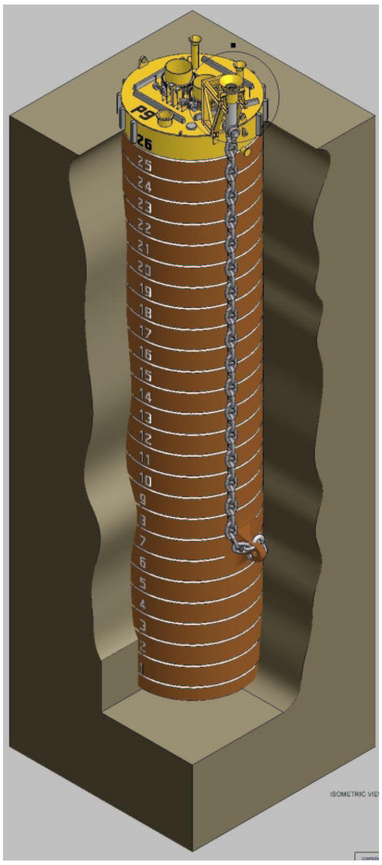

Figure 1.6: Caisson in place (Source: Mercier, 2003).

1.3 Objectives and Scope of the Study

The present work is an extension of the research reported by Vásquez (2000) and part of a comprehensive research project undertaken at the Offshore Technology Research Center (OTRC) at The University of Texas at Austin. The overall project aims at improving current understanding and developing effective procedures for the design of deep-water anchors (Olson *et al.*, 2001). The research project focuses on several different topics: laboratory tests on model caissons subjected to axial pullout and inclined loads (El-Gharbawy, 1998; Luke, 2002; and Coffman, 2003), development of a simplified prediction tool based on plastic limit analysis (Aubeny *et al.*, 2003a), development of a highly detailed finite-element computational procedure (Vásquez, 2000; and Maniar *et al.*, 2003), and reliability-based optimization of geotechnical investigations (Gambino and Gilbert, 1999; and Gilbert *et al.*, 1999).

Vásquez (2000) presented the development of a finite-element procedure to simulate the response of suction caissons subjected to axial pullout under both drained (long-term) and undrained (short-term) conditions. The procedure was applied to study the laboratory tests reported by El-Gharbawy (1998). Simulation results obtained for caisson installation process as well as response of caisson under axial pullout were reported.

The objectives of the present research study are: (1) to develop a computational framework to simulate behavior of suction caissons and to estimate their capacities under axial as well as inclined loads, including effects of both self-weight and suction installation and (2) to simulate laboratory tests, conducted on model suction caissons at The University of Texas at Austin (Luke, 2002; and Coffman, 2003), in order to calibrate as well as validate the computational procedure.

The computational procedure developed in the course of this study simulates suction caisson installation and estimates the capacities under axial as well as inclined loads. Suction caisson installation and axial pullout are analyzed under the assumption of axial symmetry. The soil is modeled with water-saturated porous finite-elements and the caisson is discretized using (impermeable) solid finite-elements. The nonlinear behavior of the clayey soil is modeled through a bounding-surface plasticity model for isotropic cohesive soils, and linear elastic behavior of caisson is assumed. The soil-caisson interfaces are modeled with a contact algorithm based on a slide-line formulation. Various remeshing tools are developed to eliminate the need for *a priori* specification of the caisson penetration path and to avoid use of excessively distorted finite elements along caisson-soil interfaces. The remeshing tool is an improvement over the procedure document by Vásquez (2000) in which the penetration path defined *a priori* as located immediately below the caisson tip and in the axial direction. This predefinition of the path did not account for the soil movement during caisson installation process. Due to the restriction on the soil movement, the selected path over (under) estimated amount of soil within the caisson interior during self-weight (suction) installation. Due to this the computed capacity might have been affected as it is function of radial stresses generated within the soil domain during installation process.

The developed formulation is used to obtain results from the simulation of the caisson installation, and reconsolidation (or setup) of surrounding soil following caisson installation, and caisson pullout. Three-dimensional caisson models under horizontal and inclined loads are analyzed using the ABAQUS/Standard program. The deformed geometry of the caisson-soil system, stresses within the soil and material state parameters obtained from axisymmetric simulation of the installation process are specified as initial conditions to carry out analysis of caisson under horizontal and inclined loads. In addition, a user-defined material subroutine for the bounding-surface plasticity model is supplied to the ABAQUS program to model behavior of the saturated clayey soil. The computed behavior of the caisson is compared with the observed behavior in the laboratory tests conducted at The University of Texas at Austin (Luke, 2002; and Coffman, 2003).

The dissertation is organized as follows: the treatment of saturated porous soil and caisson is presented in Chapters 2 and 3, respectively; the constitutive equations adopted for clayey soil and caisson are described in Chapter 4; interface conditions between soil and caisson and their contribution to the system of equations are outlined in Chapter 5; the remeshing scheme developed to determine the caisson penetration path is described in Chapter 6; the procedure for three-dimensional analysis is presented in Chapter 7; results obtained from simulation of laboratory tests are presented in Chapter 8; and a summary and conclusions along with recommendations are given in Chapter 9.

Chapter 2

SOIL AS A POROUS MEDIUM: GOVERNING EQUATIONS

2.1 Introduction

The behavior of saturated, porous, clayey soil is described using a mixture theory that accounts for coupling between soil deformation and pore-water flow. Thus, the saturated soil is viewed as a two-phase medium composed of solid (soil) and pore-fluid (water) phases. The mixture theory is based on the concept of volume fractions from the viewpoint of macromechanics. Each constituent of the porous medium is replaced by a substitute medium having reduced density, and occupying the entire control space. The principles of continuum mechanics are then available to describe the behavior of the substitute or equivalent medium at the macroscopic level.

One-dimensional consolidation of saturated-deformable-elastic-porous solids was first investigated by Terzaghi in 1923 adopting the effective stress principle. Biot (1941) extended the phenomenological approach of Terzaghi to study the generalized three-dimensional consolidation of elastic porous media. Based on the mixture theory proposed by Truesdell and Touppin (1960), Prévost (1980) developed a general framework for nonlinear consolidation of saturated porous media. A comprehensive review of historical development and current state of the porous media and mixture theories is presented by Coussy (1995) and de Boer (2000).

The balance laws governing interaction between soil deformation and pore-water flow, and their weak forms are presented in this chapter. The balance laws are derived adopting the mixture theory, and in Chapter 3 their three-field finite-element discretization is achieved adopting solid displacements, Darcy's velocities, and the excess pore-water pressure as field variables.

2.2 Governing Differential Equations: Balance Laws

Saturated soil is a two-phase material composed of solids and a liquid. It can be viewed as a “mixture” of phases that can be thought of as occupying the entire domain. The laws of continuum mechanics can be used to describe discrete behavior of the phases as if the particles behave collectively as a continuous medium (Prévost, 1980).

In this section, principles describing conservation of mixture mass, and conservation of linear momentum of mixture and fluid phase are developed considering the saturated soil medium as a continuum. For the development of the principles, an arbitrary region fixed in space is considered. The arbitrary region of volume V is denoted by Ω_t and is bounded by the surface $\partial\Omega_t$ of area A.

2.2.1 Conservation of Mixture Mass

Solid Phase

The mass of the solid phase in the region Ω_t denoted by m_s is given by the volume integral:

$$m_s = \int_{\Omega_t} \rho_s(\mathbf{x}, t)\left[1 - n_w(\mathbf{x}, t)\right] dV \tag{2.1}$$

where ρ_s is the macroscopic average mass density of the solid grains that is, in general, a function of location $\mathbf{x}$ (in the deformed configuration) and time t, and n_w is the volume fraction of the voids, also known as porosity, defined as the ratio of the volume of voids to the total volume of the mixture. Porosity is a function of location $\mathbf{x}$ and time t. For saturated soil, the voids are filled with water. The law of conservation of mass requires that the material time derivative of the solid phase mass vanish. Therefore, the material time derivative of Eq. 2.1 with use of the transport theorem is written as:

$$\frac{d(m_s)}{dt} = \int_{\Omega_t} \left\{ \frac{\partial\left[\rho_s(1 - n_w)\right]}{\partial t} + div\left[\rho_s(1 - n_w)\,\mathbf{v}^s(\mathbf{x}, t)\right] \right\} dV = 0 \tag{2.2}$$

where $\mathbf{v}^s$ is the velocity of the solid phase. The div is the spatial divergence operator and for any vector $\mathbf{a}(\mathbf{x}, t)$ it is given by (in terms of derivatives of components with respect to a rectangular cartesian coordinate system):

$$div\left(\mathbf{a}\right)=\frac{\partial a_1}{\partial x_1}+\frac{\partial a_2}{\partial x_2}+\frac{\partial a_3}{\partial x_3}=\frac{\partial a_i}{\partial x_i}=a_{i,i} \tag{2.3}$$

The integration in Eq. 2.2 is carried out over the arbitrary region Ω_t, and with the assumption that each field quantity is smooth and continuous in the region, the integrand in Eq. 2.2 must vanish everywhere in the region. Hence,

$$\frac{\partial\left[\rho_s\left(1-n_w\right)\right]}{\partial t}+div\left[\rho_s\left(1-n_w\right)\mathbf{v}^s\right]=0 \tag{2.4}$$

In this work the soil grains are assumed to be incompressible and homogeneous. The conservation of mass of the solid phase then takes the following form:

$$\frac{\partial\left(n_w\right)}{\partial t}=div\left[\left(1-n_w\right)\mathbf{v}^s\right] \tag{2.5}$$

Fluid Phase

The mass of the fluid phase in the region Ω_t denoted by m_w is given by the volume integral:

$$m_w=\int_{\Omega_t}\left[\rho_w\left(\mathbf{x},t\right)n_w\left(\mathbf{x},t\right)\right]dV \tag{2.6}$$

where ρ_w is the macroscopic average mass density of the fluid that is, in general, a function of location $\mathbf{x}$ and time t. As before, the law of conservation of mass requires that the material time derivative of the fluid phase mass vanish. Therefore, the material time derivative of Eq. 2.6 with use of the transport theorem is written as:

$$\frac{d\left(m_w\right)}{dt} = \int_{\Omega_t} \left\{ \frac{\partial\left(\rho_w n_w\right)}{\partial t} + div\left[\rho_w n_w \mathbf{v}^w\left(\mathbf{x}, t\right)\right] \right\} dV = 0 \tag{2.7}$$

where $\mathbf{v}^w$ is the velocity of the fluid phase. As the integration is carried out over the arbitrary region Ω_t, and field quantities are assumed to be smooth and continuous, the integrand in Eq. 2.7 must vanish everywhere in the region. Hence,

$$\frac{\partial\left(\rho_w n_w\right)}{\partial t} + div\left(\rho_w n_w \mathbf{v}^w\right) = 0 \tag{2.8}$$

The conservation of the fluid phase can then be expressed as:

$$n_w \frac{\partial \rho_w}{\partial t} + \rho_w \frac{\partial n_w}{\partial t} + \rho_w div\left(n_w \mathbf{v}^w\right) + n_w \left[grad\left(\rho_w\right)\right]^T \mathbf{v}^w = 0 \tag{2.9}$$

where the superscript T indicates transposition, and *grad* is the spatial gradient operator. For any scalar $a\left(\mathbf{x}, t\right)$ it is defined as:

$$\left[grad\left(a\right)\right]_i = \frac{\partial a}{\partial x_i} \tag{2.10}$$

Mixture

The conservation of mass of the mixture can be derived by inserting Eq. 2.5 into Eq. 2.9 to obtain:

$$n_w \frac{\partial \rho_w}{\partial t} + \rho_w div\left[\left(1 - n_w\right)\mathbf{v}^s\right] + \rho_w div\left(n_w \mathbf{v}^w\right) + n_w \left[grad\left(\rho_w\right)\right]^T \mathbf{v}^w = 0 \tag{2.11}$$

Isothermal conditions are assumed, and small water volume change is assumed to be related to pressure change and bulk modulus. With the use of the chain-rule of differentiation, it can be shown that:

$$\frac{\partial \rho_w}{\partial x_i} = \frac{\partial \rho_w}{\partial p^w}\frac{\partial p^w}{\partial x_i} = -\frac{\rho_w}{\lambda_w}\frac{\partial p^w(\mathbf{x},t)}{\partial x_i} \tag{2.12}$$

and

$$\frac{\partial \rho_w}{\partial t} = \frac{\partial \rho_w}{\partial p^w}\frac{\partial p^w}{\partial t} = -\frac{\rho_w}{\lambda_w}\left\{\dot{p}^w - \left[grad\left(p^w\right)\right]^T \mathbf{v}^s\right\} \tag{2.13}$$

where p^w is the (absolute) pore-water pressure, $\dot{p}^w$ is the (Eulerian) time derivative of p^w, and λ_w is the bulk modulus of water. Use of Eqs. 2.12 and 2.13 in Eq. 2.11 with a nonzero value for the fluid density, the conservation of mixture mass can be written as:

$$\begin{aligned} -\frac{n_w}{\lambda_w}\frac{\partial p^w}{\partial t} + div\left[\left(1-n_w\right)\mathbf{v}^s\right] + & \\ div\left(n_w \mathbf{v}^w\right) - \frac{n_w}{\lambda_w}\left[grad\left(p^w\right)\right]^T \mathbf{v}^w &= 0 \end{aligned} \tag{2.14}$$

The relative or Darcy's velocity is defined as:

$$\mathbf{v}^r(\mathbf{x},t) = n_w\left(\mathbf{v}^w - \mathbf{v}^s\right) \tag{2.15}$$

and represents the relative volumetric rate of flow of fluid per unit area of the deforming soil mass (Borja and Alarcón, 1995).

Use of Eq. 2.15 into Eq. 2.14 leads to the final form of the conservation of mass of the mixture:

$$div\left(\mathbf{v}^s\right) + div\left(\mathbf{v}^r\right) - \frac{n_w}{\lambda_w}\dot{p}^w - \frac{1}{\lambda_w}\left[grad\left(p^w\right)\right]^T \mathbf{v}^r = 0 \tag{2.16}$$

If fluid phase is also assumed to be incompressible, i.e., $\lambda_w \rightarrow \infty$, Eq. 2.16 reduced to:

$$div\left(\mathbf{v}^{s}\right) + div\left(\mathbf{v}^{r}\right) = 0 \tag{2.17}$$

The above equation (Eq. 2.17) is analogous to the one that governs any incompressible single-phase medium. In the present formulation, the fluid phase is considered compressible. Therefore, Eq. 2.16 will be used for further discussion.

2.2.2 Conservation of Linear Momentum

The balance of linear momentum of the mixture is developed in terms of the effective stress tensor, $\boldsymbol{\sigma}^{eff}$ and the pore-water pressure, p^{w}. The Cauchy (total) stress tensor, $\boldsymbol{\sigma}^{Total}$ can be expressed as the sum (Terzaghi, 1923)

$$\boldsymbol{\sigma}^{Total} = \boldsymbol{\sigma}^{eff} + p^{w}\mathbf{I} \tag{2.18}$$

In Eq. 2.18, $\mathbf{I}$ represents (second-order) unit (identity) tensor. The Cauchy partial stress tensors arising from the intergranular and fluid stresses are denoted by $\boldsymbol{\sigma}^{s}$ and $\boldsymbol{\sigma}^{w}$, respectively. Then the Cauchy (total) stress tensor can be represented adopting an additive decomposition (Prévost, 1980; and Borja and Alarcón, 1995):

$$\boldsymbol{\sigma}^{Total} = \boldsymbol{\sigma}^{s} + \boldsymbol{\sigma}^{w} \tag{2.19}$$

The Cauchy partial stress tensors are area-averaged quantities and are related to the effective stress tensor and pore-fluid (water) pressure as (Prévost, 1980):

$$\begin{aligned}\boldsymbol{\sigma}^s &= \boldsymbol{\sigma}^{eff} + (1-n_w)\, p^w \mathbf{I} \\ \boldsymbol{\sigma}^w &= n_w p^w \mathbf{I}\end{aligned} \tag{2.20}$$

Solid Phase

The balance of linear momentum of the solid phase in the arbitrary but fixed region Ω_t is:

$$\int_{\Omega_t} \rho_s (1-n_w)(\mathbf{b}-\mathbf{a}^s)\, dV + \int_{\partial\Omega_t} \boldsymbol{\sigma}^s \cdot \mathbf{n} dA + \int_{\Omega_t} \mathbf{h}^s dV = \mathbf{0} \tag{2.21}$$

In Eq. 2.21, $\mathbf{b}$ is the body force per unit volume; $\mathbf{a}^s$ is the acceleration of the solid phase that is defined as the time derivative of the solid phase velocity $(\partial \mathbf{v}^s/\partial t)$; $\mathbf{n}$ is the unit normal oriented outwards to the surface $\partial\Omega_t$ bounding the region Ω_t in the deformed configuration; and $\mathbf{h}^s$ is the frictional drag or seepage force per unit volume acting on the solid phase due to fluid flow. The divergence theorem is applied to the second term in Eq. 2.21 to obtain the localized form of the balance of solid phase momentum which can be written as:

$$\rho_s (1-n_w)(\mathbf{b}-\mathbf{a}^s) + div\,(\boldsymbol{\sigma}^s) + \mathbf{h}^s = \mathbf{0} \tag{2.22}$$

Fluid Phase

The balance of linear momentum of the fluid phase in the arbitrary but fixed region Ω_t is:

$$\int_{\Omega_t} \rho_w n_w \left(\mathbf{b} - \mathbf{a}^w\right) dV + \int_{\partial\Omega_t} \boldsymbol{\sigma}^w \cdot \mathbf{n} dA + \int_{\Omega_t} \mathbf{h}^w dV = \mathbf{0} \tag{2.23}$$

In this equation, $\mathbf{h}^w$ is the reactive or resistive force per unit volume exerted by the solid phase on the fluid phase as the fluid flows through the voids; and the convective acceleration of fluid phase, $\mathbf{a}^w$ relative to the solid phase is defined as:

$$\mathbf{a}^w = \frac{\partial \mathbf{v}^w}{\partial t} + grad\left(\mathbf{v}^w\right)\left(\mathbf{v}^w - \mathbf{v}^s\right) \tag{2.24}$$

where the gradient of a vector $\mathbf{a}(\mathbf{x}, t)$ is defined as:

$$\left[grad\left(\mathbf{a}\right)\right]_{ij} = \frac{\partial a_i}{\partial x_j} \tag{2.25}$$

Use of the divergence theorem to the second term of Eq. 2.23 leads to the localized form of the balance of fluid phase momentum:

$$\rho_w n_w \left(\mathbf{b} - \mathbf{a}^w\right) + div\left(\boldsymbol{\sigma}^w\right) + \mathbf{h}^w = \mathbf{0} \tag{2.26}$$

where the divergence of a second-order tensor $\mathbf{T}(\mathbf{x}, t)$ is defined as:

$$\left[div\left(\mathbf{T}\right)\right]_i = \frac{\partial T_{i1}}{\partial x_1} + \frac{\partial T_{i2}}{\partial x_2} + \frac{\partial T_{i3}}{\partial x_3} = \frac{\partial T_{ij}}{\partial x_j} = T_{ij,j} \tag{2.27}$$

The second term in Eq. 2.26 is expanded using Eq. 2.20(b) to obtain:

$$div\left(\boldsymbol{\sigma}^w\right) = n_w grad\left(p^w\right) + p^w grad\left(n_w\right) \tag{2.28}$$

The forces $\mathbf{h}^s$ and $\mathbf{h}^w$ are interfacial reactive forces, and they equilibrate each other and therefore their sum is identically zero. Prévost (1980) combined the buoyancy force and the Stokes drag to showed that the interfacial forces can be calculated as:

$$\mathbf{h}^s = -\mathbf{h}^w = p^w grad\left(n_w\right) - n_w \rho_w \mathbf{k}^{-1}\left(\mathbf{v}^s - \mathbf{v}^w\right) \tag{2.29}$$

where $\mathbf{k}$ is the diagonal permeability tensor, and the superscript -1 indicates inversion.

The definition of Darcy's velocity (Eq. 2.15) is adopted to define the relative acceleration of the fluid phase $\mathbf{a}^r$ as:

$$\mathbf{a}^r\left(\mathbf{x}, t\right) = n_w\left(\mathbf{a}^w - \mathbf{a}^s\right) \tag{2.30}$$

and, after some algebra, it can be shown that:

$$\begin{aligned}\mathbf{a}^r = \frac{\partial \mathbf{v}^r}{\partial t} - \frac{\left(1-n_w\right) div\left(\mathbf{v}^s\right)}{n_w}\mathbf{v}^r + \frac{\left[grad\left(n_w\right)\right]^T \mathbf{v}^s}{n_w}\mathbf{v}^r + \\ \frac{1}{n_w} grad\left(\mathbf{v}^r\right)\mathbf{v}^r - \frac{\left[grad\left(n_w\right)\right]^T \mathbf{v}^r}{\left(n_w\right)^2}\mathbf{v}^r + grad\left(\mathbf{v}^s\right)\mathbf{v}^r\end{aligned} \tag{2.31}$$

Use of Eqs. 2.15, 2.28, 2.29, and 2.30 in Eq. 2.26 leads to the balance of linear momentum of the fluid phase:

$$\rho_w n_w\left(\mathbf{b} - \mathbf{a}^s\right) - \rho_w \mathbf{a}^r + n_w grad\left(p^w\right) - \rho_w \mathbf{k}^{-1}\mathbf{v}^r = \mathbf{0} \tag{2.32}$$

For later reference, Eq. 2.32 is divided by the porosity (n_w) to obtain the final form of the balance of linear momentum of the fluid phase as:

$$\rho_w\left(\mathbf{b} - \mathbf{a}^s\right) - \frac{\rho_w}{n_w}\mathbf{a}^r + grad\left(p^w\right) - \frac{\rho_w}{n_w}\mathbf{k}^{-1}\mathbf{v}^r = \mathbf{0} \tag{2.33}$$

Mixture

The balance of linear momentum of the mixture is obtained as the sum of Eqs. 2.22 and 2.26. It is easy to show with use of Eq. 2.19 that,

$$\rho_s\left(1-n_w\right)\left(\mathbf{b}-\mathbf{a}^s\right)+\rho_w n_w\left(\mathbf{b}-\mathbf{a}^w\right)+div\left(\boldsymbol{\sigma}^{Total}\right)=\mathbf{0} \tag{2.34}$$

Use of Eq. 2.30 into Eq. 2.34 with Eq. 2.18 leads to the final form of linear momentum balance of the mixture:

$$\left[\rho_s\left(1-n_w\right)+\rho_w n_w\right]\left(\mathbf{b}-\mathbf{a}^s\right)-\rho_w\mathbf{a}^r+div\left(\boldsymbol{\sigma}^{eff}\right)+grad\left(p^w\right)=\mathbf{0} \tag{2.35}$$

2.3 Excess Pore-Water Pressure Formulation

The flow of water within the soil is controlled by excess pore-water pressure, $\bar{p}^w$ defined as the difference between the total or absolute pore-water pressure p^w and the static or neutral pore-water pressure p_s:

$$\bar{p}^w=p^w-p_s \tag{2.36}$$

The static pore-water pressure is given by:

$$p_s=-\left[p_0+\gamma_w\left(z_{wt}-z_s\right)\right]=-\left[p_0+\rho_w g\left(z_{wt}-z_s\right)\right] \tag{2.37}$$

where p_0 is the atmospheric pressure, γ_w is the specific weight of water, g is the gravity acceleration, z_{wt} is the vertical position of the water table, and z_s is the vertical position of the soil particle. It is appropriate to work with the balance laws developed in terms of the excess pore-water pressure.

Use Eq. 2.37 in Eq. 2.36 to obtain:

$$\begin{aligned} p^w &= \bar{p}^w - \left[p_0 + \gamma_w \left(z_{wt} - z_s\right)\right] \\ &= \bar{p}^w - \left[p_0 + \gamma_w \mathbf{1}_z^T \left(\mathbf{x}_{wt} - \mathbf{x}_s\right)\right] \end{aligned} \tag{2.38}$$

where $\mathbf{1}_z$ is a unit vector oriented in the vertical (z) direction, $\mathbf{x}_{wt}$ is the position vector of the water table, and $\mathbf{x}_s$ is the position vector of the soil particle.

The following relations can be obtained from Eq. 2.38(b):

$$\frac{\partial p^w}{\partial t} = \frac{\partial \bar{p}^w}{\partial t} \tag{2.39}$$

$$\begin{aligned} \dot{p}^w &= \frac{\partial p^w}{\partial t} + \left[grad\left(p^w\right)\right]^T \mathbf{v}^s \\ \dot{\bar{p}}^w &= \frac{\partial \bar{p}^w}{\partial t} + \left[grad\left(\bar{p}^w\right)\right]^T \mathbf{v}^s \end{aligned} \tag{2.40}$$

$$\begin{aligned} grad\left(p^w\right) &= grad\left(\bar{p}^w\right) + \gamma_w \mathbf{1}_z^T \left[grad\left(\mathbf{x}_s\right)\right] \\ &= grad\left(\bar{p}^w\right) + \gamma_w \mathbf{1}_z^T \end{aligned} \tag{2.41}$$

$$\dot{p}^w = \dot{\bar{p}}^w + \gamma_w \mathbf{1}_z^T \mathbf{v}^s \tag{2.42}$$

Use of Eqs. 2.41 and 2.42, along with Eq. 2.16, the balance of the mixture mass can be written as:

$$\begin{aligned}div\left(\mathbf{v}^s\right) + div\left(\mathbf{v}^r\right) - \frac{n_w}{\lambda_w}\dot{\bar{p}}^w - \frac{n_w \gamma_w}{\lambda_w}\mathbf{1}_z^T \mathbf{v}^s - & \\ \frac{1}{\lambda_w}\left[grad\left(\bar{p}^w\right)\right]^T \mathbf{v}^r - \frac{\gamma_w}{\lambda_w}\mathbf{1}_z^T \mathbf{v}^r &= 0\end{aligned} \tag{2.43}$$

The body force per unit volume is assumed to be only due to the action of gravity in the vertical direction:

$$\mathbf{b} = -g\mathbf{1}_z \tag{2.44}$$

With the use of Eqs. 2.41, and 2.44 in Eq. 2.35, the balance of linear momentum of the mixture can be written as:

$$\left[\rho_s\left(1 - n_w\right) + \rho_w n_w\right]\left(\mathbf{b} - \mathbf{a}^s\right) - \rho_w \mathbf{a}^r - \rho_w \mathbf{b} + div\left(\boldsymbol{\sigma}^{eff}\right) + grad\left(\bar{p}^w\right) = \mathbf{0} \tag{2.45}$$

Again, with the use of Eqs. 2.41, and 2.44 in the Eq. 2.33, the balance of linear momentum of the fluid phase can be written as:

$$-\rho_w \mathbf{a}^s - \frac{\rho_w}{n_w}\mathbf{a}^r + grad\left(\bar{p}^w\right) - \frac{\rho_w}{n_w}\mathbf{k}^{-1}\mathbf{v}^r = \mathbf{0} \tag{2.46}$$

2.4 Boundary Conditions

Appropriate boundary conditions for the governing differential equations represented by Eqs. 2.43, 2.45 and 2.46 are as follows:

$$\begin{array}{lllllllll} \mathbf{u}^s & = & \bar{\mathbf{U}}^s & \texttt{on} & \Gamma_u & \texttt{and} & \boldsymbol{\sigma}^{Total}\cdot\mathbf{n} & = & \mathbf{t}^{Total} & \texttt{on} & \Gamma_\sigma \\ \mathbf{v}^r & = & \mathbf{V}^r & \texttt{on} & \Gamma_r & \texttt{and} & \bar{p}^w\mathbf{I}\cdot\mathbf{n} & = & \bar{\mathbf{t}}^p & \texttt{on} & \Gamma_w \\ \bar{p}^w & = & \bar{P}^w & \texttt{on} & \Gamma_p & \texttt{and} & \mathbf{v}^r\cdot\mathbf{n} & = & q & \texttt{on} & \Gamma_q \end{array} \tag{2.47}$$

where:

$$\begin{aligned} \Gamma_u \cap \Gamma_\sigma &= \Gamma_r \cap \Gamma_w = \Gamma_p \cap \Gamma_q = \emptyset \\ \Gamma_u \cup \Gamma_\sigma &= \Gamma_r \cup \Gamma_w = \Gamma_p \cup \Gamma_q = \partial\Omega_t \end{aligned} \tag{2.48}$$

and $\mathbf{n}$ is the outward unit normal vector to the surface $\partial\Omega_t$, $\mathbf{t}^{Total}$ is a vector of surface traction due to the total stresses, $\bar{\mathbf{t}}^p$ is a vector of surface traction due to the excess pore-water pressure, and q is the volumetric flow or surface flux. $\cup$ is the set union symbol, $\cap$ is the set intersection symbol, and $\emptyset$ denotes an empty set.

2.5 Variational Statement of the Balance Laws

In this section, the variational statement or weak form of the balance laws governing behavior of the mixture derived in the preceding section is described. The variational form is used with an eye on three-field finite-element discretization. The field variables adopted are solid displacements ($\mathbf{u}^s$), Darcy's velocities ($\mathbf{v}^r$), and excess pore-water pressure ($\bar{p}^w$).

The weak form is written with respect to the deformed domain or current configuration (Ω_t) at time t, which is not known *a priori*. It is convenient to use a previously known or reference configuration (Ω_τ) at time $\tau < t$ for performing integration of the weak form. The incompressibility of the solid phase assumed in the derivation of the Eq. 2.5 is adopted in order to convert the domain of integration from current to the reference configuration.

Consider an infinitesimal volume of the mixture (soil) denoted by dV from the reference configuration. At time τ, the volume of voids or water present in dV is equal to $n_w|_\tau \, dV \equiv n_0 dV$, and the volume of the solid phase is equal to $(1 - n_0)\, dV$. In the current configuration, the volume of the mixture dv is equal to JdV, where J is the determinant of the deformation gradient, and referred to as the Jacobian. Since the solid phase is assumed to be incompressible, the volume of solid phase in dv is conserved at $(1 - n_0)\, dV$, and the volume of voids changes to $JdV - (1 - n_0)\, dV$. Therefore, the porosity can be updated from reference to the current configuration according to:

$$n_w|_t = \frac{JdV - (1 - n_w|_\tau)\, dV}{JdV} = 1 - \frac{(1 - n_0)}{J} \tag{2.49}$$

where J is the Jacobian defined as:

$$J = \mathtt{det}\,(\mathbf{F}) \tag{2.50}$$

with $\mathbf{F}$ being the deformation gradient calculated as:

$$\mathbf{F} = \begin{bmatrix} \frac{\partial x_1|_t}{\partial x_1|_\tau} & \frac{\partial x_1|_t}{\partial x_2|_\tau} & \frac{\partial x_1|_t}{\partial x_3|_\tau} \\ \frac{\partial x_2|_t}{\partial x_1|_\tau} & \frac{\partial x_2|_t}{\partial x_2|_\tau} & \frac{\partial x_2|_t}{\partial x_3|_\tau} \\ \frac{\partial x_3|_t}{\partial x_1|_\tau} & \frac{\partial x_3|_t}{\partial x_2|_\tau} & \frac{\partial x_3|_t}{\partial x_3|_\tau} \end{bmatrix} \tag{2.51}$$

Linear Momentum Balance: Mixture

Standard arguments leading to variational principles are followed and the variation of the solid displacements is denoted by $\delta \mathbf{u}_s$. Then the variational form of balance of linear momentum of the mixture (Eq. 2.45) is written as a functional Π^s:

$$\begin{aligned}\Pi^s \;=\; & \int_{\Omega_t} (\delta\mathbf{u}_s)^T \left[\rho_s (1-n_w) + \rho_w n_w\right] (\mathbf{b} - \mathbf{a}^s)\, dv - \\ & \int_{\Omega_t} (\delta\mathbf{u}_s)^T \rho_w \mathbf{a}^r dv - \int_{\Omega_t} (\delta\mathbf{u}_s)^T \rho_w \mathbf{b} dv + \\ & \int_{\Omega_t} (\delta\mathbf{u}_s)^T div\left(\boldsymbol{\sigma}^{eff}\right) dv + \int_{\Omega_t} (\delta\mathbf{u}_s)^T grad\left(\bar{p}^w\right) dv = 0\end{aligned} \tag{2.52}$$

The divergence theorem is applied to the fourth and fifth terms of Eq. 2.52, and after some simplification of the resulting expression, the weak form becomes:

$$\begin{aligned}\Pi^s \;=\; & \int_{\Gamma_\sigma} (\delta\mathbf{u}_s)^T \mathbf{t}^{Total} da + \int_{\Omega_t} (\delta\mathbf{u}_s)^T \left[\rho_s (1-n_w) + \rho_w n_w\right] (\mathbf{b} - \mathbf{a}^s)\, dv - \\ & \int_{\Omega_t} (\delta\mathbf{u}_s)^T \rho_w \mathbf{a}^r dv - \int_{\Omega_t} (\delta\mathbf{u}_s)^T \rho_w \mathbf{b} dv - \\ & \int_{\Omega_t} \left[grad\left(\delta\mathbf{u}_s\right)\right]^T \boldsymbol{\sigma}^{eff} dv - \int_{\Omega_t} \bar{p}^w div\left(\delta\mathbf{u}_s\right) dv = 0\end{aligned} \tag{2.53}$$

The domain of integration is converted to the reference configuration to write Eq. 2.53 as:

$$\begin{aligned}\Pi^s \;=\; & \int_{\Gamma_\sigma} (\delta\mathbf{u}_s)^T \mathbf{t}^{Total} da + \int_{\Omega_\tau} (\delta\mathbf{u}_s)^T \left[\rho_s (1-n_0) + \rho_w n_w J\right] (\mathbf{b} - \mathbf{a}^s)\, dV - \\ & \int_{\Omega_\tau} (\delta\mathbf{u}_s)^T \rho_w \mathbf{a}^r J dV - \int_{\Omega_\tau} (\delta\mathbf{u}_s)^T \rho_w \mathbf{b} J dV - \\ & \int_{\Omega_\tau} \left[grad\left(\delta\mathbf{u}_s\right)\right]^T \boldsymbol{\sigma}^{eff} J dV - \int_{\Omega_\tau} \bar{p}^w div\left(\delta\mathbf{u}_s\right) J dV = 0\end{aligned} \tag{2.54}$$

After combining terms corresponding to **b** in Eq. 2.54, the final weak form of the linear momentum balance of the mixture is obtained as:

$$
\begin{aligned}
\Pi^s \;=\;& \int_{\Gamma_\sigma} (\delta\mathbf{u}_s)^T \, \mathbf{t}^{Total} da + \int_{\Omega_\tau} (\delta\mathbf{u}_s)^T (\rho_s - \rho_w)(1 - n_0)\,\mathbf{b} dV - \\
& \int_{\Omega_\tau} (\delta\mathbf{u}_s)^T \rho_w \mathbf{a}^r J dV - \int_{\Omega_\tau} (\delta\mathbf{u}_s)^T \left[\rho_s (1 - n_0) + \rho_w n_w J\right] \mathbf{a}^s dV - \\
& \int_{\Omega_\tau} \left[grad\,(\delta\mathbf{u}_s)\right]^T \boldsymbol{\sigma}^{eff} J dV - \int_{\Omega_\tau} \bar{p}^w div\,(\delta\mathbf{u}_s)\, J dV = 0 \qquad (2.55)
\end{aligned}
$$

Linear Momentum Balance: Fluid Phase

Similarly, the variation of the Darcy's velocities is denoted by $\delta\mathbf{v}_r$. The variational form of balance of linear momentum of the fluid phase (Eq. 2.46) is then written as a functional Π^r:

$$
\begin{aligned}
\Pi^r \;=\;& -\int_{\Omega_t} (\delta\mathbf{v}_r)^T \rho_w \mathbf{a}^s dv - \int_{\Omega_t} (\delta\mathbf{v}_r)^T \frac{\rho_w}{n_w} \mathbf{a}^r dv + \\
& \int_{\Omega_t} (\delta\mathbf{v}_r)^T grad\,(\bar{p}^w)\, dv - \int_{\Omega_t} (\delta\mathbf{v}_r)^T \frac{\rho_w}{n_w} \mathbf{k}^{-1} \mathbf{v}^r dv = 0 \qquad (2.56)
\end{aligned}
$$

With the use of the divergence theorem to the third term, the weak form becomes:

$$
\begin{aligned}
\Pi^r \;=\;& \int_{\Gamma_w} (\delta\mathbf{v}_r)^T \, \bar{\mathbf{t}}^p da - \int_{\Omega_t} (\delta\mathbf{v}_r)^T \rho_w \mathbf{a}^s dv - \int_{\Omega_t} (\delta\mathbf{v}_r)^T \frac{\rho_w}{n_w} \mathbf{a}^r dv - \\
& \int_{\Omega_t} \bar{p}^w div\,(\delta\mathbf{v}_r)\, dv - \int_{\Omega_t} (\delta\mathbf{v}_r)^T \frac{\rho_w}{n_w} \mathbf{k}^{-1} \mathbf{v}^r dv = 0 \qquad (2.57)
\end{aligned}
$$

The domain of integration is converted to the reference configuration to write Eq. 2.57 as:

$$
\begin{aligned}
\Pi^r \;=\;& \int_{\Gamma_w} (\delta\mathbf{v}_r)^T \, \bar{\mathbf{t}}^p da - \int_{\Omega_\tau} (\delta\mathbf{v}_r)^T \rho_w \mathbf{a}^s J dV - \int_{\Omega_\tau} (\delta\mathbf{v}_r)^T \frac{\rho_w}{n_w} \mathbf{a}^r J dV - \\
& \int_{\Omega_\tau} \bar{p}^w div\,(\delta\mathbf{v}_r)\, J dV - \int_{\Omega_\tau} (\delta\mathbf{v}_r)^T \frac{\rho_w}{n_w} \mathbf{k}^{-1} \mathbf{v}^r J dV = 0 \qquad (2.58)
\end{aligned}
$$

Mixture Mass Balance

Similarly, the variation of the excess pore-water pressure is denoted by $\delta\bar{p}^w$. The variational form of balance of mixture mass (Eq. 2.43) is then written as a functional Π^w:

$$\begin{aligned}\Pi^w \; = \; & \int_{\Omega_t} (\delta\bar{p}^w)\, div\,(\mathbf{v}^s)\, dv + \int_{\Omega_t} (\delta\bar{p}^w)\, div\,(\mathbf{v}^r)\, dv - \\ & \int_{\Omega_t} (\delta\bar{p}^w)\, \frac{n_w}{\lambda_w} \dot{\bar{p}}^w dv - \int_{\Omega_t} (\delta\bar{p}^w)\, \frac{n_w \gamma_w}{\lambda_w} \mathbf{1}_z^T \mathbf{v}^s dv - \\ & \int_{\Omega_t} (\delta\bar{p}^w)\, \frac{1}{\lambda_w} \left[grad\,(\bar{p}^w)\right]^T \mathbf{v}^r dv - \int_{\Omega_t} (\delta\bar{p}^w)\, \frac{\gamma_w}{\lambda_w} \mathbf{1}_z^T \mathbf{v}^r dv = 0\end{aligned} \tag{2.59}$$

With the use of the divergence theorem to the second term, the weak form becomes:

$$\begin{aligned}\Pi^w \; = \; & -\int_{\Gamma_q} (\delta\bar{p}^w)^T q da + \int_{\Omega_t} (\delta\bar{p}^w)\, div\,(\mathbf{v}^s)\, dv + \\ & \int_{\Omega_t} \left[grad\,(\delta\bar{p}^w)\right]^T (\mathbf{v}^r)\, dv - \int_{\Omega_t} (\delta\bar{p}^w)\, \frac{n_w}{\lambda_w} \dot{\bar{p}}^w dv - \\ & \int_{\Omega_t} (\delta\bar{p}^w)\, \frac{n_w \gamma_w}{\lambda_w} \mathbf{1}_z^T \mathbf{v}^s dv - \int_{\Omega_t} (\delta\bar{p}^w)\, \frac{1}{\lambda_w} \left[grad\,(\bar{p}^w)\right]^T \mathbf{v}^r dv - \\ & \int_{\Omega_t} (\delta\bar{p}^w)\, \frac{\gamma_w}{\lambda_w} \mathbf{1}_z^T \mathbf{v}^r dv = 0\end{aligned} \tag{2.60}$$

The domain of integration is converted to the reference configuration to write Eq. 2.60 as:

$$
\begin{aligned}
\Pi^{w} \;=\; & -\int_{\Gamma_q} (\delta\bar{p}^{w})^{T}\, q da + \int_{\Omega_\tau} (\delta\bar{p}^{w})\, div\,(\mathbf{v}^{s})\, JdV + \\
& \int_{\Omega_\tau} \left[grad\,(\delta\bar{p}^{w})\right]^{T} (\mathbf{v}^{r})\, JdV - \int_{\Omega_\tau} (\delta\bar{p}^{w})\, \frac{n_w}{\lambda_w}\dot{\bar{p}}^{w} JdV - \\
& \int_{\Omega_\tau} (\delta\bar{p}^{w})\, \frac{n_w\gamma_w}{\lambda_w}\mathbf{1}_z^{T}\mathbf{v}^{s} JdV - \int_{\Omega_\tau} (\delta\bar{p}^{w})\, \frac{1}{\lambda_w}\left[grad\,(\bar{p}^{w})\right]^{T}\mathbf{v}^{r} JdV - \\
& \int_{\Omega_\tau} (\delta\bar{p}^{w})\, \frac{\gamma_w}{\lambda_w}\mathbf{1}_z^{T}\mathbf{v}^{r} JdV = 0
\end{aligned}
\tag{2.61}
$$

2.6 Summary

In this chapter, the balance laws governing interaction between soil deformation and pore-water flow, and their variational statements were derived. The finite-element discretization of these laws are presented in Chapter 3.

Chapter 3

SOIL-CAISSON SYSTEM DISCRETIZATION

In this chapter, the finite-element discretization of the equations governing the response of the soil-caisson system is presented. The incremental forms of the equations for use in Newton iterations are also described.

3.1 Soil Discretization

The differential equations governing soil response were presented in Chapter 2. In the following sections, the finite-element discretization of these equations and their incremental forms for Newton iterations are described.

3.1.1 Finite-Element Discretization

The discrete versions of the variational statements (Eqs. 2.55, 2.58, and 2.61) are developed by adopting approximations to the field variables and restricting the variations consistently. The approximations are obtained by interpolation of the variables from their values at nodes of a finite-element mesh.

The geometry of an element is approximated as:

$$\mathbf{x} = \mathbf{N}_G \mathbf{X} \tag{3.1}$$

where $\mathbf{N}_G$ is the matrix of interpolation functions describing the geometry of an element, and $\mathbf{X}$ is a vector containing coordinates of the nodes of the element.

The field variables and their variations within an element are approximated as:

$$\begin{array}{llll} \mathbf{u}^s = \mathbf{N}_s \mathbf{U}^s & \dot{\mathbf{u}}^s = \mathbf{N}_s \dot{\mathbf{U}}^s & \ddot{\mathbf{u}}^s = \mathbf{N}_s \ddot{\mathbf{U}}^s & \delta \mathbf{u}_s = \mathbf{N}_s \delta \mathbf{U}_s \\ \mathbf{v}^r = \mathbf{N}_r \mathbf{V}^r & \dot{\mathbf{v}}^r = \mathbf{N}_r \dot{\mathbf{V}}^r & & \delta \mathbf{v}_r = \mathbf{N}_r \delta \mathbf{V}_r \\ \bar{p}^w = \mathbf{N}_p \bar{\mathbf{P}}^w & \dot{\bar{p}}^w = \mathbf{N}_p \dot{\bar{\mathbf{P}}}^w & & \delta \bar{p}^w = \mathbf{N}_p \delta \bar{\mathbf{P}}^w \end{array} \tag{3.2}$$

where the vectors $\mathbf{U}^s$, $\mathbf{V}^r$, and $\bar{\mathbf{P}}^w$ represent the nodal values of the solid displacements, Darcy's velocities, and excess pore-water pressure, respectively. The functions $\mathbf{N}_s$, $\mathbf{N}_r$, and $\mathbf{N}_p$ are the interpolations functions for the solid displacements, Darcy's velocities, and pore-water pressure, respectively.

Axisymmetric discretization is accomplished with eight-node, quadratic, isoparametric, underintegrated finite-elements for solid displacements, and Darcy's velocities, with interpolation functions $\mathbf{N}_s$ and $\mathbf{N}_r$, respectively. Spatially continuous discretization of excess pore-water pressure is applied using four-node bilinear finite-elements with interpolation functions $\mathbf{N}_p$. The selected scheme for discretization of displacements and pore-water pressure fields has been known to perform satisfactorily for most practical problems involving incompressible as well as nearly incompressible solids (Hughes, 2000; and Zienkiewicz and Taylor, 1991).

The approximations from Eqs. 3.2 are substituted into the variational forms (Eqs. 2.55, 2.58, and 2.61). The discrete counterparts can be then written as:

$$\begin{aligned}
\hat{\Pi}^s \;=\; & \int_{\Gamma_\sigma} (\delta \mathbf{U}_s)^T \mathbf{N}_s^T \mathbf{t}^{Total} da \\
& + \int_{\Omega_\tau} (\delta \mathbf{U}_s)^T \mathbf{N}_s^T (\rho_s - \rho_w)(1 - n_0) \mathbf{b} dV \\
& - \int_{\Omega_\tau} (\delta \mathbf{U}_s)^T \mathbf{N}_s^T \rho_w \mathbf{a}^r J dV \\
& - \int_{\Omega_\tau} (\delta \mathbf{U}_s)^T \mathbf{N}_s^T [\rho_s (1 - n_0) + \rho_w n_w J] \mathbf{a}^s dV \\
& - \int_{\Omega_\tau} [grad(\mathbf{N}_s \delta \mathbf{U}_s)]^T \boldsymbol{\sigma}^{eff} J dV \\
& - \int_{\Omega_\tau} (\delta \mathbf{U}_s)^T div\left(\mathbf{N}_s^T\right) \bar{p}^w J dV = 0
\end{aligned} \tag{3.3}$$

$$\begin{aligned}
\hat{\Pi}^r \;=\; & \int_{\Gamma_w} (\delta \mathbf{V}_r)^T \mathbf{N}_r^T \bar{\mathbf{t}}^p da \\
& - \int_{\Omega_\tau} (\delta \mathbf{V}_r)^T \mathbf{N}_r^T \rho_w \mathbf{a}^s J dV \\
& - \int_{\Omega_\tau} (\delta \mathbf{V}_r)^T \mathbf{N}_r^T \frac{\rho_w}{n_w} \mathbf{a}^r J dV \\
& - \int_{\Omega_\tau} (\delta \mathbf{V}_r)^T div\left(\mathbf{N}_r^T\right) \bar{p}^w J dV \\
& - \int_{\Omega_\tau} (\delta \mathbf{V}_r)^T \mathbf{N}_r^T \frac{\rho_w}{n_w} \mathbf{k}^{-1} \mathbf{v}^r J dV = 0
\end{aligned} \tag{3.4}$$

$$
\begin{aligned}
\hat{\Pi}^{w} \;=\; & -\int_{\Gamma_q} \left(\delta \bar{\mathbf{P}}^{w}\right)^{T} \mathbf{N}_p^{T} q da \\
& -\int_{\Omega_\tau} \left(\delta \bar{\mathbf{P}}^{w}\right)^{T} \mathbf{N}_p^{T} div\left(\mathbf{v}^{s}\right) JdV \\
& +\int_{\Omega_\tau} \left(\delta \bar{\mathbf{P}}^{w}\right)^{T} \left[grad\left(\mathbf{N}_p\right)\right]^{T} \mathbf{v}^{r} JdV \\
& -\int_{\Omega_\tau} \left(\delta \bar{\mathbf{P}}^{w}\right)^{T} \mathbf{N}_p^{T} \frac{n_w}{\lambda_w} \dot{\bar{p}}^{w} JdV \\
& -\int_{\Omega_\tau} \left(\delta \bar{\mathbf{P}}^{w}\right)^{T} \mathbf{N}_p^{T} \frac{n_w \gamma_w}{\lambda_w} \mathbf{1}_z^{T} \mathbf{v}^{s} JdV \\
& -\int_{\Omega_\tau} \left(\delta \bar{\mathbf{P}}^{w}\right)^{T} \mathbf{N}_p^{T} \frac{1}{\lambda_w} \left[grad\left(\bar{p}^{w}\right)\right]^{T} \mathbf{v}^{r} JdV \\
& -\int_{\Omega_\tau} \left(\delta \bar{\mathbf{P}}^{w}\right)^{T} \mathbf{N}_p^{T} \frac{\gamma_w}{\lambda_w} \mathbf{1}_z^{T} \mathbf{v}^{r} JdV = 0
\end{aligned}
\tag{3.5}
$$

3.1.2 Incremental Equations

For any arbitrary selection of $\delta \mathbf{U}_s$, $\delta \mathbf{V}_r$, and $\delta \bar{\mathbf{P}}_w$ the system of equations represented by Eqs. 3.3-3.5 must hold. The resulting equations can be written as:

$$
\mathbf{\Psi}_t \equiv \mathbf{\Psi}\left(\mathbf{a}_t\right) \equiv \mathbf{F}^{\mathtt{I}}\left(t\right) - \mathbf{F}^{\mathtt{E}}\left(t\right) = \mathbf{0} \tag{3.6}
$$

where $\mathbf{a}$ is a vector containing all the field variables, $\mathbf{F}^{\mathtt{I}}$ is a vector containing internal nodal forces, and $\mathbf{F}^{\mathtt{E}}$ is a vector containing external nodal forces.

The nonlinear system of Eqs. 3.6 can be solved by an iterative scheme based on Newton's method:

$$
\mathbf{\Psi}\left[\mathbf{a}^{i+1}\left(t\right)\right] \approx \mathbf{\Psi}\left[\mathbf{a}^{i}\left(t\right)\right] + \left(\frac{\partial \mathbf{\Psi}}{\partial \mathbf{a}}\right)_t^i \Delta \mathbf{a} = 0 \tag{3.7}
$$

where i is the iteration counter and

$$-\frac{\partial \boldsymbol{\Psi}}{\partial \mathbf{a}} = \mathbf{K}_{\texttt{Tangent}} \tag{3.8}$$

is the tangent stiffness matrix. The incremental correction $\Delta\mathbf{a}$ to the vector $\mathbf{a}$ can be obtained by solving:

$$\mathbf{K}^{i}_{\texttt{Tangent}}\Delta\mathbf{a} = \boldsymbol{\Psi}\left[\mathbf{a}^{i}\left(t\right)\right] = \mathbf{R}^{i} = \mathbf{F}^{\texttt{I}(i)} - \mathbf{F}^{\texttt{E}(i)} \tag{3.9}$$

$\mathbf{R}^{i}$ being the residual vector or out-of-balance force vector calculated from the most recent estimate of the variables $\mathbf{a}$ at iteration i.

A series of successive approximations

$$\mathbf{a}^{i+1}\left(t\right) = \mathbf{a}\left(\tau\right) + \mathsf{d}\mathbf{a} = \mathbf{a}^{i}\left(t\right) + \Delta\mathbf{a} \tag{3.10}$$

are computed until convergence is achieved, that is when the magnitude of the residual vector becomes smaller than a specified tolerance.

The incremental equations obtained for the discrete variational forms (Eqs. 3.3-3.5) are written in a matrix form as follows:

$$\begin{bmatrix} \mathbf{M}_{ss} & \mathbf{M}_{sr} & \mathbf{0} \\ \mathbf{M}_{rs} & \mathbf{M}_{rr} & \mathbf{0} \\ \mathbf{0} & \mathbf{0} & \mathbf{0} \end{bmatrix} \begin{Bmatrix} \Delta\ddot{\mathbf{U}}^{s} \\ \Delta\dot{\mathbf{V}}^{r} \\ \Delta\ddot{\bar{\mathbf{P}}}^{w} \end{Bmatrix} + \begin{bmatrix} \mathbf{C}_{ss} & \mathbf{C}_{sr} & \mathbf{0} \\ \mathbf{C}_{rs} & \mathbf{C}_{rr} & \mathbf{0} \\ \mathbf{C}_{ps} & \mathbf{C}_{pr} & \mathbf{C}_{pp} \end{bmatrix} \begin{Bmatrix} \Delta\dot{\mathbf{U}}^{s} \\ \Delta\mathbf{V}^{r} \\ \Delta\dot{\bar{\mathbf{P}}}^{w} \end{Bmatrix}$$
$$+ \begin{bmatrix} \mathbf{K}_{\sigma} + \mathbf{K}_{ss} & \mathbf{0} & \mathbf{K}_{sp} \\ \mathbf{K}_{rs} & \mathbf{0} & \mathbf{K}_{rp} \\ \mathbf{K}_{ps} & \mathbf{0} & \mathbf{K}_{pp} \end{bmatrix} \begin{Bmatrix} \Delta\mathbf{U}^{s} \\ \Delta\mathbf{U}^{r} \\ \Delta\bar{\mathbf{P}}^{w} \end{Bmatrix} = \begin{Bmatrix} \mathbf{R}^{s} \\ \mathbf{R}^{r} \\ \mathbf{R}^{p} \end{Bmatrix} \tag{3.11}$$

where $\Delta\mathbf{U}^{s}$, $\Delta\mathbf{V}^{r}$, and $\Delta\bar{\mathbf{P}}^{w}$ are the vectors containing the increments of solid displacements, Darcy's velocities and excess pore-water pressure, respectively.

The expressions for the matrices $\mathbf{M}_{\alpha\beta}$, $\mathbf{C}_{\alpha\beta}$, and $\mathbf{K}_{\alpha\beta}$, and vectors $\mathbf{R}^{\alpha}$ are presented in Appendix A. Highly nonlinear behavior of the mixture is represented by Eqs. 3.11, and, in general, all the matrices are required to be added to the tangent stiffness matrix in order to realize the quadratic convergence of the Newton's iterative scheme.

The matrix form represented by Eqs. 3.11 can be condensed as:

$$\mathbf{M}\Delta\ddot{\mathbf{a}} + \mathbf{C}\Delta\dot{\mathbf{a}} + \mathbf{K}\Delta\mathbf{a} = \mathbf{R} \tag{3.12}$$

where the matrix $\mathbf{M}$ is the equivalent mass matrix, the matrix $\mathbf{C}$ is the equivalent damping matrix, and the matrix $\mathbf{K}$ is the equivalent stiffness matrix. The individual residual vectors $\mathbf{R}^{s}$, $\mathbf{R}^{r}$, and $\mathbf{R}^{p}$ are combined in the residual vector $\mathbf{R}$.

3.1.3 Time-Stepping

The system of equations represented by Eqs. 3.12 is discrete in space but still continuous in time. In order to solve the system, temporal discretization is necessary. The backward Euler scheme is adopted for the temporal discretization. Although the scheme is only first-order accurate, it is known to be unconditionally stable (Hughes, 1977). The time-stepping algorithm is given by:

$$\begin{aligned} \mathbf{a}_{i+1} &= \mathbf{a}_i + \dot{\mathbf{a}}_{i+1}\Delta t \\ \dot{\mathbf{a}}_{i+1} &= \dot{\mathbf{a}}_i + \ddot{\mathbf{a}}_{i+1}\Delta t \end{aligned} \tag{3.13}$$

where $\mathbf{a}$, $\dot{\mathbf{a}}$, and $\ddot{\mathbf{a}}$ are the vector containing the displacement, velocity, and acceleration of the field variables, respectively. The increment in time $(t - \tau)$ is represented by Δt. Subscript i refers to the variables at time τ, and subscript $i+1$ refers to the variables at current time t.

To obtain the tangent stiffness matrix, incremental relationships between the field variables and their derivatives are required, and for any time marching scheme they can be written as:

$$\begin{aligned} \Delta\dot{\mathbf{a}} &= \frac{1}{\alpha}\Delta\mathbf{a} \\ \Delta\ddot{\mathbf{a}} &= \frac{1}{\theta}\Delta\mathbf{a} \end{aligned} \qquad (3.14)$$

For the backward Euler scheme, Eqs. 3.14 can be specialized by adopting:

$$\begin{aligned} \alpha &= \Delta t \\ \theta &= (\Delta t)^2 \end{aligned} \qquad (3.15)$$

With the use of Eqs. 3.15 into the system of Eqs. 3.12, the tangent stiffness matrix can be written as:

$$\mathbf{K}_{\texttt{Tangent}} = \begin{bmatrix} \frac{1}{\theta}\mathbf{M}_{ss} + \frac{1}{\alpha}\mathbf{C}_{ss} + \mathbf{K}_{\sigma} + \mathbf{K}_{ss} & \frac{1}{\alpha}\mathbf{M}_{sr} + \mathbf{C}_{sr} & \mathbf{K}_{sp} \\ \frac{1}{\theta}\mathbf{M}_{rs} + \frac{1}{\alpha}\mathbf{C}_{rs} + \mathbf{K}_{rs} & \frac{1}{\alpha}\mathbf{M}_{rr} + \mathbf{C}_{rr} & \mathbf{K}_{rp} \\ \frac{1}{\alpha}\mathbf{C}_{ps} + \mathbf{K}_{ps} & \mathbf{C}_{pr} & \frac{1}{\alpha}\mathbf{C}_{pp} + \mathbf{K}_{pp} \end{bmatrix} \qquad (3.16)$$

The tangent stiffness matrix is not symmetric. A quasi-symmetric matrix can be obtained by multiplying the second set of equations by ratio θ/α, and multiplying the third set of equations by factor α. The modified system of Eqs. 3.12 is written as:

$$
\begin{bmatrix}
\frac{1}{\theta}\mathbf{M}_{ss} + \frac{1}{\alpha}\mathbf{C}_{ss} + \mathbf{K}_{\sigma} + \mathbf{K}_{ss} & \frac{1}{\alpha}\mathbf{M}_{sr} + \mathbf{C}_{sr} & \mathbf{K}_{sp} \\
\frac{1}{\alpha}\mathbf{M}_{rs} + \frac{\theta}{\alpha^2}\mathbf{C}_{rs} + \frac{\theta}{\alpha}\mathbf{K}_{rs} & \frac{\theta}{\alpha^2}\mathbf{M}_{rr} + \frac{\theta}{\alpha}\mathbf{C}_{rr} & \frac{\theta}{\alpha}\mathbf{K}_{rp} \\
\mathbf{C}_{ps} + \alpha\mathbf{K}_{ps} & \alpha\mathbf{C}_{pr} & \mathbf{C}_{pp} + \alpha\mathbf{K}_{pp}
\end{bmatrix}
\begin{Bmatrix}
\Delta\mathbf{U}^s \\
\Delta\mathbf{V}^r \\
\Delta\bar{\mathbf{P}}^w
\end{Bmatrix}
=
\begin{Bmatrix}
\mathbf{R}^s \\
\frac{\theta}{\alpha}\mathbf{R}^r \\
\alpha\mathbf{R}^p
\end{Bmatrix}
\tag{3.17}
$$

which is equivalent to

$$
\mathbf{K}_{\mathtt{Tangent}}\Delta\mathbf{a} = \mathbf{R} \tag{3.18}
$$

3.2 Caisson Modeling and Discretization

A conventional finite-element formulation for solids is adopted to describe the caisson response. In the following sections, the balance law governing response of the caisson, and their finite-element discretization and weak forms are described.

3.2.1 Balance Law: Linear Momentum Conservation

The caisson response is governed by the Cauchy's equation of motion. For writing the motion equation in a global form, an arbitrary region fixed in space is considered. The arbitrary region of volume V^c is denoted by Ω_t^c and is bounded by the surface $\partial\Omega_t^c$ of area A^c. The global form of the motion equation is written as:

$$\int_{\Omega_t^c} \rho_c \left(\mathbf{b} - \mathbf{a}^c\right) dV^c + \int_{\partial\Omega_t^c} \boldsymbol{\sigma} \cdot \mathbf{n} \, dA^c = \mathbf{0} \tag{3.19}$$

The relationship (Eq. 3.19) must hold for any arbitrary volume, therefore, the equation of motion can be written in a local form as:

$$\rho_c \left(\mathbf{b} - \mathbf{a}^c\right) + div\left(\boldsymbol{\sigma}\right) = \mathbf{0} \tag{3.20}$$

where ρ_c is the mass density of the particles, and $\mathbf{a}^c$ is the acceleration of the particles ($\mathbf{a}^c = \partial \mathbf{v}^c / \partial t = \partial^2 \mathbf{u}^c / \partial t^2$).

Appropriate boundary conditions for Eq. 3.20 are as follows:

$$\mathbf{u}^c = \bar{\mathbf{U}}^c \quad \texttt{on} \quad \Gamma_u^c \quad \texttt{and} \quad \boldsymbol{\sigma} \cdot \mathbf{n} = \mathbf{t}^c \quad \texttt{on} \quad \Gamma_\sigma^c \tag{3.21}$$

where:

$$\begin{aligned} \Gamma_u^c \cup \Gamma_\sigma^c &= \partial\Omega_t^c \\ \Gamma_u^c \cap \Gamma_\sigma^c &= \emptyset \end{aligned} \tag{3.22}$$

with $\bar{\mathbf{U}}^c$ and $\mathbf{t}^c$ as prescribed boundary displacement and traction vectors, respectively.

3.2.2 Variational Statement

Standard arguments leading to variational principle are followed, and variation of caisson displacements is denoted by $\delta \mathbf{u}_c$ to obtain the weak form or variational form of the linear momentum balance (Eq. 3.20) as a functional Π^c:

$$\Pi^c = \int_{\Omega_t^c} \left(\delta \mathbf{u}_c\right)^T \rho_c \left(\mathbf{b} - \mathbf{a}^c\right) dv^c + \int_{\Omega_t^c} \left(\delta \mathbf{u}_c\right)^T div\left(\boldsymbol{\sigma}\right) dv^c = 0 \tag{3.23}$$

The divergence theorem is applied to the second term of Eq. 3.23, and after some simplification of the resulting expression, the weak form becomes:

$$\begin{aligned}\Pi^c = \int_{\Gamma_\sigma^c} (\delta \mathbf{u}_c)^T \mathbf{t}^c da^c - \int_{\Omega_t^c} (\delta \mathbf{u}_c)^T \rho_c (\mathbf{a}^c - \mathbf{b}) \, dv^c & \\ - \int_{\Omega_t^c} [grad\,(\delta \mathbf{u}_c)]^T \boldsymbol{\sigma} dv^c &= 0 \end{aligned} \qquad (3.24)$$

The weak form (Eq. 3.24) is written with respect to the deformed domain or current configuration Ω_t^c at time t, which is not known *a priori.* It is convenient to use a previously known or reference configuration (Ω_τ^c) at time $\tau < t$ to perform integration of the weak form adopting the Jacobian J^c. After converting the domain of integration to the reference configuration, the Eq. 3.24 can be rewritten as:

$$\begin{aligned}\Pi^c = \int_{\Gamma_\sigma^c} (\delta \mathbf{u}_c)^T \mathbf{t}^c da^c - \int_{\Omega_\tau^c} (\delta \mathbf{u}_c)^T \rho_c J^c (\mathbf{a}^c - \mathbf{b}) \, dV^c & \\ - \int_{\Omega_\tau^c} [grad\,(\delta \mathbf{u}_c)]^T \boldsymbol{\sigma} J^c dV^c &= 0 \end{aligned} \qquad (3.25)$$

3.2.3 Finite-Element Discretization

The discrete version of the variational statement (Eq. 3.25) is developed by adopting approximation to the caisson displacements and restricting the variations consistently. The approximation is obtained by interpolation of the caisson displacements from their values at nodes of a finite-element mesh and is expressed as:

$$\mathbf{u}^c = \mathbf{N}_c \mathbf{U}^c \quad \dot{\mathbf{u}}^c = \mathbf{N}_c \dot{\mathbf{U}}^c \quad \ddot{\mathbf{u}}^c = \mathbf{N}_c \ddot{\mathbf{U}}^c \quad \delta \mathbf{u}_c = \mathbf{N}_c \delta \mathbf{U}_c \qquad (3.26)$$

where the vector $\mathbf{U}^c$ represent the nodal values of the caisson displacements, and the functions $\mathbf{N}_c$ are the interpolation functions for the caisson displacements. Axisymmetric discretization of the caisson is accomplished with eight-node, biquadratic, isoparametric finite-elements for the caisson displacements. The approximations from Eq. 3.26 are substituted into the variational form (Eq. 3.25) to obtain the discrete counterpart which can be written as:

$$\begin{aligned}\hat{\Pi}^c = \int_{\Gamma_\sigma^c} (\delta \mathbf{U}_c)^T \mathbf{N}_c^T \mathbf{t}^c da^c - \int_{\Omega_\tau^c} (\delta \mathbf{U}_c)^T \mathbf{N}_c^T \rho_c J^c (\mathbf{a}^c - \mathbf{b})\, dV^c \\ - \int_{\Omega_\tau^c} \left[grad\,(\mathbf{N}_c \delta \mathbf{U}_c)\right]^T \boldsymbol{\sigma} J^c dV^c &= 0\end{aligned} \tag{3.27}$$

3.2.4 Incremental Equations

The process described in Section 3.1.2 is followed to obtain the incremental equations for the discrete variational form (Eq. 3.27) in a matrix form:

$$\mathbf{M}_{cc} \Delta \ddot{\mathbf{U}}^c + \mathbf{K}_{cc} \Delta \mathbf{U}^c = \mathbf{R}^c \tag{3.28}$$

where $\Delta \mathbf{U}^c$ is the vector containing the increments of the caisson displacements. The mass matrix $\mathbf{M}_{cc}$ is written as:

$$\mathbf{M}_{cc} = \int_{\Omega_\tau^c} \mathbf{N}_c^T \rho_c J^c \mathbf{N}_c dV^c \tag{3.29}$$

The tangent stiffness matrix $\mathbf{K}_{cc}$ contains contributions from geometric and material nonlinearities and its integral equation is presented in Appendix B. The residual vector $\mathbf{R}^c$ is given by:

$$\begin{aligned}\mathbf{R}^c &= \int_{\Gamma_\sigma^c} \mathbf{N}_c^T \mathbf{t}^c da^c - \int_{\Omega_\tau^c} \mathbf{N}_c^T \rho_c J^c \left(\mathbf{a}^c - \mathbf{b}\right) dV^c \\ &\quad + \texttt{terms from} \left\{ - \int_{\Omega_\tau^c} \left[grad\left(\delta \mathbf{u}_c\right)\right]^T \boldsymbol{\sigma} J^c dV^c \right\}\end{aligned} \tag{3.30}$$

The matrix representation of third term in Eq. 3.30 is given in Appendix B.

3.2.5 Temporal Discretization

The system of equations represented by Eqs. 3.28 is discrete in space but still continuous in time. The backward Euler scheme described in Section 3.1.3 is followed to obtain the modified system of Eqs. 3.28 which is written as:

$$\left[\frac{1}{\theta}\mathbf{M}_{cc} + \mathbf{K}_{cc}\right]\{\Delta \mathbf{U}^c\} = \{\mathbf{R}^c\} \tag{3.31}$$

which is equivalent to

$$\mathbf{K}^c_{\texttt{Tangent}} \Delta \mathbf{U}^c = \mathbf{R}^c \tag{3.32}$$

3.3 Summary

The finite-element discretization of the differential equations governing the response of the soil-caisson system was presented in this chapter. The incremental forms of these equations were also derived for use in Newton iterations. Contributions to tangent stiffness matrix and residual vectors are presented in Appendices A and B.

Chapter 4

CONSTITUTIVE MODELS

4.1 Introduction

In this chapter, the constitutive models adopted for saturated clayey soil and caisson are described. Nonlinear mechanical behavior of clayey soil is described by constitutive equations based on a bounding-surface plasticity theory. Caissons are typically fabricated from steel and are not expected to undergo any inelastic deformation. The caisson material is assumed to be isotropic, linearly elastic.

Concepts of the bounding-surface plasticity model are discussed, and tangent moduli for clay and steel are presented.

4.2 Constitutive Model for Clayey Soil

Plasticity models with two yield surfaces were developed independently by Dafalias and Popov (1975) and Krieg (1975) to describe metal plasticity. In this approach, a bounding-surface is defined within which inelastic straining is allowed, if loading occurs. The development of these models utilizes a projection of the state of stress onto the bounding-surface, and an expression for the plastic modulus as a function of distance between the stress point and its “image” on the surface. In the last 30 years, bounding-surface plasticity has undergone extensions, improvements and applications to pressure-sensitive materials such as soils.

The nonlinear behavior of clayey soil is modeled through a bounding-surface plasticity model for isotropic cohesive soils (Dafalias and Herrmann, 1982a and 1986; Dafalias, 1986; and Kaliakin and Herrmann, 1991). Based on the concepts and principles of critical state soil mechanics (Wood, 1990; and Atkinson, 1993), the bounding-surface plasticity model is a reliable and versatile tool for representation of clay behavior along arbitrary and complex stress-strain paths. The constitutive model provides the relationship between soil effective stress and strain increments.

4.2.1 Theoretical Aspects

The bounding-surface plasticity model provides the relations between increments of effective stress and strain. The state of the material (clay) is assumed to be completely defined by the effective stress σ_{ij}^{eff} and plastic internal variables q_n accounting for the loading history. As expressed by Eq. 2.18, the total stress is the sum of the effective stress and pore-water pressure:

$$\sigma_{ij}^{Total} = \sigma_{ij}^{eff} + p^w \delta_{ij} \tag{4.1}$$

where δ_{ij} are the components of the Kronecker delta (identity tensor).

The three-part bounding-surface model employed in this work is illustrated in Fig. 4.1. The bounding-surface is expressed in terms of three invariants of the effective stress tensor σ_{ij}^{eff}: the first stress invariant (I), the square root of the second deviatoric stress invariant (J), and the "Lode" angle (α), given by:

$$I = \sigma_{kk}^{eff} \tag{4.2}$$

$$J = \sqrt{\frac{1}{2} s_{ij} s_{ij}} \tag{4.3}$$

$$\alpha = \frac{1}{3}\mathtt{arcsin}\left[\frac{3\sqrt{3}}{2}\left(\frac{S}{J}\right)^3\right]; \qquad -\frac{\pi}{6} \leq \alpha \leq \frac{\pi}{6} \tag{4.4}$$

where:

$$S = \left(\frac{1}{3} s_{ij} s_{jk} s_{ki}\right)^{\frac{1}{3}} \tag{4.5}$$

$$s_{mn} = \sigma_{mn}^{eff} - \sigma\delta_{mn} = \sigma_{mn}^{Total} - \frac{\sigma_{kk}^{Total}}{3}\delta_{mn} \tag{4.6}$$

$$\sigma = \frac{\sigma_{kk}^{eff}}{3} = \frac{I}{3} \tag{4.7}$$

Repeated indices imply summation (over the range of the indices). S is the third invariant of the deviatoric stress tensor s_{ij}, and σ is the mean (hydrostatic) stress. The Lode angle (α) serves in distinguishing between triaxial extension and triaxial compression.

The equations describing the three parts of the bounding-surface are of the form:

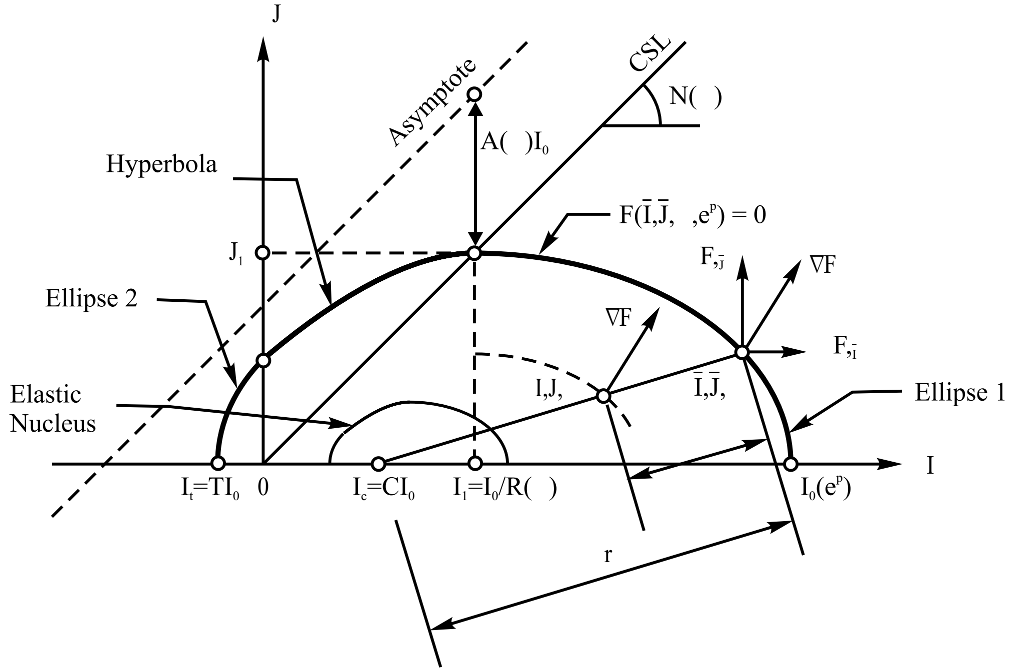

Figure 4.1: Schematic illustration of bounding-surface in stress invariant space.

$$F\left(\bar{I}, \bar{J}, \alpha, e^p\right) = 0 \tag{4.8}$$

In Eq. 4.8, e^p is inelastic (or plastic) void ratio, the only (scalar) internal or history dependent variable in the model. The barred quantities correspond to the image stress on the bounding-surface itself. The image stress $\bar{\sigma}_{ij}$ is obtained by projecting the actual stress σ_{ij}^{eff} onto the bounding-surface through a radial projection rule. The projection rule is expressed as (Dafalias, 1982b):

$$\bar{\sigma}_{ij} \;=\; b\left(\sigma_{ij}^{eff} - CI_0\right) + CI_0 \tag{4.9}$$

$$\bar{s_{ij}} \;=\; bs_{ij} \;\Rightarrow\; \bar{J} = bJ; \quad \bar{S} = bS; \quad \bar{\alpha} = b\alpha \tag{4.10}$$

where b is the projection factor ($1 \leq b \leq \infty$), I_0 is the point where the bounding-surface intersects with the positive I-axis and measures the preconsolidation pressure, C is a model parameter with $0 \leq C \leq 1$, and CI_0 is center of projection for the radial mapping rule (see Fig. 4.1).

The elastoplastic relationship between the rates of the (effective) stress $\dot{\sigma}_{ij}$ and strain $\dot{\varepsilon}_{ij}$ tensors is written as:

$$\dot{\sigma}_{ij} = D^{\mathsf{ep}}_{ijkl}\dot{\varepsilon}_{kl} \tag{4.11}$$

where D^{ep}_{ijkl} is the fourth-order elastoplastic rigidity tensor (a superimposed dot indicates the rate). The total strain rate is decomposed into elastic and plastic parts:

$$\dot{\varepsilon}_{ij} = \dot{\varepsilon}^{e}_{ij} + \dot{\varepsilon}^{p}_{ij} \tag{4.12}$$

with

$$\dot{\varepsilon}^{e}_{ij} = C_{ijkl}\dot{\sigma}_{kl} \tag{4.13}$$

where C_{ijkl} are the components of the fourth-order elastic compliance tensor.

With the use of the normality rule, the plastic strain rate is given by:

$$\dot{\varepsilon}^{p}_{ij} = \langle L \rangle \frac{\partial F}{\partial \bar{\sigma}_{ij}} \tag{4.14}$$

where L is a scalar loading index. In the sense of plasticity, loading, neutral loading, and unloading are represented by $L > 0$, $L = 0$, and $L < 0$, respectively. The Macauley brackets $\langle\ \rangle$ define the operation $\langle L \rangle = H(L)\, L$, where $H(L)$ is the Heavyside step function defined as zero at $L = 0$. The loading index is expressed analytically as:

$$L = \frac{1}{K_p} \frac{\partial F}{\partial \bar{\sigma}_{ij}} \dot{\bar{\sigma}}_{ij} = \frac{1}{K_p} \left[\frac{\partial F}{\partial \bar{I}}\, \dot{\bar{I}} + \frac{\partial F}{\partial \bar{J}}\, \dot{\bar{J}} + \frac{1}{b} \frac{\partial F}{\partial \alpha}\, \dot{\alpha} \right] \tag{4.15}$$

where K_p is the plastic modulus, determined from the so-called "consistency condition" $\dot{F} = 0$:

$$K_p = \bar{K}_p + \mathcal{H} \frac{\delta}{\langle r - S_p \delta \rangle} \tag{4.16}$$

In the above expression $\mathcal{H}$ represents the shape hardening function, and δ is the "distance" in stress space between the actual stress point and its image point on the bounding-surface (Dafalias and Popov, 1975). The elastic-zone parameter S_p in the Eq. 4.16 defines the extent of the elastic nucleus (Dafalias and Herrmann, 1986). A domain of purely elastic behavior is represented by the locus of states for which $\delta > r/S_p$. The distance in stress space between the center of projection and the image stress is denoted by r and the bounding plastic modulus at the image stress is given by:

$$\bar{K}_p = 3\,(1 + e_{in})\, \frac{\partial F}{\partial \bar{I}}\, \frac{\partial \bar{I}}{\partial I_0}\, \frac{\partial I_0}{\partial e^p} \tag{4.17}$$

where e_{in} denotes initial value of the void ratio associated with the reference configuration with respect to which the strain rate is measured.

The shape hardening function $\mathcal{H}$ is specified as:

$$\mathcal{H} = \frac{1+e_{in}}{\lambda - \kappa} P_a \left[z^m h(\alpha) + (1-z^m) h_0 \right] \left[9 \left(\frac{\partial F}{\partial \bar{I}} \right)^2 + \frac{1}{3} \left(\frac{\partial F}{\partial \bar{J}} \right)^2 \right] \tag{4.18}$$

where P_a is the atmospheric pressure, the variable z is a weighing factor with respect to $h(\alpha)$ and h_0 and it is defined by $z = J/J_1$ (see Fig. 4.1), the exponent m is a positive model parameter, λ and κ represent the slopes, in $e - ln(p)$ space, of the virgin consolidation and recompression lines respectively, for either isotropic or one-dimensional (anisotropic) consolidation, and $h(\alpha)$ is a shape hardening factor that defines the degree of hardening for points within the bounding-surface and is interpolated as a function of Lode angle as:

$$h(\alpha) = \left[\frac{2\mu}{1+\mu-(1-\mu)\,\mathtt{sin}(3\alpha)} \right] h_c \tag{4.19}$$

with $\mu = h_e/h_c$. Finally, h_0 is a hardening parameter for states in the immediate vicinity of the I-axis (i.e., $z \approx 0$) and is typically set equal to the average of the hardening parameters for triaxial compression and extension states denoted by h_c and h_e, respectively.

4.2.2 Three-Part Bounding-Surface

The three-part bounding-surface shown in Fig. 4.1 is described by the following functions:

Ellipse 1:

$$F = \left(\bar{I} - I_0 \right) \left(\bar{I} + \frac{R-2}{R} I_0 \right) + (R-1)^2 \left(\frac{\bar{J}}{N} \right)^2 = 0 \tag{4.20}$$

Hyperbola:

$$F = \left(\bar{I} - \frac{I_0}{R}\right)^2 - \left(\frac{\bar{J}}{N} - \frac{I_0}{R}\right)\left[\frac{\bar{J}}{N} - \frac{I_0}{R}\left(1 + 2\frac{RA}{N}\right)\right] = 0 \tag{4.21}$$

Ellipse 2:

$$F = \left(\bar{I} - TI_0\right)\left[\bar{I} - \left(T + 2\zeta\right)I_0\right] + \rho\bar{J}^2 = 0 \tag{4.22}$$

where:

$$\begin{aligned} \zeta &= -\frac{T\left(Z + TF'\right)}{Z + 2TF'}\,; \qquad \rho = \frac{T^2}{Z\left(Z + 2TF'\right)} \\ F' &= \frac{N}{\sqrt{1 + y^2}}\,; \qquad Z = \frac{N}{R}\left(1 + y - \sqrt{1 + y^2}\right) \\ y &= \frac{RA}{N} \end{aligned} \tag{4.23}$$

N being the slope of the critical state line, in general, a function of the Lode angle, the parameter R defining the ratio of the major to minor axes of ellipse 1, the parameter A controlling the shape of the hyperbolic portion of the bounding-surface, and the parameter T adjusting the size of ellipse 2 (associated with the tensile strength of the material). A detailed description and typical values for each parameter are given by Herrmann *et al.* (1987) and Kaliakin and Herrmann (1991).

4.2.3 Numerical Implementation

The bounding-surface plasticity model implementation described by Kaliakin and Herrmann (1991) was provided by Kaliakin (2000) for the computations presented in this dissertation. The model is numerically implemented adopting an adaptive multistep integration procedure along with local iteration and radial return algorithm as described by Herrmann *et al.* (1987).

4.2.4 Ageing of Clayey Soil

Soils are known to age and change with time. During the ageing process significant changes in soil strength have been observed (Mitchell, 1986; and Schmertmann, 1991).

The ageing of soil is considered in this work adopting an expression for the slope of the virgin consolidation curve λ as a function of time. From consolidation tests, the slope λ at initial time ($t = 0$) and its long-term value ($t \rightarrow \infty$) can be obtained. The slope λ can then be obtained at any intermediate time t by interpolation:

$$\lambda\left(p,t\right) = \lambda_0\left(p\right) + \left[\lambda_\infty\left(p\right) - \lambda_0\left(p\right)\right]\left[1 - \texttt{exp}\left(-\frac{t}{\tau}\right)\right] \tag{4.24}$$

where $\lambda_\infty\left(p\right)$ and $\lambda_0\left(p\right)$ are the slopes at time 0 and ∞, respectively and are explicitly shown as functions of the pressure p. The interpolation parameter τ appearing in Eq. 4.24 is to be determined from the observations.

4.3 Constitutive Model for Caisson

Caissons are typically fabricated from steel. The caisson material is assumed to remain isotropic and linearly elastic. Thus, the relationship between the rates of the stress $\dot{\sigma}_{ij}$ and strain $\dot{\varepsilon}_{ij}$ is given by:

$$\dot{\sigma}_{ij} = E_{ijkl}\dot{\varepsilon}_{kl} \tag{4.25}$$

where the tensor of tangent elastic moduli is given by:

$$E_{ijkl} = K\delta_{ij}\delta_{kl} + G\left(\delta_{ik}\delta_{jl} + \delta_{il}\delta_{jk} - \frac{2}{3}\delta_{ij}\delta_{kl}\right) \tag{4.26}$$

with K and G being the bulk and shear moduli, respectively.

4.4 Summary

The constitutive relationships adopted for saturated clayey soil and caisson were described in this chapter. Concepts of the bounding-surface plasticity model adopted for soil were discussed, and tangent moduli for soil and caisson were presented.

Chapter 5

INTERFACE MODELING

5.1 Introduction

The interior and exterior soil-caisson interfaces are modeled with a contact algorithm based on a slide-line formulation (Hallquist *et al.*, 1985) that allows for large relative displacements between the caisson and the soil. The slide-line formulation involves nodes on the soil side of the interface and surface elements on the caisson side.

In the contact algorithm, penetration of soil nodes into the caisson is prevented with constraints imposed on the solid displacement using Lagrange multipliers. Friction between the soil and the caisson is assumed to obey the classical Coulomb law. Two conditions, stick and slip, are distinguished on the basis of the level of interface frictional force in comparison with the Coulomb force. In addition, flow of water (Darcy's velocity) normal to the caisson surface is prevented through the contact algorithm.

Additional soil-to-soil contact elements are defined to treat interaction between “interior” and “exterior” soil interfaces below the caisson tip and along the path of caisson penetration. Continuity of solid displacements, Darcy’s velocity, and excess pore-water pressure is enforced through Lagrange multipliers. Therefore, for a node that is in contact with a surface element, contact contributions arising from constraining solid displacement, Darcy’s velocity, and excess pore-water pressure and contribution from the frictional interface are added to the tangent stiffness matrix and the residual vector during Newton iterations. The contact contributions arising from the constraints are obtained following the so-called “direct approach” discussed in Zhong (1993).

The slide-line contact formulation is developed in terms of effective forces along the interface, which are integrals of the effective traction along the interface. By the arrangement of the governing differential equations for the mixture and the corresponding weak statements, it is straightforward to extract these effective forces along the interface.

In this chapter, various contributions arising from the contact algorithm to the tangent stiffness matrix and the residual vector are described.

5.2 Solid Displacement Contribution

The slide-line algorithm requires definition of slave nodes and master segments. The slave nodes are associated with the contact surface and the master segments are associated with the master (or target) surface as shown in Fig. 5.1. The algorithm monitors penetration of the slave nodes into the master segments and once contact is established, i.e., penetration is detected, the contact contributions are added to the appropriate set of equations as long as the contact is “active”.

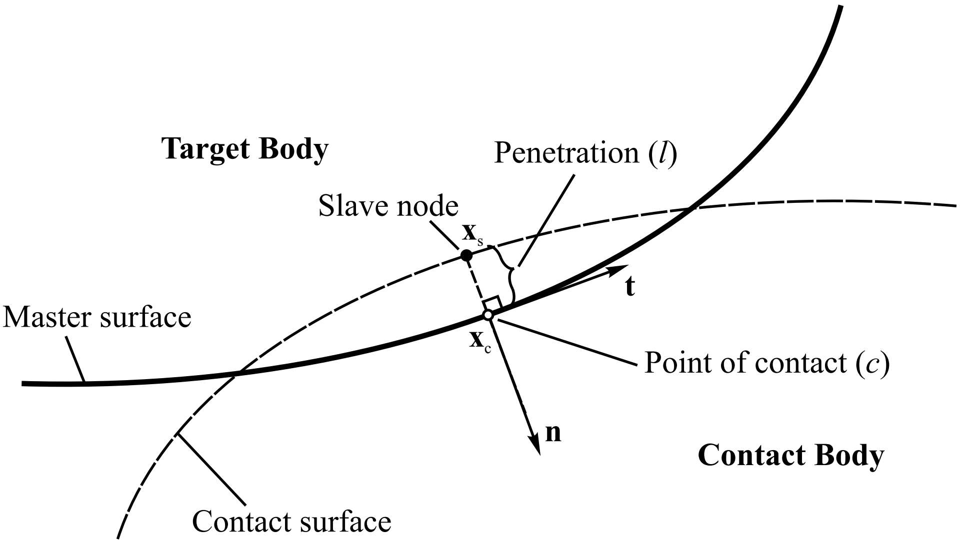

Figure 5.1: Definition of the slide-line formulation.

In general, the contact algorithm can be divided into three steps: identification of contact point; evaluation of penetration condition; and application of constraints, if contact is established.

5.2.1 Identification of Contact Point

The slave nodes that may potentially penetrate the target surface are either specified or identified. The point of contact (c) for each node is located in such a way that the distance between the slave node and the contact point is minimized. Therefore, the point of contact is the orthogonal projection of a slave node onto a master segment. In other words, the point of contact is obtained in such a way that the relative position vector ($\mathbf{x}_{sc}$) between the contact point and the slave node is normal to the tangent vector at the point of contact on the target surface. This is expressed as:

$$\mathbf{t}^T\mathbf{x}_{sc} = \mathbf{t}^T\left(\mathbf{x}_c - \mathbf{x}_s\right) = 0 \tag{5.1}$$

where $\mathbf{t}$ is a unit vector tangent to a master segment at the point of contact c having position vector $\mathbf{x}_c$, and the position vector of the slave node under consideration is denoted by $\mathbf{x}_s$. Definitions of the various vectors are shown in Fig. 5.2.

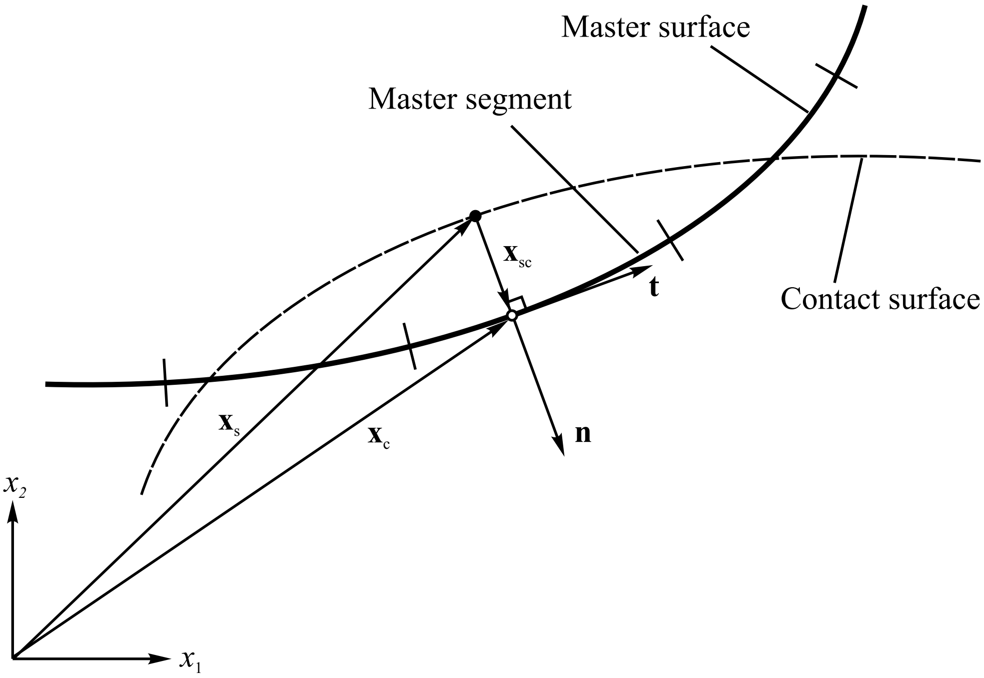

Figure 5.2: Definition of the slave node penetration into the master segment.

Upon finite-element discretization of the master segment, the position $\mathbf{x}_s$ and the tangent vector $\mathbf{t}$ can be obtained as:

$$\mathbf{x}_c = \mathbf{N}(\xi)\,\mathbf{X}_M \tag{5.2}$$

$$\mathbf{t} = \frac{\hat{\mathbf{t}}}{\|\hat{\mathbf{t}}\|}\,; \qquad \hat{\mathbf{t}} = \frac{\partial \mathbf{N}}{\partial \xi}\mathbf{X}_M = \mathbf{N}_{,\xi}\mathbf{X}_M \tag{5.3}$$

$$\mathbf{n} = -\mathbf{e}_3 \times \mathbf{t} \tag{5.4}$$

where $\mathbf{N}$ is the matrix containing interpolation functions of the natural coordinate ξ $(-1 \leq \xi \leq 1)$ of the master segment, and $\mathbf{X}_M$ is the vector containing nodal coordinates of the nodes describing the master segment. The unit vector $\mathbf{e}_3$ is directed along the positive x_3-direction and $\mathbf{n}$ is a unit normal vector to the master segment at the contact point.

With the use of Eqs. 5.2 and 5.3, Eq. 5.1 can be rewritten as:

$$(\mathbf{X}_M)^T (\mathbf{N}_{,\xi})^T [\mathbf{N}\mathbf{X}_M - \mathbf{x}_s] = 0 \tag{5.5}$$

which is nonlinear in ξ and requires an iterative scheme such as Newton's method to obtain $\hat{\xi}$ satisfying the orthogonality requirement posed by the equation. A contact element or pair is established if the value of $\hat{\xi}$ satisfies $-1 \leq \hat{\xi} \leq 1$.

5.2.2 Evaluation of Penetration Condition

The detection of slave-node penetration into the associated master segment is performed in this step. The minimum distance l between the slave node and the contact point is calculated as:

$$l = \mathbf{n}^T\mathbf{x}_{sc} = \mathbf{n}^T(\mathbf{x}_c - \mathbf{x}_s) = \mathbf{n}^T(\mathbf{N}\mathbf{X}_M - \mathbf{x}_s) = \mathbf{n}^T\mathbf{H}_s\mathbf{X} \tag{5.6}$$

where the vector $\mathbf{X}$ contains coordinates of the nodes defining the master segment and the slave node, and the matrix $\mathbf{H}_s$ is defined such that

$$(\mathbf{N}\mathbf{X}_M - \mathbf{x}_s) = \mathbf{H}_s\mathbf{X} \tag{5.7}$$

An open gap between the contact surface and the target surface at $\hat{\xi}$ is represented by a negative value of the penetration l. In that case, contributions are not added to the system of equations and the third step is omitted. Otherwise, the contact between the surfaces at $\hat{\xi}$ is established if the penetration l is positive, i.e.,

$$l > 0 \quad \Rightarrow \quad \texttt{Penetration} \tag{5.8}$$

5.2.3 Application of Constraints

Fulfillment of Eq. 5.8 indicates penetration of the slave node into the master segment. Therefore, it is necessary to enforce constraint to prevent the penetration. The constraint is applied using Lagrange multiplier λ_s to make the penetration l equal to zero, i.e., $l = 0$. The constrain is written as:

$$\lambda_s l = 0 \tag{5.9}$$

The value of the Lagrange multiplier is equal to the negative of the (compressive) force required to push the slave node back onto the master segment. The internal force vector $\mathbf{f}_{sl}$ acting on the slave node is given by:

$$\mathbf{f}_{sl} = -\lambda_s\mathbf{n} \tag{5.10}$$

In addition, equal in magnitude but opposite in direction force is consistently distributed to the nodes of the master segment as:

$$\mathbf{f}_M = \lambda_s \mathbf{N}^T \mathbf{n} \tag{5.11}$$

The virtual work performed by the nodal forces can be written as:

$$\begin{aligned}
\hat{\Pi}_s^c &= \left(\delta \mathbf{U}_M\right)^T \mathbf{f}_M + \left(\delta \mathbf{U}_{sl}\right)^T \mathbf{f}_{sl} && (5.12)\\
&= \left(\delta \mathbf{U}_s\right)^T \left\{ \begin{array}{c} \mathbf{f}_M \\ \mathbf{f}_{sl} \end{array} \right\} = \left(\delta \mathbf{U}_s\right)^T \left\{ \begin{array}{c} \lambda_s \mathbf{N}^T \mathbf{n} \\ -\lambda_s \mathbf{n} \end{array} \right\} && (5.13)\\
&= \left(\delta \mathbf{U}_s\right)^T \mathbf{H}_s^T \mathbf{n} \lambda_s && (5.14)
\end{aligned}$$

In incremental form, Eqs. 5.6 and 5.14 become:

$$\begin{aligned}
\Delta l &= \mathbf{n}^T \mathbf{H}_s \Delta \mathbf{X} = \mathbf{n}^T \mathbf{H}_s \Delta \mathbf{U}^s && (5.15)\\
\Delta \hat{\Pi}_s^c &= \left(\delta \mathbf{U}_s\right)^T \mathbf{H}_s^T \mathbf{n} \Delta \lambda_s && (5.16)
\end{aligned}$$

or, equivalently, in matrix form:

$$\begin{aligned}
&\left\{ \begin{array}{cc} \left(\delta \mathbf{U}_s\right)^T & \delta \lambda_s \end{array} \right\} \left[\begin{array}{cc} \mathbf{0} & -\mathbf{H}_s^T \mathbf{n} \\ -\mathbf{n}^T \mathbf{H}_s & 0 \end{array} \right] \left\{ \begin{array}{c} \Delta \mathbf{U}^s \\ \Delta \lambda_s \end{array} \right\} = \\
&\qquad \left\{ \begin{array}{cc} \left(\delta \mathbf{U}_s\right)^T & \delta \lambda_s \end{array} \right\} \left\{ \begin{array}{c} \mathbf{H}_s^T \mathbf{n} \lambda_s \\ l \end{array} \right\} \qquad (5.17)
\end{aligned}$$

where the matrix on the left is the contribution to the tangent stiffness matrix $\mathbf{K}_{\texttt{Tangent}}$, and the vector on the right is the contribution to the residual vector $\mathbf{R}$. For the large deformation problem at hand, additional contributions arising from the changes in $\mathbf{H}_s$ and $\mathbf{n}$ are taken into account to improve the rate of convergence (Wriggers and Simo, 1985). The complete expressions for the tangent contributions are presented in Appendix C.

The contributions expressed by Eq. 5.17 are added to the global system of equations as long as the penetration condition (Eq. 5.8) is satisfied. The contact contributions associated with the solid displacements $\Delta\mathbf{U}^s$ are assembled with the equation describing linear momentum balance of the mixture developed in Chapter 2. Hence, the internal compressive forces obtained from the Lagrange multipliers λ_s are due to the *total* stresses. Whenever an open gap condition is encountered during the analysis, the contributions are excluded. In such a case, compression forces are no longer acting at the nodes that were in contact previously. However, within the numerical implementation of the contact formulation, a small amount of separation (open gap) is considered as "contact" and all the contributions are added.

5.3 Darcy's Velocity Contribution

Once the contact is established between a slave node and corresponding point $\hat{\xi}$ on a master segment, it is necessary to consider the contact contributions arising from the equation describing linear momentum balance of the fluid phase alone. The constrain is enforced in terms of the flux across the interface. If the slave node is in contact with soil from the other side, then the water flux into one side of the interface must be equal to the water flux out of the other side of the interface. The constraint is applied by requiring that the normal component of the Darcy's velocities from both the sides of the interface equal to each other at the point of contact. The constraint is enforced using a

Lagrange multiplier to set the relative normal component of Darcy's velocity at the point of contact equal to zero (see Fig. 5.3). If the slave node is in contact with the caisson, then the normal Darcy's velocity at the slave node is constrained equal to zero.

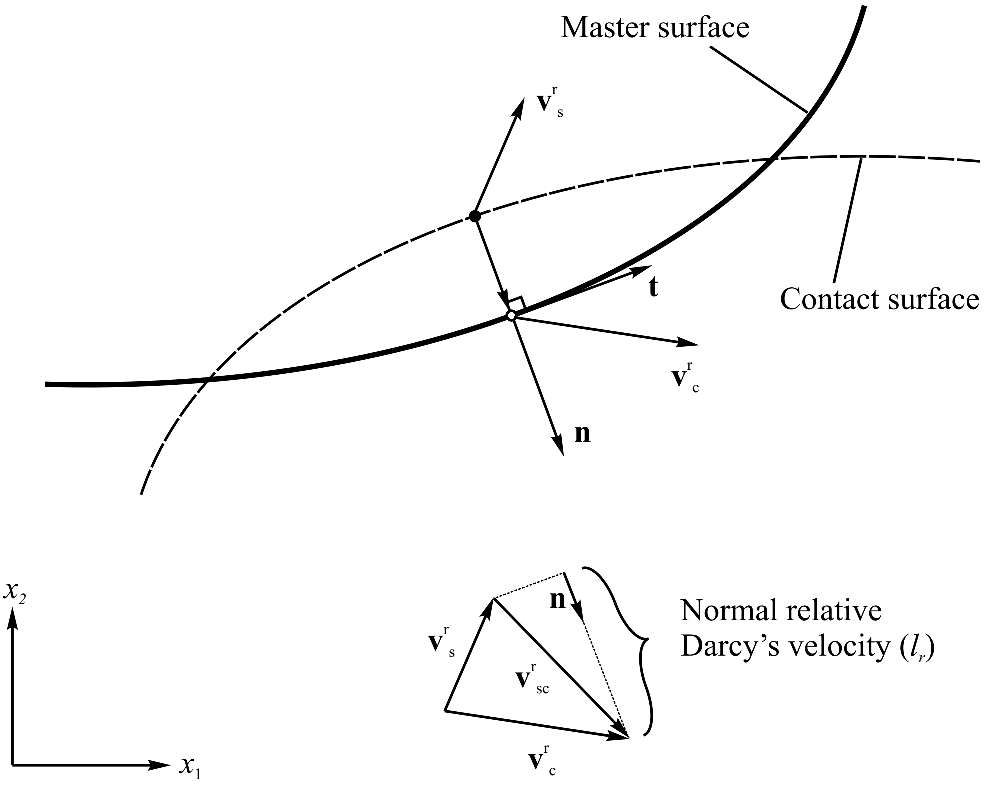

Figure 5.3: Darcy's velocity contribution.

5.3.1 Evaluation of Contact Condition

The Darcy's velocities at the slave node and the point of contact are denoted by $\mathbf{v}^r_s$ and $\mathbf{v}^r_c$, respectively. The Darcy's velocity at the point of contact is interpolated from the Darcy's velocities at the nodes associated with the master segment, and it is given by:

$$\mathbf{v}_c^r = \mathbf{N}_r \mathbf{V}_M^r \tag{5.18}$$

where $\mathbf{N}_r$ are the interpolation functions adopted for Darcy's velocity, and $\mathbf{V}_M^r$ is the vector of Darcy's velocities at the nodes of the master segment. The relative Darcy's velocity l_r at the interface in the normal direction at the point of contact is calculated as:

$$l_r = \mathbf{n}^T \mathbf{v}_{sc}^r = \mathbf{n}^T \left(\mathbf{v}_c^r - \mathbf{v}_s^r\right) = \mathbf{n}^T \left(\mathbf{N}_r \mathbf{V}_M^r - \mathbf{v}_s^r\right) = \mathbf{n}^T \mathbf{H}_r \mathbf{V}^r \tag{5.19}$$

where the vector $\mathbf{V}^r$ contains Darcy's velocities at the master segment nodes and at the slave node, and the matrix $\mathbf{H}_r$ is defined such that

$$\left(\mathbf{N}_r \mathbf{V}_M^r - \mathbf{v}_s^r\right) = \mathbf{H}_r \mathbf{V}^r \tag{5.20}$$

5.3.2 Application of Constraints

The normal relative Darcy's velocity is set to zero using Lagrange multiplier λ_r as:

$$\lambda_r l_r = 0 \tag{5.21}$$

The value of the Lagrange multiplier λ_r is equal to negative of the force required to enforce null relative flux across the interface. This force is acting at the slave node and force equal in magnitude but opposite in direction is acting on the master segment at the point of contact.

The virtual work performed by these internal nodal forces can be written as:

$$\hat{\Pi}_r^c = (\delta \mathbf{V}_r)^T \mathbf{H}_r^T \mathbf{n} \lambda_r \tag{5.22}$$

In incremental form, Eqs. 5.19 and 5.22 become:

$$\begin{aligned} \Delta l_r &= \mathbf{n}^T \mathbf{H}_r \Delta \mathbf{V}^r & (5.23) \\ \Delta \hat{\Pi}_r^c &= (\delta \mathbf{V}_r)^T \mathbf{H}_r^T \mathbf{n} \Delta \lambda_r & (5.24) \end{aligned}$$

or, equivalently, in matrix form:

$$\begin{aligned} &\left\{ \begin{array}{cc} (\delta \mathbf{V}_r)^T & \delta \lambda_r \end{array} \right\} \left[\begin{array}{cc} \mathbf{0} & -\mathbf{H}_r^T \mathbf{n} \\ -\mathbf{n}^T \mathbf{H}_r & 0 \end{array} \right] \left\{ \begin{array}{c} \Delta \mathbf{V}^r \\ \Delta \lambda_r \end{array} \right\} = \\ &\qquad \left\{ \begin{array}{cc} (\delta \mathbf{V}_r)^T & \delta \lambda_r \end{array} \right\} \left\{ \begin{array}{c} \mathbf{H}_r^T \mathbf{n} \lambda_r \\ l_r \end{array} \right\} \end{aligned} \tag{5.25}$$

where the matrix on the left is the contribution to the tangent stiffness matrix $\mathbf{K}_{\texttt{Tangent}}$, and the vector on the right is the contribution to the residual vector $\mathbf{R}$. Additional contributions to the tangent stiffness matrix arising from the changes in $\mathbf{H}_r$ and $\mathbf{n}$ are presented in Appendix C.

The contributions expressed by Eq. 5.25 are added to the global system of equation as long as the penetration condition (Eq. 5.8) is satisfied. The contact contributions associated with the Darcy's velocity $\Delta \mathbf{V}^r$ are assembled with the equation describing linear momentum balance of the fluid phase developed in Chapter 2. Hence, the internal compressive forces obtained from the Lagrange multipliers λ_r are due to the pore-water pressure. The equations related to the Darcy's velocity are multiplied by a factor of θ/α (see Section 3.1.3, Eq. 3.17). Therefore, multiplying Eq. 5.25 by the factor θ/α, the contribution to the tangent stiffness matrix is given by:

$$\begin{bmatrix} \mathbf{0} & -\mathbf{H}_r^T\mathbf{n}\frac{\theta}{\alpha} \\ -\mathbf{n}^T\mathbf{H}_r\frac{\theta}{\alpha} & 0 \end{bmatrix} \tag{5.26}$$

while the contribution to the residual vector is given by:

$$\begin{Bmatrix} \mathbf{H}_r^T\mathbf{n}\frac{\theta}{\alpha}\lambda_r \\ \frac{\theta}{\alpha}l_r \end{Bmatrix} \tag{5.27}$$

The above contributions are added when the slave node is in contact with soil from the other side, thus enforcing $l_r = 0$. If the slave node is in contact with the caisson, i.e., an impermeable boundary, then Darcy's velocity $\mathbf{V}_M^r$ associated with the master segment is equal to zero. The matrix and vector contributions (Eq. 5.26) with $\mathbf{V}_M^r = \mathbf{0}$ will set the normal Darcy's velocity component at the slave node equal to zero. Only flow tangentially to the interface is allowed.

5.4 Excess Pore-Water Pressure Contribution

Once contact is established between a slave node and the corresponding point $\hat{\xi}$ on the master segment, it is necessary to consider the contact contributions arising from the equation describing balance of mixture mass. The contribution is enforced only when the slave node is in contact with soil from the other side. A constraint is required to enforce continuity of the excess pore-water pressure across the interface. The constraint is implemented to set the difference in excess pore-water pressure across the interface equal to zero.

5.4.1 Evaluation of Contact Condition

The excess pore-water pressures at the slave node and the point of contact are denoted by $\bar{p}_s^w$ and $\bar{p}_c^w$, respectively. The excess pore-water pressure at the point of contact is interpolated from nodal values of the pressure, and it is expressed as:

$$\bar{p}_c^w = \mathbf{N}_p \bar{\mathbf{P}}_M^w \tag{5.28}$$

where the interpolation functions for the pressure are denoted by $\mathbf{N}_p$, and the vector $\bar{\mathbf{P}}_M^w$ contains values of the pressure at the nodes associated with the master segment.

The difference in pressure l_p across the interface is expressed as:

$$l_p = \bar{p}_c^w - \bar{p}_s^w = \left(\mathbf{N}_p \bar{\mathbf{P}}_M^w - \bar{p}_s^w\right) = \mathbf{H}_p \bar{\mathbf{P}}^w \tag{5.29}$$

where the vector $\bar{\mathbf{P}}^w$ contains nodal values of pressure at the master segment nodes and the slave node, and the matrix $\mathbf{H}_p$ is defined such that

$$\left(\mathbf{N}_p \bar{\mathbf{P}}_M^w - \bar{p}_s^w\right) = \mathbf{H}_p \bar{\mathbf{P}}^w \tag{5.30}$$

5.4.2 Application of Constraints

The difference in pressure l_p is set to zero using the Lagrange multiplier λ_p as:

$$\lambda_p l_p = 0 \tag{5.31}$$

The value of the Lagrange multiplier λ_p is equal to the negative of the flux required for the difference in pressure across the interface to vanish.

The virtual work performed by the internal flux can be written as:

$$\hat{\Pi}_p^c = \left(\delta \bar{\mathbf{P}}_w\right)^T \mathbf{H}_p^T \lambda_p \tag{5.32}$$

In incremental form, Eqs. 5.29 and 5.32 become:

$$\begin{aligned} \Delta l_p &= \mathbf{H}_r \Delta \bar{\mathbf{P}}^w && (5.33) \\ \Delta \hat{\Pi}_p^c &= \left(\delta \bar{\mathbf{P}}_w\right)^T \mathbf{H}_p^T \Delta \lambda_p && (5.34) \end{aligned}$$

or, equivalently, in matrix form:

$$\begin{aligned} &\left\{ \begin{array}{cc} \left(\delta \bar{\mathbf{P}}_w\right)^T & \delta \lambda_p \end{array} \right\} \left[\begin{array}{cc} \mathbf{0} & -\mathbf{H}_p^T \\ -\mathbf{H}_p & 0 \end{array} \right] \left\{ \begin{array}{c} \Delta \bar{\mathbf{P}}^w \\ \Delta \lambda_p \end{array} \right\} = \\ &\qquad \left\{ \begin{array}{cc} \left(\delta \bar{\mathbf{P}}_w\right)^T & \delta \lambda_p \end{array} \right\} \left\{ \begin{array}{c} \mathbf{H}_p^T \lambda_p \\ l_p \end{array} \right\} \end{aligned} \tag{5.35}$$

where the matrix on the left is the contribution to the tangent stiffness matrix $\mathbf{K}_{\mathtt{Tangent}}$, and the vector on the right is the contribution to the residual vector $\mathbf{R}$. An additional contribution to the tangent stiffness matrix arising from the changes in $\mathbf{H}_p$ is presented in Appendix C.

The contributions expressed by Eq. 5.35 are added to the global system of equations as long as the penetration condition (Eq. 5.8) is satisfied. Specifically, the contact contribution associated with the excess pore-water pressure

$\Delta\bar{\mathbf{P}}^w$ are assembled with the equation describing balance of the mixture mass developed in Chapter 2. Therefore, the Lagrange multiplier λ_p measures flux through the interface. The equations related to excess pore-water pressure are multiplied by a factor of α (see Section 3.1.3, Eq. 3.17). Multiplying Eq. 5.35 by the factor α, the contribution to the tangent stiffness matrix becomes:

$$\begin{bmatrix} \mathbf{0} & -\mathbf{H}_p^T\alpha \\ -\mathbf{H}_p\alpha & 0 \end{bmatrix} \tag{5.36}$$

while the contribution to the residual vector is given by:

$$\begin{Bmatrix} \mathbf{H}_p^T\alpha\lambda_p \\ \alpha l_p \end{Bmatrix} \tag{5.37}$$

The above contributions are added when the slave node is in contact with soil from the other side, enforcing $l_p = 0$. If the slave node is in contact with the caisson, i.e., an impermeable boundary, then the contributions expressed by Eq. 5.36 are excluded.

5.5 Frictional Contact Contribution

Frictional behavior between the soil and the caisson is considered by adopting the classical Coulomb law (Fig. 5.4). After contact is established between a slave node and the corresponding point $\hat{\xi}$ on a master segment, it is necessary to consider the contact contributions arising from the frictional force across the interface.

Frictional force along the interface is a function of the effective normal force, computed as the difference between interface forces due to total stress

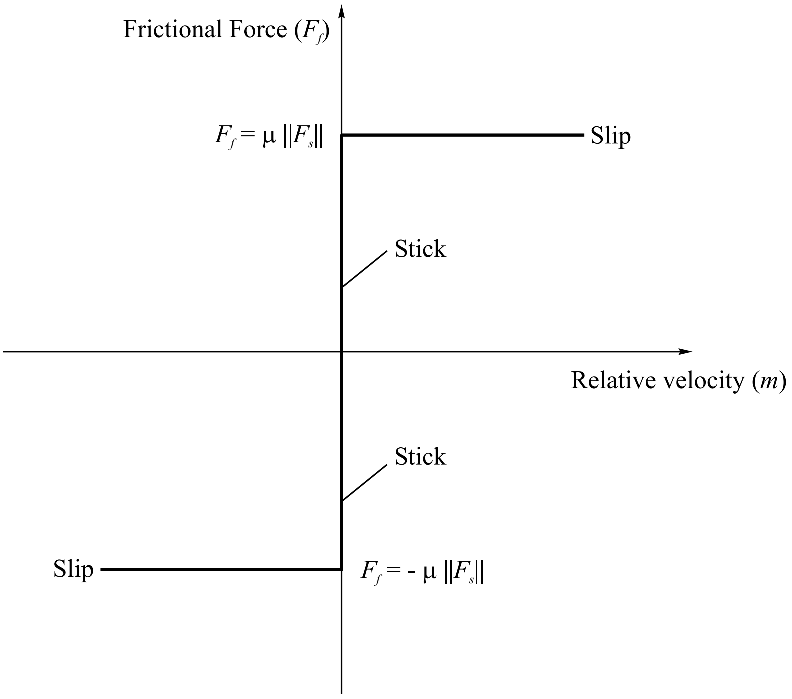

Figure 5.4: Definition of the Coulomb friction law.

and excess pore-water pressure. These interface forces are extracted from the virtual work equations presented in Chapter 2. The first term in Eq. 2.55 is the virtual work of the surface traction due to total stresses, which, within the finite-element framework, leads to the (consistent) definition of the equivalent total force. Similarly, the first term in Eq. 2.58 is the virtual work of the surface traction due to excess pore-water pressure, giving rise to the equivalent excess pore-water force. Therefore, the virtual work of the surface traction due to effective stresses, or the equivalent effective force, can be obtained as the difference between the former and the latter. This way of extracting the forces due to effective traction is possible because of the way the governing equations are crafted and the fact that the interpolation functions adopted for the solid displacements and Darcy's velocities are identical.

Two conditions, stick and slip, are distinguished on the basis of the level of interface frictional force in comparison with the Coulomb force, taken equal to the effective compressive (normal) force multiplied by the soil-caisson interface friction coefficient μ. In the stick condition, the frictional force is less than the Coulomb frictional force and, therefore, the relative motion along the interface vanishes. In the slip condition, the frictional force is set equal to the Coulomb frictional force and, therefore, finite relative motion along the interface occurs.

5.5.1 Evaluation of Contact Condition

The tangential motion along the interface is expressed in terms of the relative tangential velocity between the slave node and the point of contact ($\hat{\xi}$). The tangential velocities at the slave node and the contact point are denoted by $\mathbf{v}_s^s$ and $\mathbf{v}_c^s$, respectively, and the various vectors are defined as in Fig. 5.5. Then the tangential velocity at the contact point can be interpolated from the velocities at the nodes associated with the master segment and expressed as:

$$\mathbf{v}_c^s = \mathbf{N}_s \mathbf{V}_M^s \tag{5.38}$$

where the interpolation functions for the velocity are denoted by $\mathbf{N}_s$, and the vector $\mathbf{V}_M^s$ contains velocities of the nodes of the master segment.

The relative tangential velocity (m) along the interface is calculated as:

$$m = \mathbf{t}^T \mathbf{v}_{sc}^s = \mathbf{t}^T \left(\mathbf{v}_c^s - \mathbf{v}_s^s \right) = \mathbf{t}^T \left(\mathbf{N} \mathbf{V}_M^s - \mathbf{v}_s^s \right) = \mathbf{t}^T \mathbf{H}_s \mathbf{V}^s \tag{5.39}$$

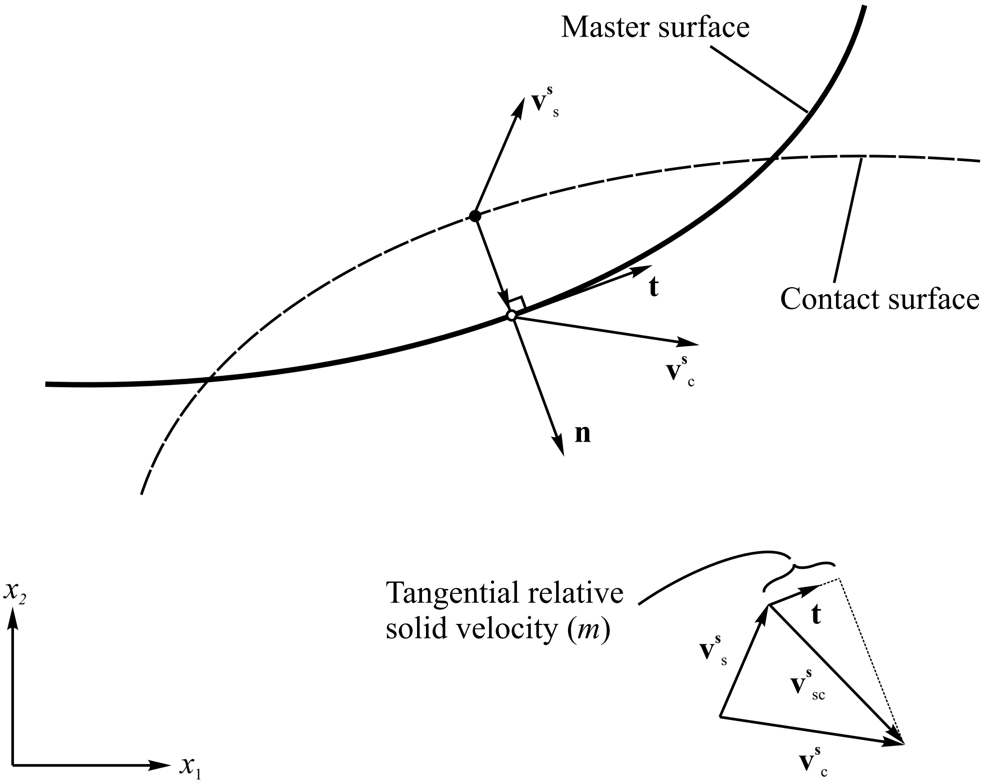

Figure 5.5: Definition of relative tangential velocity at contact.

where the vector $\mathbf{V}^s$ contains the (solid) velocities at the master segment nodes and the slave node, and the matrix $\mathbf{H}_s$ is defined by Eq. 5.7.

5.5.2 Stick Condition

For the stick condition, the relative tangential velocity along the interface vanishes. This constraint is enforced using the Lagrange multiplier λ_f, and can be written as:

$$\lambda_f m = 0 \tag{5.40}$$

The value of the Lagrange multiplier λ_f is equal to the negative of the frictional force acting at the interface, on the slave node as well as the master segment nodes. This frictional force performs virtual work given by:

$$\hat{\Pi}^c_{F,\,\texttt{Stick}} = (\delta \mathbf{U}_s)^T \mathbf{H}_s^T \mathbf{t} \lambda_f \tag{5.41}$$

In incremental form, Eqs. 5.39 and 5.41 become:

$$\begin{aligned} \Delta m &= \mathbf{t}^T \mathbf{H}_s \Delta \mathbf{V}^s && (5.42) \\ \Delta \hat{\Pi}^c_{F,\,\texttt{Stick}} &= (\delta \mathbf{U}_s)^T \mathbf{H}_s^T \mathbf{t} \Delta \lambda_f && (5.43) \end{aligned}$$

With the use of the relationship between the increment of (solid) displacements $\Delta \mathbf{U}^s$, and the increment of (solid) velocities $\Delta \mathbf{V}^s$ obtained for the backward Euler time-stepping scheme, the following matrix form can be obtained from Eqs. 5.42 and 5.43:

$$\begin{aligned} &\left\{ \begin{array}{cc} (\delta \mathbf{U}_s)^T & \delta \lambda_f \end{array} \right\} \left[\begin{array}{cc} \mathbf{0} & -\mathbf{H}_s^T \mathbf{t} \\ -\frac{1}{\alpha} \mathbf{t}^T \mathbf{H}_s & 0 \end{array} \right] \left\{ \begin{array}{c} \Delta \mathbf{U}^s \\ \Delta \lambda_f \end{array} \right\} = \\ &\qquad \left\{ \begin{array}{cc} (\delta \mathbf{U}_s)^T & \delta \lambda_f \end{array} \right\} \left\{ \begin{array}{c} \mathbf{H}_s^T \mathbf{t} \lambda_f \\ m \end{array} \right\} \end{aligned} \tag{5.44}$$

where the matrix on the left is the contribution to the tangent stiffness matrix $\mathbf{K}_{\texttt{Tangent}}$, and the vector on the right is the contribution to the residual vector $\mathbf{R}$. Additional contributions to the tangent stiffness matrix arising from the changes in $\mathbf{H}_s$ and $\mathbf{t}$ are presented in Appendix C.

5.5.3 Slip Condition

For the slip condition, the frictional force is set equal to the Coulomb frictional force and finite relative motion along the interface is allowed. The frictional force is calculated as:

$$F_f = \mu F_s f\left(m\right) \tag{5.45}$$

where F_f is the internal frictional force acting along the interface, μ is the coefficient of friction, $f\left(m\right)$ is a function that provides the direction of the frictional force and it is defined as $f\left(m\right) = \mathtt{sign}\left(m\right) = m/\|m\|$, and F_s is the normal force due to *effective* stresses. The normal force F_s is calculated as the difference between the normal forces due to total stresses and pore-water pressure:

$$F_s = \left(-\lambda_s\right) - \left(-\lambda_r\right) \tag{5.46}$$

The virtual work performed by the frictional force is given by:

$$\hat{\Pi}^c_{F,\,\mathtt{Slip}} = -\left(\delta\mathbf{U}_s\right)^T\mathbf{H}^T_s\mathbf{t}F_f = \left(\delta\mathbf{U}_s\right)^T\mathbf{H}^T_s\mathbf{t}\mu\left(\lambda_s - \lambda_r\right)f\left(m\right) \tag{5.47}$$

In incremental form, Eq. 5.47 becomes:

$$\Delta\hat{\Pi}^c_{F,\,\mathtt{Slip}} = \left(\delta\mathbf{U}_s\right)^T\mathbf{H}^T_s\mathbf{t}\mu\left(\Delta\lambda_s - \Delta\lambda_r\right)f\left(m\right) \tag{5.48}$$

which can be rewritten in matrix form as:

$$\left\{ \begin{array}{ccc} (\delta\mathbf{U}_s)^T & \delta\lambda_s & \delta\lambda_r \end{array} \right\} \left[\begin{array}{ccc} \mathbf{0} & -\mathbf{H}_s^T\mathbf{t}\mu f\left(m\right) & \mathbf{H}_s^T\mathbf{t}\mu f\left(m\right) \\ \mathbf{0} & 0 & 0 \\ \mathbf{0} & 0 & 0 \end{array} \right] \left\{ \begin{array}{c} \Delta\mathbf{U}^s \\ \Delta\lambda_s \\ \Delta\lambda_r \end{array} \right\}$$

$$= \left\{ \begin{array}{ccc} (\delta\mathbf{U}_s)^T & \delta\lambda_s & \delta\lambda_r \end{array} \right\} \left\{ \begin{array}{c} -\mathbf{H}_s^T\mathbf{t}F_f \\ 0 \\ 0 \end{array} \right\} \tag{5.49}$$

where the matrix on the left is the contribution to the tangent stiffness matrix $\mathbf{K}_{\texttt{Tangent}}$, and the vector on the right is the contribution to the residual vector $\mathbf{R}$. Additional contributions to the tangent stiffness matrix arising from the changes in $\mathbf{H}_s$ and $\mathbf{t}$ are presented in Appendix C.

5.5.4 Stick-Slip Transition

Within every Newton iteration, the contact algorithm monitors changes in the frictional contact conditions. The transition from stick condition to slip condition and vice-versa is handled according to the following procedure:

- **Stick condition**: The frictional force is set equal to the negative of the Lagrange multiplier λ_f, and the following two cases are checked:
    1. If the frictional force is smaller than the Coulomb frictional force, the contact condition remains as stick.
    2. Otherwise, the contact condition is changed to slip and the frictional force is set equal to the Coulomb frictional force.
- **Slip condition**: The sign of the relative tangential velocity (m) is monitored, and the following two cases are considered:

1. If m changes sign, then the contact condition is changed to stick.
2. Otherwise, the contact condition remains as slip.

5.6 Contribution at Release Condition

If the penetration condition (Eq. 5.8) is not satisfied, then there will be an open gap between the interfaces and, therefore, the contact contributions developed in the Section 5.2 are excluded. The open gap in the porous media is filled with water, therefore, the excess pore-water pressure acts on both the sides of the interface. In terms of the Lagrange multipliers λ_r, the virtual work performed by the excess pore-water pressure is expressed as:

$$\hat{\Pi}_R^c = (\delta \mathbf{U}_s)^T \mathbf{H}_s^T \mathbf{n} \lambda_r \tag{5.50}$$

In incremental form, the virtual work (Eq. 5.50) is given by:

$$\Delta \hat{\Pi}_R^c = (\delta \mathbf{U}_s)^T \mathbf{H}_s^T \mathbf{n} \Delta \lambda_r \tag{5.51}$$

and in matrix form:

$$\left\{ \begin{array}{ccc} (\delta \mathbf{U}_s)^T & \delta \lambda_s & \delta \lambda_r \end{array} \right\} \begin{bmatrix} \mathbf{0} & \mathbf{0} & -\mathbf{H}_s^T \mathbf{n} \\ \mathbf{0} & 0 & 0 \\ \mathbf{0} & 0 & 0 \end{bmatrix} \left\{ \begin{array}{c} \Delta \mathbf{U}^s \\ \Delta \lambda_s \\ \Delta \lambda_r \end{array} \right\} =$$

$$\left\{ \begin{array}{ccc} (\delta \mathbf{U}_s)^T & \delta \lambda_s & \delta \lambda_r \end{array} \right\} \left\{ \begin{array}{c} \mathbf{H}_s^T \mathbf{n} \lambda_r \\ 0 \\ 0 \end{array} \right\} \tag{5.52}$$

where the matrix on the left is the contribution to the tangent stiffness matrix $\mathbf{K}_{\texttt{Tangent}}$, and the vector on the right is the contribution to the residual vector $\mathbf{R}$. Additional contributions to the tangent stiffness matrix arising from the changes in $\mathbf{H}_s$ and $\mathbf{n}$ are presented in Appendix C.

5.7 Summary

In this chapter. the treatment of contact between caisson-soil interfaces and soil-soil interface below the caisson tip was developed based on a slide-line formulation. Various contributions arising from the contact algorithm to the tangent stiffness matrix and the residual vector were derived, and their expressions are presented in Appendix C.

Chapter 6

REMESHING SCHEME

During simulation of the caisson installation process, the contact algorithm described in Chapter 5 requires *a priori* knowledge of penetration path of the caisson. This requirement imposes a limitation as the actual path is not known. A remeshing tool is developed to remove this limitation.

In this chapter, the remeshing strategy, mapping of field and state variables from the old finite-element mesh to the new one, and implementation of the remeshing algorithm within the computational procedure are described.

6.1 Definition of the Penetration Path

The term "path of penetration" for the caisson wall is described with reference to Fig. 6.1. The path of penetration is defined as the locus of soil material points in the undeformed (initial) configuration that comes in contact with the caisson wall in the deformed (final) configuration. As illustrated in Fig. 6.1, the caisson penetrates along the dotted vertical line $a-b$ (or $a'-b'$). The path represented by the solid line $a-o-b$ (or $a'-o'-b'$) in the initial (undeformed) configuration (see Fig. 6.1a) comes in contact with the caisson wall in the final (deformed) configuration (see Fig. 6.1b). The solid line $a-o-b$ (or $a'-o'-b'$) in undeformed configuration is defined as the path of penetration.

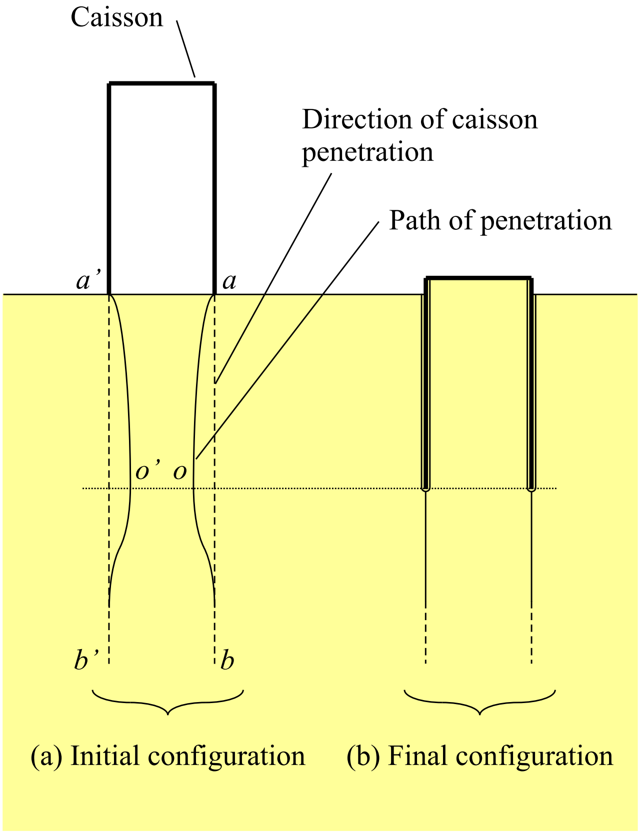

Figure 6.1: Definition of the caisson penetration path.

6.2 Necessity of Remeshing

In the earlier numerical study by Vásquez (2000), the path of penetration was assumed to be in the axial direction and aligned with the center-line of the caisson wall. In addition, during the analysis, the path of penetration was held in position by not allowing the nodes, lying along the interface, to move laterally. This fictitious requirement imposes constraints on soil deformation during caisson penetration thus affecting the state of stress in the soil. In turn, the estimated capacity of the caisson may be influenced by the soil condition in the vicinity of the caisson wall. Therefore, it is desirable to eliminate *a priori* assumption regarding the path of penetration.

The remeshing tool described below determines the path of penetration as installation of the caisson progresses. For this remeshing scheme, the assumed path of penetration is allowed to move freely. As the installation of the caisson progresses, the deformed penetration path is adjusted by means of the remeshing scheme so that it remains straight in the axial direction during the course of installation.

6.3 Remeshing Algorithm and Implementation

A typical remeshing algorithm requires generation of a new (adjusted) mesh from the old mesh, and mapping of field variables (at nodes) and state variables (at integration points) from the old mesh to the new mesh. This section provides details regarding the remeshing algorithm and its implementation within the computational procedure.

6.3.1 Selection of Elements for Remeshing

The remeshing or adjustment to the finite-element mesh is performed locally below the caisson tip, and along the interior-exterior soil interface. At a particular instant of remeshing, based on the location of the caisson tip, one column of elements from each side of the interface is selected as shown in Fig. 6.2.

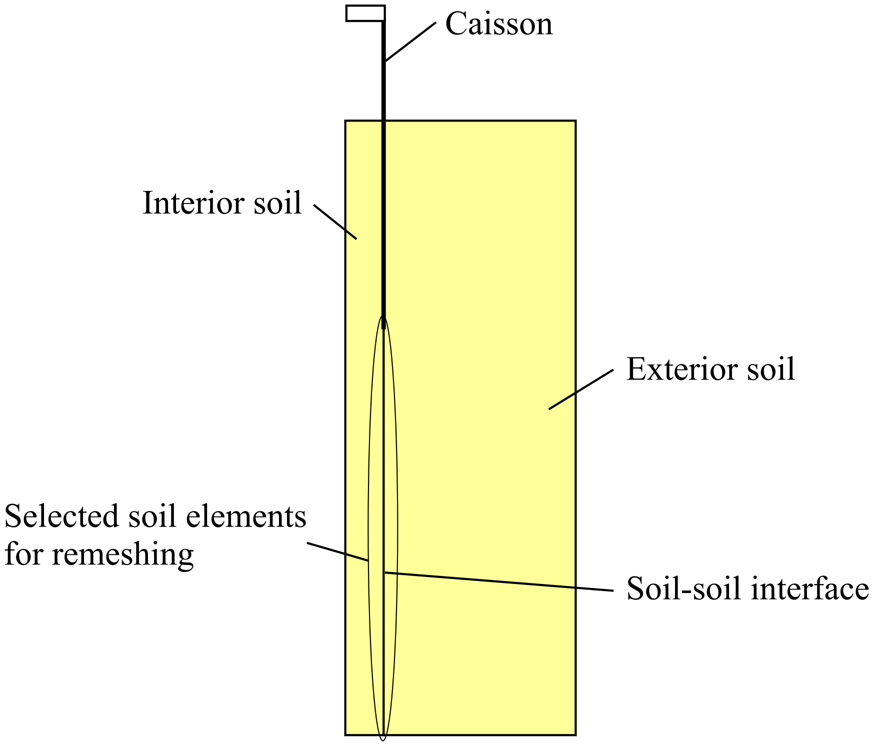

Figure 6.2: Selection of finite-elements for remeshing.

To select the elements, first the nodes located below the caisson tip and associated with both surfaces of the interface are identified. Identification of the nodes is achieved by comparing their radial coordinate with the radial coordinate of the caisson tip. Therefore, if a node is located below the caisson tip and has difference between its radial coordinate and the caisson tip radial coordinate less than a specified tolerance ε, then the node is selected for adjustment. The strategy for the identification of the nodes can be expressed as:

$$z_{tip} > z_{node} \quad \texttt{and} \quad \|r_{tip} - r_{node}\| \leq \varepsilon \quad \Rightarrow \quad \texttt{node be adjusted} \tag{6.1}$$

where z_{tip} (r_{tip}) and z_{node} (r_{node}) are the vertical (radial) coordinates of the caisson tip and the node, respectively. In the course of caisson penetration, the number of nodes selected for adjustment decreases as only the nodes below the caisson tip are selected.

From the nodes identified as per Eq. 6.1, the elements containing these nodes are selected for remeshing. The selection of elements is based on position of its interface nodes with respect to position of the caisson tip, therefore, elements both partially or completely below the caisson tip are selected. Two columns of elements selected for adjustment are shown in Fig. 6.3.

6.3.2 Generation of New Mesh

After selection of the elements to be adjusted, the new mesh is generated in such a way that the line of nodes associated with the interface becomes axially straight below the caisson tip as shown in Fig. 6.3. The elements before and after adjustment are plotted in Fig. 6.3 as dotted and solid lines, respectively. Similarly, the nodes before and after adjustment are plotted as hollow and solid circles, respectively. The interface that is “off” the axial direction before remeshing becomes axially straight after remeshing. The volume contained between (spatial) locations of the interface before and after remeshing represents amount of soil flowing from one side of the interface to the other. The amount of displaced soil is shown as hatched area in Fig. 6.3.

As mentioned earlier, the remeshing is performed locally. Therefore, only a few of the nodes of an element selected for remeshing are affected.

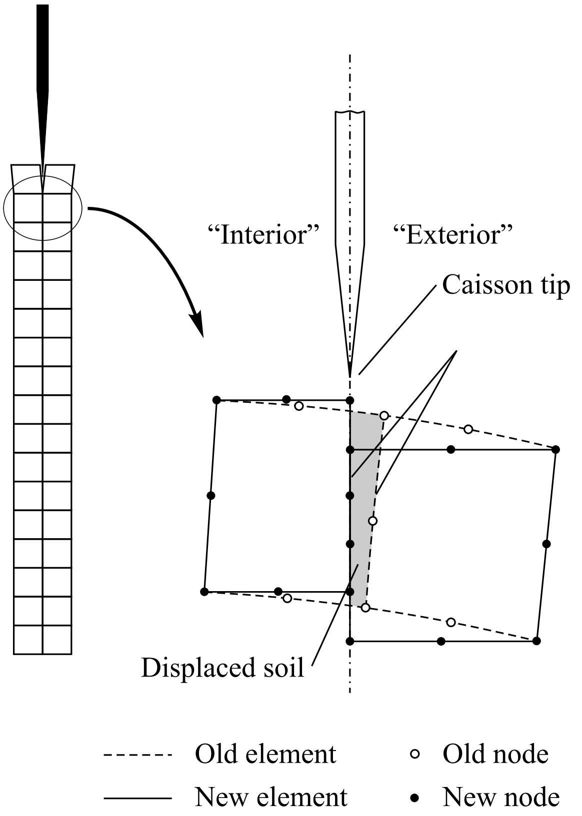

Figure 6.3: Selected finite-element columns for remeshing (*left*), and remeshing of typical elements (*right*).

The number of nodes relocated during remeshing depends on the location of the caisson tip with respect to the element. As demonstrated in Fig. 6.4, if the element is located completely below the tip, then five out of eight nodes require relocation. If there are two nodes below the tip then three nodes require relocation, and if there is only one node below the tip, then two nodes require relocation.

The nodes which are not relocated are fixed during remeshing as other elements attached to them are not being adjusted. Capabilities for gener-

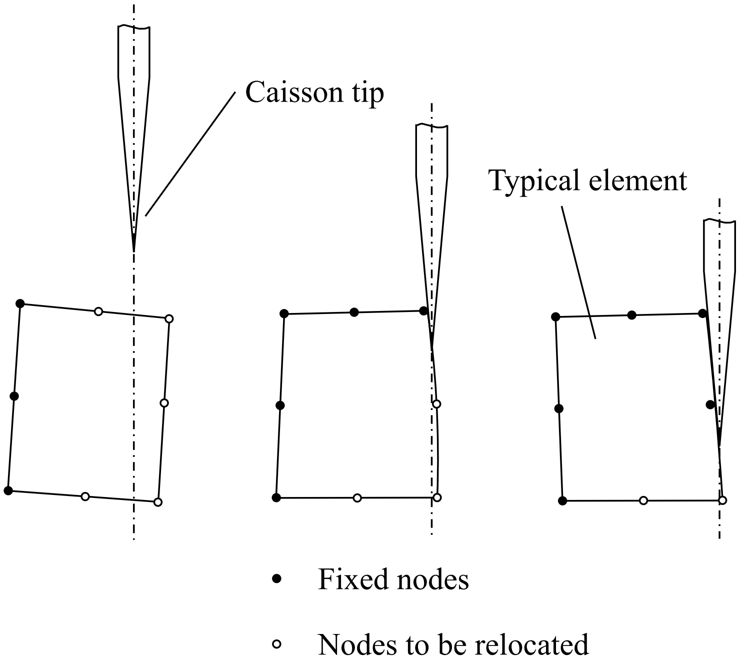

Figure 6.4: Number of nodes to be relocated.

ating a new mesh that is conforming along the interface as well as a non-conforming one have been implemented. In this section, conforming as well as non-conforming mesh generation is described. In the computations, only the conforming mesh generation is adopted based on the choice made for contact algorithm (see Chapter 5).

Generation of a conforming mesh requires knowledge of element data from the two sides of the interface. Therefore, special care needs to be exercised to make the required data available for calculation of coordinates of the new nodes. On the other hand, generation of a non-conforming mesh does not require information regarding neighboring elements and, therefore, its implementation is straightforward.

Conforming Mesh

In the conforming mesh, the new nodes along the interface are relocated in such a way that they are aligned with the corresponding nodes from the other side of the interface. The remaining (middle) nodes are shifted appropriately and maintained at the midpoints of the element sides. The nodes-relocation procedure is shown in Fig. 6.5.

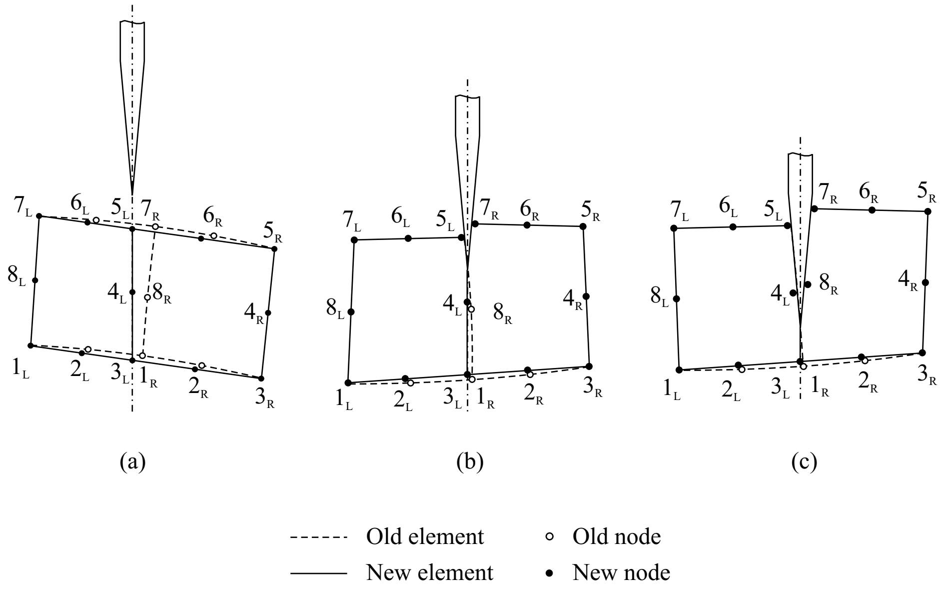

(a) (b) (c)

Figure 6.5: Relocation of nodes to generate conforming mesh.

For the element located completely below the tip (see Fig. 6.5a), the following sequence is adopted:

- Relocate nodes 3_L and 1_R at the intersection of a line joining nodes 1_L and 3_R and the axial line passing through the tip;
- Similarly, relocate nodes 5_L and 7_R at the intersection of a line joining

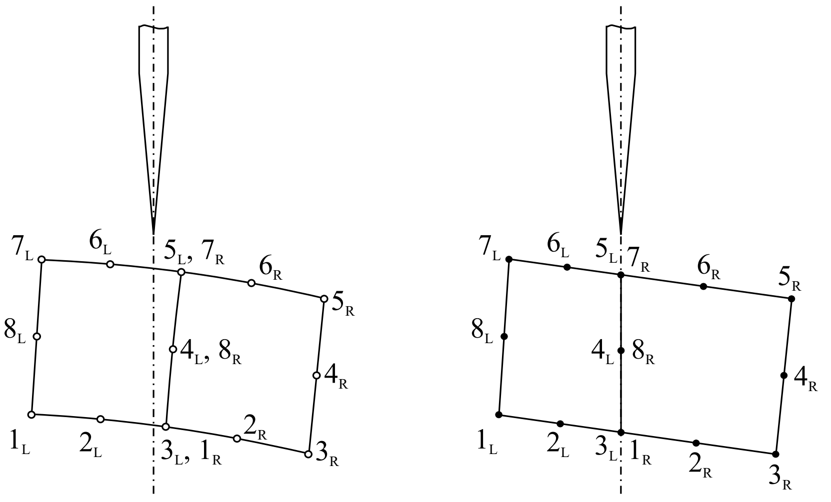

Before remeshing

After remeshing

Figure 6.6: Node-relocation scheme for three nodes below the tip.

nodes 7_L and 5_R and the axial line passing through the tip;

- Node 4_L (8_R) is relocated at the middle between nodes 3_L and 5_L (1_R and 7_R);
- Node 2_L (2_R) is relocated at the middle between nodes 1_L and 3_L (1_R and 3_R);
- Node 6_L (6_R) is relocated at the middle between nodes 7_L and 5_L (7_R and 5_R).

A detailed view of the finite-elements, located completely below the tip, before and after remeshing is presented in Fig. 6.6.

For the element having two nodes at the interface located below the tip (see Fig. 6.5b), the following sequence is adopted:

- Relocate nodes 3_L and 1_R at the intersection of a line joining nodes 1_L and 3_R and the axial line passing through the tip;
- Node 2_L (2_R) is relocated at the middle between nodes 1_L and 3_L (1_R and 3_R);
- Node 4_L (8_R) is relocated at the middle between the midpoints of sides 3_L-5_L and 1_R-7_R.

For the element having one node at the interface located below the tip (see Fig. 6.5c), the following sequence is adopted:

- Relocate nodes 3_L and 1_R at the intersection of a line joining nodes 1_L and 3_R and the axial line passing through the tip;
- Node 2_L (2_R) is relocated at the middle between nodes 1_L and 3_L (1_R and 3_R).

Non-Conforming Mesh

In the non-conforming mesh, the new nodes are relocated in such a way that the element edges in the radial direction become horizontal after remeshing, thus preventing the new nodes from becoming conformal along the interface. The node-relocation procedure is shown in Fig. 6.7.

For the element located completely below the tip (see Fig. 6.7a), the following sequence is adopted:

- Node 3_L is relocated at the radial projection of node 1_L onto the axial line passing through the tip;

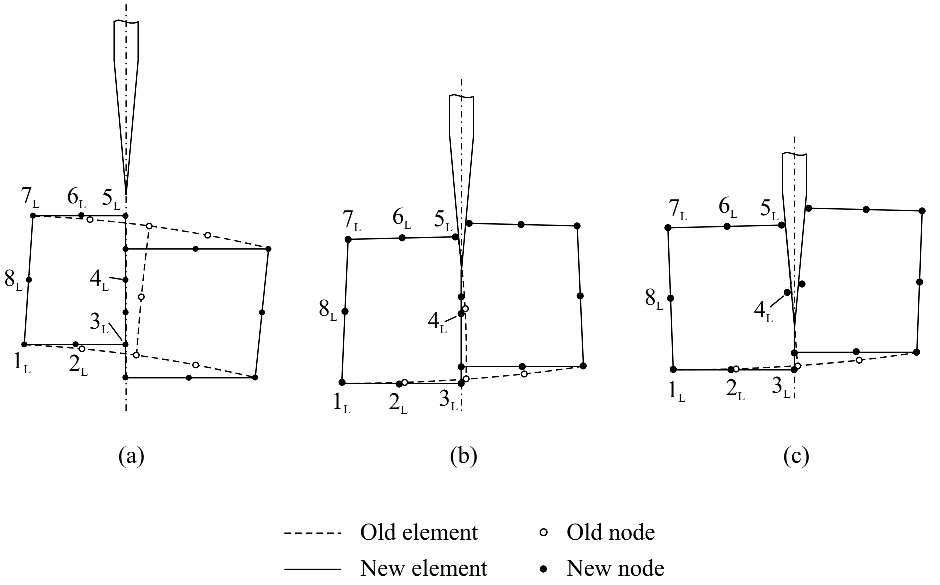

Figure 6.7: Relocation of nodes to generate non-conforming mesh.

- Similarly, node 5_L is relocated at the radial projection of node 7_L onto the axial line passing through the tip;
- Node 4_L is relocated at the middle between nodes 3_L and 5_L;
- Node 2_L is relocated at the middle between nodes 1_L and 3_L;
- Node 6_L is relocated at the middle between nodes 7_L and 5_L.

For the element having two nodes at the interface located below the tip (see Fig. 6.7b), the following sequence is adopted:

- Node 3_L is relocated at the radial projection of node 1_L onto the axial line passing through the tip;
- Node 4_L is relocated at the middle between nodes 3_L and 5_L;

- Node 2_L is relocated at the middle between nodes 1_L and 3_L.

For the element having one node at the interface located below the tip (see Fig. 6.7c), the following sequence is adopted:

- Node 3_L is relocated at the radial projection of node 1_L onto the axial line passing through the tip;
- Node 2_L is relocated at the middle between nodes 1_L and 3_L.

For the elements on the other (right) side of the interface, the nodes are relocated using a similar procedure (see Fig. 6.7).

6.3.3 Mapping of Field and State Variables

In this section, the mapping of field variables at nodes and state variables at integration points between the old mesh and new meshes is described.

Nodal Field Variables

After generation of the new mesh, the nodal quantities are transferred or mapped from the old mesh to the new mesh using the corresponding element shape functions. As described in Chapter 2, the finite-element discretization is applied to solid displacements, Darcy's velocities, and excess pore-water pressure. Therefore, variables related to the three fields and their time derivatives need to be mapped. Mapping of nodal field variables is performed only for the relocated nodes. For the fixed nodes mapping is not required as their spatial position does not change due to remeshing.

Before mapping the variables to a new node n, it is required to determine the element E_0 in the old mesh that contains this node (see Fig. 6.8). Within a typical remeshing algorithm, determination of the element E_0 is performed through efficient search algorithms such as those based on triangulation and search tree data structures (Krause and Rank, 1996). As a relatively small number of elements are involved in remeshing in the present study, a straightforward search is adopted. For a node under consideration such as node n, a search within the elements selected for remeshing is performed until the element E_0 is found.

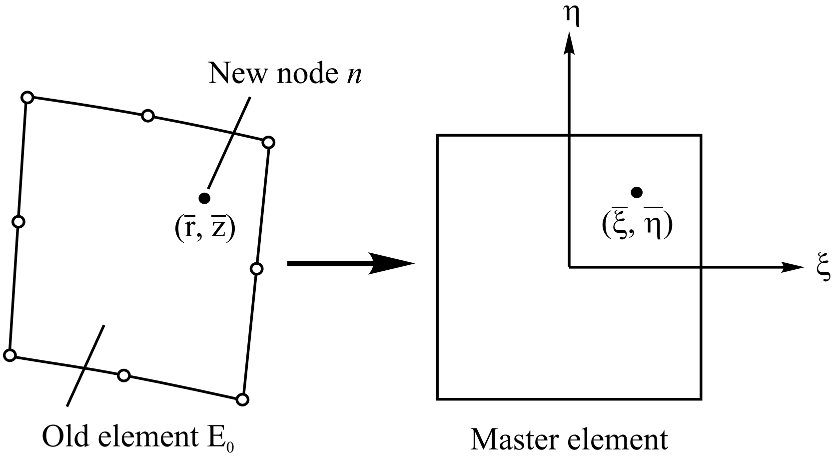

Figure 6.8: Determination of the element containing the new node.

With the use of the finite-element discretization of computational domain, coordinates of a point $\mathbf{x}$ within an element is interpolated using coordinates $\mathbf{X}$ of the nodes associated with the element. The interpolation of coordinates is expressed as:

$$\mathbf{x} = \mathbf{N}(\xi, \eta)\,\mathbf{X} \tag{6.2}$$

where the matrix $\mathbf{N}$ contains interpolation functions. The vector of coordinates $\mathbf{x}_n = [\bar{r}, \bar{z}]^T$ of node n is known. Therefore, the inverse of the mapping expressed by Eq. 6.2 is required (Murti and Valliappan, 1986). The inverse isoparametric mapping is represented by:

$$\mathbf{N}(\xi, \eta)\,\mathbf{X} - \mathbf{x}_n = \mathbf{0} \tag{6.3}$$

Eq. 6.3 is nonlinear in ξ and η, and requires an iterative scheme such as the Newton's method to obtain the inverse mapping (Carey, 1997). The iterative scheme will return the values of $\bar{\xi}, \bar{\eta}$ that satisfy Eq. 6.3 for the given $\mathbf{x}_n$. If the condition $-1 \leq (\bar{\xi}, \bar{\eta}) \leq 1$ is satisfied, then the element E_0 contains the node n.

After determination of the element E_0, mapping of the nodal variables is obtained as:

$$\mathbf{g}^{\texttt{New}} = \mathbf{N}^g\left(\bar{\xi}, \bar{\eta}\right)\mathbf{G}^{\texttt{Old}} \tag{6.4}$$

where the vector $\mathbf{g}$ represents a generic nodal variable (at node n) such as solid displacement, Darcy's velocity, excess pore-water pressure and their time derivatives, the vector $\mathbf{G}$ represent corresponding nodal variable at the old nodes of the element E_0, and the shape functions $\mathbf{N}^g$ represents eight-node biquadratic functions for solid displacements and Darcy's velocities, and four-node bilinear functions for excess pore-water pressure.

Integration-Point State Variables

The state variables to be mapped at integration points are stress components σ_{ij}, size of the bounding-surface I_0, and porosity n_w. In order to achieve mapping of integration-point variables, it is first required to obtain values of the variables at the old nodes. The variables are then interpolated to a new integration point after locating the point in an old element.

The nodal values are estimated using *global* least-squares smoothening of the state variables from their known values at the old integration points of the elements selected for remeshing. The least-squares smoothening procedure involves minimization of the square of difference between known and estimated values of the field variables at the old integration points (Hinton and Campbell, 1974).

Let the vector $\mathbf{h}$ contain known values of the state variables (prior to smoothening) at an old integration point, and the vector $\mathbf{H}$ contain unknown values of the state variables (to be determined by smoothening) at the old nodes. The smoothened values of the state variables $\hat{\mathbf{h}}$ in an old element are obtained using:

$$\hat{\mathbf{h}} = \mathbf{N}\mathbf{H} \tag{6.5}$$

where the matrix $\mathbf{N}$ contains interpolation functions adopted to represent elementwise approximation of the state variables. The least-squares problem involves finding the vector $\mathbf{H}$ that minimize the functional:

$$\begin{aligned} \pi &= \int_{\Omega_R} \left(\hat{\mathbf{h}} - \mathbf{h}\right)^2 dV \\ &= \int_{\Omega_R} \left(\mathbf{N}\mathbf{H} - \mathbf{h}\right)^2 dV \end{aligned} \tag{6.6}$$

where Ω_R is the domain of elements selected for remeshing. For π to be minimum:

$$\frac{\partial \pi}{\partial \mathbf{H}} = \mathbf{0} \tag{6.7}$$

The minimization Eq. 6.7 produces a set of linear simultaneous equations in $\mathbf{H}$ that can be solved easily by standard solution procedure. The resulting linear system is expressed as:

$$\hat{\mathbf{M}}\mathbf{H} = \hat{\mathbf{R}} \tag{6.8}$$

where:

$$\begin{aligned} \hat{\mathbf{M}} &= \int_{\Omega_R} \mathbf{N}^T \mathbf{N} dV \\ \hat{\mathbf{R}} &= \int_{\Omega_R} \mathbf{N}^T \mathbf{h} dV \end{aligned} \tag{6.9}$$

where the “mass” like matrix $\hat{\mathbf{M}}$ is a well-conditioned, positive definite symmetric matrix.

Once nodal quantities are obtained using the least-squares procedure, mapping of the integration state variables is performed adopting the following steps (see Fig. 6.9):

- The position (r, z) of a new integration point $(\xi, \eta)_{\texttt{new}}$ within a new element is obtained using interpolation of the new nodal coordinates;
- The old element E_0 that contains the position (r, z) is determined using the inverse isoparametric mapping technique described by Eq. 6.3. The procedure determines the old element E_0 and the local coordinates $(\xi, \eta)_{\texttt{old}}$ of the new integration point;

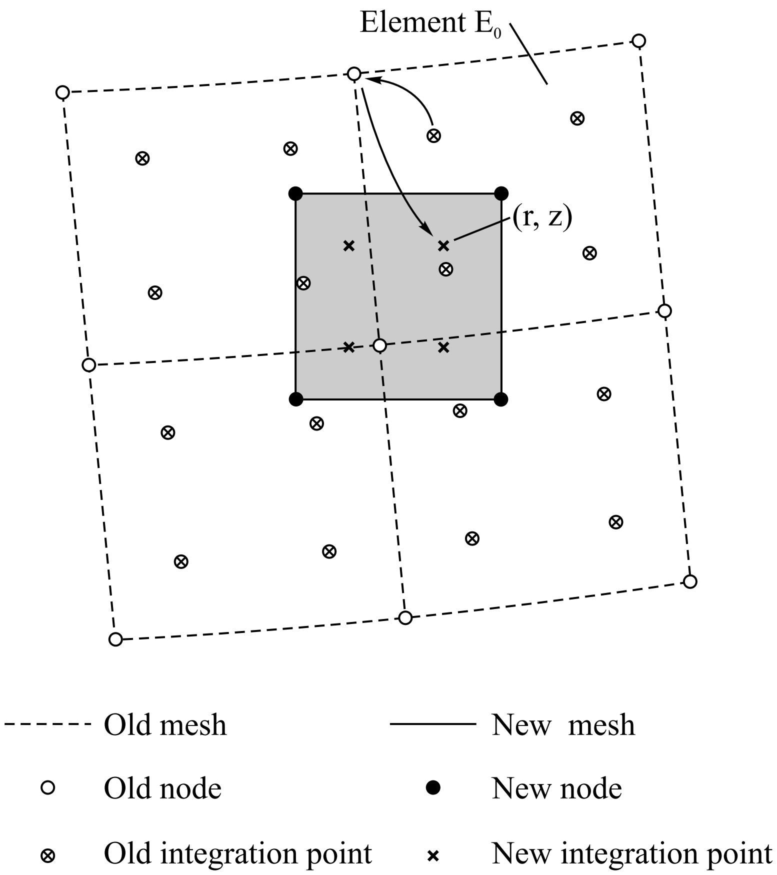

Figure 6.9: Mapping of state variables at integration points.

- From the smoothened nodal state variables obtained by the least-squares procedure described earlier (Eq. 6.8), and knowing $(\xi, \eta)_{\texttt{old}}$, the variables are mapped to the new integration point using interpolation functions.

The procedure described above can be written as:

$$(\xi, \eta)_{\texttt{new}} \rightarrow (r, z) \rightarrow \{E_0, (\xi, \eta)_{\texttt{old}}\} \Rightarrow \mathbf{N}\,(\xi, \eta)_{\texttt{old}}\,\mathbf{H} = \mathbf{h}_{\texttt{new}} \tag{6.10}$$

where $\mathbf{h}_{\texttt{new}}$ is the vector of interpolated values of the state variables at the new integration point.

6.3.4 Mesh Update

After generation of the new mesh and mapping of nodal as well as integration-point variables, data structures containing the old coordinates and variables are replaced by the new coordinates and variables. The analysis of caisson installation then resumes with the new mesh.

6.4 Another Remeshing Tool

Another remeshing tool has been developed to adjust the finite-element mesh along the caisson-soil interfaces. This tool is intended for eliminating distortion of the soil elements along the caisson-soil interfaces and is convenient in cases where a high coefficient of friction on the soil-caisson interfaces leads to significant finite-element distortion. This remeshing tool was not used in the simulation described in this dissertation, as it turned out to be unnecessary for the cases investigated.

6.5 Summary

The remeshing strategy developed to predict the path of caisson penetration was described in this chapter. In addition, mapping of field and state variables from the old finite-element mesh to the new one, and implementation of the remeshing algorithm within the computational procedure were presented.

Chapter 7

THREE-DIMENSIONAL ANALYSIS

Three-dimensional problems arising for caissons subjected to inclined loads are analyzed using ABAQUS, a commercially available finite-element program. The deformed geometry and field as well as state variables obtained from the caisson installation analysis, performed using the computational procedure developed in the previous chapters, are specified as initial geometry and conditions for the three-dimensional analysis.

An overview of the ABAQUS software and details regarding generation of three-dimensional model of soil-caisson system subjected to inclined loads are presented in this chapter.

7.1 ABAQUS

ABAQUS is a general purpose finite-element analysis program developed by Hibbitt, Karlsson & Sorenson, Inc. (HKS, 1998 and 2000). It includes three core products: ABAQUS/Standard, ABAQUS/Explicit, and ABAQUS/CAE. ABAQUS/Standard was adopted to perform three-dimensional simulation of laterally-loaded caisson behavior. ABAQUS/Standard provides programs to perform implicit finite-element analyses such as static, dynamic, and thermal, with possibilities of contact interaction and material nonlinearities.

ABAQUS/Standard has an extensive library of elements to analyze a variety of engineering problems. Families of elements available to perform stress analysis are: continuum (solid) elements, shell elements, beam elements, rigid elements, membrane elements, infinite-elements, truss elements, connector elements, and other special-purpose elements. ABAQUS/Standard has a comprehensive library of material models to represent linear, nonlinear, viscoelastic, isotropic, and anisotropic behavior of common engineering materials. ABAQUS/Standard provides procedures to perform a variety of analysis, such as static analysis, dynamic analysis, steady-state transport analysis, thermal-stress analysis, electrical analysis, coupled pore-fluid flow and stress analysis, mass diffusion analysis, acoustic analysis, and underwater shock analysis. In addition, user-defined subroutines can be incorporated to use element formulations and material models that are not available in ABAQUS/Standard.

For additional information regarding ABAQUS/Standard, reference is made to the ABAQUS/Standard-User's Manual (HKS, 2000).

7.2 ABAQUS Treatment of Porous Media

ABAQUS/Standard incorporates a formulation applicable to multiphase media and adopts the effective stress principle described in Chapter 2. Fully-saturated porous media are formulated in terms of solid displacements and excess pore-water pressure. This is commonly known as the u-p formulation in the literature on porous media (Zienkiewicz and Shiomi, 1984).

The equilibrium statement for the porous medium is identical to Eq. 2.45 developed in Chapter 2. Equilibrium of the finite-element model is approximated by introducing interpolation functions for the solid displacements. The fluid-phase flow is assumed to be governed by Darcy's law to obtain an equation describing continuity of the fluid phase, similar to Eq. 2.43.

For complete details regarding the treatment of porous media in ABAQUS, implementation of tangent contributions, and solution strategy for coupled problems, reference is made to the ABAQUS-Theory Manual (HKS, 1998).

7.3 Soil Plasticity Model

For the axisymmetric analysis of the caisson installation, nonlinear behavior of the saturated clay is modeled using the bounding-surface plasticity model described in Chapter 4. This plasticity model is not available within ABAQUS. Therefore, the FORTRAN subroutine for the plasticity model provided by Kaliakin (2000) is supplied to ABAQUS/Standard. Interface between ABAQUS and the plasticity routine is created through the use of a user-defined subroutine named `UMAT`. Initial values of history dependent variables (Solution Dependent Variables - SDV) required in the model are specified using `SDVINI` user-defined subroutine.

7.4 Three-Dimensional Mesh Generation

A three-dimensional finite-element mesh is generated from location of the nodes in the deformed configuration obtained from the axisymmetric analysis. Depending on availability of computational resources, it may be necessary to use relatively coarse mesh compared to the one used for the axisymmetric analysis. In such a case, transfer of nodal field variables and integration-point state variables should be carried out appropriately. If the inclined load is assumed to act in an azimuthal plane then it is necessary to model only half of the geometry.

7.5 Transfer of State Variables

The initial state of the soil is described by the stress components σ_{ij}, porosity n_w, and size of the bounding-surface I_0. Therefore, it is necessary to transfer the state parameters obtained at the end of the axisymmetric analysis to ABAQUS input for three-dimensional analysis. The initial stress components are specified using `SIGINI` user-defined subroutine within ABAQUS. Both porosity and size of the bounding-surface are specified using the `SDVINI` user-defined subroutine within ABAQUS.

Stress components available from the axisymmetric analysis are with respect to the cylindrical coordinate system. The `SIGINI` routine requires initial stress components to be specified with respect to a rectangular cartesian coordinate system. Therefore, depending on the azimuthal location of an integration-point within an element, the stress components are transformed from the cylindrical system to the rectangular cartesian system using the transformation law described as:

$$\boldsymbol{\sigma}^{XYZ} = \mathcal{R}\left(\theta\right)^{T} \boldsymbol{\sigma}^{R\theta Z} \mathcal{R}\left(\theta\right) \tag{7.1}$$

where $\boldsymbol{\sigma}^{XYZ}$ is the stress tensor in the rectangular cartesian coordinate system, and $\boldsymbol{\sigma}^{R\theta Z}$ is the stress tensor in the cylindrical coordinate system. The rotation tensor is denoted by $\mathcal{R}$, and its components are calculated in terms of trigonometric functions of the azimuthal angle θ between cylindrical and rectangular axes.

In addition to the state parameters, it may be necessary to transfer the excess pore-water pressure, obtained at the end of the axisymmetric analysis, for three-dimensional analysis. The initial value of the pressure can be specified using `UPOREP` user-defined subroutine available within ABAQUS.

7.6 Caisson-Soil Interfaces

Appropriate contact surfaces are defined to represent non-penetration of the soil (slave) nodes into the caisson (master) surface. Contact-surface pairs for interior and exterior caisson-soil interfaces are used. The contact surfaces are generated from the element faces. It is assumed that relative slip between soil and caisson is negligible for the caisson subjected to inclined loads. Furthermore, formation of gap between caisson and soil was not observed during laboratory tests reported in Coffman *et al.* (2004) on caisson subjected to horizontal load. Therefore, complete “tied” contact between soil and caisson is specified. Frictional slip along the interfaces is not considered as ABAQUS does not support frictional models based on effective normal stresses acting along contact surfaces.

7.7 Application of Inclined Load

During the laboratory tests, the inclined load is applied to the caisson by pulling a thin cable vertically through a pulley as illustrated in Fig. 7.1. The pulley is located radially at about 12 inch away from face of the caisson. The vertical position of the pulley can be adjusted to apply load at required inclination θ as shown in Fig. 7.1.

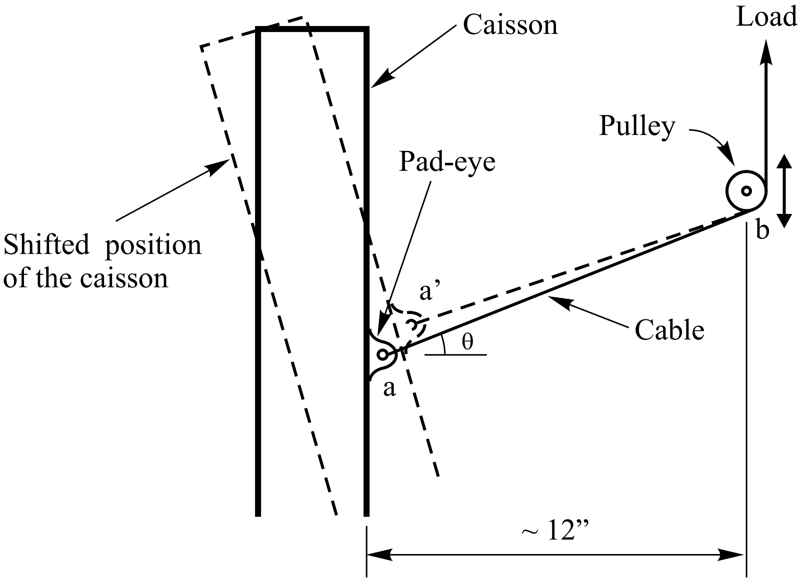

Figure 7.1: Application of inclined load.

The inclined load applied to the caisson is acting in the direction of the line joining point of load application (pad-eye) and position of the pulley. Therefore, the direction of load application is continuously changing with the deformation of caisson-soil system under the load. Initially, the load is acting along line ab, and at an instant after application of the load, it is acting along line $a'b$ (see Fig. 7.1). In order to simulate the load application correctly, a constraint is imposed on the inclined load such that it is always acting along the line joining current position of the pad-eye and the pulley.

7.8 Summary

In this chapter, an overview of the ABAQUS software and details regarding generation of three-dimensional model of soil-caisson system subjected to inclined loads were presented.

Chapter 8

SIMULATION RESULTS AND COMPARISONS

The computational procedure developed in the previous chapters is applied to analyze model suction caissons installed and tested at the Offshore Technology Research Center (OTRC) of The University of Texas at Austin. In this chapter, the computational results are presented and verified by comparison with the experimental observations. An overview of the experimental program is presented followed by computational results obtained for test-bed preparation, caisson installation, reconsolidation or setup followed by installation, and caissons subjected to axial pullout and inclined load.

8.1 Experimental Program

A comprehensive experimental research study is in progress at OTRC on model suction caissons installed in normally consolidated kaolinite clay deposit simulating deep seafloor soil conditions. The model suction caisson constructed from 4.0 inch (100 mm) diameter anodized aluminum tube having a wall thickness of 0.032 inch is used for all the tests. Overall length of the model caisson is 36.0 inch (900 mm). A 2.0 inch (50 mm) thick top cap extends into the caisson and restricts installation of the caisson to about 34.0 inch. An aluminum stiffener is welded to the lower half of the caisson to act as pad-eye for attaching a loading cable for inclined load tests. Sensors such as load cells, displacement and pore-water pressure transducers are mounted on the caisson to monitor its response and movement. Additional details regarding the experimental program are documented by Pedersen (2001), Mecham (2001), Luke (2002), and Coffman (2003).

8.1.1 Laboratory Test Sequence

A thick deposit of normally consolidated test-bed is first obtained from kaolinite slurry. A typical laboratory test setup is presented in Fig. 8.1. The model suction caisson is then installed into the test-bed either by self-weight installation only or self-weight installation followed by suction installation. After caisson installation, the excess pore-water pressure generated in the soil is allowed to dissipate during the so-called "setup" phase (Luke, 2002), during which reconsolidation of the disturbed soil surrounding the caisson takes place. The caisson is then subjected to axial (Luke, 2002) or lateral loads (Coffman, 2003). Both rapid and slow rates of axial pullout are considered to simulate undrained and drained conditions, respectively. During each sequence of testing measurements, such as displacement of caisson, excess pore-water pressure, and loads were recorded.

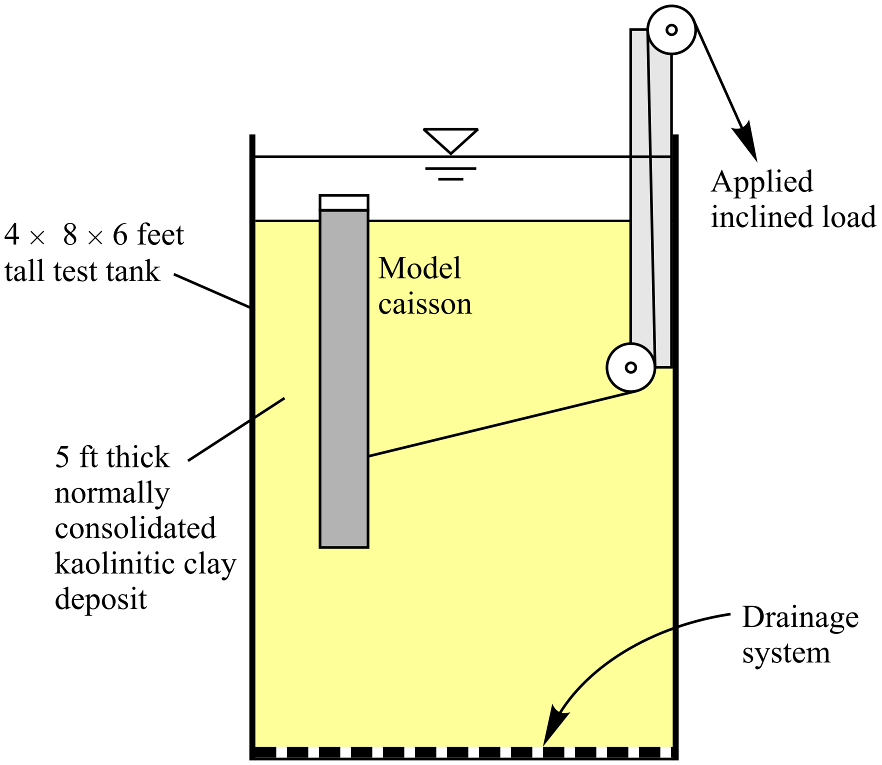

Figure 8.1: Experimental setup.

8.2 Soil Properties

To obtain the void-ratio–pressure $(e - p)$ relationship, Pedersen (2001) performed a series of consolidation tests on small specimens of the slurry. The consolidation tests were performed using a specialized "slurry consolidometer" developed by Pedersen (2001). Slurry samples were prepared to obtain target moisture content of 165%. The relationship between void ratio and effective pressure as obtained from one of these tests is shown in Fig. 8.2.

The internal friction angle ϕ for kaolinite is assumed to be equal to 28° as selected in the work by Vásquez (2000). A constant coefficient of permeability

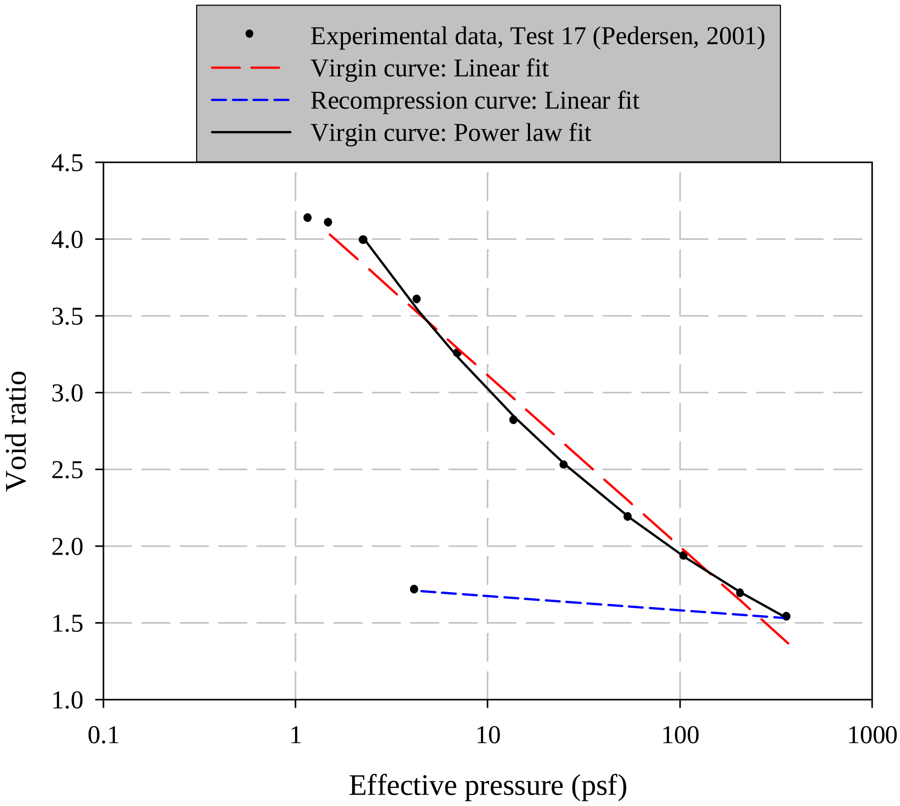

Figure 8.2: Relationship between void ratio and effective pressure.

of the slurry equal to 0.8×10^{-8} cm/sec is assumed.

8.2.1 Bounding-Surface Plasticity Model Parameters

The slopes of the loading (virgin) and unloading (recompression) curves, denoted by λ and κ, respectively, are obtained from the $e - ln(p)$ relationship available for the slurry from consolidation tests performed on small specimens. Constant values of λ and κ equal to 0.49 and 0.04, respectively, are calculated from a linear-fit of the test data. It is clear from the $e - log(p)$ graph presented in Fig. 8.2 that the relationship is best described by a power law function, which is expressed as:

$$e\left(p\right) = 4.68\left(p\right)^{-0.19} \tag{8.1}$$

From the above equation (Eq. 8.1), the variable slope of the virgin curve is obtained as:

$$\lambda\left(p\right) = -\frac{\mathrm{d}e}{\mathrm{d}ln\left(p\right)} = 0.89\left(p\right)^{-0.19} \tag{8.2}$$

The stress ratio, calculated as the ratio of deviator (q) stress to mean stress (p) at perfectly plastic conditions in soil represents slope of critical state line (CSL) in $p - q$ stress space denoted by M. On the basis of the Mohr-Coulomb failure criterion, the values of M for compression and extension triaxial tests can be related to the internal friction angle ϕ (Wood, 1990; and Atkinson, 1993):

$$M_c = \frac{6sin\phi}{3 - sin\phi} \tag{8.3}$$

$$M_e = \frac{6sin\phi}{3 + sin\phi} \tag{8.4}$$

where subscripts c and e represent compression and extension triaxial tests, respectively.

The slope of the critical state line in the $I - J$ stress-invariant space is denoted by N and related to M as follows:

$$N = \frac{1}{3\sqrt{3}}M \tag{8.5}$$

The parameter R (see Fig. 4.1) is obtained using the values of M, λ, κ, and Poisson ration (ν), and adopting a closed-form analytical relation developed by Dafalias and Herrmann (1986) for K_0-consolidation:

$$\begin{aligned} -\frac{1}{2}gl\eta^3+\eta^2-\sqrt{\Delta}\left(\frac{M}{R-1}\right)^2 & \\ +\frac{3\eta}{2}\left[(1-l)\left(1+\sqrt{\Delta}\right)+\frac{1}{3}gl\sqrt{\Delta}\left(\frac{M}{R-1}\right)^2\right] &= 0 \end{aligned} \tag{8.6}$$

where:

$$\Delta=1+R\,(R-2)\left[1+(R-1)^2\left(\frac{\eta}{M}\right)^2\right] \tag{8.7}$$

$$\eta=\frac{q}{p}=\frac{3\,(1-K_0)}{(1+2K_0)} \tag{8.8}$$

$$l=\frac{\kappa}{\lambda} \tag{8.9}$$

$$g=\frac{2\,(1+\nu)}{3\,(1-2\nu)} \tag{8.10}$$

In Eq. 8.8, K_0 is the coefficient of lateral earth pressure at rest, obtained as the ratio of effective horizontal and vertical stresses. The coefficient of earth pressure at rest under normal consolidation is denoted by K_{0nc} and can be approximated as (Jaky, 1944):

$$K_{0nc}=1-sin\,(\phi) \tag{8.11}$$

Use of Eqs. 8.6 and 8.11 with the values of M_c (M_e), λ, κ, and ν, the value of the parameter R_c (R_e) corresponding to compression (extension) triaxial test is obtained. Values for the remaining bounding-surface parameters were assumed on the basis of recommendations from earlier applications of the plasticity model (Dafalias and Herrmann, 1986; Herrmann *et al.*, 1987; and Kaliakin and Herrmann, 1991). The values of all the plasticity model parameters are listed in Table 8.1.

Table 8.1: Bounding-surface plasticity parameters

Model Parameter	**Symbol**	**Value**
Virgin slope	λ	0.49
Recompression slope	κ	0.04
Poisson ratio	ν	0.30
Slope of CSL (compression)	N_c	0.21
Slope of CSL (extension)	N_e	0.16
Shape parameter (compression)	R_c	1.54
Shape parameter (extension)	R_e	1.23
Shape parameter (compression)	A_c	0.01
Shape parameter (extension)	A_e	0.01
Tension shape parameter	T	0.01
Projection center parameter	C	0.50
Elastic zone parameter	s_p	1.20
Hardening parameter (compression)	h_c	1.00
Hardening parameter (extension)	h_e	1.00

It is assumed that the stress point lies on the first ellipse (see Fig. 4.1) of the bounding-surface during the consolidation test. Eq. 4.20 along with the selected model parameters (from Table 8.1) can be used in rewriting Eq. 8.2 as:

$$\lambda\left(I_0\right) = 0.41\left(I_0\right)^{-0.19} \tag{8.12}$$

where I_0 is the size of bounding-surface specified in psi units. In order to account for ageing of soil as described by Eq. 4.24, the variation of λ at early times is taken as Eq. 8.12, and, in the long term, λ is expressed as:

$$\lambda\left(I_0\right)_\infty = 0.36\left(I_0\right)^{-0.13} \tag{8.13}$$

Therefore, there are three alternate ways of specifying the virgin slope (λ) of the slurry: constant values of λ equals to 0.49, variation of λ as described by Eq. 8.12, and ageing of soil as represented by Eq. 4.24 along with Eqs. 8.12 and 8.13. In the simulation results presented in this chapter, the value of τ in Eq. 4.24 is selected to achieve complete ageing of soil in about 10 days.

8.3 Simulation Sequence

Computational simulation of various test stages is carried out in the sequence followed in the laboratory:

- **Test-bed preparation**: Simulation of kaolinite slurry consolidation under the effect of its own weight to obtain normally consolidated test-bed representing soil conditions at deep-water sites, such as the Gulf of Mexico.
- **Caisson installation**: Simulation of installation of caisson in the test-bed by self-weight or self-weight installation followed by suction installation.
- **Reconsolidation or setup**: Simulation of dissipation of excess pore-water pressure generated during the installation process.

- **Axial or inclined pullout**: Simulation of pullout of caisson under axial or inclined loads.

The slurry settlement curve computed from test-bed preparation simulation was compared with the measured curve reported by Pedersen (2001). Computed caisson behavior during installation and setup simulations was compared with the behavior reported by Luke (2002) and Coffman (2003). Computed axial and horizontal capacities were compared with the measured ones reported by Luke (2002) and Coffman (2003), respectively.

The finite-element mesh adopted for the axisymmetric simulations is presented in Fig. 8.3. 3D finite-element meshes adopted for inclined load pullout simulation presented in Figs. 8.70 and 8.71 are generated from the deformed axisymmetric finite-element mesh obtained at the end of reconsolidation simulation.

8.4 Sign Conventions

Normal stress components are positive if tensile. Excess pore-water pressure is negative if compressive. Thus, positive excess pore-water pressure indicates suction. In ABAQUS software, the sign convention for excess pore-water pressure is the opposite.

8.5 Results: Test-Bed Preparation

A thick deposit of normally consolidated kaolinite clay was first prepared from kaolinite slurry. The slurry was thoroughly mixed to obtain a uniform consistency in a large rectangular steel tank with dimensions of 4 ft by 8 ft in plan and

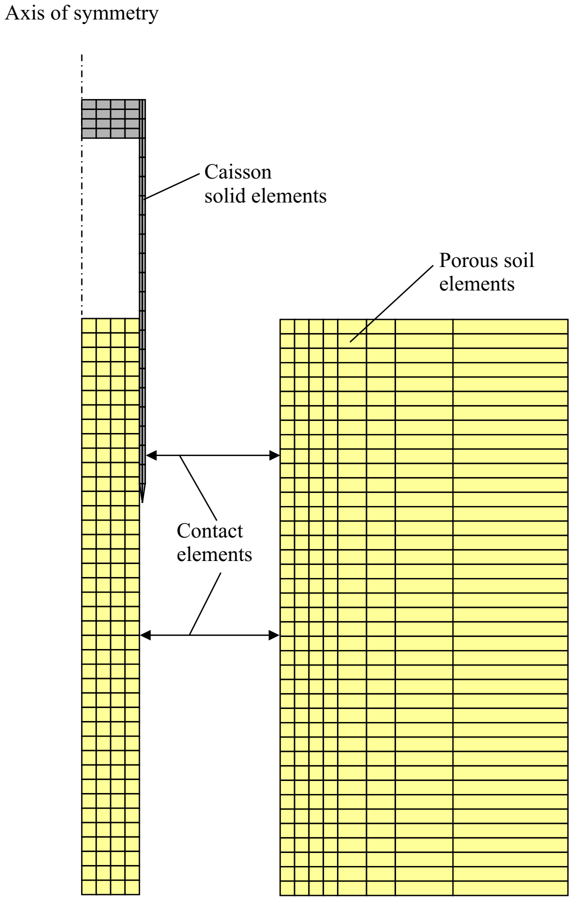

Figure 8.3: The axisymmetric finite-element mesh.

6 ft tall. The slurry was then allowed to settle under the effect of self-weight, resulting in a normally consolidated test-bed to represent common deep-water offshore conditions. The tank was provided with a bottom drainage system to accelerate the consolidation process by shortening the drainage path. Details of the preparation and consolidation of the test-bed are presented elsewhere (Pedersen, 2001; Coffman, 2003; and Olson *et al.*, 2003). Nearly-complete consolidation of the slurry was obtained in about seven months (Pedersen, 2001).

During the seven month period, the initial slurry height of about 61 inch was reduced to about 45 inch (see Fig. 8.4).

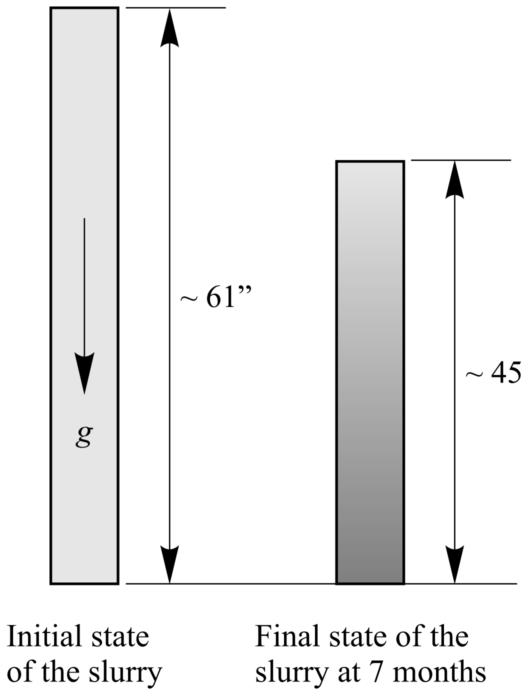

Figure 8.4: Schematic showing preparation of the normally consolidated testbed.

8.5.1 Initial Conditions

The initial state of the slurry for one-dimensional and axisymmetric consolidation simulations is assumed to be uniform as presented in Fig. 8.5 with (constant) void ratio equal to 4.26 (porosity $\approx$ 0.81), corresponding to 164% water content and 2.6 specific gravity of the particles is obtained from the laboratory measurements (Pedersen, 2001). Furthermore, the initial vertical effective stress is set to a constant value of 0.1 psf, the initial lateral stresses are calculated assuming that the coefficient of lateral stress at rest is equal to 0.53 (see Eq. 8.11) and the initial excess pore-water pressure was calculated to obtain total equilibrium of the slurry.

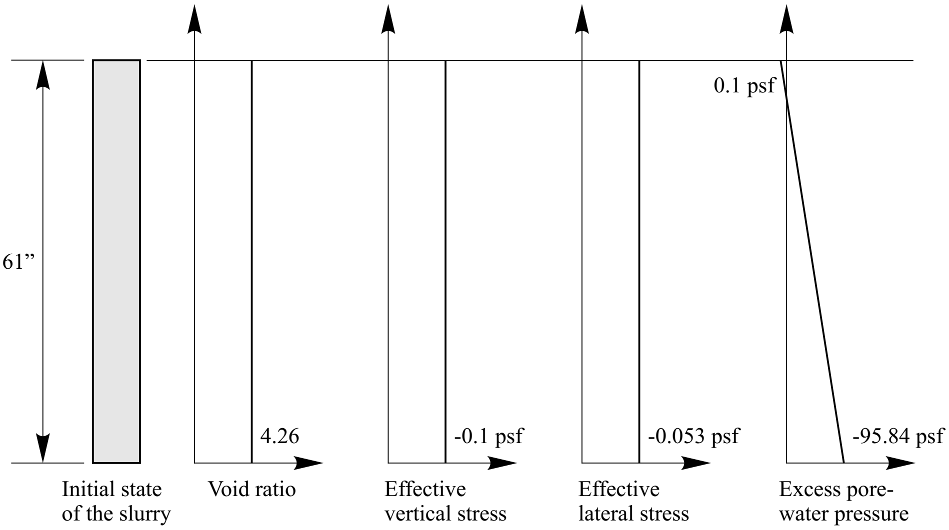

Figure 8.5: Assumed uniform initial state of the slurry.

8.5.2 Simulation Results

In order to obtain a rational state of stress within the soil, the consolidation of kaolinite slurry was simulated. The simulation of slurry consolidation was performed adopting both one-dimensional slurry domain and axisymmetric slurry domain in a 2 ft diameter circular tank. Three alternatives for specifying the virgin curve slope of the slurry as described in Section 8.2.1 were used for each domain. The cases investigated for the consolidation simulation are listed in Table 8.2.

For all the cases, the initial height of the slurry was taken as 61 inch with

Table 8.2: Consolidation simulation cases

Case ID	**Dimensionality of Domain**	**Specification of Virgin Curve Slope**
1D-CON	One-dimension	Constant $\lambda = 0.49$
1D-VAR	One-dimension	Variable λ as per Eq. 8.12
1D-AGE	One-dimension	Ageing of slurry as per Eq. 4.24
3D-CON	Axisymmetric	Constant $\lambda = 0.49$
3D-VAR	Axisymmetric	Variable λ as per Eq. 8.12
3D-AGE	Axisymmetric	Ageing of slurry as per Eq. 4.24

initial conditions as shown in Fig. 8.5 while for the axisymmetric simulations, the friction coefficient between the tank wall and slurry was taken as 0.45. Higher values of friction coefficient were also considered but the selection of the coefficient was based on the required strength profile (see Fig. 8.8). In all the cases, a free-drainage boundary condition was specified at top and bottom surfaces of the slurry to represent free surface at the top and bottom drainage system at the bottom, respectively.

Settlement curves for slurry surface computed from one-dimensional consolidation are presented in Fig. 8.6. The settlement curves corresponding to cases 1D-CON and 1D-AGE are similar to each other and both agree well with the experimental observations reported by Pedersen (2001). Computed slurry settlement for 1D-VAR case is consistently higher than the observed settlement, and overpredicts the final settlement of the slurry by 23%.

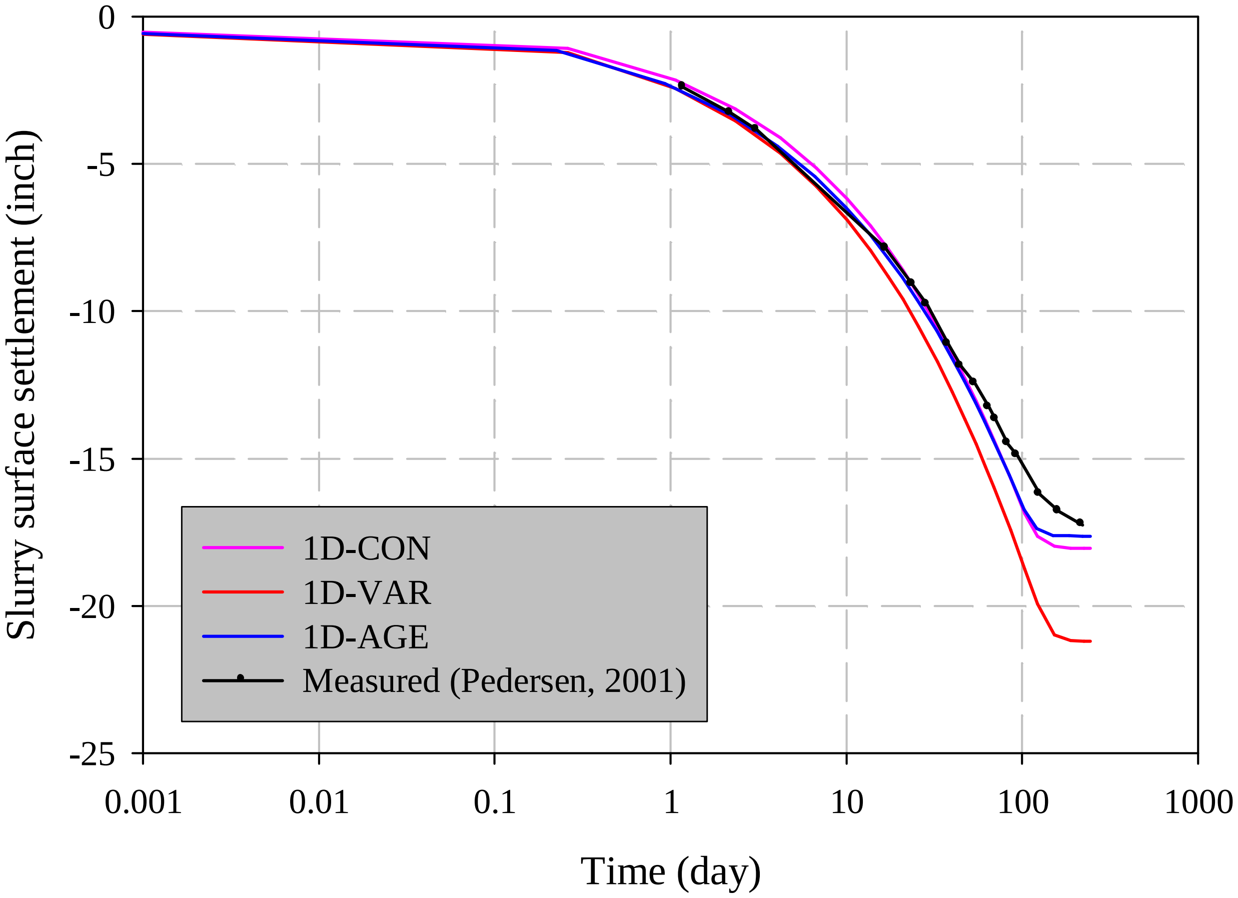

Figure 8.6: Slurry surface settlement curves obtained from one-dimensional simulations.

Settlement curves for slurry surface computed from axisymmetric consolidation simulation in a circular tank are shown in Fig. 8.7. Consistently with one-dimensional simulations, slurry settlement curves computed for cases 3D-CON and 3D-AGE agree well with the experimental observations. In addition, the case 3D-VAR overpredicts the final slurry settlement by 14%.

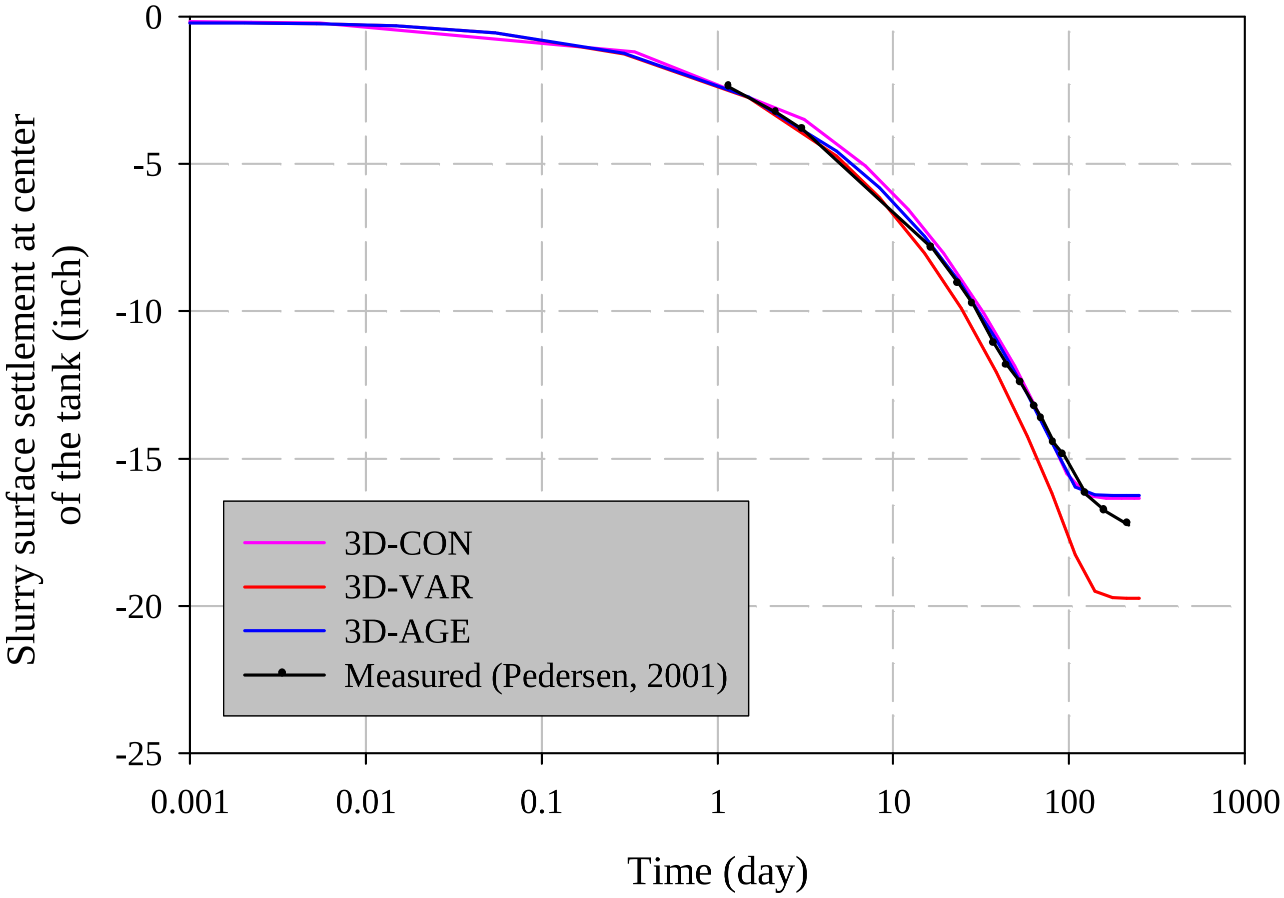

Figure 8.7: Slurry surface settlement curves obtained from axisymmetric simulations.

The computed slurry settlement for each case from one-dimensional consolidation simulation was consistently higher than the computed slurry settlement for corresponding case from axisymmetric consolidation simulation. Computed lower settlements from axisymmetric simulations is due to effect of wall friction.

For both one-dimensional and axisymmetric simulations, the computed slurry settlement for constant virgin slope (λ) and ageing of soil is in good agreement with the test data. At present, there is limited information available to quantify the ageing effect. During laboratory tests, an increase in strength of consolidated test-bed was observed. However, Coffman (2003) from a separate consolidation test, has reported additional surface settlement of 1.5 inch during 17 months following end of primary consolidation along with decrease in void ratio and attributed the increase in slurry strength to secondary compression of the slurry. Considering the relative ease in obtaining the constant slope of virgin curve, and lack of data to support a description of slurry ageing, the remaining simulations were carried out adopting a constant value of virgin curve slope (λ).

Undisturbed undrained shear strength profiles were obtained from the final states of the slurry for cases 1D-CON and 3D-CON. For the 3D-CON case, the shear strength profile was computed at the center of the tank and at 4 inch away from the wall. The shear strength profiles were computed from simulations of the triaxial compression test. The measurements of undisturbed undrained shear strength profiles at several locations in the rectangular test tank are reported by Coffman (2003) and were obtained by inserting a T-bar into the slurry. Computed shear strength profiles along with measured profiles are presented in Fig. 8.8.

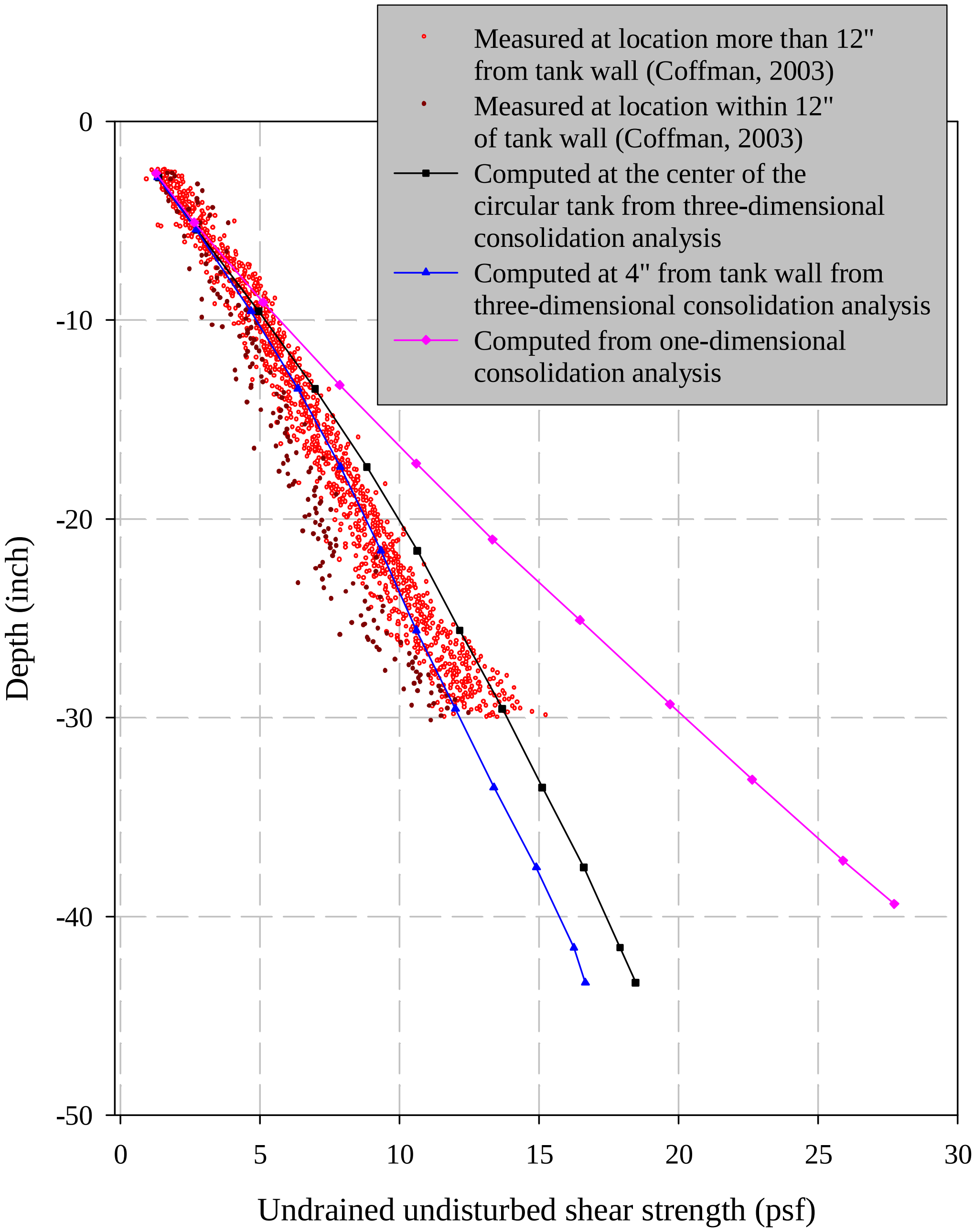

Figure 8.8: Computed and measured undisturbed undrained shear strength profiles of the slurry.

The shear strength profile computed for the 1D-CON case is higher than the measured profile. On the other hand, the computed shear strength profile for the 3D-CON case falls within the measured minimum and maximum bounds of the strength. In addition, as observed in the experiment (see Fig. 8.8), the computed shear strength at 4 inch away from the tank wall is smaller than the one computed at the center. Of course, the strength profile computed from one-dimensional simulation is invariant with respect to the location in the tank since the effects of sidewall friction are not accounted for in the one-dimensional simulations. The average reduction in measured shear strength within 12 inch of the wall is about 22% and the reduction in shear strength calculated at 4 inch from the tank wall is 12%. Coffman (2003) has attributed reduction in the shear strength near walls to higher void ratios in the slurry near walls due to frictional effects.

For 3D-CON case, the computed slurry settlement curve and shear strength profile match the measured surface settlement and shear strength profile, respectively. Therefore, further simulations of caisson installation, setup and pullout were carried out using the state of the slurry obtained at the end of 3D-CON simulation. In the following paragraphs, additional numerical results available from the 3D-CON simulation are presented.

Additional Results for 3D-CON Case

At seven months of consolidation simulation, the slurry with initial height of 61 inch was reduced to 44.7 inch. Undeformed and deformed configurations of the slurry are shown in Fig. 8.9. Finite-elements adopted to discretize the slurry are 1 inch deep, and their width varies from 0.5 inch near the tank center to 4 inch near the tank wall. The top surface of the slurry in the deformed configuration remains almost horizontal, since the slurry near the tank wall settles only 0.12 inch less than the slurry at the tank center. Laboratory consolidation test data presented by Pedersen (2001) shows difference in settlements at the rectangular tank center and wall of about 1.5 inch. However, recent consolidation tests conducted by Coffman (2003) show that the slurry along the rectangular tank wall settled by about the same amount as the slurry at the center of the tank. Although the wall effect is not noticeable in the settlement of slurry surface, shearing of finite-elements near the tank wall is visible in Fig. 8.9(b).

The computed slurry settlement from 3D-CON case at the circular tank center is again compared with observed slurry settlement at the center of the rectangular tank, available from the laboratory consolidation test in Fig. 8.10. As noted earlier, good agreement was found between observed and computed consolidation curves for the slurry.

Final State of the Slurry

The distribution of effective vertical stress within the slurry at the end of the consolidation process is shown in Fig. 8.11(a). At any depth, the maximum vertical stress occurs at the center of the circular tank and decreases with increase in radial distance. The minimum vertical stress can be seen near the tank wall. Clearly, the reduction in vertical stress is due to the presence of the wall. Some of slurry weight is transferred to the wall through friction between slurry and the wall, causing reduction in the vertical stress. At the bottom of the tank, the maximum vertical stress is about 0.47 psi. The (constant) value at the bottom of the tank obtained from one-dimensional consolidation analysis is 0.67 psi [see Fig. 8.11(b)], equal to submerged weight of the slurry

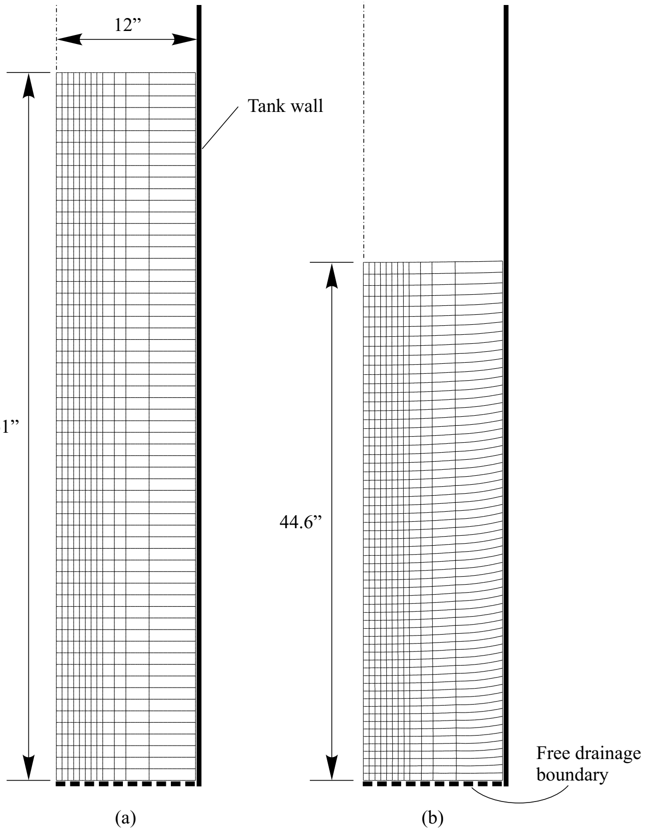

Figure 8.9: (*a*) Undeformed and (*b*) deformed axisymmetric configurations of the slurry.

per unit tank area. The remaining weight of the slurry corresponding to 0.20 psi vertical stress is transferred to the wall through shearing stresses developed in the slurry. It is worth noting that the frictional effects observed from the axisymmetric consolidation simulation (3D-CON) may exceed those in the rectangular tank used for the laboratory tests.

The distribution of effective radial (lateral) stress within the slurry at the end of consolidation process is shown in Fig. 8.12. Radial stresses are

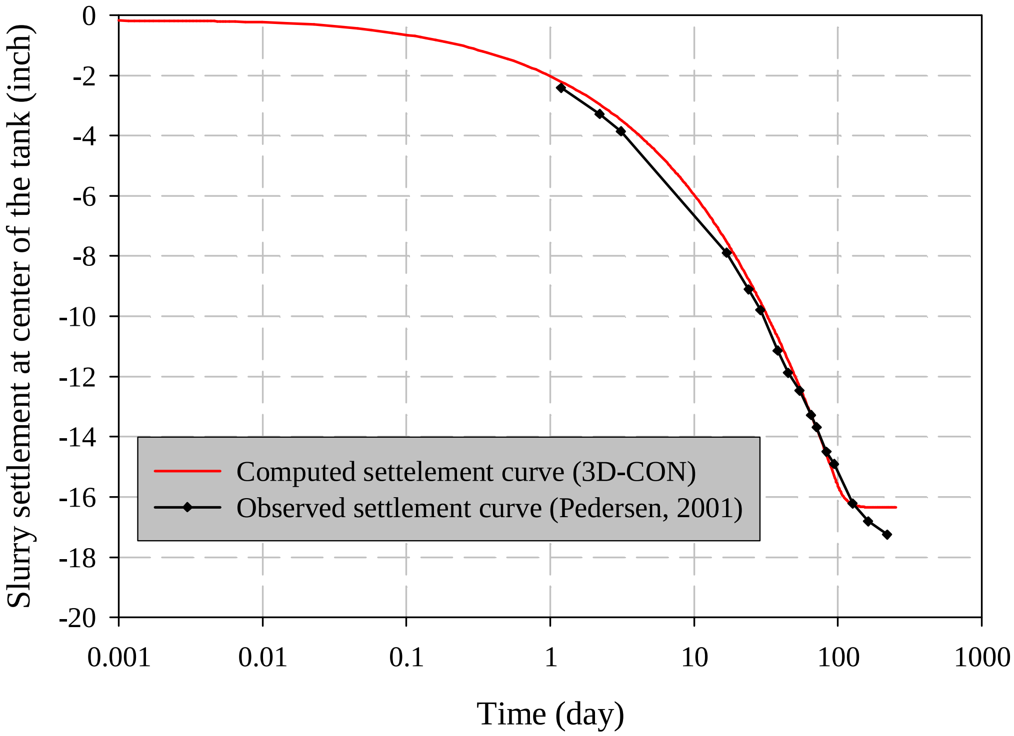

Figure 8.10: Observed and computed (3D-CON) settlement curves for the kaolinitic slurry.

affected by the presence of the wall and, at any depth, the maximum radial stress occurs at the center of the tank and decreases towards the wall. Therefore, the slurry near the center of the tank is most confined. Reduction of both vertical and confining stresses, as the tank wall is approached, is consistent with reduction in shear strength profile close to the wall.

Profiles of effective vertical and lateral stresses through the depth at the tank center are shown in Fig. 8.13. The profiles are nonlinear functions of depth. In addition, the ratio of lateral stress to vertical stress through the

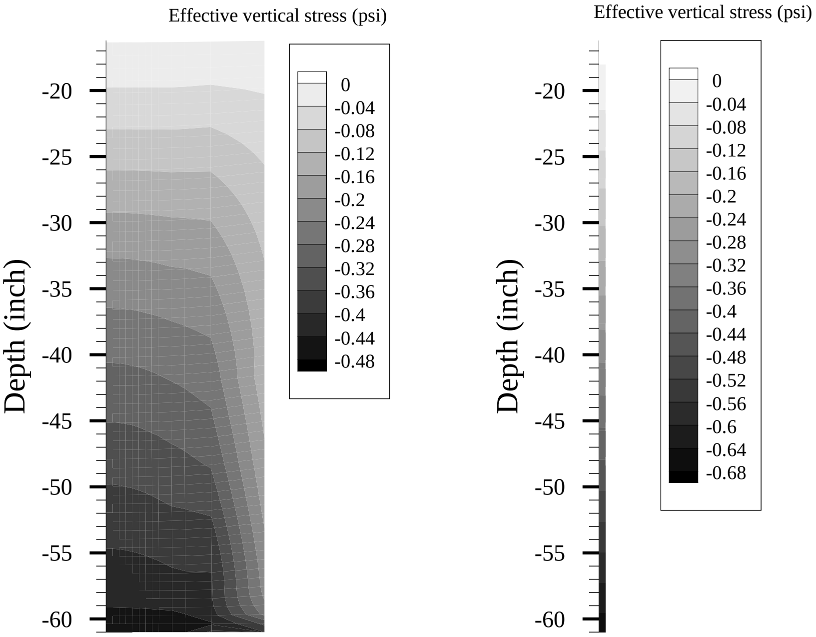

(a) Axisymmetric simulation

(b) 1D simulation

Figure 8.11: Distributions of effective vertical stress obtained from axisymmetric and 1D consolidation simulations.

depth varies between 0.48 to 0.57. It is clear that the state of stress within the slurry calculated assuming constant submerged unit weight of slurry and a constant value for the earth pressure coefficient at rest may not be appropriate. Furthermore, this simplified approach does not account for frictional effects due to the presence of the wall.

The distribution of porosity and bounding-surface size (defined as in Fig. 4.1) within the slurry at the end of consolidation process is shown in Fig. 8.14. The porosity is minimum near the center of the tank (most com-

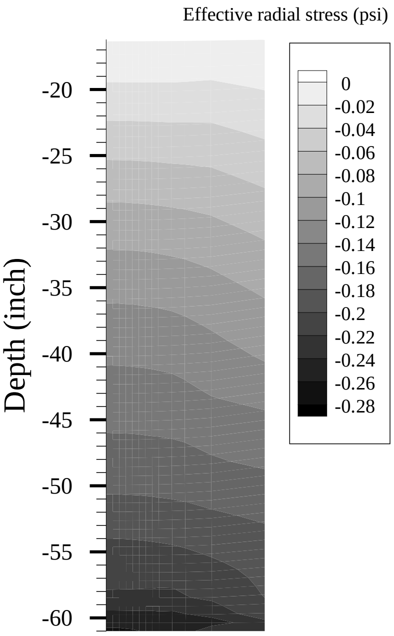

Figure 8.12: Distribution of effective radial stress obtained from axisymmetric consolidation simulation.

pressed state of the slurry) in agreement with higher vertical and radial stresses at the center. The compression of the slurry near the center of the tank is also consistent with the greater size of bounding-surface in Fig. 8.14(b) suggesting that the slurry is consolidated to higher stresses. Coffman (2003) has reported higher values of the void ratio of slurry samples obtained from locations close to the wall.

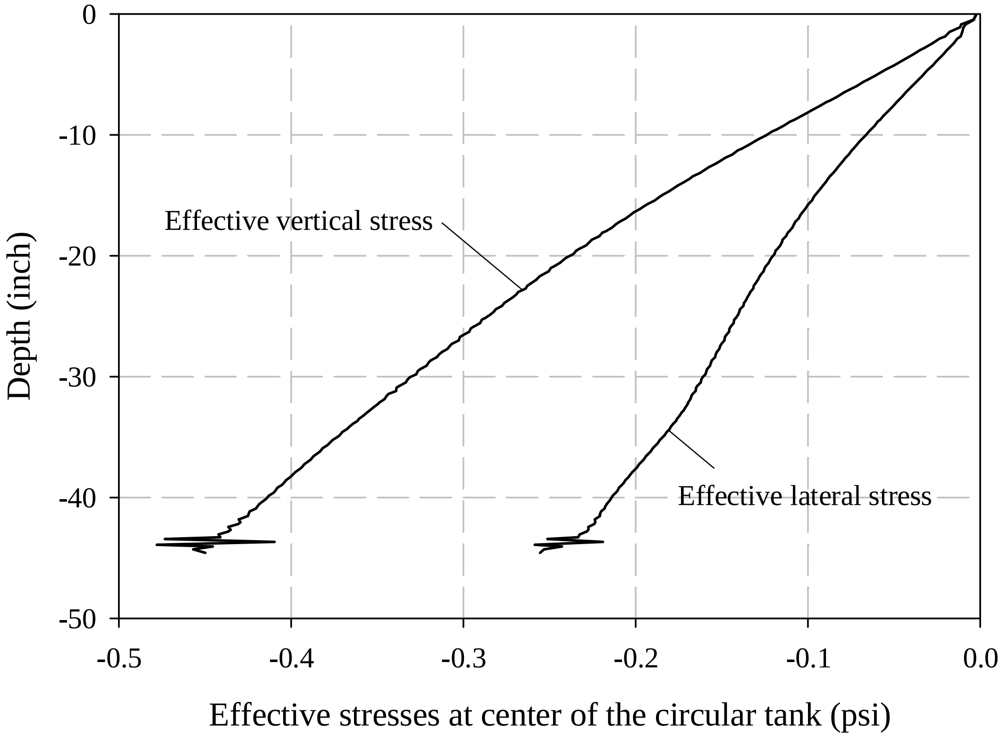

Figure 8.13: Profiles of effective vertical and lateral stresses at the tank center.

Dissipation of Excess Pore-Water Pressure

As described earlier, the initial profile of excess pore-water pressure through the depth was specified to satisfy total equilibrium of the slurry. With consolidation of the slurry, dissipation of pore-water pressure begins. Computed isochrones of excess pore-water pressure through the depth at the tank center are presented in Fig. 8.15. The essentially parallel but displaced isochrones in the upper part of the tank are the result of an essentially uniform upward hydraulic gradient and surface settlement.

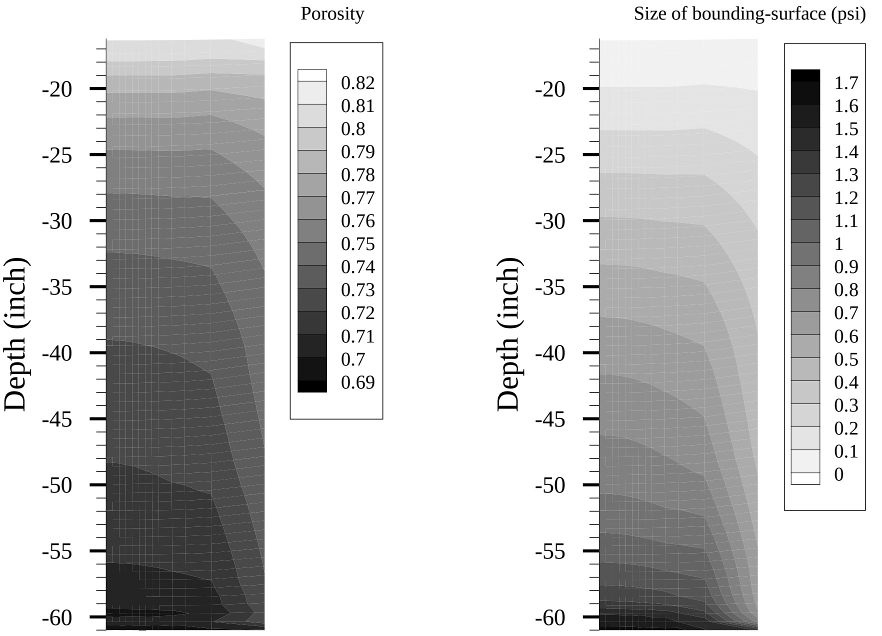

(a) Porosity (b) Size of bounding-surface

Figure 8.14: Distributions of (a) porosity and (b) size of bounding-surface (see Fig. 4.1) obtained from axisymmetric consolidation simulation.

The excess pore-water pressure in the slurry was not completely dissipated in 112 days but only a small increase in surface settlement was calculated after 112 days. Complete dissipation took place in about 204 days. The shape of isochrones indicates that the excess pore-water pressure near the bottom drainage system dissipate more rapidly than the pressure at the surface. A similar observation is reported by Coffman (2003) from measured excess pore-water pressure in the slurry at different times and locations.

Dissipation of excess pore-water pressure in the slurry with time is

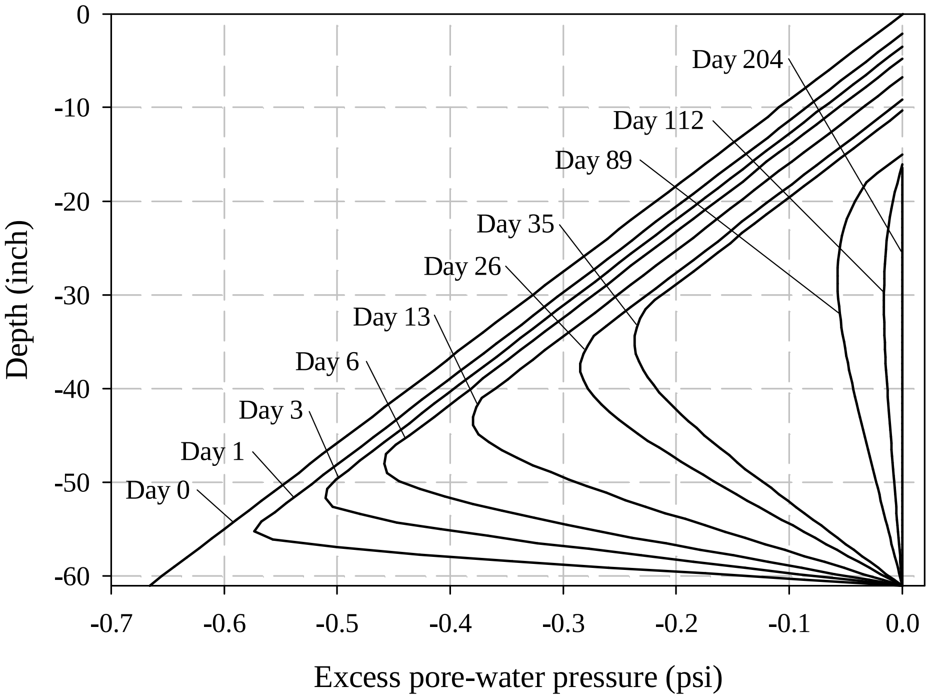

Figure 8.15: Isochrones of excess pore-water pressure at the tank center.

shown in Fig. 8.16 at depths 15, 30, and 45 inch below the (initial) slurry surface. Dissipation of excess pore-water pressure at 45 inch depth started earlier than at the other two depths. It can be concluded that as bottom of the tank is approached, the excess pore-water pressure is dissipated at higher rate than near the surface. This conclusion is in agreement with the measured excess pore-water dissipation behavior reported by Coffman (2003).

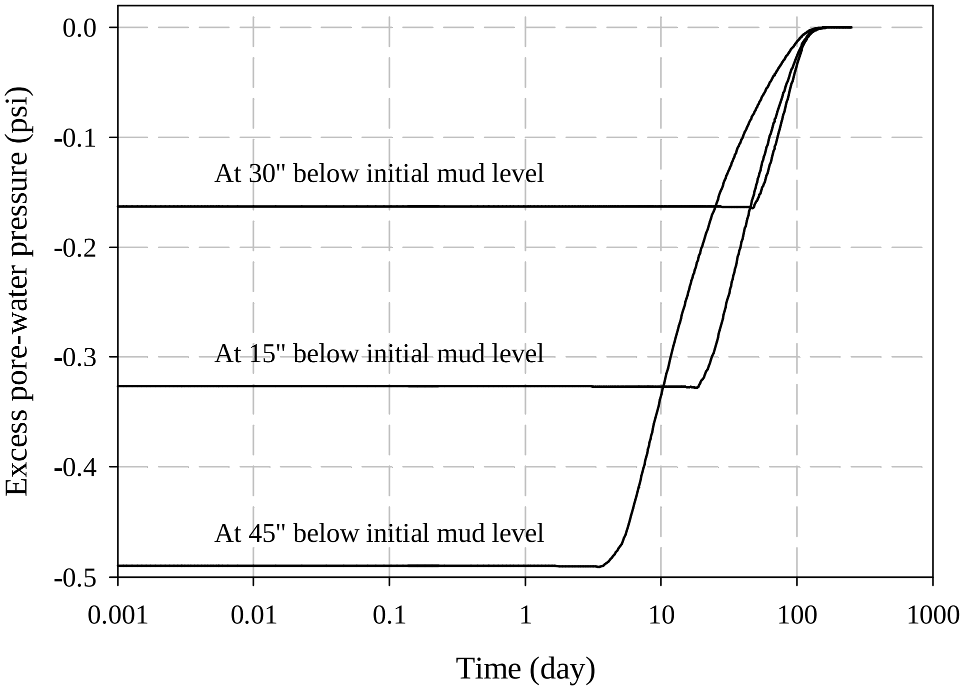

Figure 8.16: Dissipation of excess pore-water pressure with time at different depths.

8.6 Results: Caisson Installation

Computed results obtained from caisson installation simulations are presented in this section. Caissons installed by both self-weight, and self-weight followed by suction are considered. The deformed geometry and final state of soil obtained at the end of slurry consolidation simulation (3D-CON) were taken as the initial geometry and state of the soil for caisson installation simulations. For each installation simulation, a 36 inch long model caisson having 4 inch diameter was installed to 32 inch in the normally consolidated test-bed obtained from 3D-CON simulation presented in Section 8.5. Installation simulation by self-weight is identified as “SWP”, and installation simulation by self-weight followed by suction is identified as “SUC”.

Simulation of caisson installation, reconsolidation following installation, and caisson axial pullout were carried out adopting a constant friction coefficient along interior and exterior caisson-soil interfaces. A constant value of 0.16 was selected by calibration of total soil resistance measured during initial self-weight caisson installation reported in El-Sherbiny (2004) for Test 100603. Higher values of friction coefficient were also considered but the selection of the coefficient was based on required soil resistance during initial caisson installation by self-weight (see Fig. 8.33 and accompanying discussion).

8.6.1 Self-Weight Installation Only

During the laboratory test, the caisson was installed in the test-bed to 32 inch depth in about 200 seconds with a constant rate of installation. The history of caisson self-weight installation followed during laboratory Test 1-040802 reported in Luke (2002) is presented in Fig. 8.17. For simulation of self-weight installation, a comparable rate of caisson installation was specified (see Fig. 8.17). Caisson installation history from 31 to 32 inch was modified to obtain zero velocity of caisson at 32 inch of installation.

Test 1-040802 reported in Luke (2002) is the only self-weight installation test for which excess pore-water pressure were measured. The caisson behavior measured during and after installation in this test is compared with the computed behavior. The test was performed at a distance 12 inch away from the tank wall. The average undisturbed undrained shear strength profile

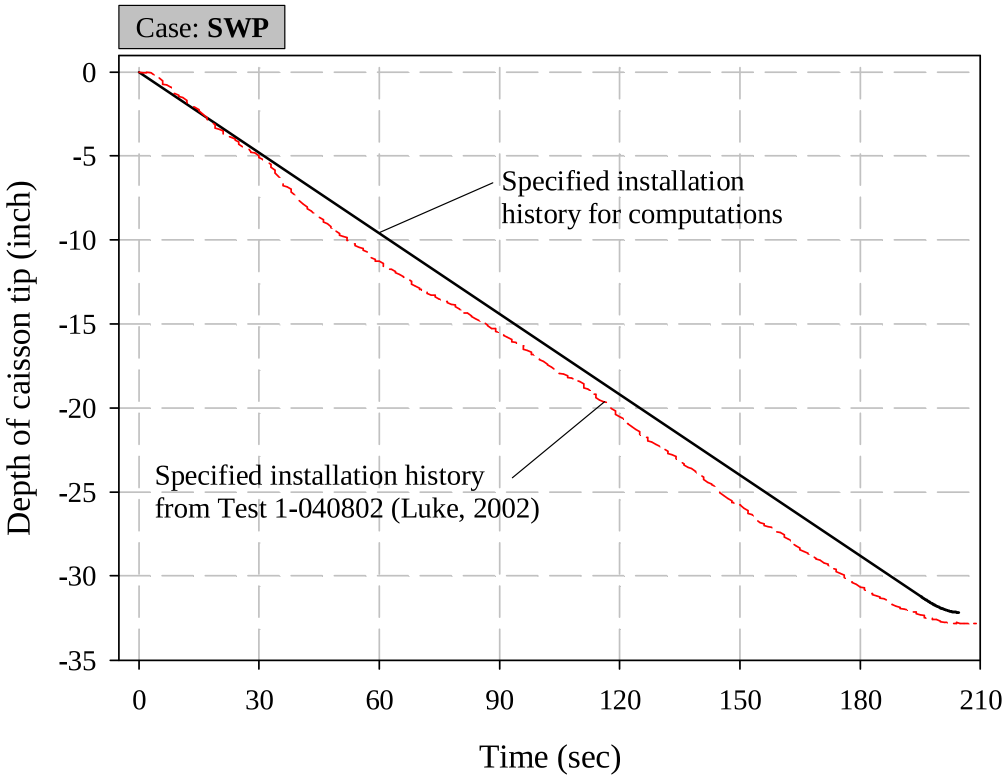

Figure 8.17: Time history of caisson installation by self-weight.

reported in Luke (2002) from the tank used for the test was about 60% of the strength reported at the center of tank from three-dimensional analysis in Fig. 8.8.

The reference soil-caisson configuration at the beginning of installation is shown in Fig. 8.18(a). Both the geometry and state of the soil are those obtained from simulation of slurry consolidation. The deformed configuration at the end of self-weight installation is shown in Fig. 8.18(b). The soil in the interior of the caisson, known as plug, has been pushed down by about 0.64

inch due to caisson insertion.

Observations made during laboratory test suggest that the soil plug heaved during self-weight installation. This was evident from the observed slurry flow through the vent holes in the top cap (Luke, 2002). This was not observed in the simulation of caisson instillation by self-weight presented here. Simulation results for caisson installation in overconsolidated clay test-bed presented by Vásquez (2000) showed upward movement of the soil plug using the soil material model adopted in this study. The reason for the difference in observed and computed movements of the soil plug presented here is unclear at this time.

The force required to install the caisson at the specified rate is plotted against location of caisson tip in Fig. 8.19. At the beginning of the installation process, an upward force of 2.12 lb is acting on the caisson which is equal to submerged weight of the caisson. At the end of installation, a downward total force of 15.07 lb is acting on the caisson. The insertion force at about 11 inch of penetration is negligible, suggesting that the submerged weight of the caisson is transferred to the soil completely. If were caisson were allowed to penetrate under its own weight during the insertion simulation, then according to Fig. 8.19 it would penetrate to about 11 inch depth.

The frictional forces along the exterior and interior soil-caisson interfaces are plotted in Fig. 8.20 against location of caisson tip. In addition, the computed total soil resistance is compared with the measured total soil resistance (Luke, 2002) in Fig. 8.20. Measured total soil resistance is about 60% of the computed total soil resistance. The difference of 40% is likely due to lower shear strength of the actual test-bed compared to the one used in the computations. Higher frictional force can be seen along the exterior interface than

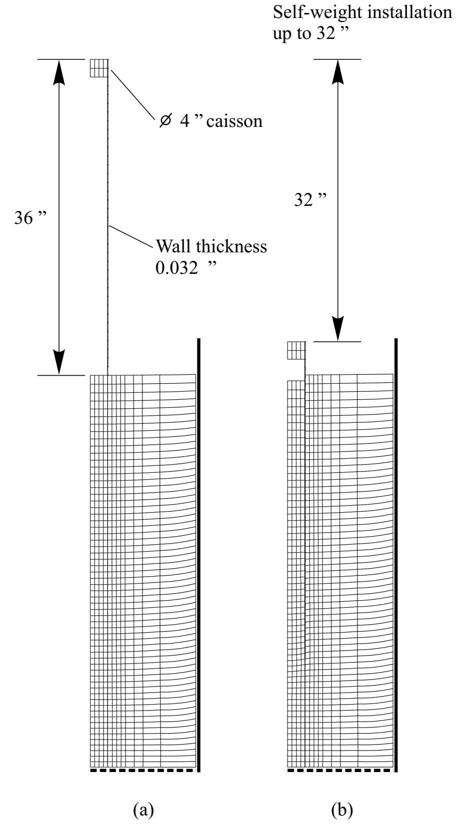

Figure 8.18: (a) Reference and (b) deformed (at the end of self-weight installation) configurations.

along the interior interface. It is worth recalling that the simulation of test-bed preparation was calibrated based on measured strength profiles reported by Coffman (2003).

The excess pore-water pressure was measured during the test at five sensor locations (pore-water pressure transducers mounted on caisson walls), shown in Fig. 8.21. Computed (solid lines) and measured (dotted lines) values of excess pore-water pressure are plotted against location of caisson tip in Fig. 8.22. The computed excess pore-water pressure near the interior of the

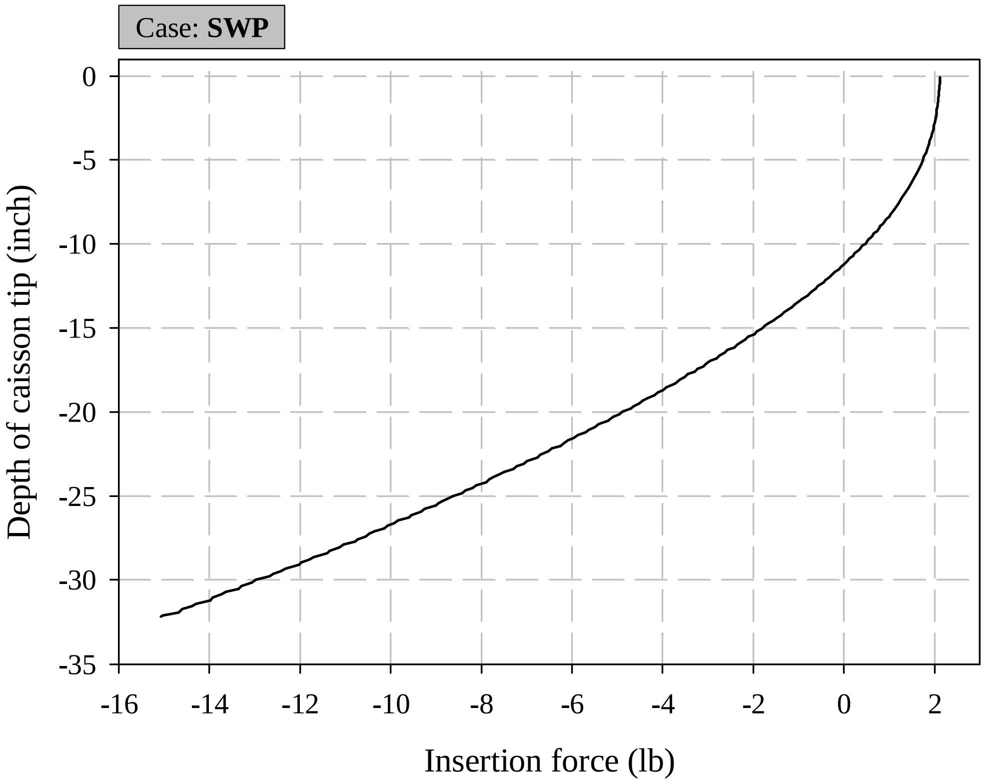

Figure 8.19: Force required to install the caisson during self-weight installation.

caisson tip (Sensor I3) is higher than the one computed near exterior of the caisson tip (sensor O2). Measured pore-water pressures at sensors I3 and O2 are similar to each other. At other sensor locations, computed and measured excess pore-water pressures are in good agreement.

The path of caisson penetration is shown in Fig. 8.23(a). The penetration path is defined in Section 6.1 with reference to Fig. 6.1. For reference, the caisson wall boundaries (dashed lines) and the caisson tip trajectory (dashed/dotted center line) are shown in the figure. The soil material parti-

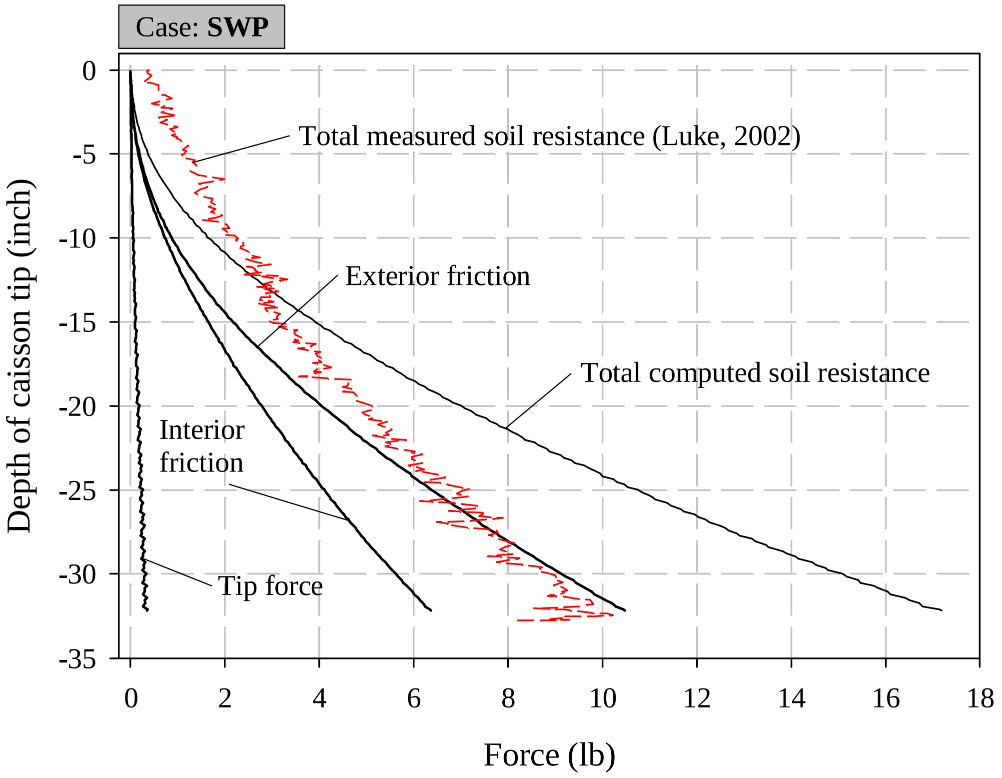

Figure 8.20: Development of interfacial forces during self-weight installation.

cles located along the solid line in the reference configuration came in contact with caisson walls in the deformed configuration at the end of installation. The cumulative volume of soil displaced due to caisson insertion is shown in Fig. 8.23(b). About 7 cu. inch of soil from caisson interior has moved towards exterior. The volume of caisson inserted into the soil is about 12.4 cu. inch and the soil plug volume was reduced by about 7.8 cu. inch due to caisson insertion.

The finite-element meshes before and after remeshing performed to-

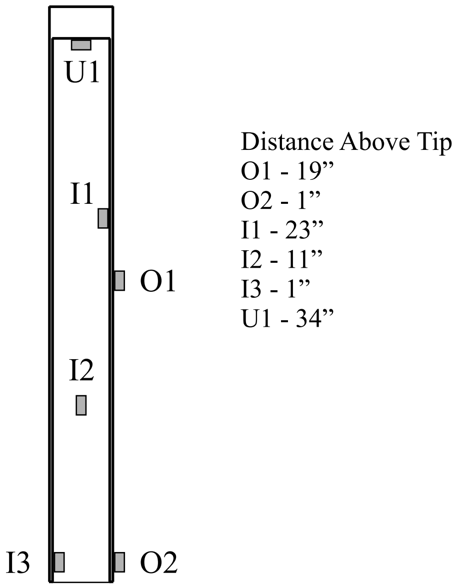

Figure 8.21: Layout of pore-pressure transducers mounted on the model caisson.

wards the end of self-weight installation are shown in Fig. 8.24. Before remeshing the interface between interior and exterior soil domains below the caisson tip was off the axial direction, and after remeshing the interface became aligned with the caisson tip in the axial direction. For this instant of remeshing, it can be seen that the soil from the interior is moving towards exterior. The elements plotted in solid lines are in the current configuration, and the ones plotted in dotted line are in original configuration at the beginning of the installation. The elements plotted in solid lines are in current configurations, and the ones plotted in dotted line are in the original configuration at the beginning of the installation.

The distributions of effective radial (lateral) and vertical stresses within the soil at the end of self-weight installation are shown in Fig. 8.25(a) and (b),

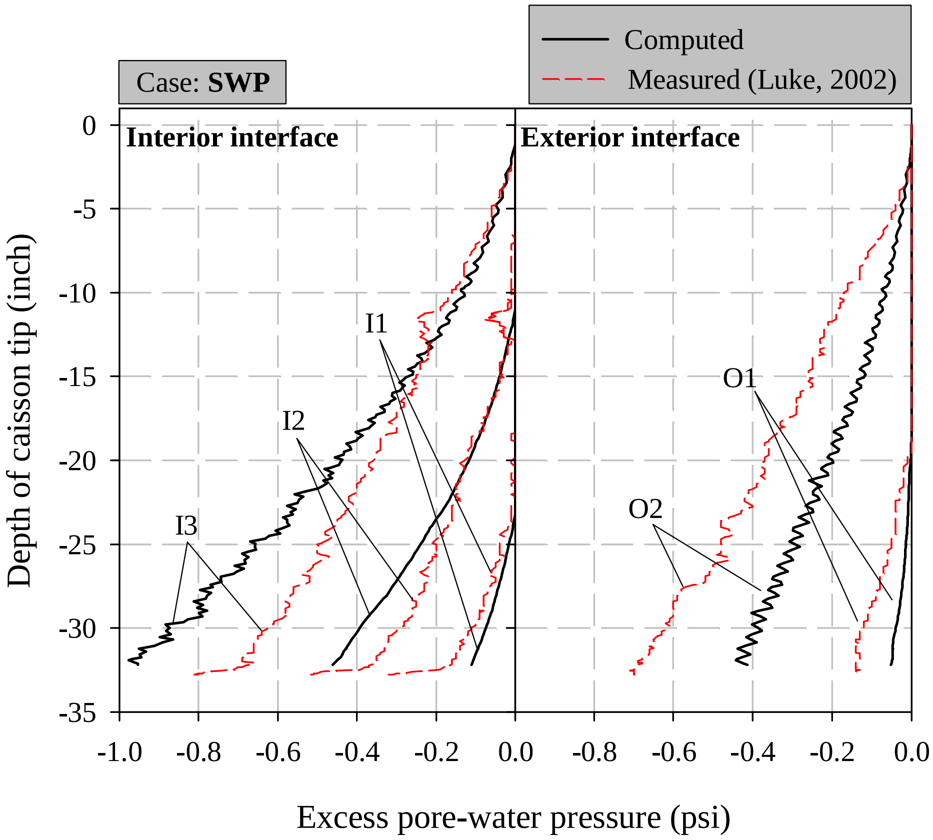

Figure 8.22: Excess pore-water pressure at five sensor locations during self-weight installation.

respectively. Radial and vertical stresses within the soil plug are reduced. An increase in radial stress around caisson exterior can be seen as well as a maximum increase near the exterior tip of the caisson. The vertical stress around the caisson exterior has decreased due to caisson insertion. It is worth mentioning that despite reduction in the effective vertical stresses within the soil in the vicinity of the caisson, the total vertical stresses in this region were found to increase in the magnitude. The magnitude of excess pore-water

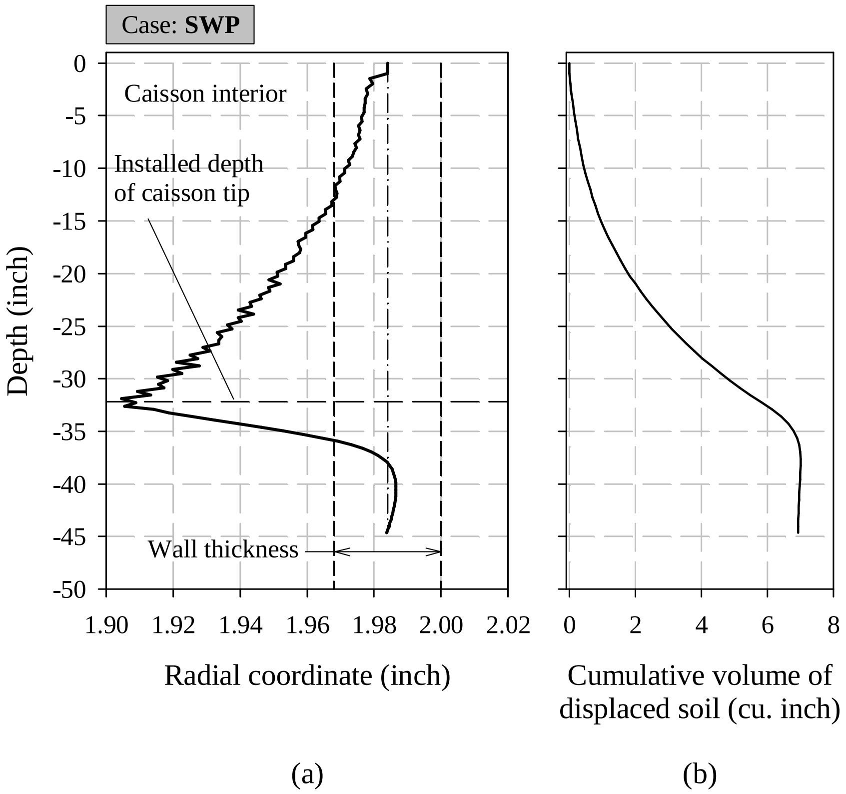

Figure 8.23: (*a*) Path of caisson penetration and (*b*) cumulative volume of soil displaced during self-weight installation.

pressure (see Fig. 8.26) was increased within the soil in the vicinity of the caisson due to insertion. The increase in the magnitude of excess pore-water pressure caused reduction in the magnitude of effective vertical stress.

The distribution of excess pore-water pressure within the soil domain at the end of self-weight installation is shown in Fig. 8.26. Higher pore-water pressure is generated in the interior soil than in the exterior soil, with maximum pressure of about 1.0 psi near interior caisson tip.

The distributions of porosity and bounding-surface size within the soil

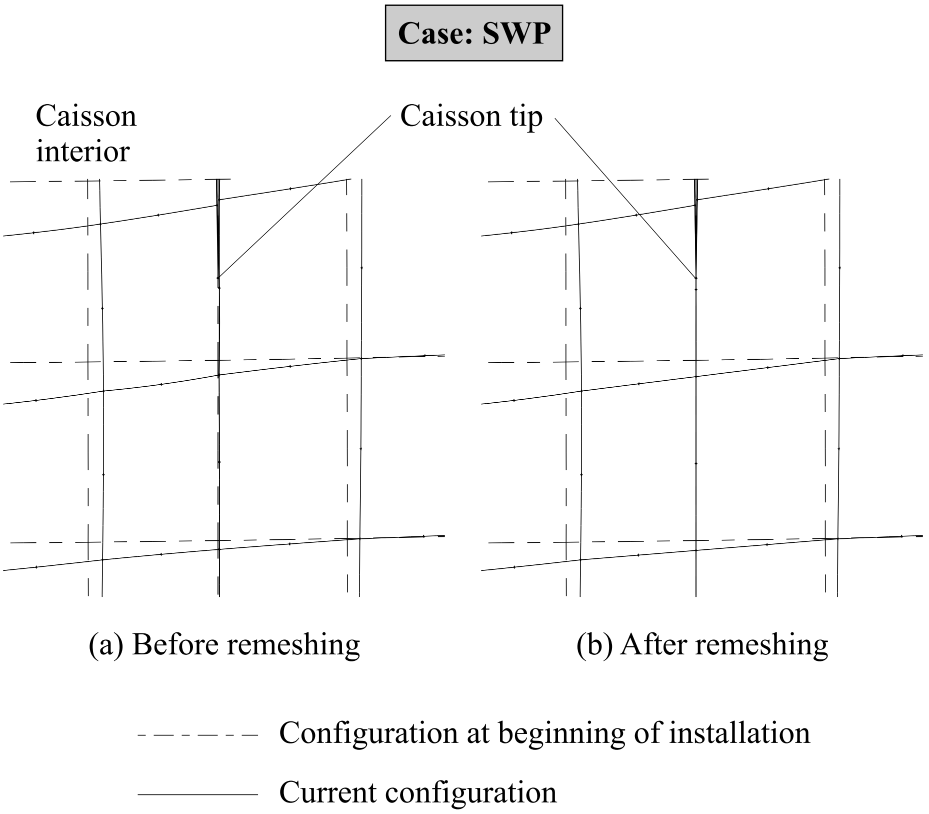

Figure 8.24: Effect of (conforming) remeshing during self-weight installation.

at the end of self-weight installation are shown in Figs. 8.27(a) and (b), respectively. Comparison of porosity distributions at the end of consolidation (test-bed preparation) simulation [see Fig. 8.14(a)] and at the end of self-weight installation [see Fig. 8.27(a)] shows a small increase in porosity within the soil plug and the soil near the exterior vicinity of the caisson at the end of self-weight installation. On the other hand, comparison of bounding-surface size distributions at the end of consolidation [see Fig. 8.14(b)] and at the end of self-weight installation [see Fig. 8.27(b)] shows negligible change in the size

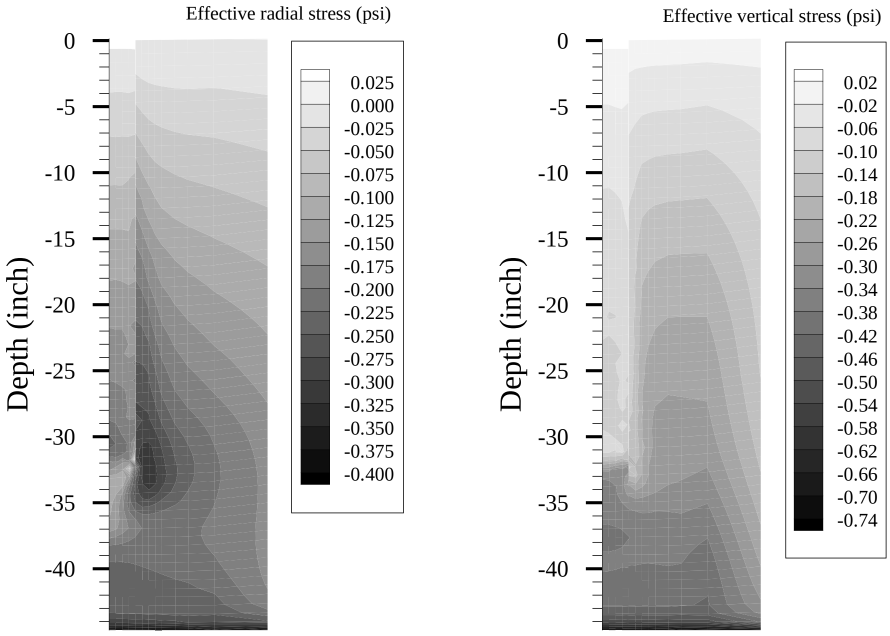

(a) Effective radial stress (b) Effective vertical stress

Figure 8.25: Distributions of stresses within the soil domain at the end of self-weight installation.

within the soil domain at the end of self-weight installation.

Discussion

For the caisson installed completely by self-weight, soil from the caisson interior moved towards the exterior (see Fig. 8.23). Consequently, the radial stress in the interior decreased and in the exterior increased [see Fig. 8.25(a)]. Frictional forces along interior and exterior interfaces are in accordance with changes in radial stress (see Fig. 8.20), i.e., higher frictional force along the exterior

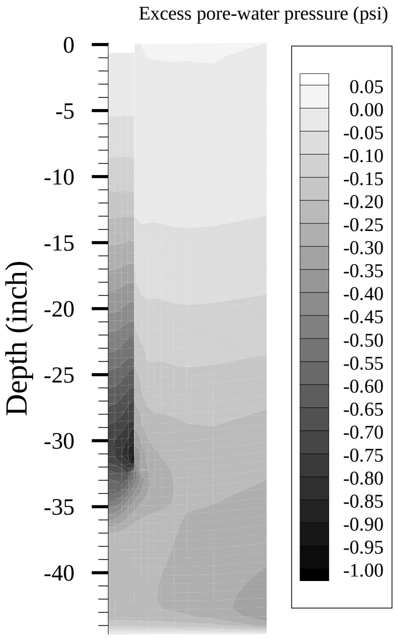

Figure 8.26: Distribution of excess pore-water pressure within the soil domain at the end of self-weight installation.

interface than along the interior interface.

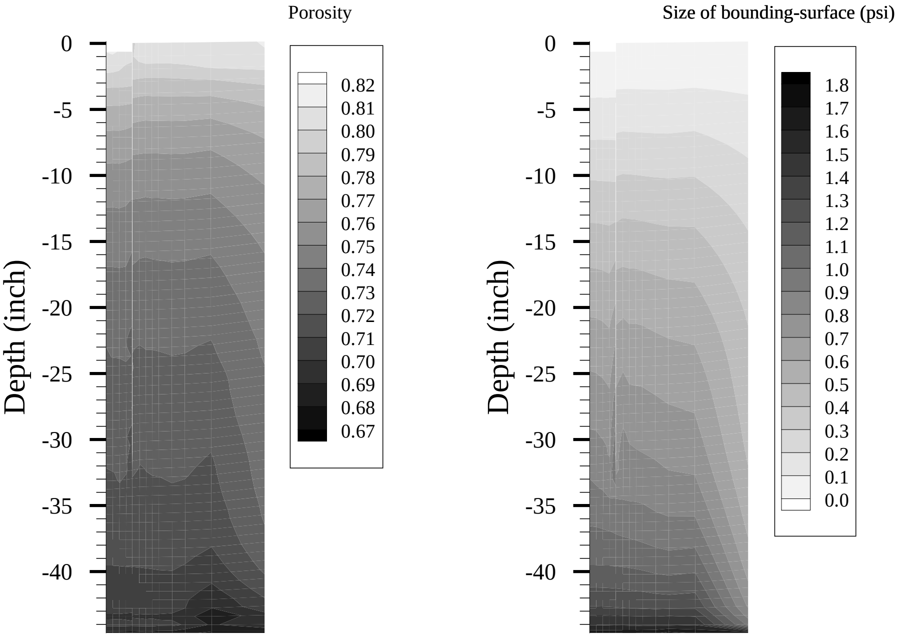

(a) Porosity (b) Size of bounding-surface

Figure 8.27: Distributions of (a) porosity and (b) size of bounding-surface within the soil domain at the end of self-weight installation.

8.6.2 Self-Weight Installation Followed by Suction Installation

During the laboratory test, the caisson was installed in the test-bed to 16 inch depth in 69 seconds with a constant rate of installation, and an additional 16 inch of installation was achieved in 420 seconds by application of suction. The history of caisson installation followed during laboratory Test 100603 reported by Coffman (2003) is shown in Fig. 8.28. In the tests, the typical time interval between end of initial self-weight installation and beginning of suction installation is between 1 to 2 minutes. This time interval is not shown in the caisson installation history of Fig. 8.28. For simulations, comparable installation rates were specified during self-weight and suction installations (see Fig. 8.28). Caisson installation histories from 14 to 16 inch and from 31 to 32 inch were modified to obtain zero velocity of caisson at 16 and 32 inch of installation, respectively.

The caisson behavior measured during and after installation in Test 100603 reported by El-Sherbiny (2004) will be compared with the computed behavior. Computed and measured (Coffman, 2003) undisturbed undrained shear profiles are shown in Fig. 8.8. The test was performed at a distance 12 inch away from the tank wall.

The reference soil-caisson configuration at the beginning of installation is shown in Fig. 8.29(a). Both the geometry and state of the soil are those obtained from simulation of slurry consolidation. The deformed configurations at the end of self-weight and suction installations are presented in Fig. 8.29(b) and (c), respectively. The soil plug has moved up by about 0.06 inch during self-weight installation, and at the end of suction installation an upward

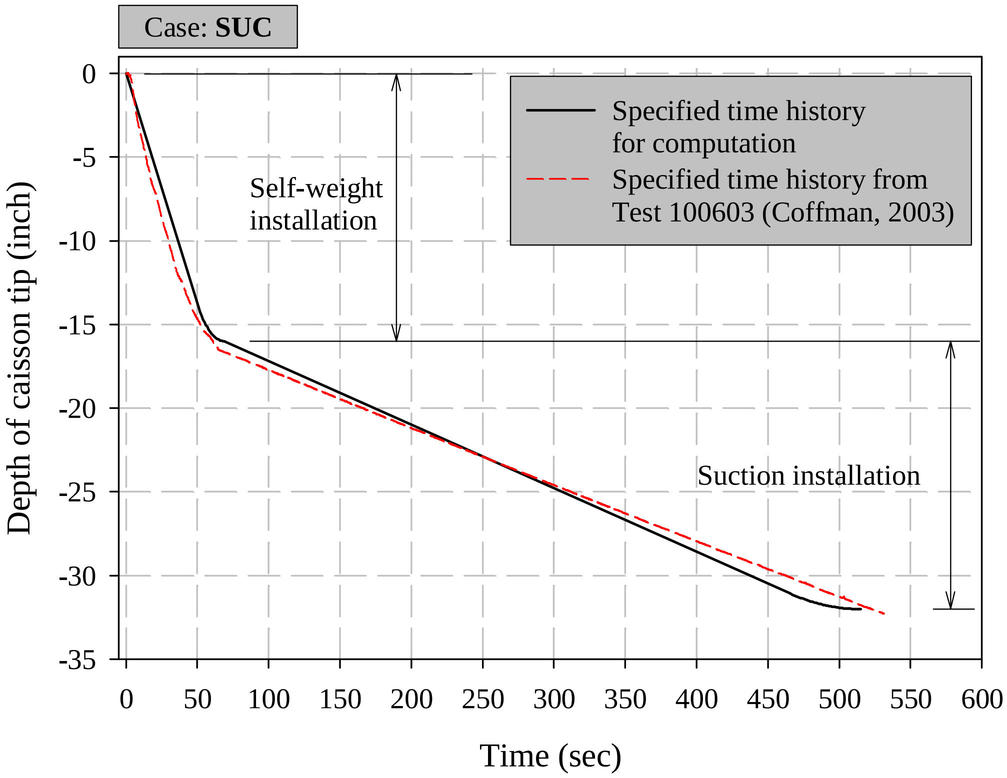

Figure 8.28: Time history of caisson installation by self-weight and suction.

plug movement of 1.14 inch was calculated. Observations made during the laboratory test also suggest that the soil plug moved upwards during suction installation.

The force required to install the caisson at the specified rate during self-weight installation is plotted against location of caisson tip in Fig. 8.30. At the beginning of the installation process, an upward force of 2.12 lb is acting on the caisson, equal to the submerged weight of the caisson. At the end of self-weight installation, a downward force of 2.36 lb is acting on the caisson.

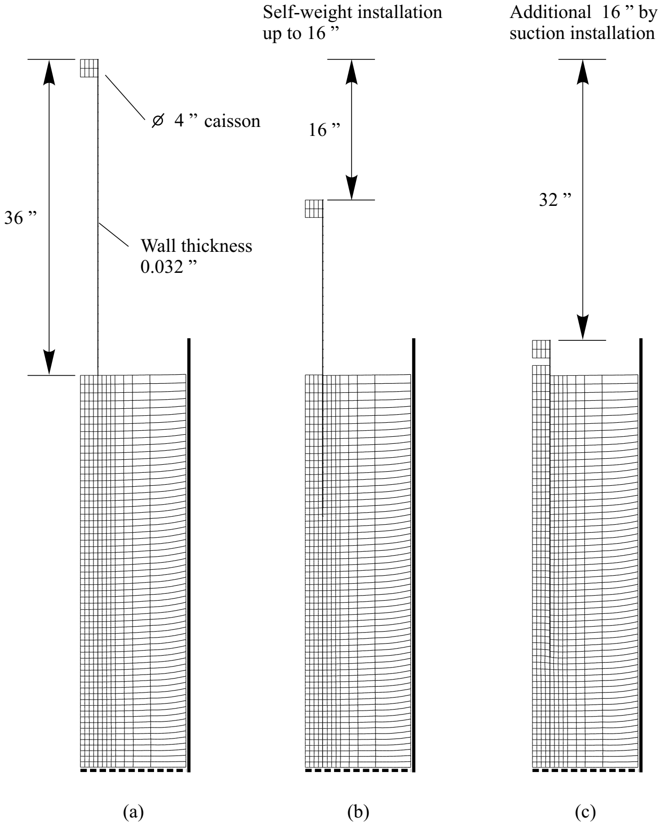

Figure 8.29: (*a*) Reference configuration, and deformed configurations at the end of (*b*) self-weight installation and (*c*) suction installation.

Insertion force at about 11 inch of penetration is negligible, suggesting that the submerged weight of the caisson is transferred to the soil completely. If the caisson were allowed to penetrate under its own weight during an insertion simulation then according to Fig. 8.30 it would penetrate to about 11 inch depth.

The computed excess suction required to install the caisson to additional 16 inch is plotted against location of caisson tip and compared with the time

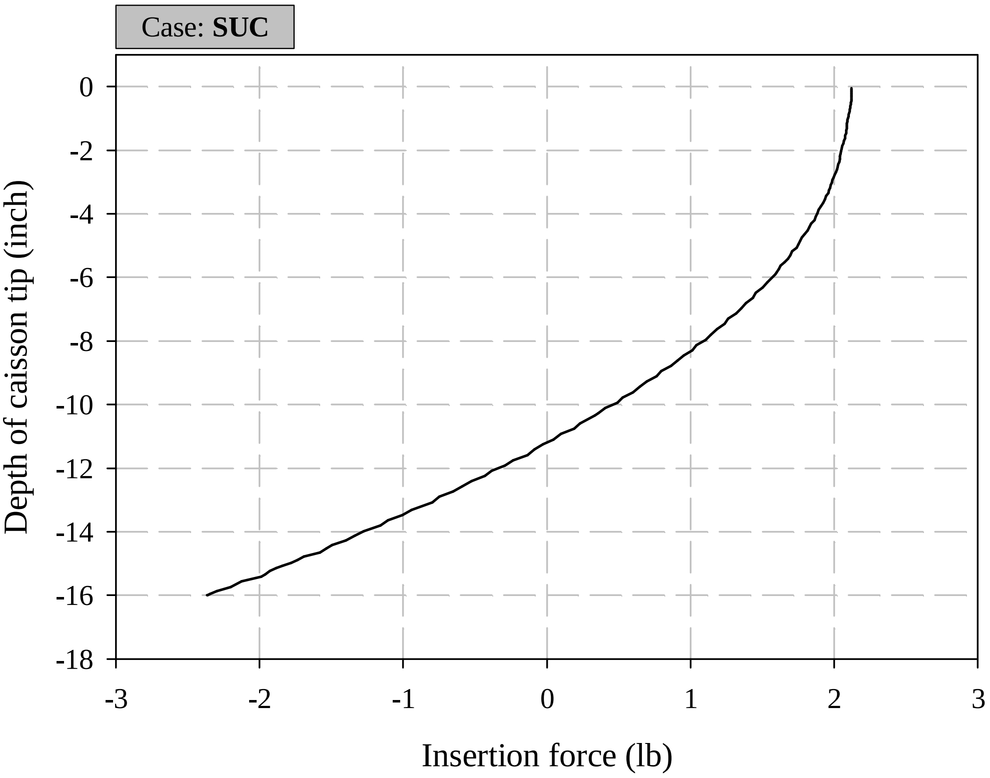

Figure 8.30: Force required to install the caisson during initial self-weight installation.

history of suction specified at the top of the soil plug in Fig. 8.31. Computed and measured (El-Sherbiny, 2004) excess suction under the caisson cap are in good agreement.

Frictional forces along the exterior and interior soil-caisson interfaces are plotted in Fig. 8.32 against location of caisson tip. In addition, the computed total soil resistance is compared with the measured total soil resistance (El-Sherbiny, 2004) in Fig. 8.32. During self-weight installation phase, the computed and measured total soil resistances agree well with each other. Calibra-

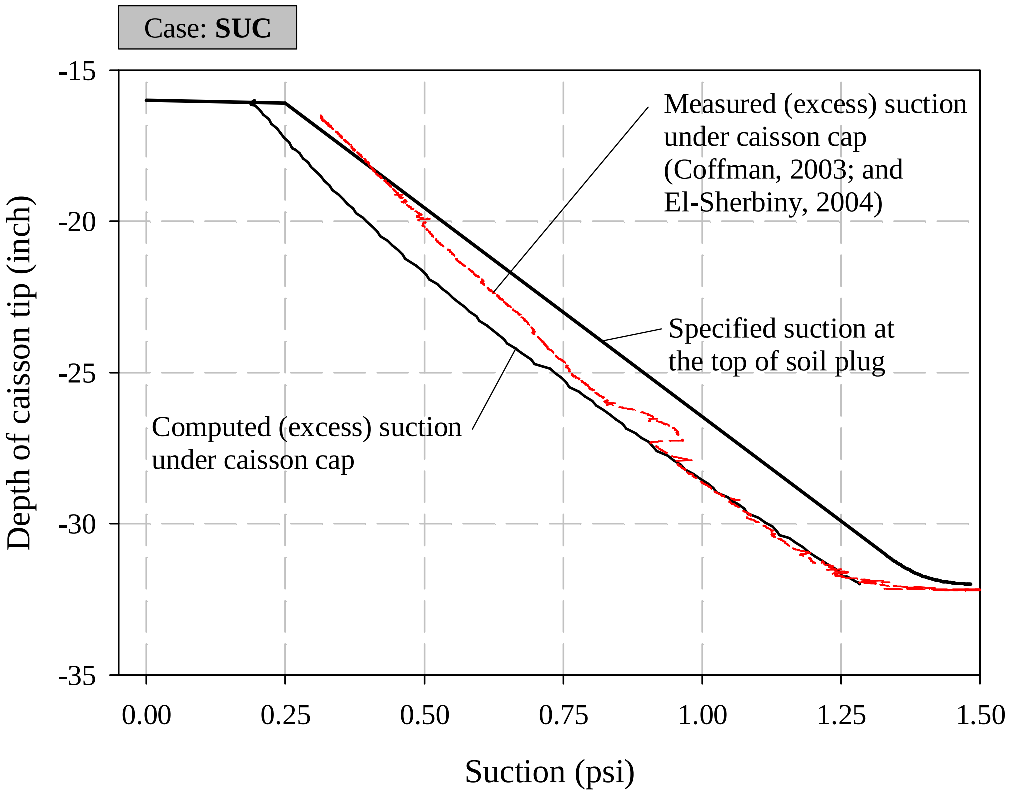

Figure 8.31: Suction generation below caisson cap during suction installation.

tion of the friction coefficient was carried out using the soil resistance measured during initial self-weight installation. The good match between measured and computed soil resistance during self-weight installation indicates appropriate calibration.

The total soil resistance and frictional forces shown in Fig. 8.32 were obtained for a constant value of coefficient of friction equal to 0.16. Higher values of friction coefficient were also considered. Total soil resistance curves during initial self-weight installation were computed using friction coefficient equal to

0.16, 0.32, and 0.45. They are compared in Fig. 8.33 with the measured total soil resistance curve reported by El-Sherbiny (2004). It can be noticed from the comparison that the computed soil resistance for friction coefficient equal to 0.16 matches the measured soil resistance well. This calibration of friction coefficient was conducted prior to performing caisson installation simulations.

During the suction installation phase, the computed total soil resistance is higher than the measured one. The distribution of radial stress within the soil domain presented later in this section [see Figs. 8.37(a) and (b)] indicates increase in radial stress within the lower half of the soil plug as well as in the lower exterior vicinity of the caisson. It is worth noting that the coefficient of friction was observed to decrease with increase in effective normal pressure (Pedersen *et al.*, 2003). The difference between computed and measured total soil resistance during suction installation is due to use of a constant friction coefficient during simulation of caisson installation by suction. During both phases of installation, the computed frictional forces along exterior and interior interfaces are almost identical. On the other hand, for the caisson installed by self-weight only, the computed frictional force along the exterior interface is higher than along the interior interface (see Fig. 8.20).

The computed excess pore-water pressures at five sensors (see Fig. 8.21) are plotted as solid lines against location of caisson tip in Fig. 8.34, while the dotted lines represent measured excess pore-water pressure (El-Sherbiny, 2004) at the sensors.

The excess pore-water pressure computed at five locations during self-weight installation phase is in good agreement with the measured excess pore-water pressure. Application of suction immediately affects pore-water pressure within the soil plug. During the suction installation phase, the pressure com-

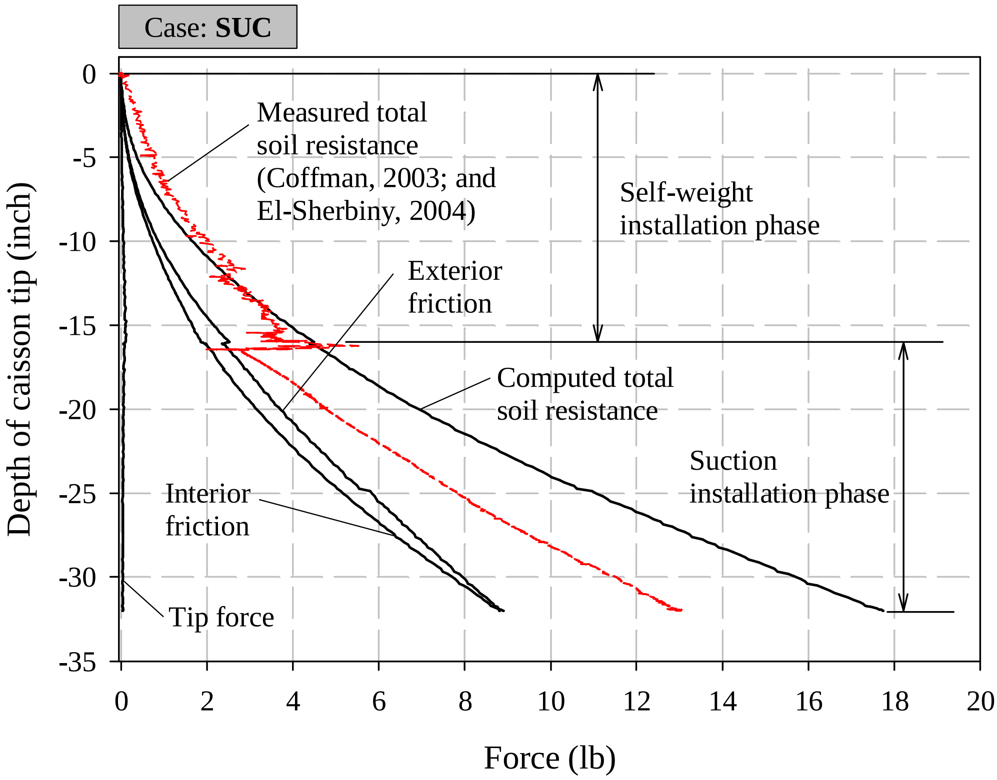

Figure 8.32: Development of interfacial forces during self-weight and suction installations.

puted along the interior interface is suction (positive pressure), and along exterior interface the computed pressure remains negative. The computed suction along the interior interface (at sensors I1, I2, and I3) during suction installation compares well with measured suction. At sensors O1 and O2 located on the exterior interface, suction is measured but the computed pressure is negative. The computed pore-water pressure at sensor location O2 is affected by application of suction as the computed pressure remains almost constant albeit negative during suction installation phase, but the applied suction is

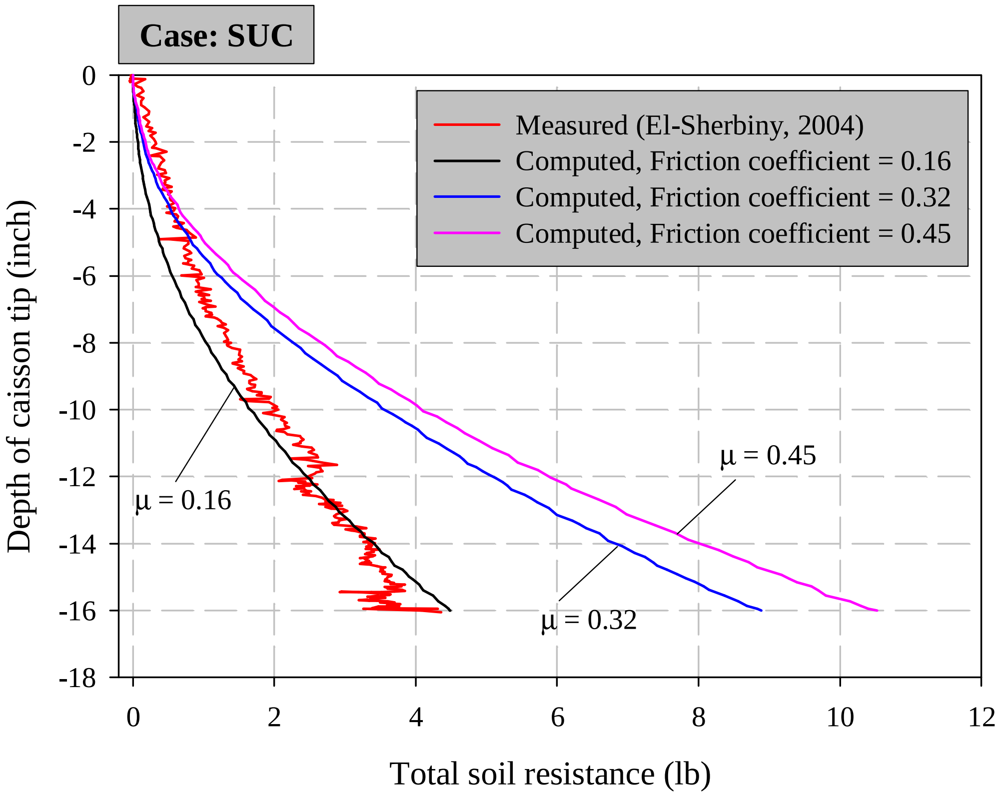

Figure 8.33: Measured and computed total soil resistance during initial self-weight installation.

not sufficient to produce suction at this sensor location. Computed pore-water pressure during suction installation phase at sensor location O1 does not appear to be affected by applied suction.

The path of caisson penetration is shown in Fig. 8.35(a). The penetration path is defined in Section 6.1 with reference to Fig. 6.1. For reference, the caisson wall boundaries (dashed lines) and caisson tip trajectory (dashed/dotted center line) are shown in the figure. The soil material particles located along the solid line in the reference configuration came in contact

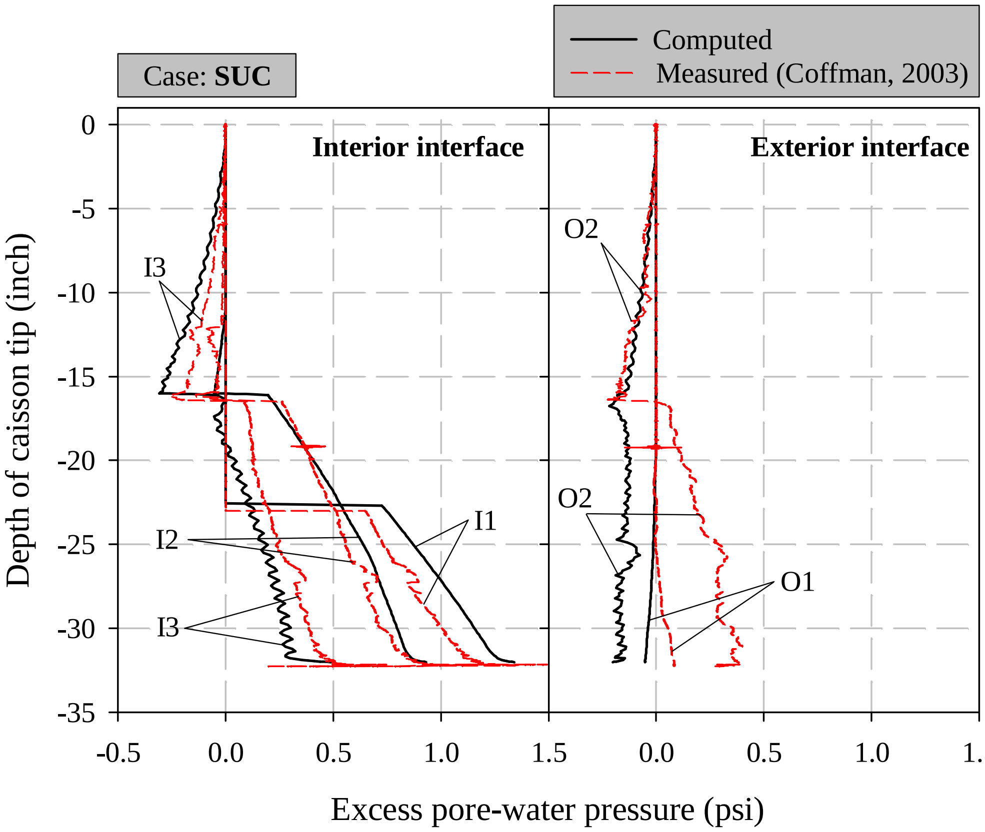

Figure 8.34: Excess pore-water pressure at five sensor locations during self-weight and suction installations.

with caisson walls in the deformed configuration at the end of installation. The cumulative volume of soil displaced due to caisson insertion is shown in Fig. 8.35(b). During self-weight installation about 1.1 cu. inch of soil displaced from interior to exterior. With the application of suction, the soil from exterior started moving towards interior. At completion of suction installation, about 3.5 cu. inch of soil moved from the exterior to the interior. It is worth recalling that for the self-weight installation discussed in Section 8.6.1, outward movement of soil throughout caisson insertion process was computed. The total volume of caisson inserted into the soil is about 12.4 cu. inch and the soil plug volume increased by about 13.9 cu. inch due to application of the suction.

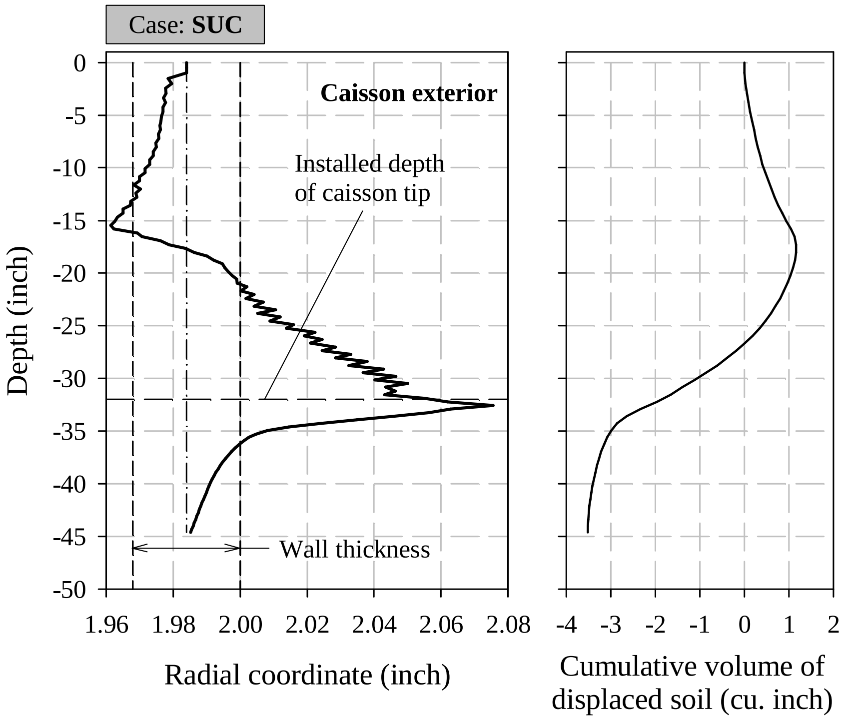

(a) (b)

Figure 8.35: (*a*) Path of caisson penetration and (*b*) cumulative volume of soil displaced during self-weight and suction installations.

The finite-element meshes before and after remeshing performed towards the end of suction installation are shown in Fig. 8.36. Before remeshing the interface between interior and exterior soil domains below the caisson tip was off the axial direction, and after remeshing the interface became aligned with the caisson tip in the axial direction. For this instant of remeshing, it can be seen that the soil from the exterior is moving towards interior.

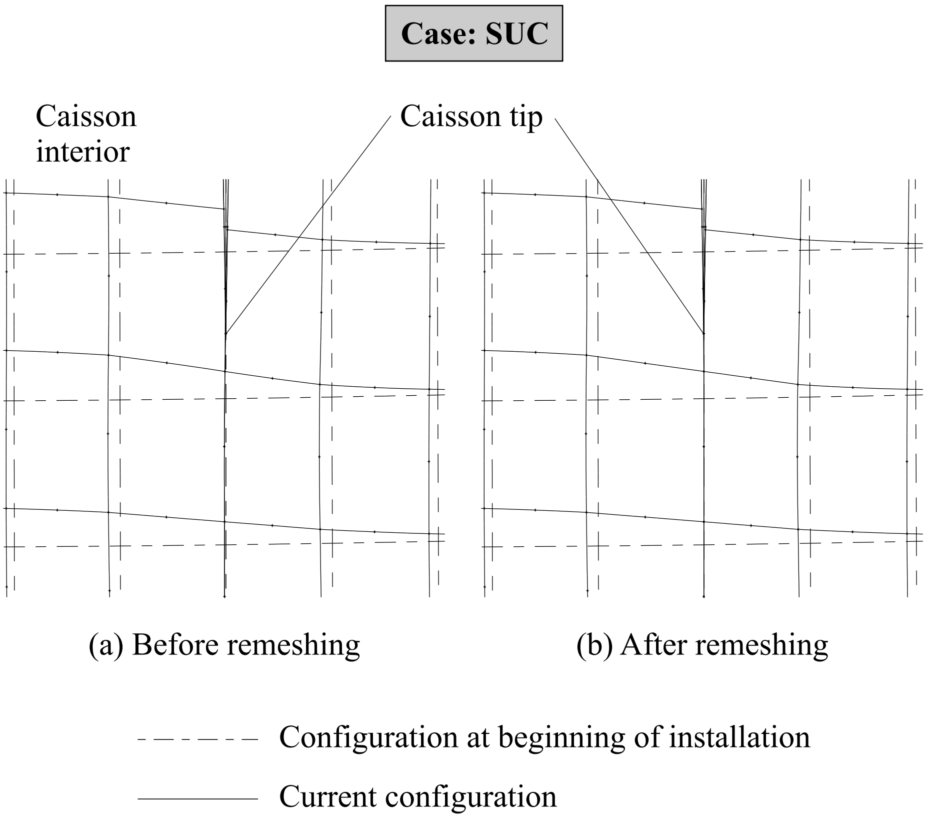

Figure 8.36: Effect of (conforming) remeshing during suction installation.

The distributions of effective radial (lateral) stress within the soil domain at the end of self-weight installation are compared with those at the end of suction installation in Figs. 8.37(a) and (b), respectively. Clearly, the radial stress within the soil plug at the end of self-weight installation is lower than the radial stress towards the caisson exterior. This difference in radial stress distribution in the vicinity of the caisson is likely due to the outward soil movement. At the end of suction installation, the radial stress near the exterior of the caisson tip has been reduced significantly. Inward soil movement during suction installation has resulted in increase in radial stress within the lower half of the soil plug. A small increase in radial stress within the upper half of the soil plug as well as in the lower exterior vicinity of the caisson is also noticed during suction installation.

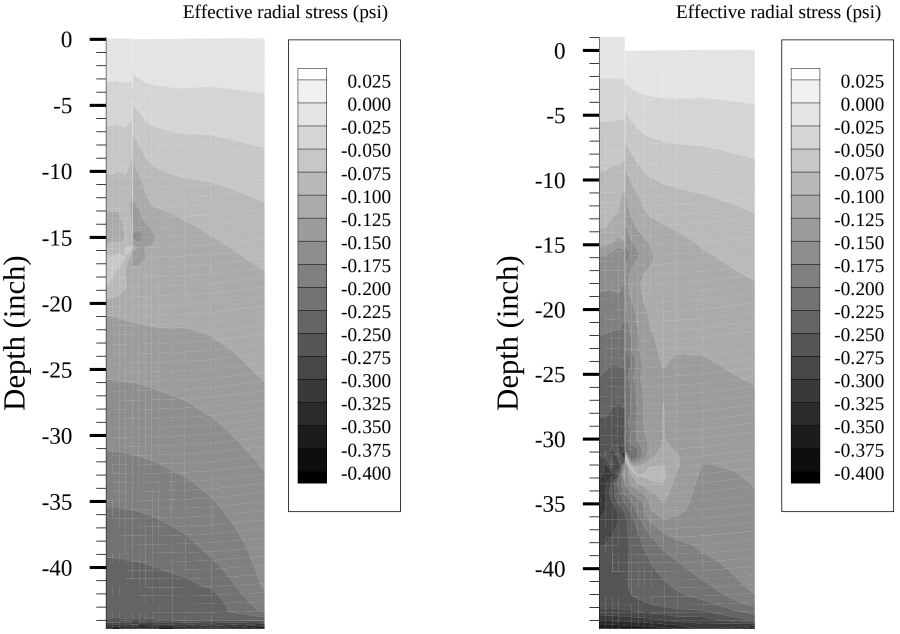

(a) End of self-weight installation

(b) End of suction installation

Figure 8.37: Distributions of effective radial stress within the soil domain at the end of self-weight and suction installations.

The distributions of effective vertical stress within the soil domain at the end of self-weight installation and suction installation are shown in Figs. 8.38(a) and (b), respectively. As discussed in Section 8.6.1 for self-weight installation, the vertical stress within the soil plug and soil domain near caisson exterior has been reduced. This is the case at the end of suction installation as well. The effective vertical stress near the caisson tip and soil plug [bulb region around caisson tip in Fig. 8.38(b)] is reduced due to the applied suction. Reduction in vertical stress does not occur in this soil region for the caisson installed by self-weight only [see Fig. 8.25(b)].

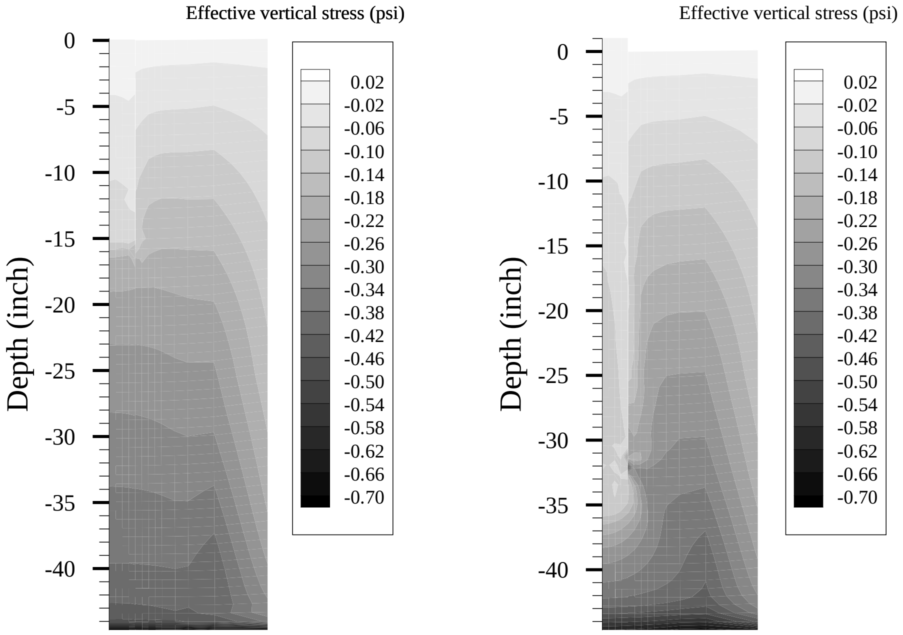

(a) End of self-weight installation

(b) End of suction installation

Figure 8.38: Distributions of effective vertical stress within the soil domain at the end of self-weight and suction installations.

The distributions of excess pore-water pressure within the soil domain at the end of self-weight installation and suction installation are shown in

Figs. 8.39(a) and (b), respectively. At the end of self-weight installation, the excess pore-water pressure calculated along the interior interface is higher than the one calculated along the exterior interface. At the end of suction installation, pressure within the soil plug is entirely suction (positive pressure). The computed pressure towards the exterior of caisson remains negative but is affected by applied suction, as computed excess pore-water pressure at sensor location O2 is lower (in magnitude) than the one computed at the end of self-weight installation to 32 inch (see Fig. 8.26).

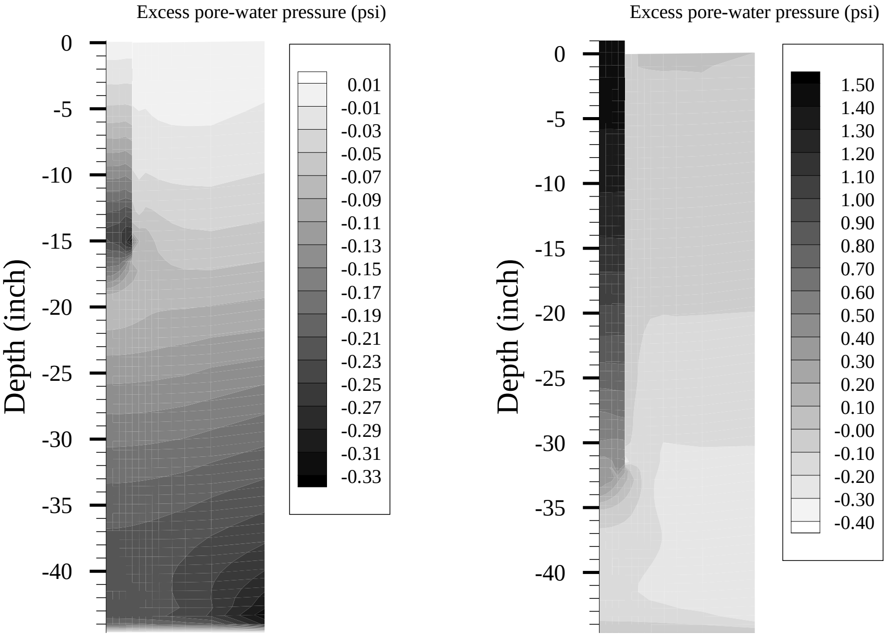

(a) End of self-weight installation (b) End of suction installation

Figure 8.39: Distributions of excess pore-water pressure within the soil domain at the end of self-weight and suction installations.

The distributions of porosity within the soil domain at the end of self-weight installation and suction installation are shown in Figs. 8.40(a) and (b), respectively. Comparison of porosity distributions at the end of consolidation [see Fig. 8.14(a)] and at the end of self-weight and suction installations [see Figs. 8.40(a) and (b), respectively] shows a small increase in porosity within the soil plug and the soil near exterior vicinity of the caisson at the end of self-weight and suction installations.

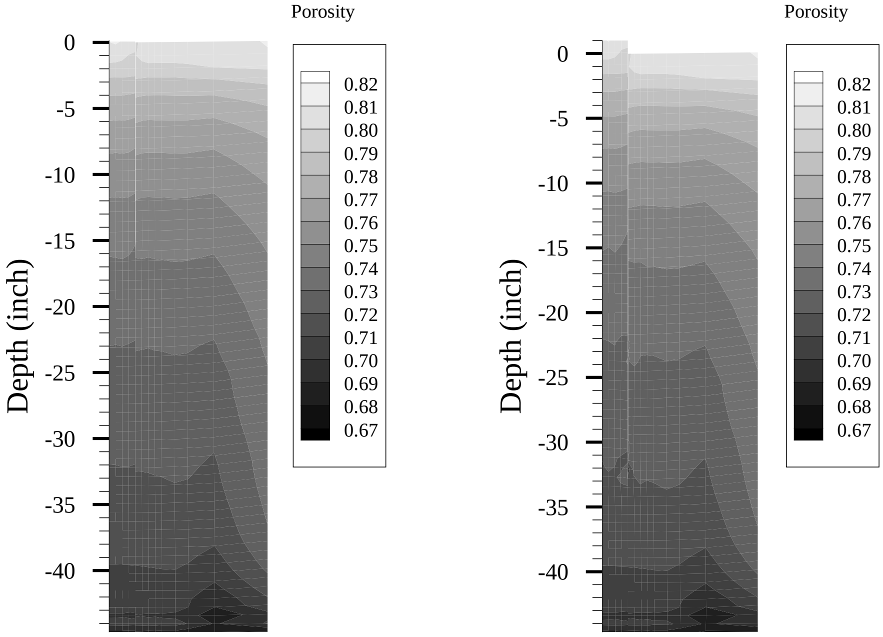

(a) End of self-weight installation (b) End of suction installation

Figure 8.40: Distributions of porosity within the soil domain at the end of self-weight and suction installations.

The distributions of size of bounding-surface within the soil domain at the end of self-weight installation and suction installation are shown in Figs. 8.41(a) and (b), respectively. Comparison of bounding-surface size distributions at the end of consolidation [see Fig. 8.14(b)] and at the end of self-weight and suction installations [see Figs. 8.41(a) and (b), respectively] shows a small change in the size within the soil domain in the caisson vicinity at the end of self-weight and suction installations.

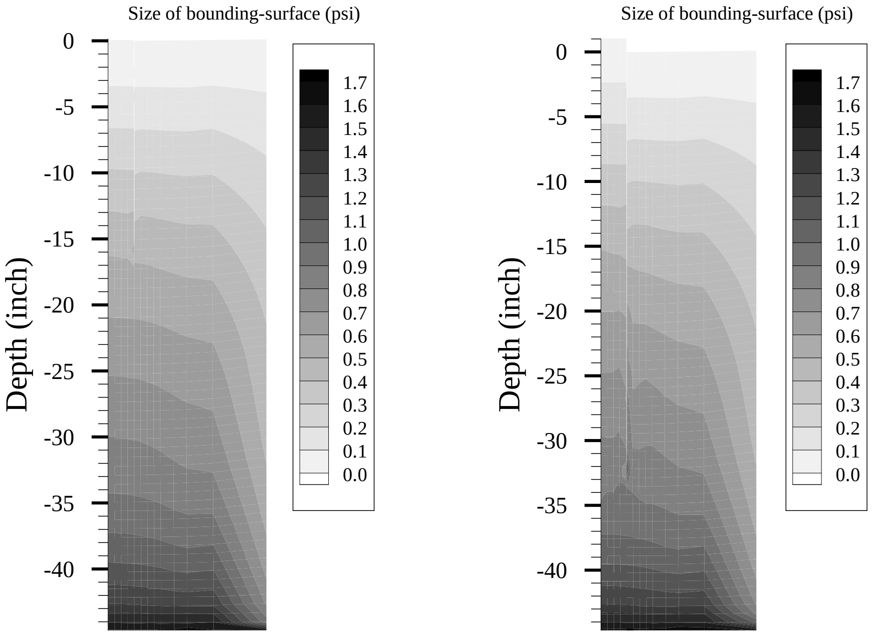

(a) End of self-weight installation (b) End of suction installation

Figure 8.41: Distributions of size of bounding-surface within the soil domain at the end of self-weight and suction installations.

Discussion

For the caisson installed by self-weight followed by suction, soil moved from the interior to the exterior during self-weight installation, and from the exterior to the interior during suction installation (see Fig. 8.35). Inward movement of soil during suction installation produced higher radial stress within the lower half of the soil plug than the stress in the vicinity of caisson exterior. Applied suction reduced effective vertical stress near interior caisson tip and below the soil plug.

8.7 Results: Reconsolidation or Setup

After caisson installation, excess pore-water pressure generated during the insertion phase is dissipated as the disturbed soil around the caisson reconsolidates. The simulation of reconsolidation or setup of soil was carried out for about 48 hours after complete caisson installation to 32 inch by self-weight installation, and self-weight followed by suction installation. Setup simulation following self-weight installation is identified as "SWP-Setup", and setup simulation followed by suction installation is identified as "SUC-Setup". The caisson was allowed to move freely during setup simulations.

8.7.1 Setup After Self-Weight Installation (SWP-Setup)

The displacements of soil surface and caisson tip during 48-hour setup is plotted in Fig. 8.42. It can be seen that the caisson, soil plug and soil-surrounding caisson settled by about 0.4 inch during 48-hour setup.

The computed frictional forces along interior and exterior interfaces during SWP-Setup are plotted in Fig. 8.43. At the beginning of setup, the insertion force acting on the caisson was reduced to zero during the initial 8 seconds of setup simulation. After removal of the insertion force, only the submerged weight of the caisson was resisted by frictional forces along the interfaces.

Computed and measured (Luke, 2002) dissipation of excess pore-water pressures at sensors I1, I2, I3, O1, and O2 during reconsolidation are compared in Fig. 8.44. Both computed and measured excess pore-water pressures decrease with time over a period of about 2 days. The match between measured and computed rates of excess pore-water pressure dissipation at all sensors is good.

The distributions of effective radial (lateral) and vertical stresses in the soil domain at the end of 48-hour setup simulation are shown in Figs. 8.45(a) and (b), respectively. It can be seen that the effective radial stress concentration near the caisson exterior tip [see Fig. 8.25(a)] is reduced at the end of setup simulation [see Fig. 8.45(a)]. At the end of setup, the radial stresses in the caisson exterior remain higher than in the caisson interior. Comparison of the distributions of effective vertical stress at the beginning of setup [Fig. 8.25(b)] and at the end of setup [Fig. 8.45(b)] shows that the vertical stress near the caisson tip increases during setup.

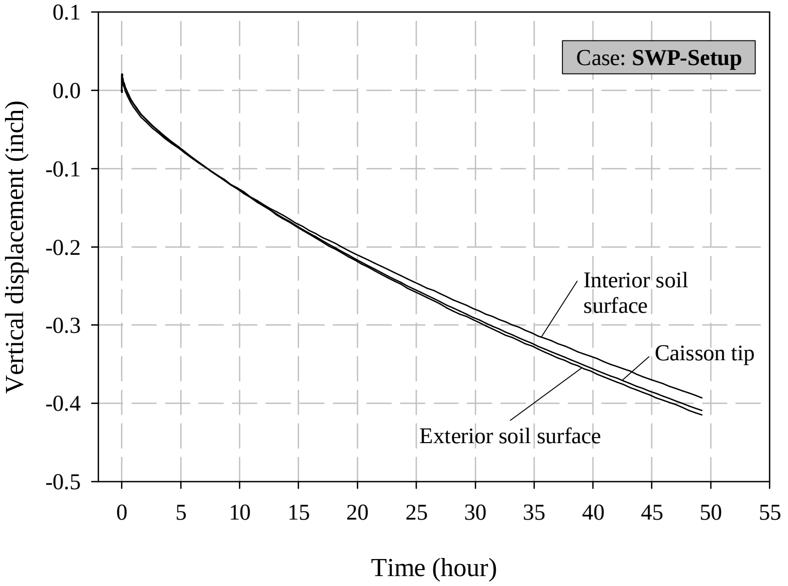

Figure 8.42: Displacements of soil surface and caisson tip during setup after self-weight installation.

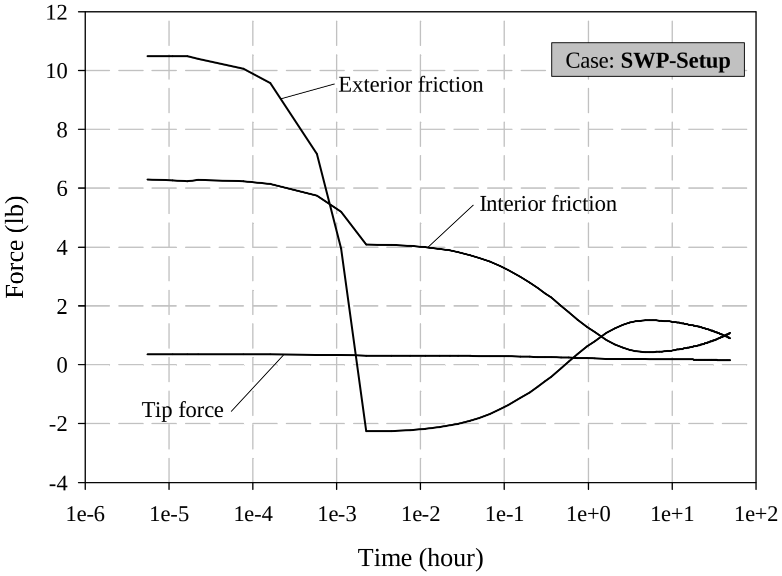

Figure 8.43: Interfacial forces during setup after self-weight installation.

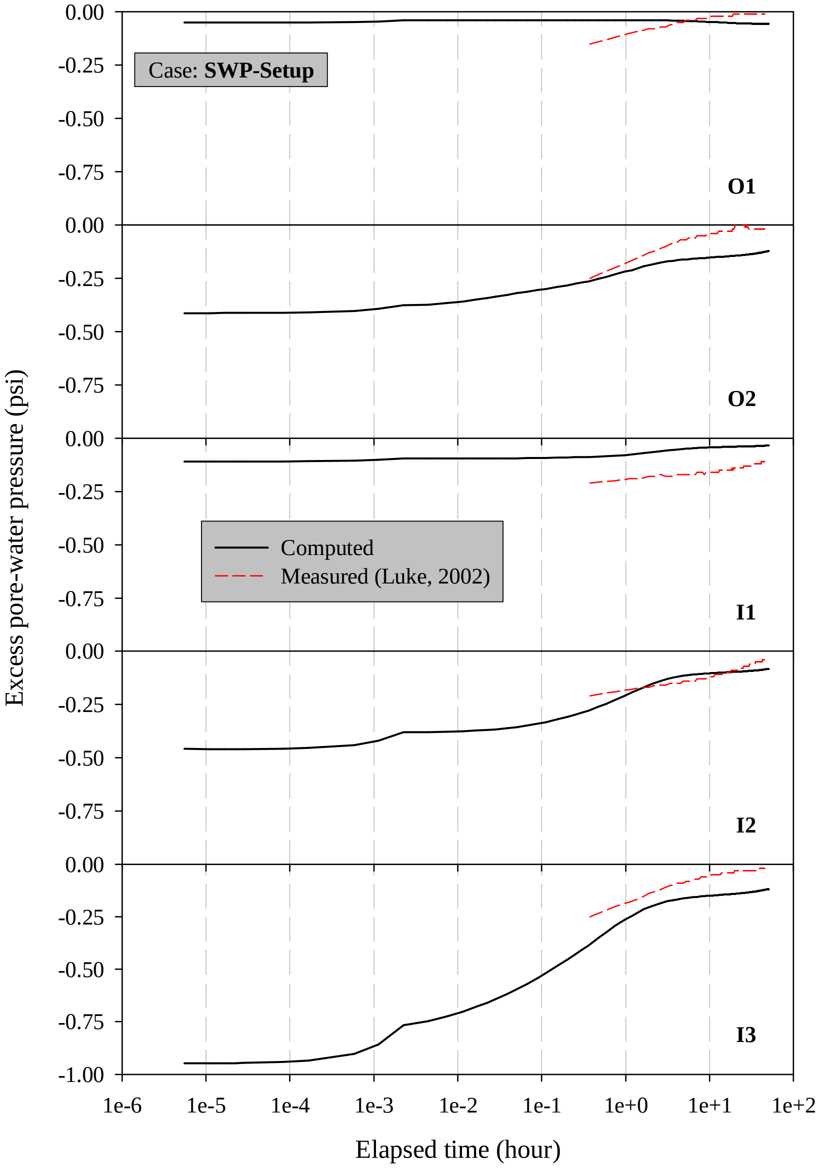

Figure 8.44: Dissipation of excess pore-water pressure at sensors during setup after self-weight installation.

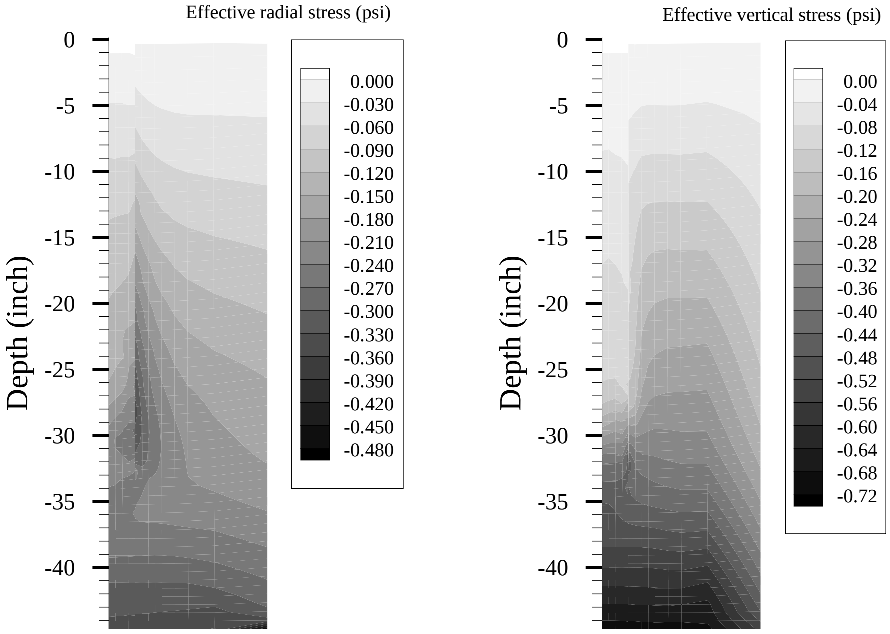

(a) Effective radial stress (b) Effective vertical stress

Figure 8.45: Distributions of effective radial and vertical stresses within the soil domain at the end of setup after self-weight installation.

The distribution of excess pore-water pressure within the soil domain at the end of 48-hour setup is shown in Fig. 8.46(a). Excess pore-water pressures were dissipated within the entire soil domain except around the caisson tip after 48 hours of setup (see Fig. 8.44). From the distribution, it can be noticed that the maximum excess pore-water pressure was about 0.13 psi after 48-hour setup. Caisson displacement did not cease during the 48-hour setup causing pore-water pressures to take longer time to dissipate completely.

The reconsolidation simulation was continued till 96 hours of setup to investigate long-term dissipation of excess pore-water pressure. The distribution of excess pore-water pressure within the soil domain at the end of 96-hour setup is shown in Fig. 8.46(b). From the distribution, it can be noticed that the maximum excess pore-water pressure within the soil was less than 0.1 psi after 96-hour setup. From laboratory tests it was observed that the excess pore-water pressures at sensors after 96 hours of setup were within the precision of the pressure transducers (El-Sherbiny, 2004). The pressure transducer precision reported by Luke (2002) is approximately 0.04 psi.

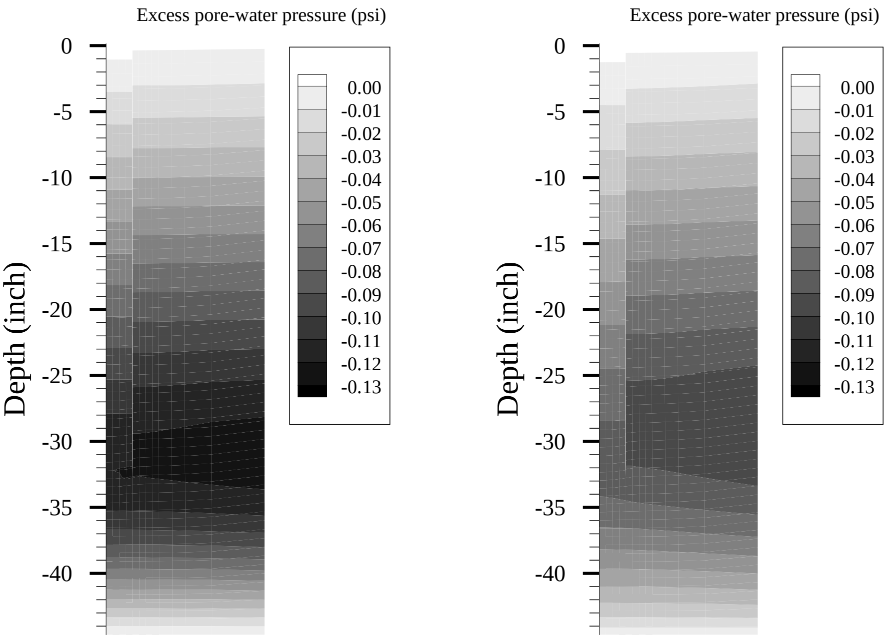

(a) 48-hour setup

(b) 96-hour setup

Figure 8.46: Distributions of excess pore-water pressure within the soil domain at the end of setup after self-weight installation.

The distribution of bounding-surface size within the soil domain at the end of 48-hour setup after self-weight installation is shown in Fig. 8.47. From the comparison between this distribution and the distribution of bounding-surface size at the end of self-weight installation [see Fig. 8.27(b)], it can be noticed that the size of the surface within the soil in the vicinity of the caisson tip increases during setup.

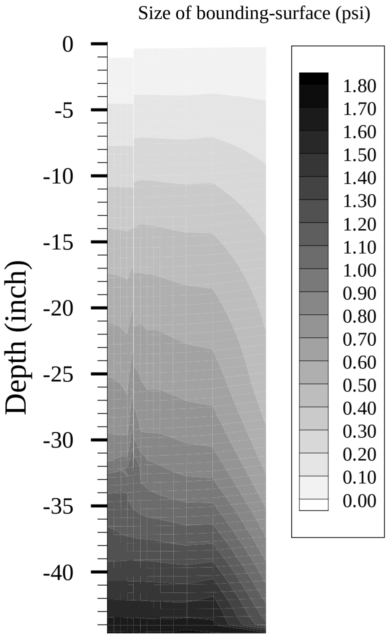

Figure 8.47: Distribution of size of bounding-surface within the soil domain at the end of setup after self-weight installation.

8.7.2 Setup After Suction Installation (SUC-Setup)

The displacements of soil surface and caisson tip during 48-hour SUC-Setup are plotted in Fig. 8.48. The caisson, soil plug and soil-surrounding caisson settled by about 0.4 inch during 48-hour setup.

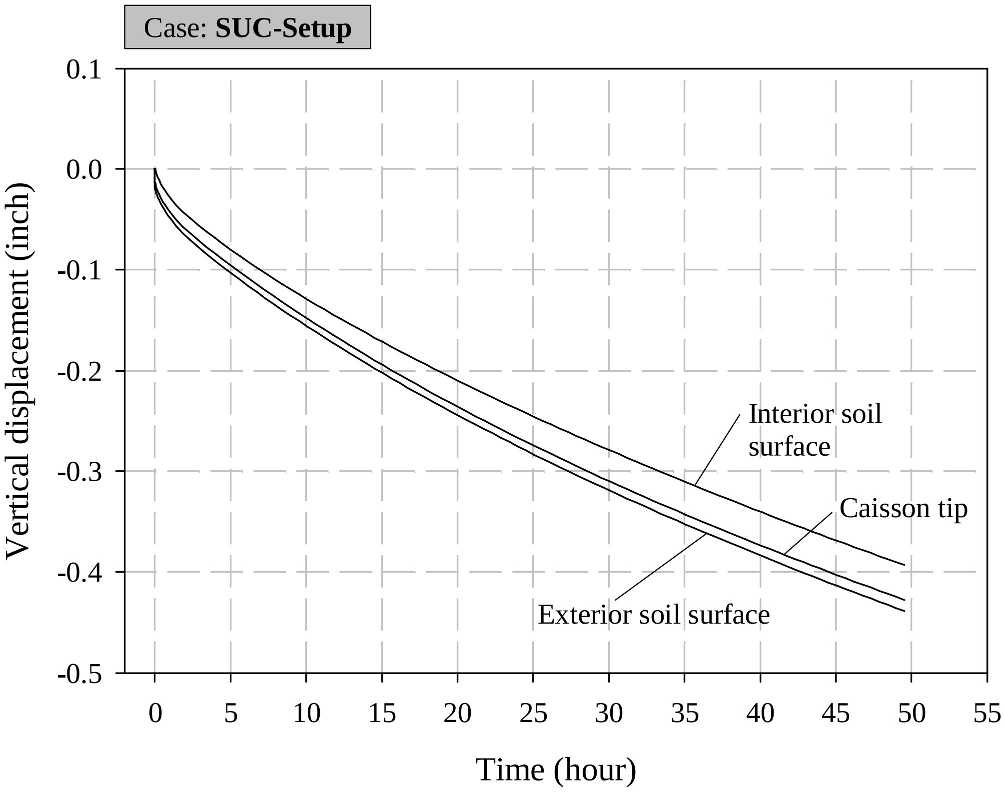

Figure 8.48: Displacements of soil surface and caisson tip during setup after suction installation.

The computed frictional forces along interior and exterior interfaces during setup are plotted in Fig. 8.49. At the beginning of setup, the suction acting on the caisson was reduced to zero during the initial 8 seconds of setup simulation. After removal of suction, only the submerged weight of the caisson was resisted by frictional forces along the interfaces.

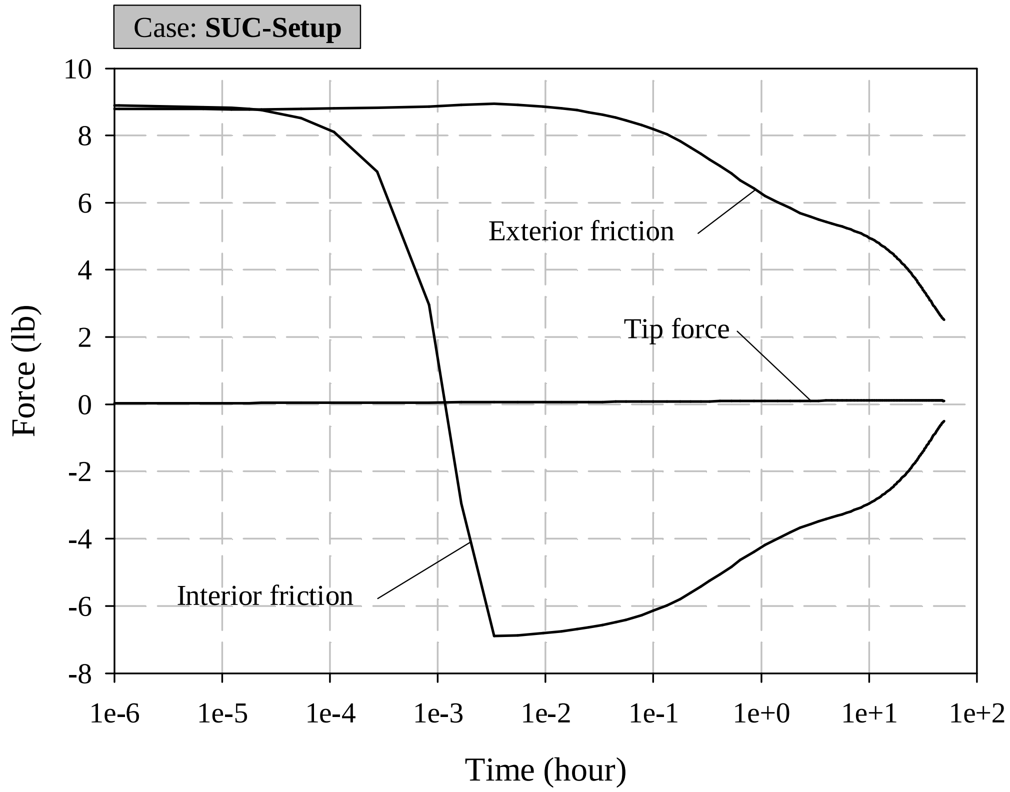

Figure 8.49: Interfacial forces during setup after suction installation.

The computed and measured (El-Sherbiny, 2004) excess pore-water pressures at sensors I1, I2, I3, O1, and O2 during reconsolidation are compared in Fig. 8.50. Both computed and measured excess pore-water pressures decrease with time over a period of about 2 days. The match between measured and computed rates of excess pore-water pressure dissipation at all sensors is excellent.

The distributions of effective radial (lateral) and vertical stresses in the soil domain at the end of 48-hour setup simulation are shown in Figs. 8.51(a) and (b), respectively. It can be seen that the effective radial stress concentration near the caisson interior tip [see Fig. 8.37(b)] is reduced at the end of setup simulation [see Fig. 8.51(a)]. At the end of setup, the radial stresses in the caisson interior remain higher than in the caisson exterior. Comparison of the distributions of effective vertical stress at the beginning of setup [Fig. 8.38(b)] and at the end of setup [Fig. 8.51(b)] shows that the vertical stress near the caisson tip increases during setup.

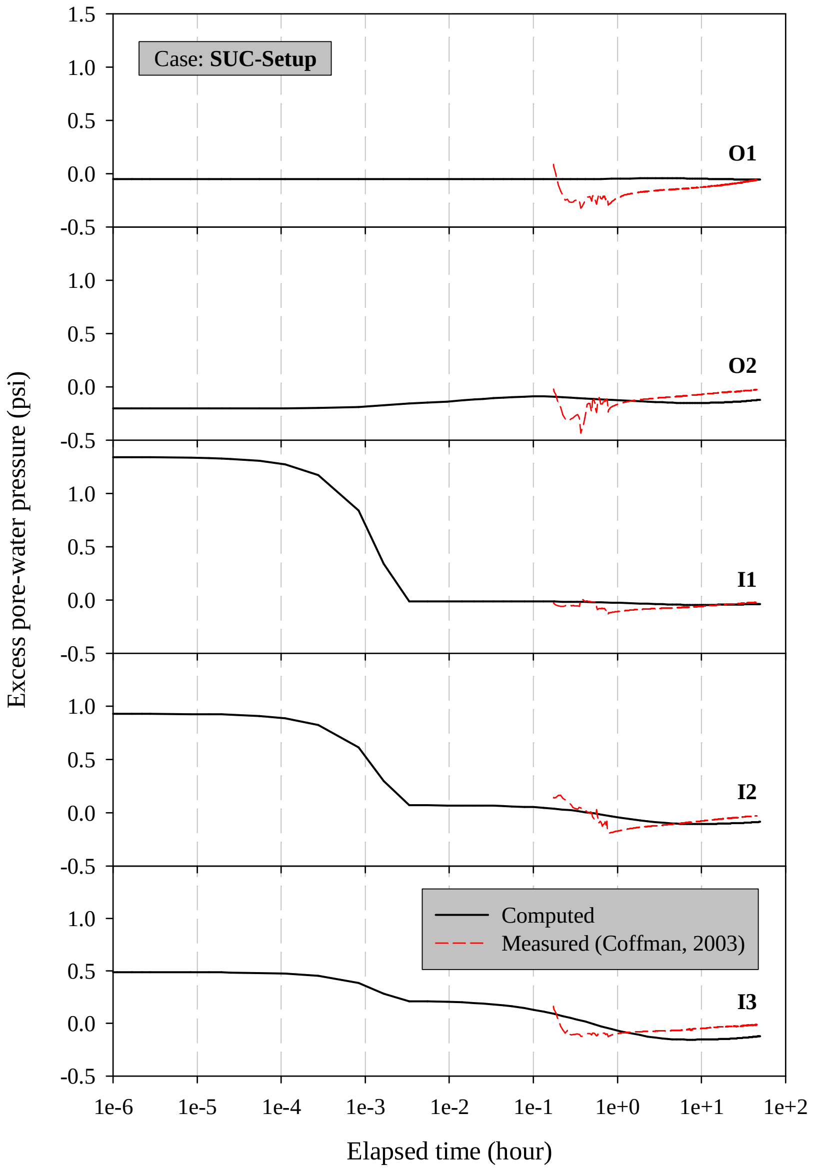

Figure 8.50: Dissipation of excess pore-water pressure at sensors during setup after suction installation.

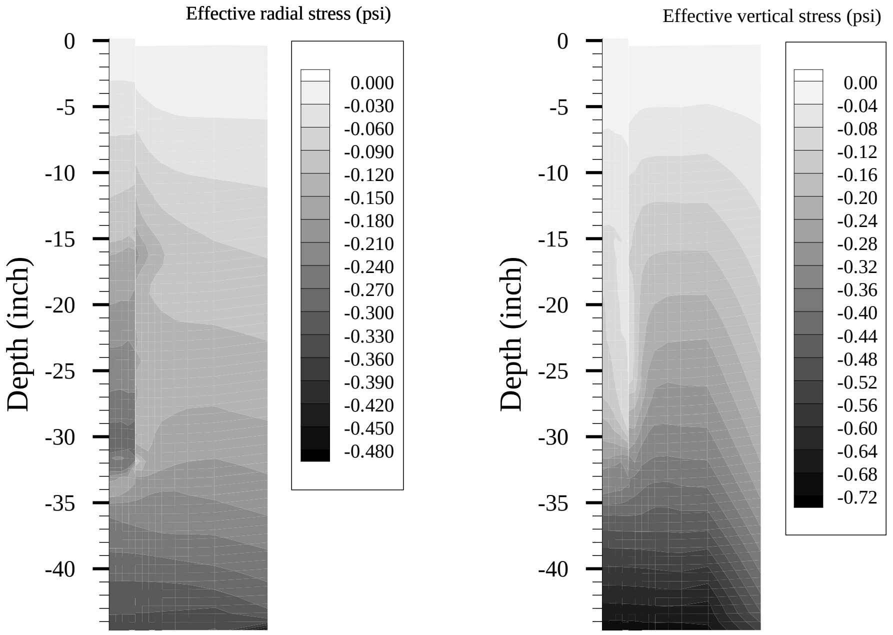

(a) Effective radial stress

(b) Effective vertical stress

Figure 8.51: Distributions of effective radial and vertical stresses within the soil domain at the end of setup after suction installation.

The distribution of excess pore-water pressure within the soil domain at the end of 48-hour setup is shown in Fig. 8.52(a). Excess pore-water pressure was dissipated within the entire soil domain except around the caisson tip after 48 hours of setup (see Fig. 8.50). Caisson displacement did not cease during setup causing pore-water pressures to take longer time to dissipate completely. Based on 96-hour setup simulation following self-weight installation [see Fig. 8.46(b)], it can be concluded that the excess pore-water pressure within the soil domain after suction installation would take more than 96 hours to dissipate completely.

The distribution of bounding-surface size within the soil domain at the end of 48-hour setup after suction installation is shown in Fig. 8.52(b). From the comparison between this distribution and the distribution of bounding-surface size at the end of suction installation [see Fig. 8.41(b)], it can be noticed that the size of the surface within the soil in the vicinity of the caisson tip increases during setup.

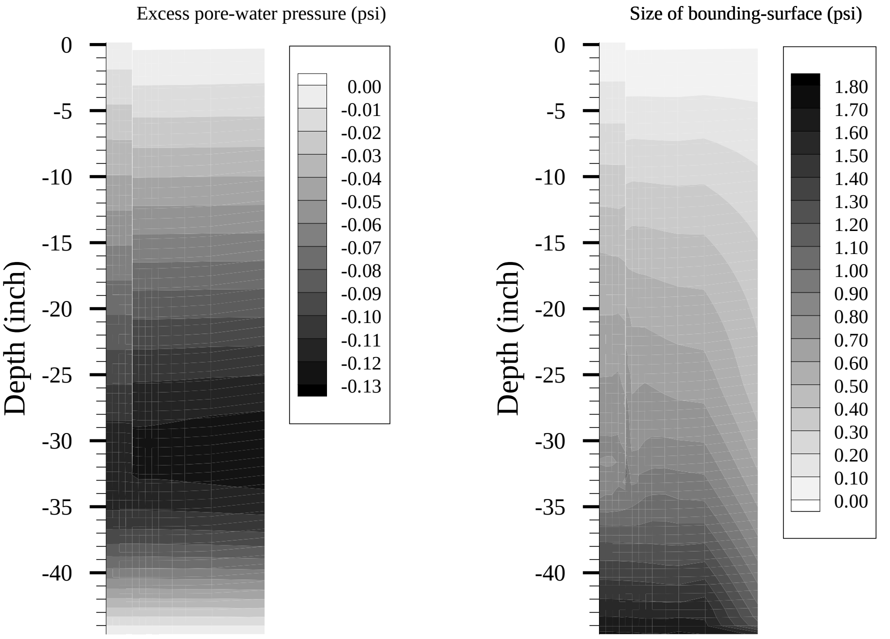

(a) Excess pore-water pressure (b) Size of bounding-surface

Figure 8.52: Distributions of excess pore-water pressure and size of bounding-surface within the soil domain at the end of setup after suction installation.

8.7.3 Discussion

Simulations of soil reconsolidation or setup for 48 hours after caisson installation were carried out. The caisson was allowed to move freely during setup simulations. At the end of 48 hours of setup, caisson displacement did not cease, causing delay in dissipation of excess pore-water pressure around the caisson tip. In general, after 48 hours of setup, the excess pore-water pressure was dissipated within the entire soil domain except around the caisson tip. During setup, both radial and vertical stresses were found to increase.

8.8 Results: Axial Pullout

Simulations of caisson axial pullout were performed following reconsolidation of the soil domain. During the simulations, the caisson was pulled out axially at different rates with the caisson cap either vented or closed. The axial pullout simulations carried out are listed in Table 8.3.

Computed axial pullout capacities are compared with the measured capacities reported in Luke (2002). Axial pullout tests were performed on caisson installed by self-weight only and self-weight followed by suction. For the caisson installed by suction, initial self-weight penetration was achieved under the effect of self-weight of caisson. Therefore, initial self-weight installation depth varies from 9 to 11 inch. For the computations, initial self-weight installation depth was fixed to 16 inch. For the caisson installed by self-weight only, caisson penetration to 32 inch was achieved in the tests as well as the computations.

Each of the simulations listed in Table 8.3 is described in the following sections.

Table 8.3: Caisson axial pullout cases

Simulation	**Self-weight insertion** (inch)	**Suction insertion** (inch)	**Pullout rate**	**Top cap condition**
SWP-VR	32.0	0.0	1.0 inch/sec	Vented
SWP-VS	32.0	0.0	1.0 inch/ 2 days	Vented
SWP-VD	32.0	0.0	Load controlled †	Vented
SWP-CR	32.0	0.0	1.0 inch/sec	Closed
SUC-VR	16.0	16.0	1.0 inch/sec	Vented
SUC-VS	16.0	16.0	1.0 inch/ 2 days	Vented
SUC-VD	16.0	16.0	Load controlled †	Vented
SUC-CR	16.0	16.0	1.0 inch/sec	Closed

† Load applied in 2.5 lb increments at 6-hour interval till detection of excessive caisson displacement.

8.8.1 Vented Top, Rapid Axial Pullout

The caissons installed by self-weight only (SWP-VR) and self-weight followed by suction (SUC-VR) were pulled axially at 1 inch/sec to investigate undrained behavior with the top open. For vented caisson top, free drainage of water was allowed from top of the interior soil plug in order to have zero excess pore-water pressure. Computed capacities from SWP-VR and SUC-VR simulations were compared with the measured caisson capacities from Tests 1-040802 and 1-041002, respectively, reported by Luke (2002).

SWP-VR

The total axial pullout force and frictional forces along the soil-caisson interfaces are plotted against location of caisson tip in Fig. 8.53. The computed ultimate capacity was about 20.4 lb, while the measured value was about 24.0 lb (Luke, 2002). As mentioned earlier, the undisturbed undrained shear strength of soil used in the test reported by Luke (2002) is about 40% lower than the one used for the computations. The higher strength profile used in the axial capacity simulations does not explain the difference between measured and computed caisson capacities for SWP-VR case. The lower computed caisson capacity is likely due to use of a lower friction coefficient in the present simulations. The computed frictional force along the exterior interface turned out higher than the interior frictional force.

The components of ultimate axial capacity are identified in Fig. 8.54. About 90% of the capacity is derived from the frictional force on the interior and exterior interfaces of the caisson. The computed tip resistance was negligible compared to ultimate capacity, but it is worth mentioning that it was acting in the upward direction. This means the soil at the caisson tip was pushing the caisson out, and not providing resistance to pullout. A similar observation was made by Luke (2002) on the basis of calculated (from test results) values of end bearing forces.

SUC-VR

The total axial pullout force and frictional forces along the soil-caisson interfaces are plotted against location of caisson tip in Fig 8.55. The computed ultimate capacity was about 18.2 lb, while the measured value was about 19.2 lb. As expected from the comparison of effective radial stresses in the interior and exterior of the caisson, the computed frictional force along the interior interface was higher than along the exterior interface.

The components of ultimate axial capacity are identified in Fig. 8.56.

About 90% of the capacity is derived from frictional force on the interior and exterior caisson interfaces. The computed tip resistance was negligible, and as with SWP-VR acted in the upward direction.

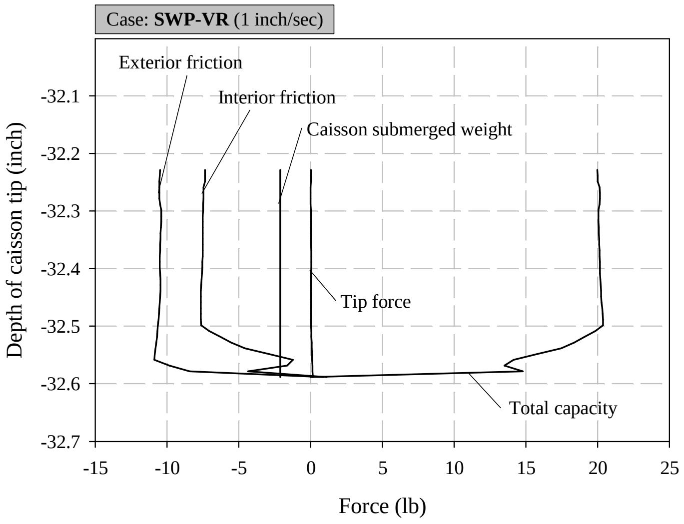

Figure 8.53: Vented axial capacity of caisson at 1 in/sec pullout rate after self-weight installation.

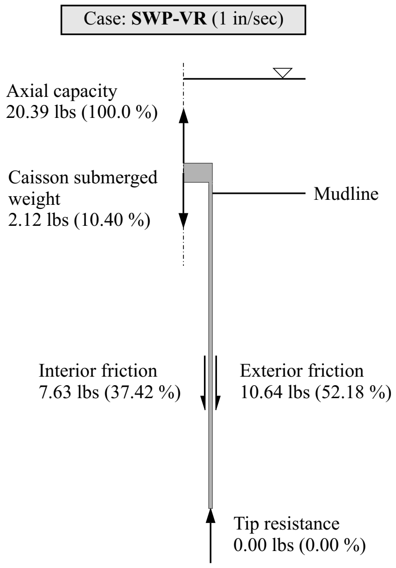

Figure 8.54: Components of ultimate axial capacity for SWP-VR.

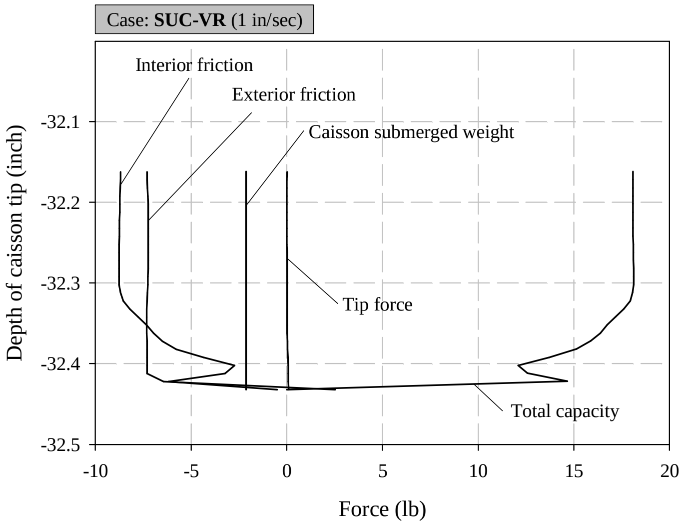

Figure 8.55: Vented axial capacity of caisson at 1 in/sec pullout rate after suction installation.

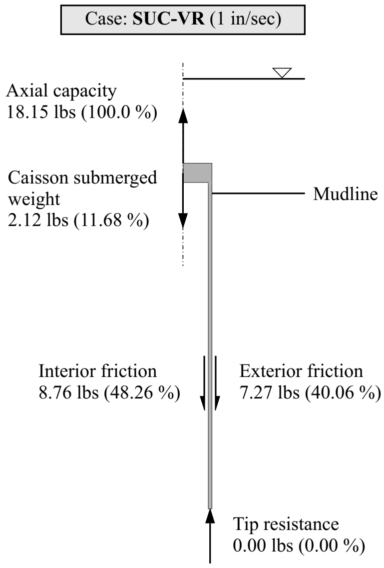

Figure 8.56: Components of ultimate axial capacity for SUC-VR.

8.8.2 Vented Top, Slow Axial Pullout

The caissons installed by self-weight only (SWP-VS) and self-weight followed by suction (SUC-VS) were pulled axially at 1 inch per 2 days to investigate drained behavior with top of the caisson open. Measured caisson capacities are not available from tests.

SWP-VS

The total axial pullout force and the frictional forces along the soil-caisson interfaces are plotted against location of caisson tip in Fig. 8.57. The computed ultimate capacity was 17.8 lb. The frictional force along the exterior interface was higher than along the interior interface.

The components of ultimate axial capacity are identified in Fig. 8.58. About 90% of the capacity derived from the frictional force on the interior and exterior interfaces of the caisson. Computed tip resistance was negligible and acted in the upward direction.

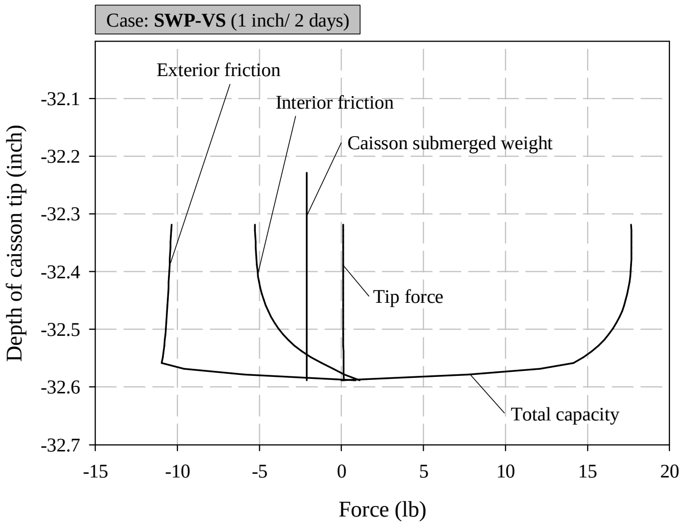

Figure 8.57: Vented axial capacity of caisson at 1 in per 2 days pullout rate after self-weight installation.

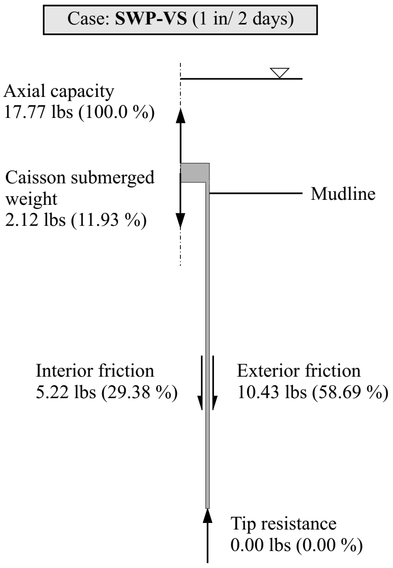

Figure 8.58: Components of ultimate axial capacity for SWP-VS.

SUC-VS

The total axial pullout force and the frictional forces along the soil-caisson interfaces are plotted against location of caisson tip in Fig. 8.59. The computed ultimate capacity was 14.8 lb. The frictional force along the exterior interface was higher than along the interior interface.

The components of ultimate axial capacity are identified in Fig. 8.60. About 85% of the capacity comes from the frictional force on the interior and exterior interfaces of the caisson. The computed tip resistance was negligible and acted in the upward direction.

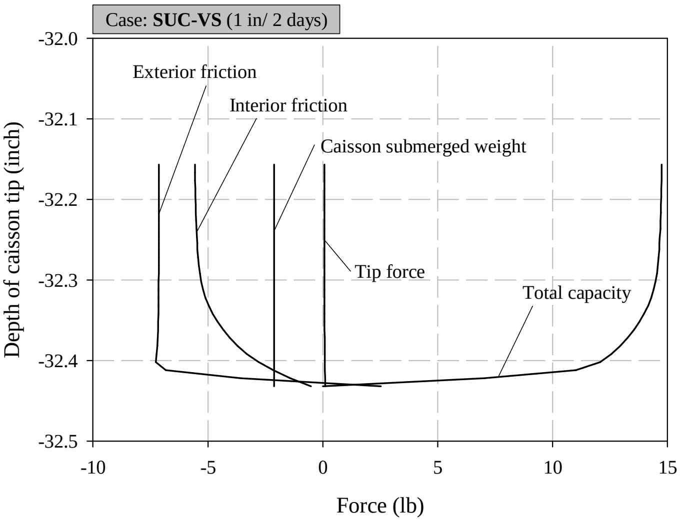

Figure 8.59: Vented axial capacity of caisson at 1 in per 2 days pullout rate after suction installation.

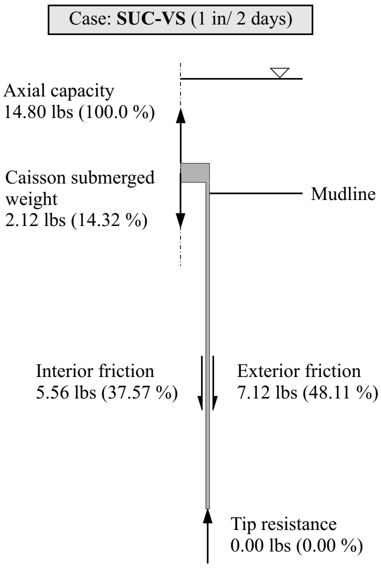

Figure 8.60: Components of ultimate axial capacity for SUC-VS.

8.8.3 Vented Top, Drained Axial Pullout

The caissons installed by self-weight only (SWP-VD) and self-weight followed by suction (SUC-VD) were considered for vented-top drained axial pullout simulations (SWP-VD and SUC-VD respectively). The caissons were subjected to a specified axial pullout load time history. The axial load was applied in 2.5 lb increments at a 6-hour interval until excessive displacement of the caisson was detected. The computed capacity from SUC-VD simulation was compared with the measured caisson capacity from Test 1-042502 reported by Luke (2002). During the laboratory drained axial pullout tests, the increment of axial load was controlled with respected to desired increase in excess pore-water pressure, and the load was kept constant until complete dissipation of generated excess pore-water pressure was achieved. Therefore, both the load increment and the time interval between two successive load increments were irregular. Measured caisson capacity for self-weight installation case is not available from the tests.

SWP-VD

The specified history of axial pullout load along with the computed frictional forces are shown in Fig. 8.61(a). The maximum axial load applied to the caisson during simulation was about 18.5 lb. During the initial 24-hour period, most of the resistance to applied load came from the frictional force along the exterior interface.

The computed history of caisson tip location is shown in Fig. 8.61(d). During the initial 30-hour period, the caisson tip moved downward by about 0.07 inch and then started moving upwards with increase in axial pullout force.

The development and dissipation of computed excess pore-water pressure along the exterior interface (at sensors O1, and O2) and the interior interface (at sensors I1, I2, and I3) are shown in Figs. 8.61(b) and (c), respectively. At low levels of axial load, the computed excess pore-water pressures at all sensor locations were less affected, and pressure continued to decrease. At higher levels, the computed excess pore-water pressures along the interior interface were affected more than along the exterior interface.

The components of ultimate axial capacity are identified in Fig. 8.62. About 88% of the capacity is derived from the frictional forces on the interior and exterior interfaces of the caisson. The computed frictional force along the exterior interface was about 1.5 times the frictional force along the interior interface. Negligible tip resistance was computed, acting in the upward direction.

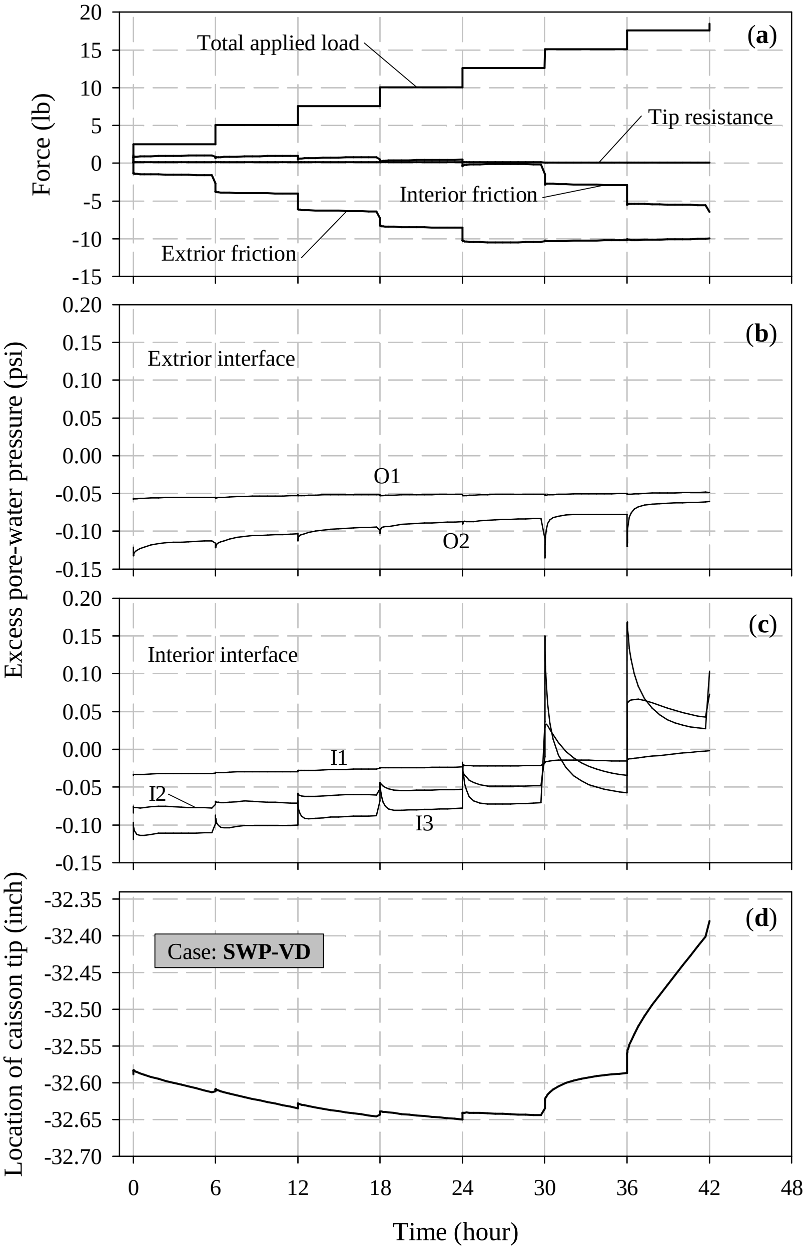

Figure 8.61: Vented axial capacity of caisson under drained condition after self-weight installation.

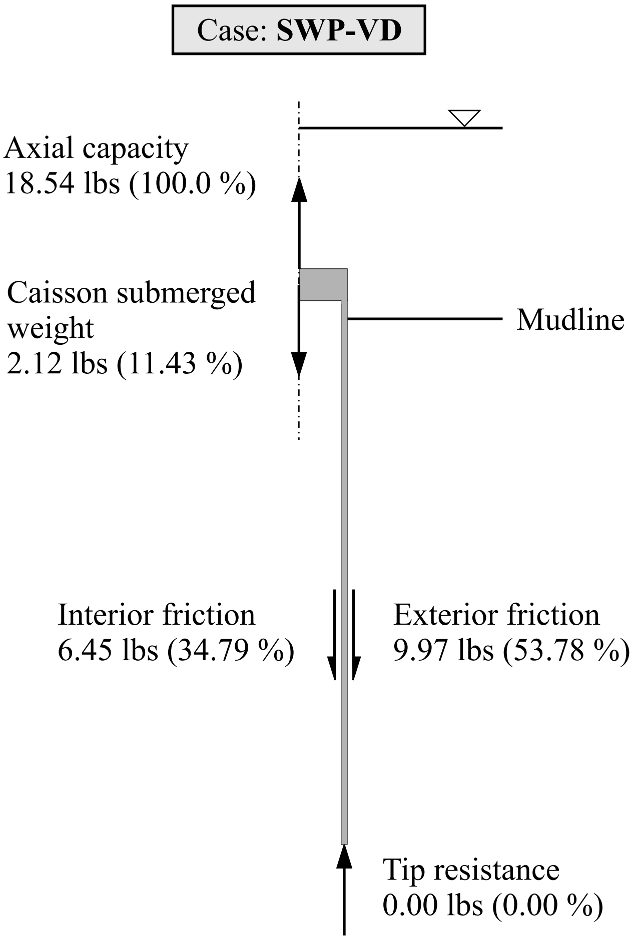

Figure 8.62: Components of ultimate axial capacity for SWP-VD.

SUC-VD

The specified history of axial pullout load along the computed frictional forces are shown in Fig. 8.63(a). The maximum axial load applied to the caisson during simulation was about 17.3 lb. During the initial 24-hour period, most of the resistance to applied load came from the frictional force along the exterior interface.

The computed history of caisson tip location is shown in Fig. 8.63(d). During the initial 30-hour period, the caisson tip moved downward by about 0.08 inch and then started moving upwards with increase in axial pullout force.

The development and dissipation of computed excess pore-water pressure along the exterior interface (at sensors O1, and O2) and the interior interface (at sensors I1, I2, and I3) are shown in Figs. 8.63(b) and (c), respectively. At low levels of axial load, the computed excess pore-water pressures at all sensor locations were less affected, and pressure continued to decrease. At higher levels, computed excess pore-water pressures along interior interfaces were affected more than along exterior interfaces.

The components of ultimate axial capacity are identified in Fig. 8.64. About 88% of the capacity derived from frictional forces on the interior and exterior interfaces of the caisson. The frictional force along the exterior interface was about 0.9 times the frictional force along the interior interface. Negligible tip resistance was computed, acting in the upward direction.

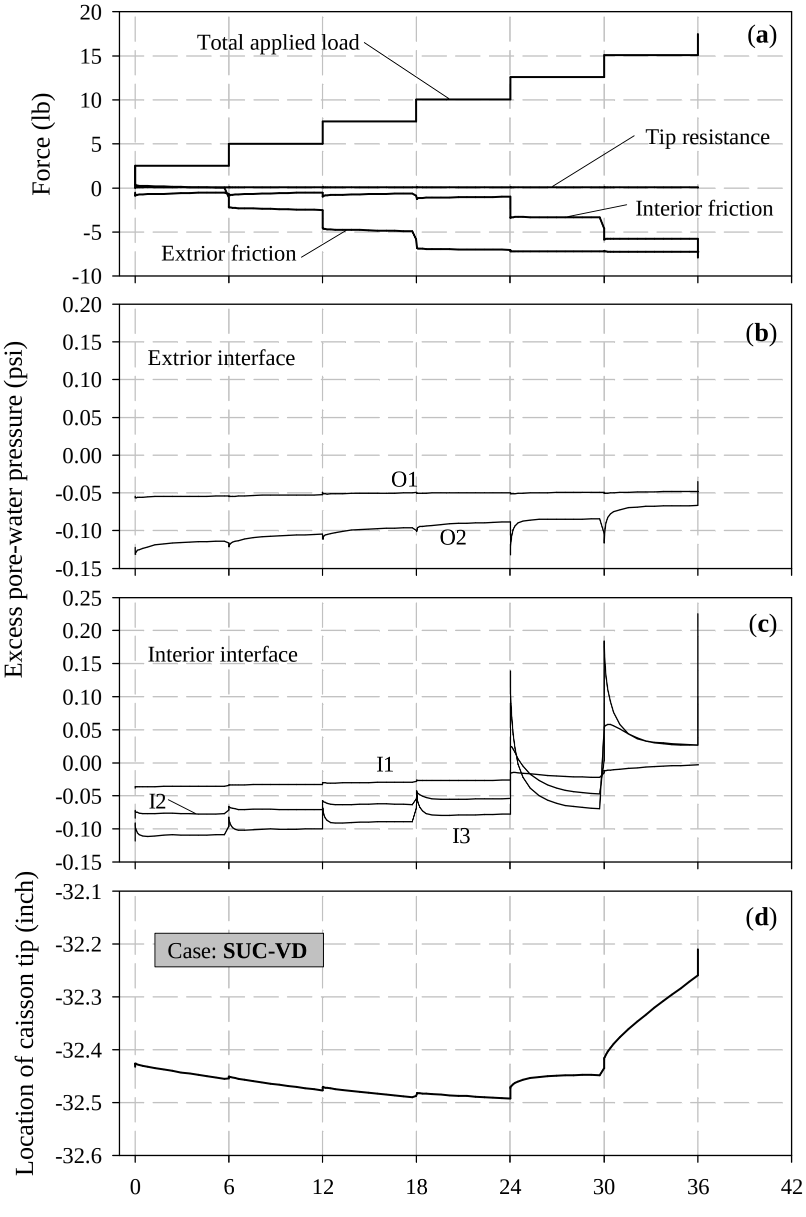

Figure 8.63: Vented axial capacity of caisson under drained condition after suction installation.

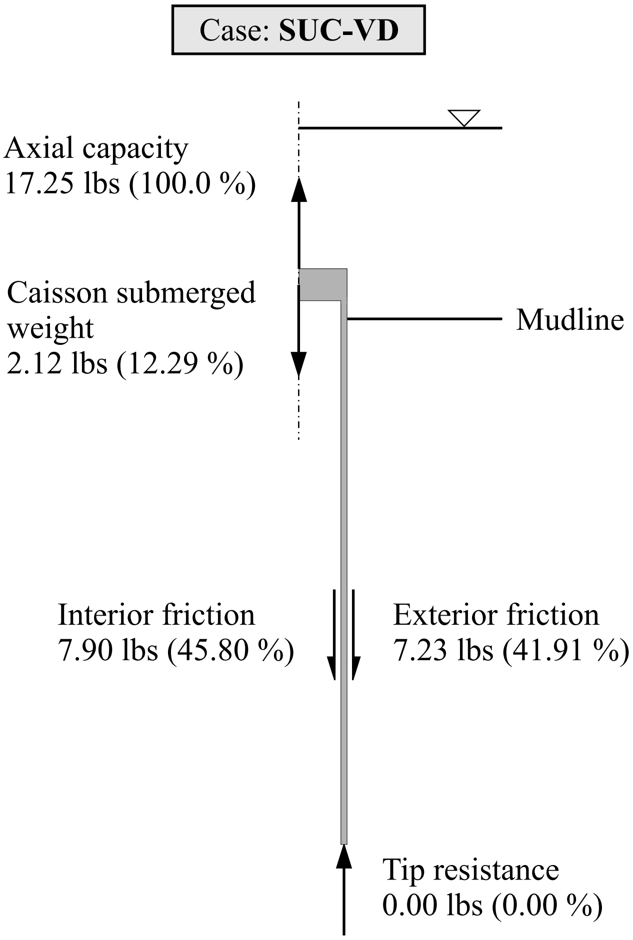

Figure 8.64: Components of ultimate axial capacity for SUC-VD.

8.8.4 Closed Top, Rapid Axial Pullout

The caissons installed by self-weight only (SWP-CR) and self-weight followed by suction (SUC-CR) were pulled axially at 1 inch/sec to investigate undrained behavior with the top closed. In the computations, the excess pore-water pressure at the top of soil plug was considered as unknown. It was assumed that this unknown amount of suction was also acting under the caisson cap. The computed capacities from SWP-CR and SUC-CR simulations were compared with the measured caisson capacities from Tests 1-030102 and 1-030802, respectively, reported by Luke (2002).

SWP-CR

The total axial pullout force along with the frictional forces along the soil-caisson interfaces and suction force under the caisson cap are plotted against location of caisson tip in Fig. 8.65. The computed ultimate capacity was about 23.4 lb, while the measured value was about 28.0 lb (Luke, 2002). The computed frictional force along the exterior interface was higher than the interior frictional force.

The components of ultimate capacity are identified in Fig. 8.66. About 42% of the capacity is derived from suction generated under the caisson cap, while the computed frictional force along the exterior interface contributed about 42% to the capacity, and the frictional force along the interior interface contributed only about 7% to the capacity. Negligible tip resistance was computed, acting in the upward direction.

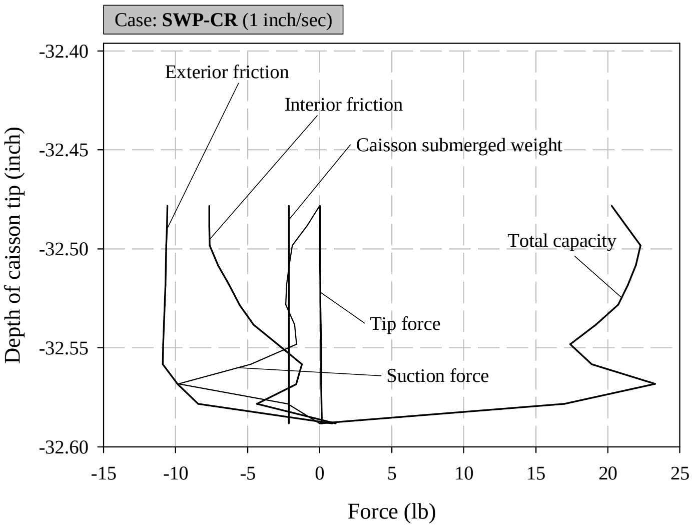

Figure 8.65: Closed axial capacity of caisson at 1 inch/sec pullout rate after self-weight installation.

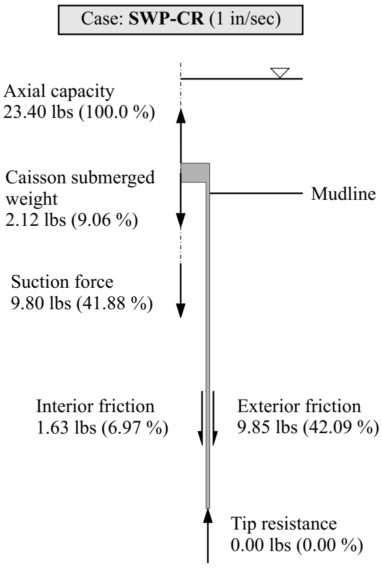

Figure 8.66: Components of ultimate axial capacity for SWP-CR.

SUC-CR

The total axial pullout force along with frictional forces along the soil-caisson interfaces and suction force under the caisson cap are plotted against location of caisson tip in Fig. 8.67. The computed ultimate capacity was about 22.7 lb, while the measured value was about 18.6 lb (Luke, 2002). The frictional force along the interior interface was higher than the exterior frictional force.

The components of ultimate capacity are identified in Fig. 8.68. About 44% of the capacity is derived from suction generated under the caisson cap. The frictional force along the exterior interface contributed about 32% to the capacity, and the frictional force along the interior interface contributed only about 14% to the capacity. Negligible tip resistance was computed, acting in the upward direction.

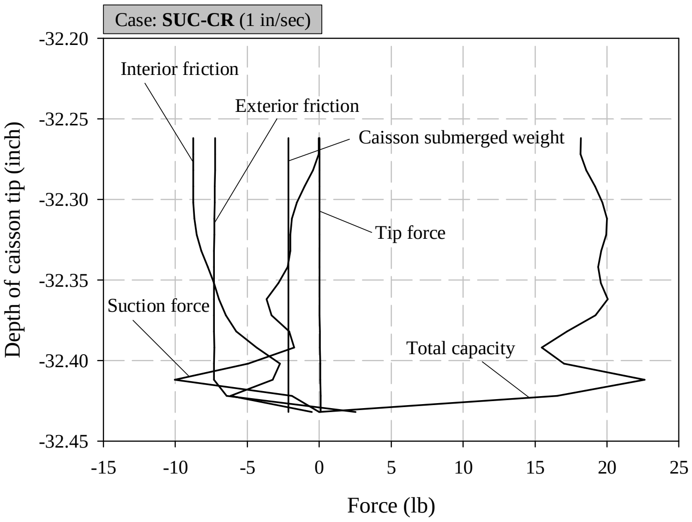

Figure 8.67: Closed axial capacity of caisson at 1 inch/sec pullout rate after suction installation.

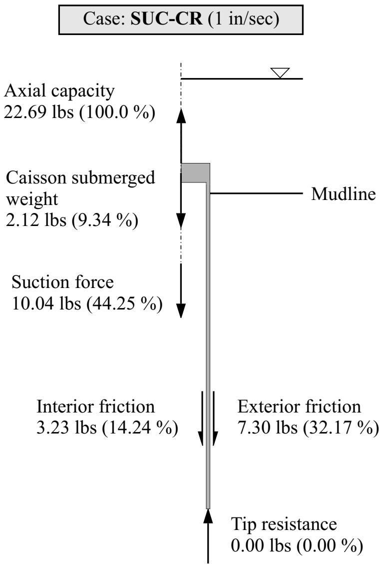

Figure 8.68: Components of ultimate axial capacity for SUC-CR.

8.8.5 Summary of Axial Pullout Simulation Results

Computed ultimate axial pullout capacities of caisson installed by self-weight alone and self-weight followed by suction are compared with the measured values in Fig. 8.69. The computed ultimate capacity and its frictional as well as suction components are listed in Table 8.4 (along with the measured capacity) for each of the cases considered.

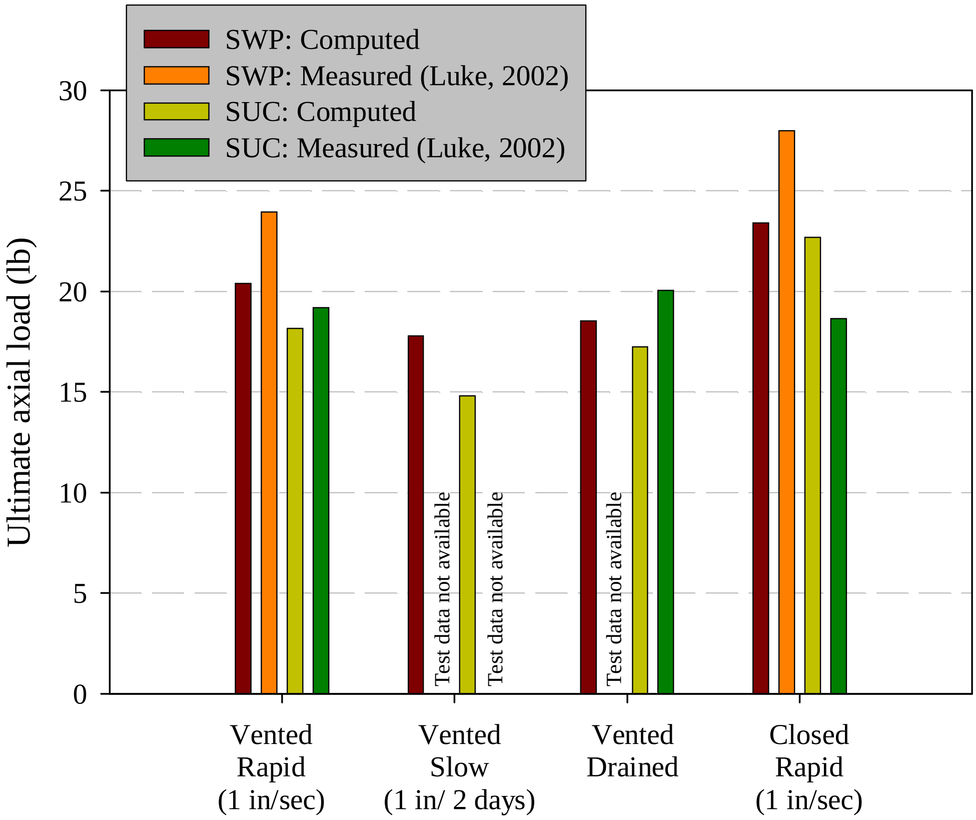

Figure 8.69: Summary of axial pullout capacity and comparison with laboratory test results (Luke, 2002).

Computed axial capacities for caisson installed by suction are smaller than for the caisson installed by self-weight alone. Close examination of the distributions of bounding-surface size (soil history dependent variable, I_0) at the end of setup after self-weight installation (see Fig. 8.47) and suction installation [see Fig. 8.52(b)] indicates that the size within the soil in the vicinity of the caisson is larger for caisson installed by self-weight alone. This material parameter is a measure of soil strength, and its larger value suggest stronger soil. The comparison of the size suggests that the suction application caused reduction in the soil strength. Computed axial capacities of the caissons are consistent with this observation.

For axial pullout with vented top, about 85 to 90% of the ultimate capacity is derived from frictional forces along caisson-soil interfaces. For caisson installed by self-weight alone and pulled axially with vented top, the frictional force along the exterior interface is higher than the frictional force along the interior interface. The higher frictional force along the exterior interface is consistent with the distribution of radial stresses within the soil near the caisson exterior. For caisson installed by suction and pulled axially with vented top, except for SUC-VS case, the frictional force along the interior interface is higher than the frictional force along the exterior interface. The higher frictional force along the interior interface is consistent with the distribution of radial stresses within the soil plug. The exterior caisson interface attracts higher force under vented slow axial pullout condition (SWP-VS and SUC-VS).

For the caisson installed by self-weight alone and pulled axially with closed top, the contribution from suction generated below the cap is about 41.9%, and for the caisson installed by suction, the contribution from suction is about 44.3%. In both cases, the frictional force along the exterior interface is much higher than the frictional force along the interior interface.

Table 8.4: Caisson axial pullout capacity

Simulation	**Insertion method**	**Measured capacity** (lb) (Luke, 2002)	**Computed capacity** (lb)	**A** ‡ (%)	**B** ⋆ (%)	**C** ⋆⋆ (%)
SWP-VR	SWP	24.0	20.4	52.2	37.4	–
SWP-VS	SWP	†	17.8	58.7	29.4	–
SWP-VD	SWP	†	18.5	53.8	34.8	–
SWP-CR	SWP	28.0	23.4	42.1	7.0	41.9
SUC-VR	SWP+SUC	19.2	18.2	40.1	48.3	–
SUC-VS	SWP+SUC	†	14.8	48.1	37.6	–
SUC-VD	SWP+SUC	20.0	17.3	41.9	45.8	–
SUC-CR	SWP+SUC	18.6	22.7	32.2	14.2	44.3

† Test data not available.
‡ Exterior frictional force contribution.
⋆ Interior frictional force contribution.
⋆⋆ Suction contribution.

Overall there is good agreement between computed and measured axial capacities under all drainage and loading conditions.

8.9 Results: Inclined capacity

The ultimate capacity of caissons installed by self-weight alone and self-weight followed by suction and subjected to inclined load was computed using ABAQUS software. First, the horizontal load capacity of the caisson was computed for various pad-eye locations. Then, the inclined load capacity of the caisson was computed for the pad-eye location where maximum horizontal capacity was obtained.

8.9.1 3D Geometry

The deformed axisymmetric mesh of caisson-soil system obtained at the end of reconsolidation simulation was transformed to a 3D mesh. This 3D mesh was specified as initial geometry for ABAQUS to perform simulation of caisson behavior subjected to inclined loads. Three-dimensional meshes obtained for self-weight installation only and self-weight followed by suction installation are shown in Figs. 8.70 and 8.71, respectively. The inclined load was assumed to act in an azimuthal plane. Thus, one-half of the caisson-soil system was modeled. Appropriate boundary conditions were specified on the plane of symmetry. Additional details regarding three-dimensional analysis using ABAQUS can be found in Chapter 7.

8.9.2 Horizontal Capacity

Simulations of the caisson subjected to horizontal load at various pad-eye locations were performed. Pad-eye locations of 1, 8, 9, 10, 11, 12, 15, 17, and 36 inch from the caisson tip were considered for caissons installed by self-weight only and self-weight followed by suction. Computed horizontal capacities at various pad-eye locations for caisson installed by self-weight alone and self-weight followed by suction along with measured horizontal capacities for caisson installed by self-weight followed by suction are shown in Table. 8.5.

Caisson Installed by Self-Weight Only

The computed ultimate horizontal capacities of caissons installed by self-weight only and subjected to horizontal load at different pad-eye locations are presented in Fig. 8.72. Measured horizontal capacities are not available

Table 8.5: Caisson horizontal load capacity

Depth of load attachment below mudline (Location above caisson tip) (inch)	**Computed capacity (SWP)**$\star$ (lb)	**Computed capacity (SUC)**$\star\star$ (lb)	**Measured capacity** (Coffman, 2003)$\star\star$ (lb)
+4.0 (36.0)	18.0	17.3	†
-15.0 (17.0)	47.3	46.0	42.1
-17.0 (15.0)	55.3	54.0	†
-20.0 (12.0)	71.9	69.9	68.2
-21.0 (11.0)	78.5	76.4	74.1
-22.0 (10.0)	85.5	81.9	73.9
-23.0 (9.0)	81.4	77.9	†
-24.0 (8.0)	76.4	73.1	73.7
-31.0 (1.0)	43.4	44.8	48.4

$\star$ Caisson installed by self-weight only.
$\star\star$ Caisson installed by self-weight and suction, and measured capacity corrected for pulley friction.
† Test data not available.

from test data for these cases. Maximum computed ultimate horizontal capacity of caisson was achieved for pad-eye located at 10 inch above the caisson tip.

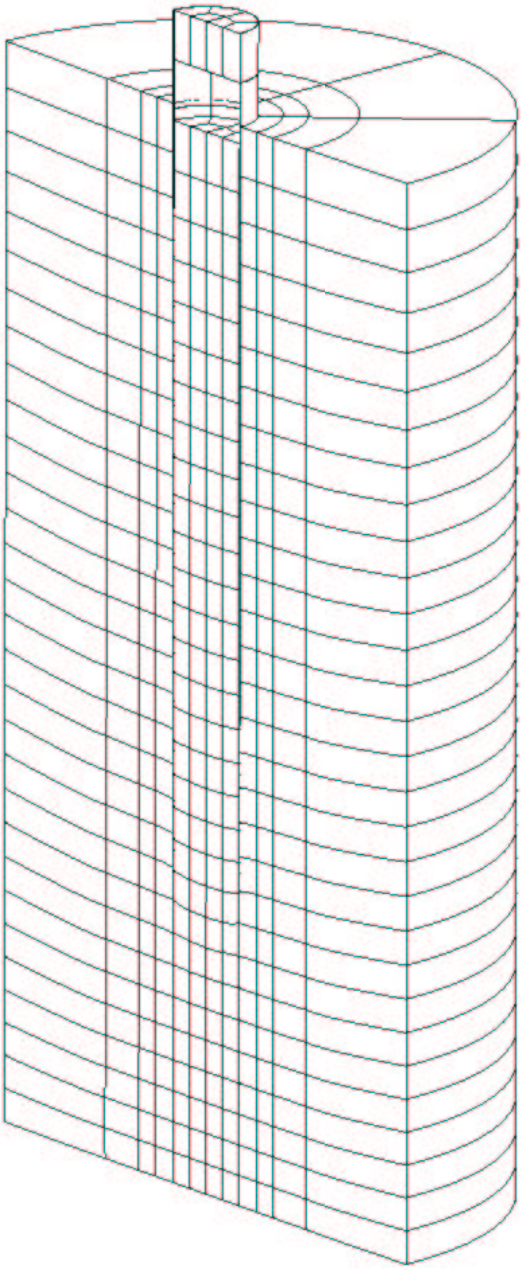

Figure 8.70: Caisson-soil 3D mesh at the end of 48-hour setup following self-weight installation.

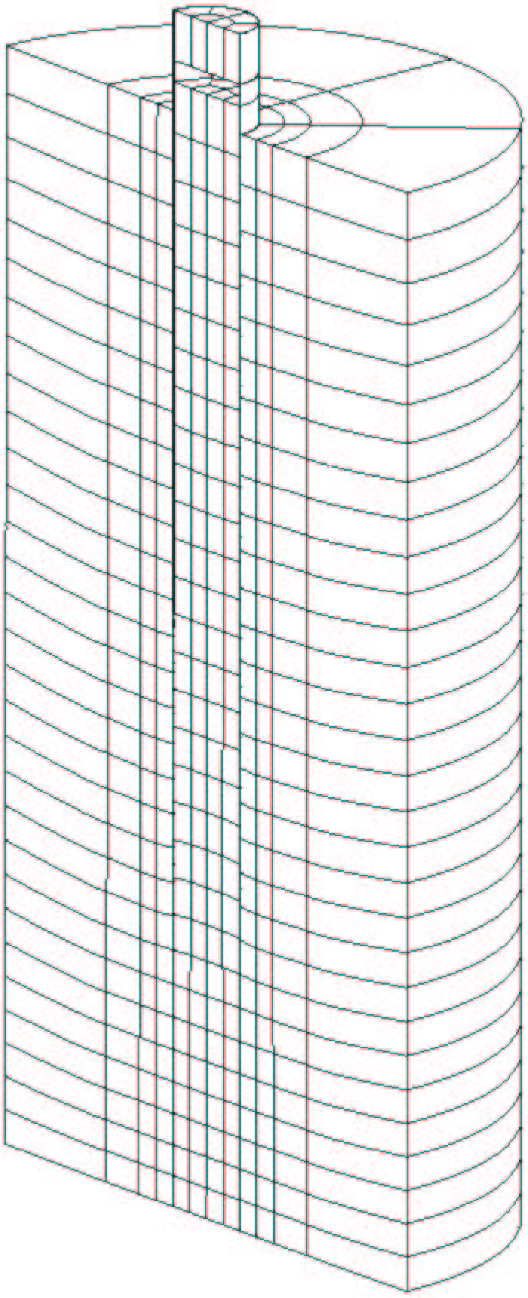

Figure 8.71: Caisson-soil 3D mesh at the end of 48-hour setup following suction installation.

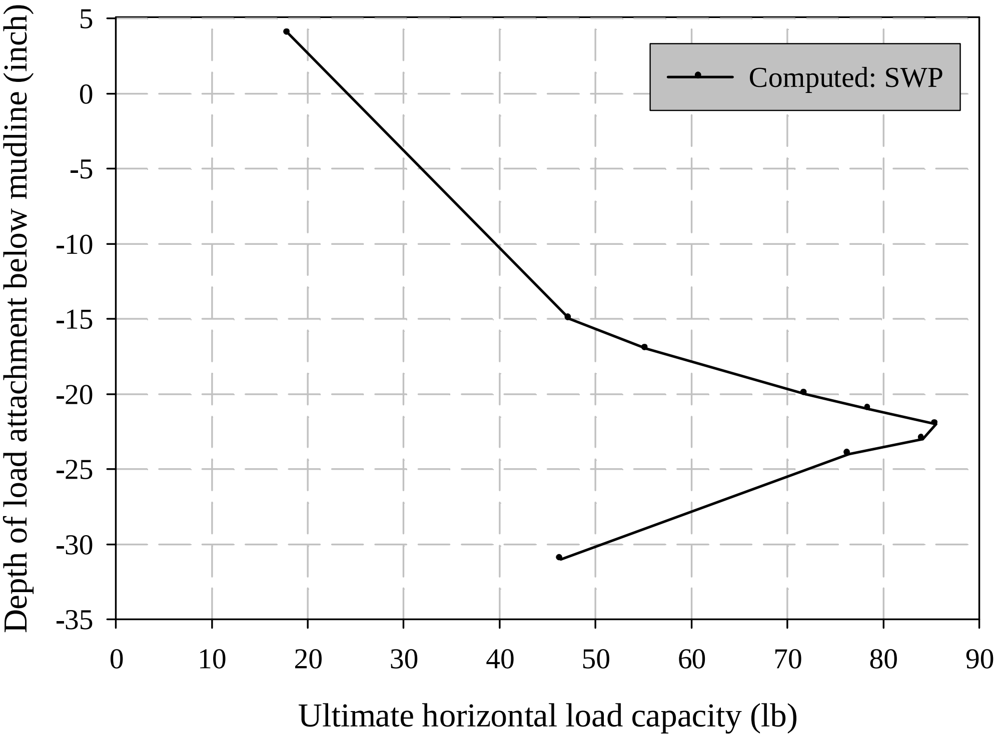

Figure 8.72: Ultimate horizontal load capacity of caisson installed by self-weight.

The horizontal load as a function of horizontal displacement of the pad-eye located at 10 inch above the caisson tip is presented in Fig. 8.73. The ultimate horizontal load capacity of about 85.5 lb was achieved at about 1 inch of lateral pad-eye movement. In Test 100603, the corrected measured horizontal load of 73.9 lb was achieved at about 0.5 inch lateral pad-eye movement (Coffman, 2003). The distribution of excess pore-water pressure in the soil domain at ultimate horizontal load for pad-eye located at 10 inch from the caisson tip is shown in Fig. 8.74. Excess pore-water pressure developed within the soil in the vicinity of caisson front. Suction developed in the back of the caisson.

The distribution of effective radial stress in the soil domain at ultimate horizontal load for pad-eye located at 10 inch from the caisson tip is shown in Fig. 8.75. It is worth mentioning that the effective radial stresses within the soil in the back of the caisson are greatly reduced due to development of suction but remain compressive.

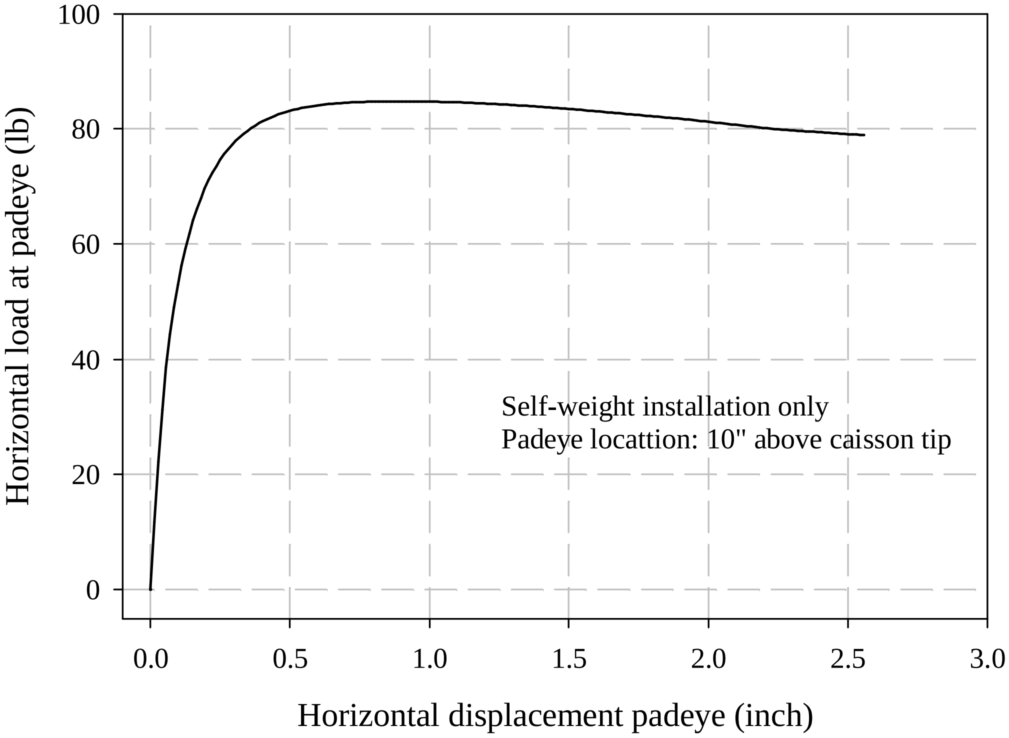

Figure 8.73: Load-displacement curve for caisson installed by self-weight and subjected to horizontal load at 10 inch above caisson tip.

Caisson Installed by Self-Weight and Suction

The computed ultimate horizontal capacity of caisson installed by self-weight and suction and subjected to horizontal load at different pad-eye locations is presented in Fig. 8.76. Also shown in the figure is the ultimate horizontal capacity measured by Coffman (2003) for caisson installed by suction. Pad-eye load was measured with a load cell connected to the load cable above the water line and was corrected for frictional losses in the buried pulley on the basis of calibration tests (Coffman, 2003 and 2004). About 10 to 20% of the measured load was lost to pulley friction (Coffman, 2004). Due to significant uncertainty in the magnitude of pulley friction, an error band for the corrected capacity reported by Coffman (2004) is also shown in Fig. 8.76. The match between (corrected) measured and computed horizontal load capacity of caisson is excellent. Maximum computed ultimate horizontal capacity of caisson was achieved for pad-eye located at 10 inch above the caisson tip.

The horizontal load as a function of the horizontal displacement of the pad-eye located at 10 inch above the caisson tip is presented in Fig. 8.77. The ultimate horizontal load capacity of about 81.9 lb was achieved at about 0.9 inch of lateral pad-eye movement. In the Test 100603, the corrected measured horizontal load of 73.9 lb was achieved at about 0.5 inch lateral pad-eye movement (Coffman, 2003). The distribution of excess pore-water pressure in the soil domain at ultimate horizontal load for pad-eye located at 10 inch from the caisson tip is shown in Fig. 8.78. Excess pore-water pressure developed within the soil in the vicinity of caisson front. Suction developed in the back of the caisson.

The distribution of effective radial stress in the soil domain at ultimate horizontal load for pad-eye located at 10 inch from the caisson tip is shown in Fig. 8.79. It is worth mentioning that the effective radial stresses within the soil in the back of the caisson are greatly reduced due to development of suction but remain compressive.

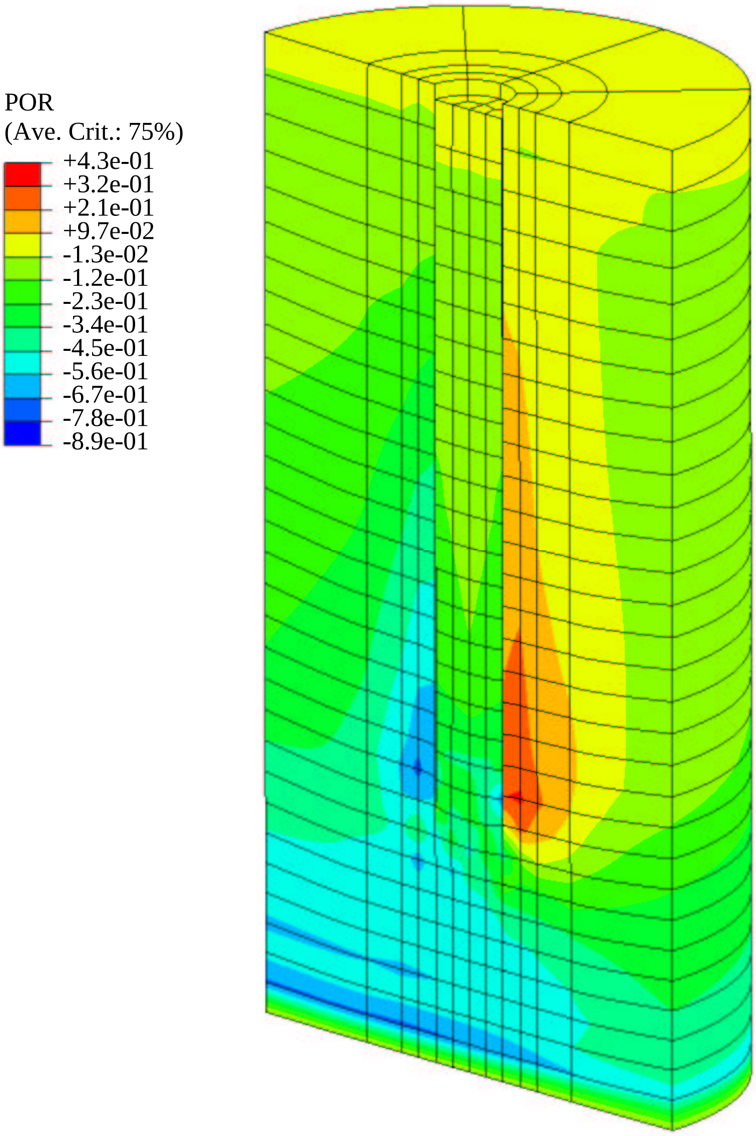

Figure 8.74: Distribution of excess pore-water pressure at ultimate horizontal load acting at 10 inch above tip of the caisson installed by self-weight [−ve value indicates suction (ABAQUS sign convention for excess pore-water pressure)].

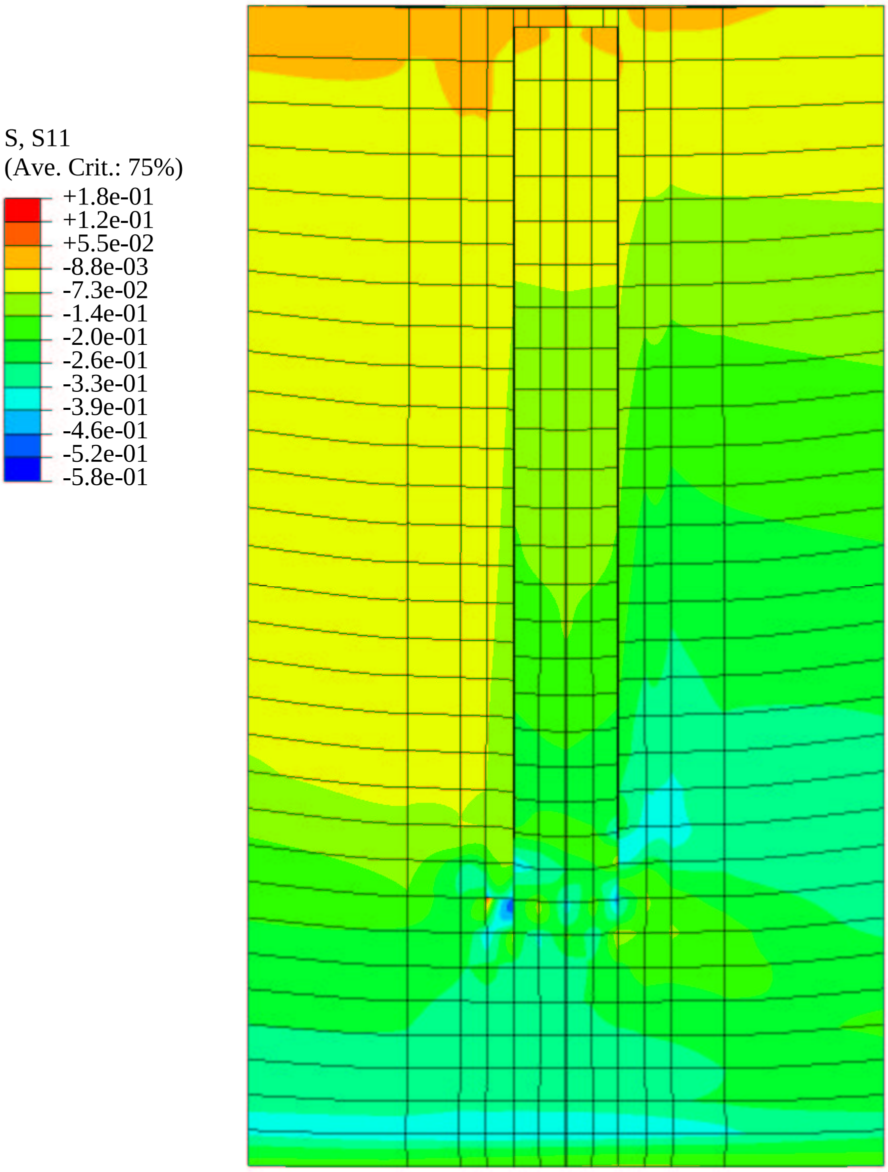

Figure 8.75: Distribution of effective radial stress at ultimate horizontal load acting at 10 inch above tip of the caisson installed by self-weight (−ve value indicates compressive stress).

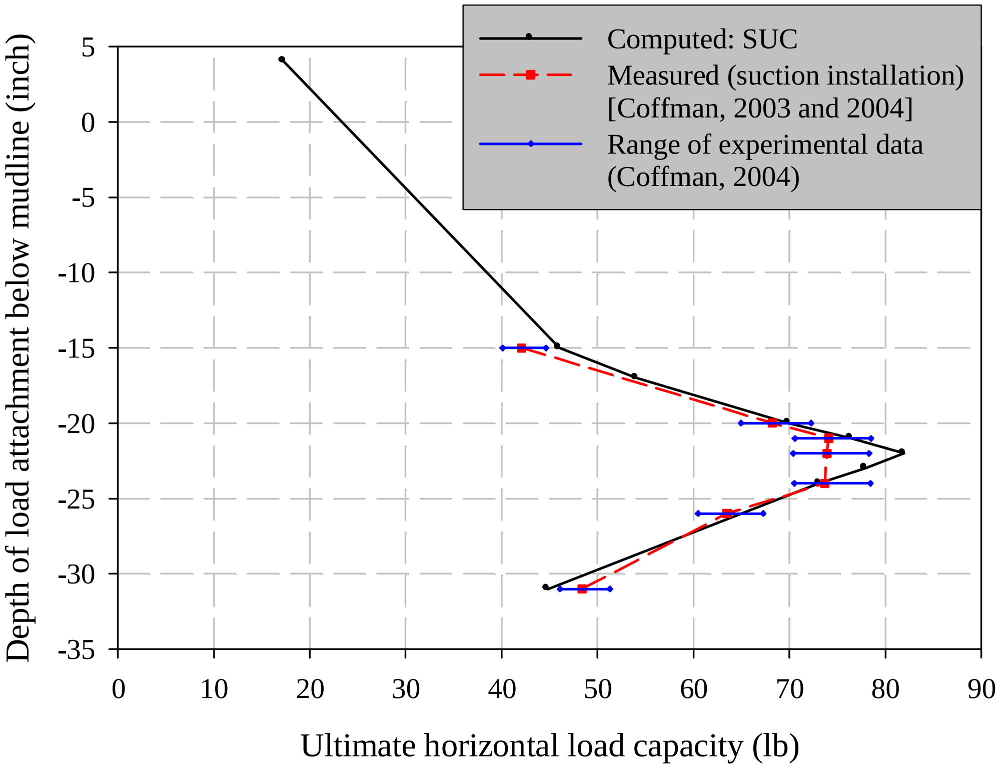

Figure 8.76: Ultimate horizontal load capacity of caisson installed by self-weight and suction.

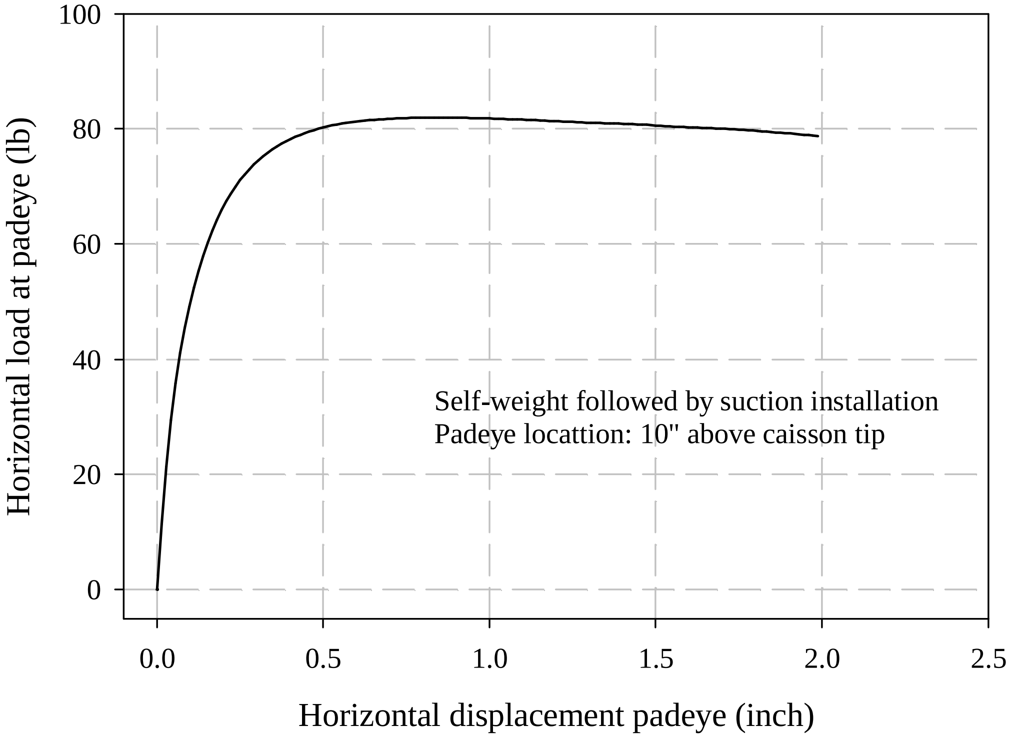

Figure 8.77: Load-displacement curve for caisson installed by suction and subjected to horizontal load at 10 inch above caisson tip.

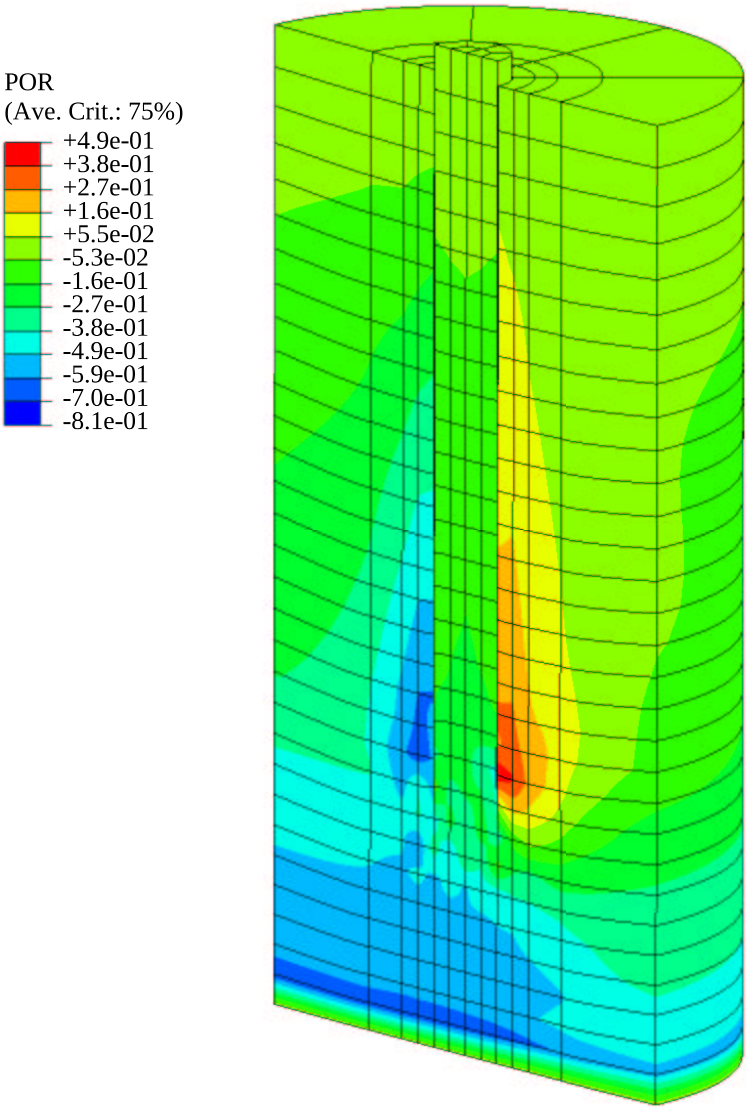

Figure 8.78: Distribution of excess pore-water pressure at ultimate horizontal load acting at 10 inch above tip of the caisson installed by suction [−ve value indicates suction (ABAQUS sign convention for excess pore-water pressure)].

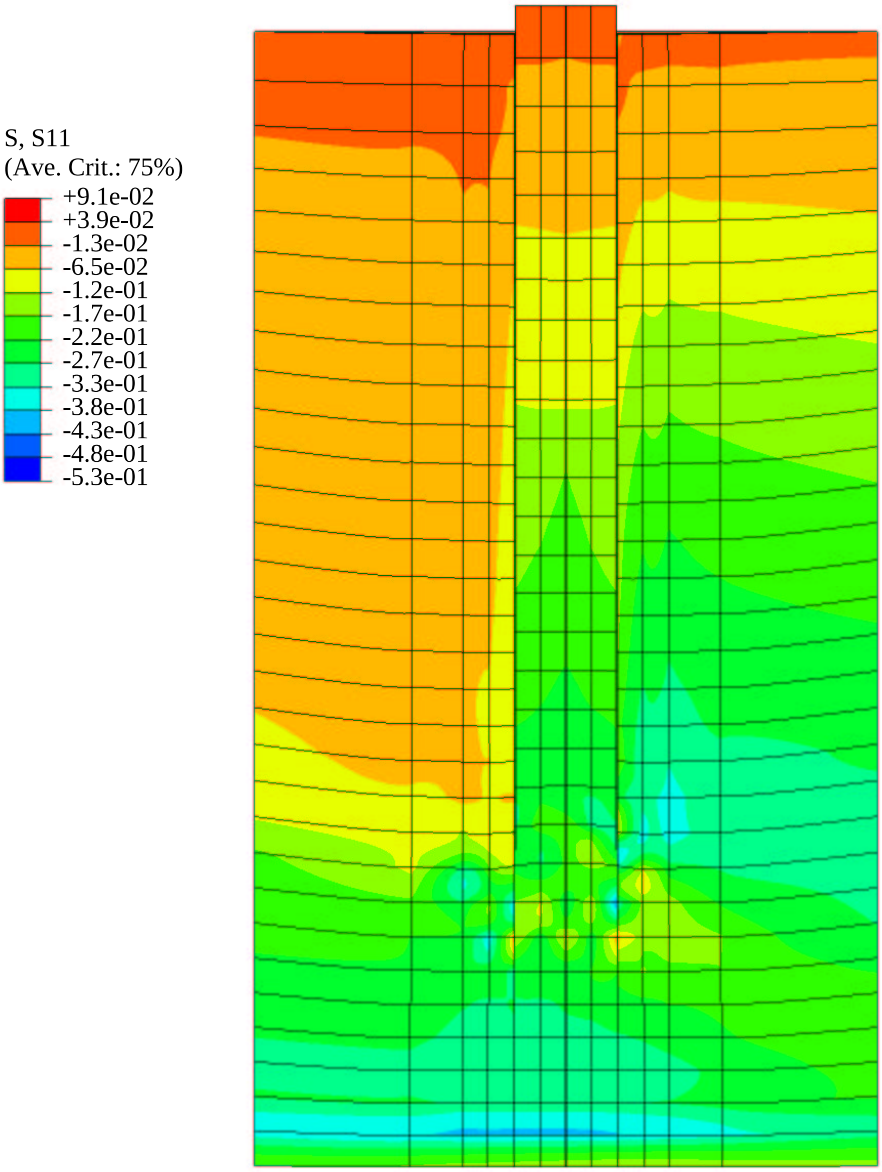

Figure 8.79: Distribution of effective radial stresses at ultimate horizontal load acting at 10 inch above tip of the caisson installed by suction ($-$ve value indicates compressive stresses).

Comparison of Computed Horizontal Capacities

A comparison of horizontal capacities computed for caisson installed by self-weight alone and by self-weight followed by suction is presented in Fig. 8.80. Computed capacities for caisson installed by suction were found to be smaller than computed capacities for caisson installed by self-weight alone.

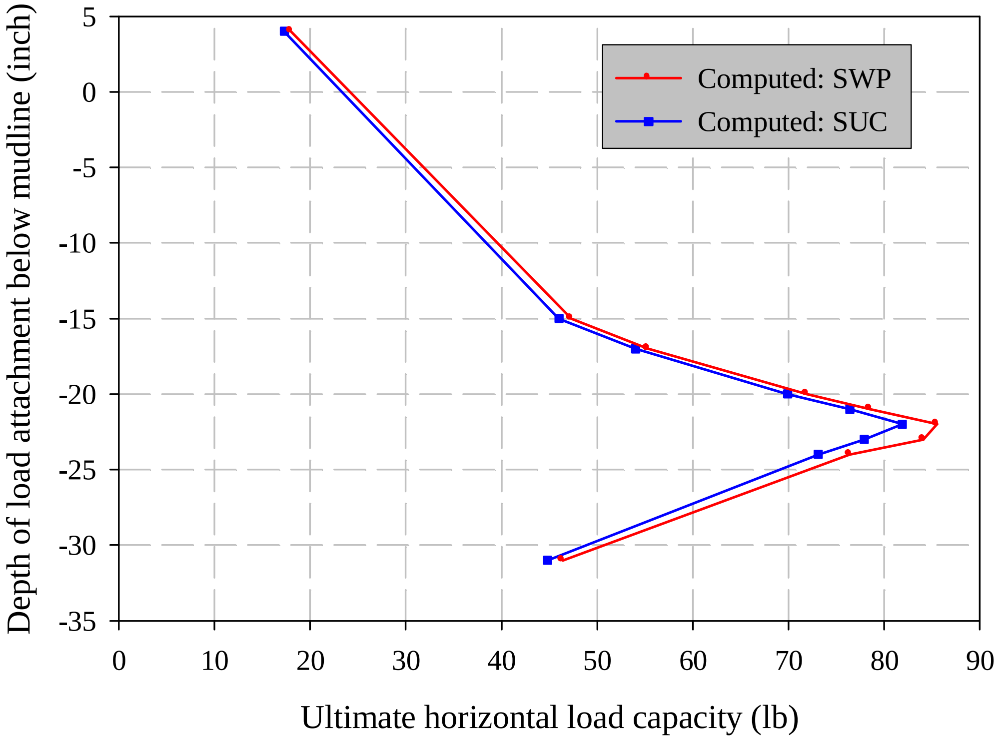

Figure 8.80: Comparison of computed horizontal capacities.

As noted earlier, the bounding-surface size in the vicinity of the caisson at the end of setup after self-weight installation (see Fig. 8.47) was found to be larger than the size at the end of setup after suction installation [see

Fig. 8.52(b)]. This comparison indicates lower soil strength in the vicinity of the caisson installed by suction. The computed horizontal capacities of the caissons are consistent with this observation.

8.9.3 Interaction Diagram

Simulations of caisson subjected to inclined load at 10 inch above the caisson tip were performed for the caisson installed by self-weight only and self-weight followed by suction. Angles of load inclination investigated are 0, 15, $22\frac{1}{2}$, 30, 45, 60, and 90 degree. Computed inclined load capacities are shown in Table 8.6.

Table 8.6: Caisson inclined load capacity

Load inclination (degree)	**Computed capacity** for **SWP**† **(Horizontal, Vertical)** (lb)	**Computed capacity** for **SUC**‡ **(Horizontal, Vertical)** (lb)
0	85.5, 0.0	81.9, 0.0
15	72.1, 20.4	69.4, 19.4
$22\frac{1}{2}$	59.5, 26.1	56.9, 24.7
30	45.0, 28.7	42.6, 26.8
45	26.1, 29.8	24.4, 27.6
60	15.1, 30.0	14.0, 27.7
90	0.1, 30.1	0.1, 27.8

† Caisson installed by self-weight only.
‡ Caisson installed by self-weight and suction.

From the simulations, the interaction diagram between ultimate horizontal and vertical loads was obtained. While the horizontal and vertical loads reach their maximum values at different level of displacement, the ultimate horizontal and vertical loads are identified as the ones for which the second-order work becomes zero. The interaction diagrams obtained for the caissons installed by self-weight and self-weight followed by suction are presented in Fig. 8.81. The capacity of the caisson subjected to inclined load and installed by application of suction is smaller by about 4% than that of the caisson installed by self-weight only. Reduction in the inclined load capacity for the caisson installed by suction is consistent with the reduced soil strength in the vicinity of the caisson due to application of suction. Effect of caisson rotation on the load angle at ultimate state can be noticed in Fig. 8.81 (see, for example, dotted line at 45°).

For load angles up to 15°, caisson moves almost horizontally, and for load angle greater than 30° caisson moves almost vertically. Transition from horizontal movement to vertical movement occurs for load angles between 20° to 25°.

8.9.4 Summary of Inclined Load Simulation Results

Maximum ultimate horizontal capacity, for caisson installed by self-weight alone and self-weight followed by suction, was achieved for the pad-eye located at 10 inch above the caisson tip. Recalling that the caisson was installed to 32 inch, the “optimum location” of the pad-eye for horizontal load was found to be at about two thirds of the embedded depth. The match between (corrected) measured (Coffman, 2003) and computed horizontal capacities is excellent.

For all the pad-eye locations, except for the pad-eye located at 1.0 inch from the caisson tip, the ultimate horizontal capacity was lower (see Table 8.5)

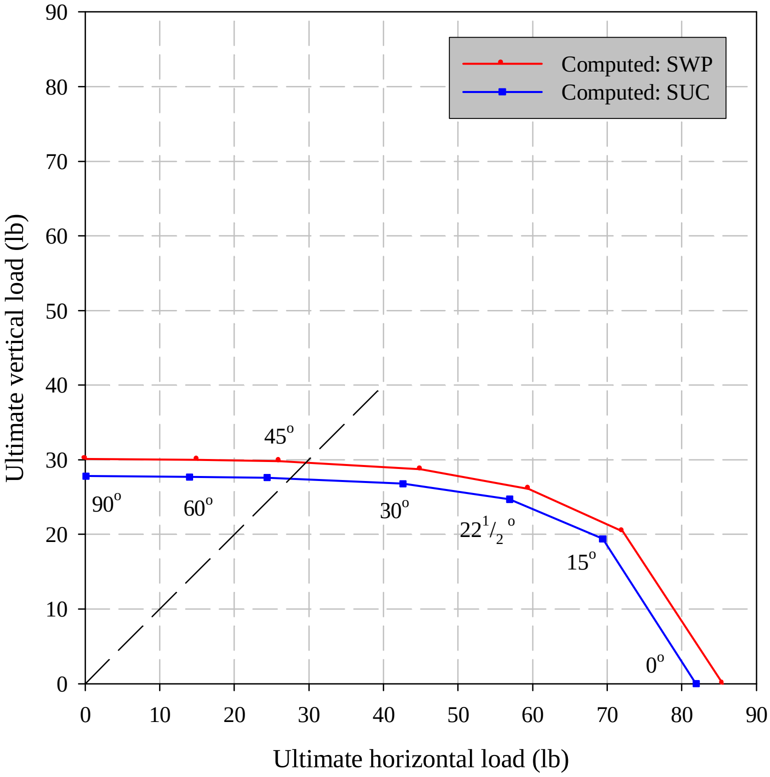

Figure 8.81: Ultimate horizontal and vertical loads interaction diagram for caisson subjected to inclined load at 10 inch above caisson tip.

for the caisson installed by suction then for the caisson installed by self-weight only. The computed interaction diagram for pad-eye located at 10 inch from tip of caisson installed by suction was completely contained by the diagram computed for caisson installed by self-weight alone and pad-eye located at 10 inch from the tip (see Fig. 8.81).

8.10 Summary

In this chapter, the computational procedure developed in the previous chapters was employed in the analysis of model suction caissons installed and tested at the Offshore Technology Research Center (OTRC) of The University of Texas at Austin. The computational results along with comparisons with the experimental observations were presented. Test-bed preparation, caisson installation, soil reconsolidation or setup following installation, and caissons subjected to axial pullout and inclined load were analyzed and studied. For each of the simulations, computed results were observed to be in good agreement with the measured data.

Chapter 9

SUMMARY AND CONCLUSIONS

9.1 Review of Project Scope and Objectives

This dissertation has documented a research study investigating the behavior of suction caissons installed in normally consolidated clayey soil and subjected to axial and inclined loads. Specifically, the research study has been focused on the development of a computational procedure for the analysis of suction caissons subjected to various loading and drainage conditions.

Suction caissons are hollow cylinders capped at the top. In deep-water applications, the caissons are lowered to the seafloor and allowed to penetrate the bottom sediments under self-weight, then pushed to the required depth via differential (suction) pressure applied by pumping water out of the caisson interior. Use of suction caissons as foundations for deep-water offshore structures and anchors for mooring lines has been increasing in the last decade.

Suction caissons are an attractive option with regard to providing anchorage for floating structures in deep-water as they offer a number of advantages in that environment.

In contrast to driven piles, the offshore industry has not reached consensus on design guidelines for suction caissons as several issues and uncertainties related to capacity estimation and failure mechanisms are still not resolved. Several attempts have been made in the past toward understanding caisson behavior from field tests, laboratory tests, and numerical simulations.

This study is part of a comprehensive research project on improving current understanding and developing effective design procedures for deep-water anchors. The objectives of this study are: (1) to develop a computational framework to simulate behavior of suction caissons and to estimate their capacities under axial as well as inclined loads, including effects of both self-weight and suction installations; and (2) to calibrate and validate the computational procedure by comparing computed caisson behavior with the measured behavior during laboratory tests conducted on model suction caissons at The University of Texas at Austin (Luke, 2002; and Coffman, 2003).

9.2 Summary of Major Project Tasks and Findings

In order to study behavior of suction caissons subjected to various loading and drainage conditions, a finite-element computational framework was developed. In addition, to validate and calibrate the procedure, simulations of laboratory caisson model tests performed at the Offshore Technology Research Center of

The University of Texas at Austin, were carried out. In the following paragraphs, the major tasks related to the development of the procedure and the computed results are summarized.

9.2.1 Modeling of Saturated Soil and Caisson

The behavior of the saturated, porous, clayey soil was described using a mixture theory accounting for coupling between the soil deformation and the pore-water flow. Saturated soil was thus modeled as a two-phase medium composed of soil and pore-water phases. The governing differential equations of the medium were expressed in terms of solid displacements, Darcy's velocities and excess pore-water pressure.

Axisymmetric discretization of the soil medium was accomplished with eight-node, quadratic, isoparametric, underintegrated finite-elements for solid displacements and Darcy's velocities. Continuous discretization of excess pore-water pressure was applied using four-node bilinear finite-elements. The caisson was represented using conventional, axisymmetric, eight-node solid finite-elements for displacements.

9.2.2 Modeling of Soil Constitutive Behavior

The nonlinear behavior of the clayey soil was modeled through a bounding-surface plasticity model for isotropic cohesive soils. The model is based on the concepts and principles of critical state soil mechanics. The bounding-surface is a reliable and versatile concept for representation of clay behavior along arbitrary stress and strain paths. The constitutive model provided the relationship between soil effective stress and strain increments.

9.2.3 Modeling of Soil-Caisson Interfaces

The interior and exterior soil-caisson interfaces were modeled with a contact algorithm based on a slide-line formulation allowing for large relative displacements between the caisson and the soil. The slide-line formulation involved nodes on the soil side of the interface and surface elements on the caisson side.

In the contact algorithm, penetration of soil nodes into the caisson was prevented by means of constraints imposed on the solid displacement using Lagrange multipliers. In addition, continuity of Darcy's velocity and excess pore-water pressure were enforced using Lagrange multipliers. Friction between the soil and the caisson was assumed to obey the classical Coulomb law. Stick and slip conditions were distinguished according to the level of interface frictional force in comparison with the Coulomb force, which was taken equal to the effective compressive (normal) force multiplied by the soil-caisson interface friction coefficient. Therefore, for a slave node in contact with a surface element, contact contributions arising from constraining solid displacement, Darcy's velocity, and excess pore-water pressure and contribution from the frictional interface were added to the tangent stiffness matrix and the residual vector during Newton iterations.

9.2.4 Remeshing Scheme

A remeshing tool was developed to eliminate the need for *a priori* specification of the caisson penetration path. As installation of the caisson progresses, the finite-element mesh was adjusted so that the line of nodes below the tip remained straight in the axial direction. By performing this adjustment, it was possible to eliminate over- or under-confinement of the soil in the caisson interior, and also permitted calculation of the path of penetration in the soil domain.

Mapping of field variables from the current finite-element mesh to the adjusted one was carried out using least-squares estimation, also referred to as global smoothening procedure, applied over the selected set of finite-elements below the caisson tip and along the soil-soil interface.

9.2.5 Three-Dimensional Analysis

Three-dimensional problems arising for caissons subjected to inclined loads were analyzed using ABAQUS, a commercially available finite-element program. The deformed geometry, and field as well as state variables obtained from the caisson installation analysis, performed using the developed computational procedure, were specified as initial geometry and conditions for the three-dimensional analysis.

The FORTRAN routine for the bounding-surface plasticity model was supplied to ABAQUS using `UMAT` user-defined subroutine. The 3-D model of the caisson-soil system was generated from the final locations of the nodes obtained from axisymmetric installation analysis followed by setup. Initial conditions such as stresses, history dependent variables for the soil, and excess pore-water pressure were specified using `SIGINI`, `SDVINI`, and `UPOREP` user-defined subroutines, respectively. Complete "tied" contact between soil and caisson was specified assuming negligible relative slip between the two under inclined loads.

9.2.6 Simulation Procedure

Computations were carried out in a sequence that closely follows laboratory model tests. The sequence of steps was: a) preparation of the soil test-bed starting with the original slurry; b) installation of the caisson by self-weight and suction; c) reconsolidation or setup of the soil; and d) application of axial or inclined load on the caisson under either drained or undrained conditions. For the first step, the initial state of the soil domain was obtained from the experimental data. For each of the remaining steps, the initial state of the soil domain was obtained from end of the previous step.

9.2.7 Simulation Results

Simulations were performed on model caissons in the sequence outlined in the preceding section. The computed behavior of the caisson was compared with the observed behavior from laboratory tests conducted at Offshore Technology Research Center on model caissons and reported by Luke (2002) and Coffman (2003). In the following sections, findings from each simulation are presented along with comparison with test data.

Test-Bed Preparation

Simulation of slurry consolidation was performed to obtain a normally consolidated test-bed. One-dimensional as well as three-dimensional axisymmetric consolidation simulations were carried out with three alternative void-ratio–pressure relationships. The axisymmetric consolidation simulation was devised to take into account effects of the tank wall on the consolidation process and final state of the slurry. The test-bed obtained from axisymmetric consolidation analysis with a constant value of virgin slope (3D-CON) was considered further for simulation of caisson installation. The slurry settlement curve obtained from the 3D-CON simulation was found to agree well with measured slurry settlement curve reported by Pedersen (2001). In addition, undisturbed undrained shear strength profiles, at the center of the tank and near the tank wall, computed for the simulated test-bed matched the measured shear strength profiles reported by Coffman (2003).

Caisson Installation

Installation simulations were carried out for caissons installed by self-weight alone and self-weight followed by suction. The normally consolidated test-bed obtained from 3D-CON analysis was taken as the initial soil condition with 36 inch long model caisson having 4 inch diameter.

- **Caisson installed by self-weight alone:** For the caisson installed by self-weight alone, the installation depth of 32 inch was achieved in about 200 seconds with a constant rate of penetration. The computed behavior of caisson during self-weight installation was compared with the measured behavior during laboratory test 1-040802 reported by Luke (2002).

  The remeshing algorithm developed to determine the caisson penetration path showed that soil from interior of caisson moved towards the exterior during self-weight installation. The soil plug moved down by about 0.64 inch with caisson insertion. Due to outward soil movement, effective radial stresses within the soil plug were computed to be smaller than the stresses computed near caisson exterior. Consequently, the computed frictional force along the interior interface was smaller than the force along the exterior interface. Due to caisson insertion, reductions in effective vertical stress within the soil plug as well as near the exterior of caisson were noted. The computed excess pore-water pressure towards caisson interior was higher than the pressure computed near caisson exterior.

Computed and measured excess pore-water pressures at five sensor locations were compared. Maximum discrepancy between computed and measure pressures was found for the sensors (I3, and O2) located near caisson tip. For other sensors (I2, I1, and O1) the match between computed and measured pressures was good.

- **Caisson installed by self-weight followed by suction:** For the caisson installed by self-weight followed by suction, initial self-weight installation to 16 inch was achieved in about 69 seconds, and additional penetration of 16 inch was achieved in about 420 seconds with application of suction. The computed behavior of the caisson during self-weight and suction installations was compared with measured behavior during laboratory Test 100603 reported by Coffman (2003).

  The remeshing algorithm developed to determine the caisson penetration path showed that soil from interior of caisson moved towards exterior during initial self-weight installation, and soil moved from the exterior towards the interior during suction installation. The soil plug moved upwards by about 1.14 inch at the end of suction installation. Effective radial stresses within the soil plug were found to be higher than those near the exterior of the caisson. The computed frictional forces along exterior and interior interfaces were about the same. Reduction in effective vertical stress was calculated during self-weight as well as suction caisson installations. The computed excess pore-water pressure within the soil plug was higher than the pressure computed near the caisson exterior during the initial self-weight installation phase.

The computed and measured excess pore-water pressures at five sensor locations were compared. The match between computed and measured pressure at all sensor locations during initial self-weight installation phase was very good. Excess pore-water pressures computed along the interior interface (at sensors I3, I2, and I1) during suction installation were in excellent agreement with the measured pressure. Excess pore-water pressure along the exterior interface (at sensors O1, and O2) during suction installation remained negative (compressive) while suction (positive pressure) was measured at these sensors.

Overall a good match between computed and measured behavior of caisson during installation phases was found.

Reconsolidation or Setup

Two days of reconsolidation or setup simulation of soil after caisson installation was performed. During the setup time of two days, the excess pore-water pressures generated within the soil due to caisson insertion were allowed to dissipate. The computed rates of excess pore-water pressure dissipation for caisson installed by self-weight alone and self-weight followed by suction were compared with the measured rates from Tests 1-040802 (Luke, 2002) and 100603 (Coffman, 2003), respectively.

Although computed and measured dissipation rates were found to be in good agreement, it became evident that complete dissipation of excess pore-water pressure was not achieved after two days of setup. In addition, movement of caisson did not cease after the two-days period. Therefore, it is recommended that additional reconsolidation simulations be carried out to compute setup time for complete dissipation of excess pore-water pressure.

Axial Pullout Capacity

Caisson axial pullout simulations were performed following soil reconsolidation. The caisson was axially pulled out rapidly or slowly with the top vented or closed. Comparisons of computed axial capacities and the capacities reported by Luke (2002) showed good agreement. The axial capacity computed for the caisson installed by suction was found to be smaller than the capacity computed for the caisson installed by self-weight alone.

For the caisson axially pulled with vented top, the frictional force along caisson-soil interfaces contributed about 90% of the resistance. On the other hand, for caisson installed by self-weight alone and axially pulled with closed top, about 42% of the resistance was obtained from suction generated below the cap, and additional 42% of resistance was obtained from the frictional force along the exterior interface. For the caisson installed by suction and axially pulled with closed top, about 44% of the resistance was obtained from suction generated below the cap, additional 32% of resistance was obtained from the frictional force along the exterior interface.

Inclined Load Capacity

The deformed configuration and state of soil obtained at the end of reconsolidation simulation were used in generating a three-dimensional mesh and the initial conditions for ABAQUS input to perform simulations of caissons subjected to inclined loads.

The ultimate horizontal load capacity was computed for several pad-eye locations, and compared with measured and corrected values reported by Coffman (2003). Excellent agreement was found between measured and computed capacities. For the caisson installed by self-weight alone as well as self-weight followed by suction, the maximum ultimate horizontal capacity was obtained with the pad-eye located at 10 inch from caisson tip, i.e., at about two thirds of the embedded depth of the caisson. The computed horizontal capacity for caisson installed by suction was found to be smaller than the capacity computed for caisson installed by self-weight alone.

Interaction diagrams for ultimate horizontal and vertical loads were obtained for the caissons installed by self-weight alone and self-weight followed by suction, and pad-eye located at “optimum point” (at 10 inch from caisson tip). The computed inclined load capacity for the caisson installed by suction was found to be smaller than the capacity for the caisson installed by self-weight alone.

9.3 Recommendations for Future Study

This numerical study has suggested a number of possibilities for future research and improvements to the computational procedure:

- **Bounding-Surface Plasticity Model Parameters:** There is need for performing additional, preferably triaxial, tests for improved calibration of bounding-surface plasticity model.

- **Coefficient of Friction:** Higher value of coefficient of friction at lower normal interfacial pressure was observed during experiments (Pedersen, *et al.*, 2003). Therefore, there is a need for improving the contact formulation to allow the coefficient of friction to be a function of normal interfacial pressure.

  Reduction in friction coefficient during suction installation can be expected due to increase in radial stress within lower half of soil plug. Simulation of caisson installation by suction was carried out with a constant coefficient of friction. The measured soil resistance during suction installation was smaller than the computed resistance. This suggests that decrease in friction coefficient during suction installation is an important phenomenon and can be incorporated within the frictional contact algorithm by considering the friction coefficient as a function of effective normal pressure.

  Caisson installation as well as axial pullout simulations were carried out adopting a constant friction coefficient. Computed axial pullout capacity was lower than measured axial pullout capacity. If evidence of change in coefficient of friction during setup becomes available then axial pullout simulations should be repeated adopting the updated friction coefficient.

  The friction coefficient along caisson-soil interface is an important factor governing behavior of caisson during installation as underload. A detailed analytical study will provide insight into the effects of coefficient of friction on caisson behavior.

- **Assumed State of Stress:** Axial as well as inclined loading simulations with assumed state of stress should be carried out in order to fully understand the effects of caisson installation process.

- **Relative Slip under Inclined Loads:** For analysis of caissons subjected to inclined loads, slip along the caisson-soil interfaces was not allowed. Slip along the interface is expected to occur and may have some effect on caisson capacity. In order to investigate any effect of slip along the interface, it is necessary to carry out additional simulations in which slip along the interface is allowed to occur.

- **Three-Dimensional Implementation:** An axisymmetric implementation of the computational procedure was employed in the present study. A three-dimensional implementation of the procedure with comparable capabilities is highly desirable.

- **Capacity under Time-Varying Loads:** Additional simulations of caissons subjected to complex time-varying loads should be carried out in order to fully characterize the pullout behavior.

- **Misalignment of Inclined Load:** Inclined loads are generally not aligned along an azimuthal plane. In such cases, it is necessary to model the complete geometry of caisson-soil system, a computationally demanding yet important effort.

- **Setup Time for Suction Installed Caissons:** Computed dissipation of excess pore-water pressure for caisson installed by self-weight alone and self-weight followed by suction showed that pressure was not dissipated completely after two days of setup time. It is necessary to carry out additional setup simulations to compute the time required for complete dissipation of excess pore-water pressure, and study the effect of longer setup time on the capacity.

- **Suction Induced Capacity Reduction:** It was speculated by Coffman (2003) that caisson capacity was reduced by the application of suction during installation. The computed results presented in Chapter 8 also show smaller capacity, under axial as well as inclined loads, for caissons installed by suction. The difference between computed capacities for caisson installed by self-weight alone and self-weight followed by suction turned out to be rather small. Further studies, experimental and computational, of this issue are appropriate.

- **Shape of Caisson Tip:** The amount and direction of displaced soil during installation can be controlled by the shape of the caisson tip. Therefore, it may be beneficial to study the effect of shape of the caisson tip in order to optimize the overall performance.

- **Caisson Stiffeners:** Stiffeners, both circumferential and vertical, provided in the caisson interior for stability during installation may have some influence on caisson capacity. To quantify such effects on the capacity it is necessary to perform additional experiments and simulations of caissons with stiffeners.

- **Domain Truncation:** The soil domain selected for simulations was truncated at a radial distance of 12 inch from center of the caisson.

The selected size of truncated domain is based on the laboratory test on model caisson installed at 12 inch away from the tank wall. This boundary may have an effect on computed behavior of the caisson. To eliminate any influence of truncated soil domain on the caisson capacity, additional simulations with a greater soil domain should be performed.

- **Coefficient of Permeability:** The simulations were carried out with a constant coefficient of permeability of the slurry. However, coefficient of permeability is generally found to be a function of void ratio as presented by Mesri and Olson (1971) and Pedersen (2001). It is therefore necessary to perform additional simulations with variable permeability coefficient to study its effect on behavior of the caisson and setup time.

  In the development of governing equations for soil, permeability tensor was assumed to be isotropic. Anisotropy of permeability tensor can be included into the formulation easily to study its effect on caisson behavior.

- **Comparison with Limit Plasticity Solution:** A limit plasticity solution has been developed by Aubeny *et al.* (2003a and 2003b) for predicting capacity of caisson subjected to inclined loads. The procedure can be refined or improved by comparison with the finite-element simulation results presented in Chapter 8.

- **Calculation of α and N_c Values:** The factor α is ratio of caisson-soil shearing stress to undrained shearing strength of soil, and N_c is end bearing capacity factor. These two are most important factors in the development of simplified equations to calculate capacity of caisson subjected to various loading and drainage conditions. It would be helpful to design engineers if these factors are extracted from the computed capacities presented in Chapter 8.

9.4 Conclusions

The results of this numerical study have elucidated several aspects of caisson behavior under various loading and drainage conditions. A computational procedure has been developed, capable of simulating caisson installation process, by self-weight followed by suction, and subsequent removal under axial loads and failure under inclined loads. The results obtained from the simulations were compared with the measurements available from the model tests on caissons. Good agreement between computations and measurements points to the usefulness of the computational procedure as a tool in understanding caisson behavior and estimating load capacities.

Appendix A

Components of Tangent Stiffness and Residuals

A.1 Incremental Equation

For reference purposes the incremental equation (Eq. 3.11) is reproduced here as:

$$\begin{bmatrix} \mathbf{M}_{ss} & \mathbf{M}_{sr} & \mathbf{0} \\ \mathbf{M}_{rs} & \mathbf{M}_{rr} & \mathbf{0} \\ \mathbf{0} & \mathbf{0} & \mathbf{0} \end{bmatrix} \begin{Bmatrix} \Delta\ddot{\mathbf{U}}^s \\ \Delta\dot{\mathbf{V}}^r \\ \Delta\ddot{\bar{\mathbf{P}}}^w \end{Bmatrix} + \begin{bmatrix} \mathbf{C}_{ss} & \mathbf{C}_{sr} & \mathbf{0} \\ \mathbf{C}_{rs} & \mathbf{C}_{rr} & \mathbf{0} \\ \mathbf{C}_{ps} & \mathbf{C}_{pr} & \mathbf{C}_{pp} \end{bmatrix} \begin{Bmatrix} \Delta\dot{\mathbf{U}}^s \\ \Delta\mathbf{V}^r \\ \Delta\dot{\bar{\mathbf{P}}}^w \end{Bmatrix}$$
$$+ \begin{bmatrix} \mathbf{K}_\sigma + \mathbf{K}_{ss} & \mathbf{0} & \mathbf{K}_{sp} \\ \mathbf{K}_{rs} & \mathbf{0} & \mathbf{K}_{rp} \\ \mathbf{K}_{ps} & \mathbf{0} & \mathbf{K}_{pp} \end{bmatrix} \begin{Bmatrix} \Delta\mathbf{U}^s \\ \Delta\mathbf{U}^r \\ \Delta\bar{\mathbf{P}}^w \end{Bmatrix} = \begin{Bmatrix} \mathbf{R}^s \\ \mathbf{R}^r \\ \mathbf{R}^p \end{Bmatrix} \tag{A.1}$$

Expressions for the submatrices are provided in the following sections.

A.2 Residual Vectors

Conservation of Linear Momentum of the Mixture

$$\begin{aligned}
\mathbf{R}_s \;=\;& +\int_{\Gamma_\sigma} (\mathbf{N}_s)^T \mathbf{t}^{Total} da \\
& -\int_{\Omega_t} [grad(\delta\mathbf{u})]^T \boldsymbol{\sigma}^{eff} dv \\
& -\int_{\Omega_\tau} [div(\mathbf{N}_s)]^T \bar{p}^w J dV \\
& +\int_{\Omega_\tau} (\mathbf{N}_s)^T (\rho_s - \rho_w)(1-n_0)\mathbf{b} dV \\
& -\int_{\Omega_\tau} (\mathbf{N}_s)^T [\rho_s(1-n_0) + \rho_w n_w J]\mathbf{a}^s dV \\
& -\int_{\Omega_\tau} (\mathbf{N}_s)^T \rho_w J \mathbf{a}^r dV
\end{aligned} \tag{A.2}$$

The matrix representation of second term in Eq. A.2 is given in Appendix B.

Conservation of Linear Momentum of the Fluid Phase

$$\begin{aligned}
\mathbf{R}_r \;=\;& +\int_{\Gamma_w} (\mathbf{N}_r)^T \bar{\mathbf{t}}^p da \\
& -\int_{\Omega_\tau} [div(\mathbf{N}_r)]^T \bar{p}^w J dV \\
& -\int_{\Omega_\tau} (\mathbf{N}_r)^T \rho_w J \mathbf{a}^s dV \\
& -\int_{\Omega_\tau} (\mathbf{N}_r)^T \frac{\rho_w J}{n_w} \mathbf{a}^r dV \\
& -\int_{\Omega_\tau} (\mathbf{N}_r)^T \frac{\rho_w J}{n_w k} \mathbf{v}^r dV
\end{aligned} \tag{A.3}$$

Conservation of Mixture Mass

$$
\begin{aligned}
\mathbf{R}_p \;=\; & -\int_{\Gamma_q} (\mathbf{N}_p)^T q da \\
& +\int_{\Omega_\tau} [grad(\mathbf{N}_p)]^T \mathbf{v}^r J dV \\
& -\int_{\Omega_\tau} (\mathbf{N}_p)^T div(\mathbf{v}^s) J dV \\
& +\int_{\Omega_\tau} (\mathbf{N}_p)^T \frac{n_w J}{\lambda_w} \dot{\bar{p}}^w dV \\
& +\int_{\Omega_\tau} (\mathbf{N}_p)^T \frac{J}{\lambda_w} [grad(\bar{p}_w)]^T \mathbf{v}^r dV \\
& +\int_{\Omega_\tau} (\mathbf{N}_p)^T \frac{n_w \gamma_w J}{\lambda_w} \mathbf{1}_z^T \mathbf{v}^s dV \\
& +\int_{\Omega_\tau} (\mathbf{N}_p)^T \frac{\gamma_w J}{\lambda_w} \mathbf{1}_z^T \mathbf{v}^r dV
\end{aligned}
\tag{A.4}
$$

A.3 Equivalent Mass Matrices

$$
\mathbf{M}_{ss} = +\int_{\Omega_\tau} (\mathbf{N}_s)^T [\rho_s(1-n_0) + \rho_w n_w J] \mathbf{N}_s dV \tag{A.5}
$$

$$
\mathbf{M}_{sr} = +\int_{\Omega_\tau} (\mathbf{N}_s)^T \rho_w J \mathbf{N}_r dV \tag{A.6}
$$

$$
\mathbf{M}_{rs} = +\int_{\Omega_\tau} (\mathbf{N}_r)^T \rho_w J \mathbf{N}_s dV \tag{A.7}
$$

$$
\mathbf{M}_{rr} = +\int_{\Omega_\tau} (\mathbf{N}_r)^T \frac{\rho_w J}{n_w} \mathbf{N}_r dV \tag{A.8}
$$

A.4 Equivalent Damping Matrices

$$\begin{aligned}\mathbf{C}_{ss} &= +\int_{\Omega_\tau} (\mathbf{N}_s)^T \rho_w J grad(\mathbf{N}_s)\mathbf{v}^r dV \\ &\quad -\int_{\Omega_\tau} (\mathbf{N}_s)^T \rho_w \frac{(1-n_0)}{n_w}\mathbf{v}^r div(\mathbf{N}_s) dV \end{aligned} \tag{A.9}$$

$$\begin{aligned}\mathbf{C}_{sr} &= -\int_{\Omega_\tau} (\mathbf{N}_s)^T \rho_w \frac{(1-n_0)}{n_w} div(\mathbf{v}_s)\mathbf{N}_r dV \\ &\quad +\int_{\Omega_\tau} (\mathbf{N}_s)^T \frac{\rho_w J}{n_w} grad(\mathbf{N}_r)\mathbf{v}^r dV \\ &\quad +\int_{\Omega_\tau} (\mathbf{N}_s)^T \frac{\rho_w J}{n_w} grad(\mathbf{v}_r)\mathbf{N}_r dV \\ &\quad +\int_{\Omega_\tau} (\mathbf{N}_s)^T \rho_w J grad(\mathbf{v}_s)\mathbf{N}_r dV \end{aligned} \tag{A.10}$$

$$\begin{aligned}\mathbf{C}_{rs} &= -\int_{\Omega_\tau} (\mathbf{N}_r)^T \rho_w \frac{(1-n_0)}{(n_w)^2} div(\mathbf{N}_s)\mathbf{v}_r dV \\ &\quad +\int_{\Omega_\tau} (\mathbf{N}_r)^T \frac{\rho_w J}{n_w} grad(\mathbf{N}_s)\mathbf{v}^r dV \end{aligned} \tag{A.11}$$

$$\begin{aligned}\mathbf{C}_{rr} &= +\int_{\Omega_\tau} (\mathbf{N}_r)^T \frac{\rho_w J}{n_w k}\mathbf{N}_r dV \\ &\quad -\int_{\Omega_\tau} (\mathbf{N}_r)^T \frac{\rho_w (1-n_0) div(\mathbf{v}^s)}{(n_w)^2}\mathbf{N}_r dV \\ &\quad +\int_{\Omega_\tau} (\mathbf{N}_r)^T \frac{\rho_w J}{(n_w)^2} grad(\mathbf{N}_r)\mathbf{v}^s dV \\ &\quad +\int_{\Omega_\tau} (\mathbf{N}_r)^T \frac{\rho_w J}{(n_w)^2} grad(\mathbf{v}^r)\mathbf{N}_r dV \\ &\quad +\int_{\Omega_\tau} (\mathbf{N}_r)^T \frac{\rho_w J}{n_w} grad(\mathbf{v}^s)\mathbf{N}_r dV \end{aligned} \tag{A.12}$$

$$\begin{aligned}\mathbf{C}_{ps} &= +\int_{\Omega_\tau} (\mathbf{N}_p)^T J div(\mathbf{N}_s) dV \\ &\quad -\int_{\Omega_\tau} (\mathbf{N}_p)^T \frac{n_w \gamma_w J}{\lambda_w} \mathbf{1}_z^T \mathbf{N}_s dV \end{aligned} \tag{A.13}$$

$$\begin{aligned}\mathbf{C}_{pr} &= -\int_{\Omega_\tau} [grad(\mathbf{N}_p)]^T \mathbf{N}_r J dV \\ &\quad -\int_{\Omega_\tau} (\mathbf{N}_p)^T \frac{J}{\lambda_w} [grad(\bar{p}^w)]^T \mathbf{N}_r dV \\ &\quad -\int_{\Omega_\tau} (\mathbf{N}_p)^T \frac{\gamma_w J}{\lambda_w} \mathbf{1}_z^T \mathbf{N}_r dV \end{aligned} \tag{A.14}$$

$$\mathbf{C}_{pp} = -\int_{\Omega_\tau} (\mathbf{N}_p)^T \frac{n_w J}{\lambda_w} \mathbf{N}_p dV \tag{A.15}$$

A.5 Equivalent Stiffness Matrices

$$\mathbf{K}_\sigma = +\int_{\Omega_t} \mathbf{B}^T \mathbf{D}^{nl} \mathbf{B} dv \tag{A.16}$$

$$\begin{aligned}
\mathbf{K}_{ss} = &+\int_{\Omega_\tau} [div(\mathbf{N}_s)]^T \bar{p}^w \mathbf{N}_J dV \\
&+\int_{\Omega_\tau} (\mathbf{N}_s)^T \rho_w \mathbf{a}^s \mathbf{N}_J dV \\
&+\int_{\Omega_\tau} (\mathbf{N}_s)^T \rho_w \frac{\partial \mathbf{v}^r}{\partial t} \mathbf{N}_J dV \\
&+\int_{\Omega_\tau} (\mathbf{N}_s)^T \rho_w \frac{(1-n_w)^2}{(n_w)^2} div(\mathbf{v}^s) \mathbf{v}^r \mathbf{N}_J dV \\
&+\int_{\Omega_\tau} (\mathbf{N}_s)^T \rho_w \frac{2n_w - 1}{(n_w)^2} grad(\mathbf{v}^r) \mathbf{v}^r \mathbf{N}_J dV \\
&+\int_{\Omega_\tau} (\mathbf{N}_s)^T \rho_w grad(\mathbf{v}^s) \mathbf{v}^r \mathbf{N}_J dV \\
&-\int_{\Omega_\tau} \left\{ [grad(\mathbf{N}_s)]^T : grad(\mathbf{N}_s) + \frac{\mathbf{N}_s^T}{r} \frac{\mathbf{N}_s}{r} \right\} \bar{p}^w J dV \\
&+\int_{\Omega_\tau} (\mathbf{N}_s)^T \rho_w \frac{(1-n_0)}{n_w} \left\{ [grad(\mathbf{v}^s)]^T : grad(\mathbf{N}_s) + \frac{v^s[0]}{r} \frac{\mathbf{N}_s}{r} \right\} \mathbf{v}^r dV \\
&-\int_{\Omega_\tau} (\mathbf{N}_s)^T \frac{\rho_w J}{n_w} grad(\mathbf{v}^r) grad(\mathbf{N}_s) \mathbf{v}^r dV \\
&-\int_{\Omega_\tau} (\mathbf{N}_s)^T \rho_w J grad(\mathbf{v}^s) grad(\mathbf{N}_s) \mathbf{v}^r dV
\end{aligned} \tag{A.17}$$

$$\mathbf{K}_{sp} = +\int_{\Omega_\tau} [div(\mathbf{N}_s)]^T J \mathbf{N}_p dV \tag{A.18}$$

Derivation of Eq. A.16 is presented in Appendix B. In Eq. A.17, the matrix $\mathbf{N}_J$ relates the increment in the Jacobian, ΔJ, to the increment of the solid displacements $\Delta \mathbf{U}^s$, i.e., $\Delta J = \mathbf{N}_J \Delta \mathbf{U}^s$.

$$\begin{aligned}
\mathbf{K}_{rs} \;=\; & +\int_{\Omega_\tau} [div(\mathbf{N}_r)]^T \bar{p}^w \mathbf{N}_J dV \\
& +\int_{\Omega_\tau} (\mathbf{N}_r)^T \rho_w \mathbf{a}^s \mathbf{N}_J dV \\
& +\int_{\Omega_\tau} (\mathbf{N}_r)^T \frac{\rho_w}{k} \frac{(2n_w - 1)}{(n_w)^2} \mathbf{v}^r \mathbf{N}_J dV \\
& +\int_{\Omega_\tau} (\mathbf{N}_r)^T \rho_w \frac{(2n_w - 1)}{(n_w)^2} \frac{\partial \mathbf{v}^r}{\partial t} \mathbf{N}_J dV \\
& +\int_{\Omega_\tau} (\mathbf{N}_r)^T \frac{2\rho_w (1 - n_w)^2 div(\mathbf{v}^s)}{(n_w)^3} \mathbf{v}^r \mathbf{N}_J dV \\
& +\int_{\Omega_\tau} (\mathbf{N}_r)^T \rho_w \frac{(3n_w - 2)}{(n_w)^3} grad(\mathbf{v}^r) \mathbf{v}^r \mathbf{N}_J dV \\
& +\int_{\Omega_\tau} (\mathbf{N}_r)^T \rho_w \frac{(2n_w - 1)}{(n_w)^2} grad(\mathbf{v}^s) \mathbf{v}^r \mathbf{N}_J dV \\
& -\int_{\Omega_\tau} \left\{ [grad(\mathbf{N}_r)]^T : grad(\mathbf{N}_s) + \frac{\mathbf{N}_r^T}{r} \frac{\mathbf{N}_s}{r} \right\} \bar{p}^w J dV \\
& +\int_{\Omega_\tau} (\mathbf{N}_r)^T \frac{\rho_w (1 - n_0)}{(n_w)^2} \left\{ [grad(\mathbf{v}^s)]^T : grad(\mathbf{N}_s) + \frac{v^s[0]}{r} \frac{\mathbf{N}_s}{r} \right\} \\
& -\int_{\Omega_\tau} (\mathbf{N}_r)^T \frac{\rho_w J}{(n_w)^2} grad(\mathbf{v}^r) grad(\mathbf{N}_s) \mathbf{v}^r dV \\
& -\int_{\Omega_\tau} (\mathbf{N}_r)^T \frac{\rho_w J}{n_w} grad(\mathbf{v}^s) grad(\mathbf{N}_s) \mathbf{v}^r dV
\end{aligned} \tag{A.19}$$

$$\mathbf{K}_{rp} \;=\; +\int_{\Omega_\tau} [div(\mathbf{N}_r)]^T J \mathbf{N}_p dV \tag{A.20}$$

$$
\begin{aligned}
\mathbf{K}_{ps} \;=\; & -\int_{\Omega_\tau} [grad(\mathbf{N}_p)]^T \mathbf{v}^r \mathbf{N}_J dV \\
& + \int_{\Omega_\tau} (\mathbf{N}_p)^T div(\mathbf{v}^s) \mathbf{N}_J dV \\
& - \int_{\Omega_\tau} (\mathbf{N}_p)^T \frac{\dot{\bar{p}}^w}{\lambda_w} \mathbf{N}_J dV \\
& - \int_{\Omega_\tau} (\mathbf{N}_p)^T \frac{1}{\lambda_w} [grad(\bar{p}^w)]^T \mathbf{v}^r \mathbf{N}_J dV \\
& - \int_{\Omega_\tau} (\mathbf{N}_p)^T \frac{\gamma_w}{\lambda_w} \mathbf{1}_z^T \mathbf{v}^s \mathbf{N}_J dV \\
& - \int_{\Omega_\tau} (\mathbf{N}_p)^T \frac{\gamma_w}{\lambda_w} \mathbf{1}_z^T \mathbf{v}^r \mathbf{N}_J dV \\
& - \int_{\Omega_\tau} (\mathbf{N}_p)^T \left\{ [grad(\mathbf{v}^s)]^T : grad(\mathbf{N}_s) + \frac{v^s[0]}{r} \frac{\mathbf{N}_s}{r} \right\} J dV \\
& + \int_{\Omega_\tau} [grad(\mathbf{N}_p)]^T grad(\mathbf{N}_s) \mathbf{v}^r J dV \\
& + \int_{\Omega_\tau} (\mathbf{N}_p)^T \frac{J}{\lambda_w} [grad(\bar{p}^w)]^T grad(\mathbf{N}_s) \mathbf{v}^r dV
\end{aligned} \tag{A.21}
$$

$$
\mathbf{K}_{pp} \;=\; -\int_{\Omega_\tau} (\mathbf{N}_p)^T \frac{J}{\lambda_w} [grad(\mathbf{N}_p)]^T \mathbf{v}^r dV \tag{A.22}
$$

Appendix B

Large-Deformation Analysis

In this appendix, the contributions of virtual work related to stress in the solid phase appearing in the solid momentum balance equation is obtained. For Newton iterations contributions to both the tangent matrix and the residual vector are obtained following the approximation proposed by Nagtegaal (1982). This approximation leads to an updated Lagrangian formulation, in which the geometry and field variables are updated upon convergence in a step, and for the following step variables are referred to the updated configuration.

For reference purposes, the virtual work term related to (effective) stress ($\boldsymbol{\sigma}^{eff} \equiv \ \boldsymbol{\sigma}$) in solid is written again as:

$$-\int_{\Omega_t} \left[grad\left(\delta\mathbf{u}\right)\right]^T \boldsymbol{\sigma} dv \tag{B.1}$$

The Green-Lagrange strain tensor $\mathbf{E}$ is related to the displacements $\mathbf{u}$ as:

$$\mathbf{E} = \frac{1}{2}\Big\{grad\left(\mathbf{u}\right) + \left[grad\left(\mathbf{u}\right)\right]^T + \left[grad\left(\mathbf{u}\right)\right]^T \left[grad\left(\mathbf{u}\right)\right]\Big\} \tag{B.2}$$

The increment in the Green-Lagrange strain tensor $d\mathbf{E}$ is related to increment in the displacements $d\mathbf{u}$ as:

$$d\mathbf{E} = \frac{1}{2}\left\{grad\,(d\mathbf{u}) + [grad\,(d\mathbf{u})]^T + [grad\,(d\mathbf{u})]^T\,[grad\,(d\mathbf{u})]\right\} \tag{B.3}$$

The variation in the Green-Lagrange strain tensor $\delta\mathbf{E}$ is related to the variation in displacement $\delta\mathbf{u}$ and $d\mathbf{u}$ as:

$$\begin{aligned}\delta\mathbf{E} \;=\; & \frac{1}{2}\Big\{grad\,(\delta\mathbf{u}) + [grad\,(\delta\mathbf{u})]^T \\ & + [grad\,(d\mathbf{u})]^T\,[grad\,(\delta\mathbf{u})] + [grad\,(\delta\mathbf{u})]^T\,[grad\,(d\mathbf{u})]\Big\}\end{aligned} \tag{B.4}$$

The deformed position $\mathbf{x}_t \equiv \mathbf{x}$ at the end of a step is related to reference position $\mathbf{x}_\tau$ and $d\mathbf{u}$ as:

$$\mathbf{x} = \mathbf{x}_\tau + d\mathbf{u} \quad \Rightarrow \quad grad\,(\mathbf{x}) = \mathbf{I} + grad\,(d\mathbf{u}) \tag{B.5}$$

With the uses of Eq. B.5 into Eq. B.4, $\delta\mathbf{E}$ can be simplified as:

$$\delta\mathbf{E} = \frac{1}{2}\left\{[grad\,(\mathbf{x})]^T\,[grad\,(\delta\mathbf{u})] + [grad\,(\delta\mathbf{u})]^T\,[grad\,(\mathbf{x})]\right\} \tag{B.6}$$

The Cauchy stress tensor $\boldsymbol{\sigma}$ and second Piola-Kirchhoff stress tensor $\mathbf{S}$ are related by the transformation:

$$\boldsymbol{\sigma} = \frac{1}{J}\mathbf{F}\mathbf{S}\mathbf{F}^T \tag{B.7}$$

or equivalently

$$\mathbf{S} = J\mathbf{f}\boldsymbol{\sigma}\mathbf{f}^T \tag{B.8}$$

where the deformation gradient $\mathbf{F}$, its inverse $\mathbf{f}$, and the Jacobian J are given by:

$$\begin{aligned} \mathbf{F} &= grad\,(\mathbf{x}) && \text{(B.9)} \\ \mathbf{f} &= \mathbf{F}^{-1} && \text{(B.10)} \\ J &= det\,[\mathbf{F}] && \text{(B.11)} \end{aligned}$$

The virtual work represented by Eq. B.1 contributes to the residual vector $\mathbf{R}$ as:

$$-\int_{\Omega_\tau} \delta\mathbf{E}\,(\mathbf{S}+d\mathbf{S})\,dV \xrightarrow{+} \mathbf{R} \tag{B.12}$$

In Newton iterations, the corresponding contribution to the tangent stiffness matrix $\mathbf{K}_{\texttt{Tangent}}$ is given by:

$$\int_{\Omega_\tau} \{\delta\mathbf{E}\Delta\mathbf{S} + (\mathbf{S}+d\mathbf{S})\,\Delta\,(\delta\mathbf{E})\}\,dV \xrightarrow{+} \mathbf{K}_{\texttt{Tangent}} \tag{B.13}$$

From Eq. B.6

$$\Delta\,(\delta\mathbf{E}) = \frac{1}{2}\left\{[grad\,(\Delta\mathbf{u})]^T\,[grad\,(\delta\mathbf{u})] + [grad\,(\delta\mathbf{u})]^T\,[grad\,(\Delta\mathbf{u})]\right\} \tag{B.14}$$

and due to symmetry of the second Piola-Kirchhoff stress tensor

$$(\mathbf{S}+d\mathbf{S})\,\Delta\,(\delta\mathbf{E}) = (\mathbf{S}+d\mathbf{S})\,[grad\,(\Delta\mathbf{u})]^T\,[grad\,(\delta\mathbf{u})] \tag{B.15}$$

With the uses of Eq. B.15, Eq. B.13 can be rewritten as:

$$\int_{\Omega_\tau} \left\{\delta\mathbf{E}\Delta\mathbf{S} + (\mathbf{S}+d\mathbf{S})\,[grad\,(\Delta\mathbf{u})]^T\,[grad\,(\delta\mathbf{u})]\right\} dV \xrightarrow{+} \mathbf{K}_{\texttt{Tangent}} \tag{B.16}$$

The objective of the following discussion is to approximate $\Delta\mathbf{S}$ adopting a suitable form of constitutive relation for large-deformation problems.

The constitutive relation between rate of the Cauchy stress $\dot{\boldsymbol{\sigma}}$ and the deformation rate $\mathbf{D}$ is given by:

$$\dot{\boldsymbol{\sigma}} = \mathcal{D}\mathbf{D} \tag{B.17}$$

where $\mathcal{D}$ is the material stiffness tensor. The relationship represented by Eq. B.17 can be written in corotational Cartesian system as:

$$\dot{\boldsymbol{\sigma}}^c = \mathcal{D}^c\mathbf{D}^c \tag{B.18}$$

where:

$$\dot{\boldsymbol{\sigma}}^c = \mathcal{R}\boldsymbol{\sigma}\mathcal{R}^T \tag{B.19}$$

$$\mathbf{D}^c = \mathcal{R}\mathbf{D}\mathcal{R}^T \tag{B.20}$$

In the above expressions $\mathcal{R}$ is the (orthogonal) rotation tensor in the polar decomposition of the deformation gradient given by:

$$\mathbf{F} = \mathcal{R}\mathcal{U} \tag{B.21}$$

Therefore,

$$\mathbf{f} = \mathbf{F}^{-1} = \mathcal{U}^{-1}\mathcal{R}^{-1} = \mathbf{V}\mathcal{R}^T \tag{B.22}$$

with $\mathcal{U}$ being the right stretch tensor that is symmetric and positive definite.

The relation between deformation rate $\mathbf{D}$ and the Green-Lagrange strain rate is given as:

$$\mathbf{D} = \mathbf{f}^T \dot{\mathbf{E}} \mathbf{f} \tag{B.23}$$

Use of Eqs. B.22 and B.23 into Eq. B.20 leads to

$$\mathbf{D}^c = \mathbf{V} \dot{\mathbf{E}} \mathbf{V} \tag{B.24}$$

A corotational logarithmic strain increment $d\mathbf{e}^c$ is calculated by integration of $\mathbf{D}^c$ as:

$$d\mathbf{e}^c = \int_\tau^t \mathbf{D}^c \, dt = \int_\tau^t \mathbf{V} \dot{\mathbf{E}} \mathbf{V} dt \tag{B.25}$$

With the use of the expression

$$\mathbf{V}\mathbf{V} = [\mathbf{I} + 2\mathbf{E}]^{-1} \tag{B.26}$$

a series expansion of $\mathbf{V}$ is obtained as:

$$\mathbf{V} = \mathbf{I} - \mathbf{E} + \frac{3}{2}\mathbf{E}\mathbf{E} - \frac{5}{2}\mathbf{E}\mathbf{E}\mathbf{E} + \dots \tag{B.27}$$

With the use of Eq. B.27 in Eq. B.25, the corotational logarithmic strain increment $d\mathbf{e}^c$ is approximated as:

$$d\mathbf{e}^c \approx \left(\mathbf{I} - \frac{1}{2} d\mathbf{E}\right) d\mathbf{E} \left(\mathbf{I} - \frac{1}{2} d\mathbf{E}\right) \tag{B.28}$$

It is assumed that the $\dot{\mathbf{e}}^c = \mathbf{D}^c$ is constant during the increment Δt

$$\dot{\mathbf{e}}^c = \mathbf{D}^c = \left(\mathbf{I} - \frac{1}{2} d\mathbf{E}\right) \frac{d\mathbf{E}}{\Delta t} \left(\mathbf{I} - \frac{1}{2} d\mathbf{E}\right) \tag{B.29}$$

Therefore, the increment in the corotational logarithmic strain within an iteration is approximated after linearization of Eq. B.28 as:

$$\Delta \mathbf{e}^c = (\mathbf{I} - d\mathbf{E})\, \Delta \mathbf{E}\, (\mathbf{I} - d\mathbf{E}) = \mathbf{V} \Delta \mathbf{E} \mathbf{V} \tag{B.30}$$

With the use of the above equation, Eq. B.18 becomes:

$$\Delta \boldsymbol{\sigma}^c = \mathcal{D}^c \mathbf{V} \Delta \mathbf{E} \mathbf{V} \tag{B.31}$$

From Eqs. B.8 and B.22, the second Piola-Kirchhoff stress tensor can be written as:

$$\mathbf{S} = J \mathbf{V} \boldsymbol{\sigma}^c \mathbf{V} \tag{B.32}$$

Therefore, the increment of $\mathbf{S}$ is given by:

$$\Delta \mathbf{S} = J \mathbf{V} \Delta \boldsymbol{\sigma}^c \mathbf{V} + J \Delta \mathbf{V} \boldsymbol{\sigma}^c \mathbf{V} + J \mathbf{V} \boldsymbol{\sigma}^c \Delta \mathbf{V} + \frac{\Delta J}{J} \mathbf{S} \tag{B.33}$$

With the assumption that $\mathbf{V}$ is close to unity, following approximations are obtained

$$\begin{aligned} \Delta \mathbf{V} &= \mathbf{V} \Delta \mathbf{E} && \text{(B.34)} \\ \frac{\Delta J}{J} &= \mathbf{V} \cdot \Delta \mathbf{E} && \text{(B.35)} \end{aligned}$$

Use of Eq. B.31 along with the approximations from Eqs. B.34 and B.35, Eq. B.33 is rewritten as:

$$\Delta \mathbf{S} = J \mathbf{V} \left(\mathcal{D}^c \mathbf{V} \Delta \mathbf{E} \mathbf{V} \right) \mathbf{V} + \Delta \mathbf{E} \mathbf{S} + \mathbf{S} \Delta \mathbf{E} + \left(\mathbf{V} \cdot \Delta \mathbf{E} \right) \mathbf{S} \tag{B.36}$$

Now adopting the finite-element discretization:

$$\mathbf{u} = \mathbf{N}\mathbf{U} \tag{B.37}$$

Define a matrix $\mathbf{B}$ such that

$$grad\left(\mathbf{u}\right) = \mathbf{B}\mathbf{U} \tag{B.38}$$

$$grad\left(\delta\mathbf{u}\right) = \mathbf{B}\delta\mathbf{U} \tag{B.39}$$

and $\bar{\mathbf{B}}$ such that

$$\delta\mathbf{B} = \bar{\mathbf{B}} grad\left(\delta\mathbf{u}\right) = \bar{\mathbf{B}}\mathbf{B}\delta\mathbf{U} \tag{B.40}$$

$$\Delta\mathbf{B} = \bar{\mathbf{B}} grad\left(\Delta\mathbf{u}\right) = \bar{\mathbf{B}}\mathbf{B}\Delta\mathbf{U} \tag{B.41}$$

The above definitions are used to write the contribution shown in Eq. B.12 as:

$$-\int_{\Omega_\tau} \delta\mathbf{E}\left(\mathbf{S} + d\mathbf{S}\right) dV = -\int_{\Omega_\tau} \left(\delta\mathbf{U}\right)^T \left(\mathbf{B}\right)^T \left(\bar{\mathbf{B}}\right)^T J\mathbf{V}\left(\boldsymbol{\sigma}^c + d\boldsymbol{\sigma}^c\right)\mathbf{V} dV \tag{B.42}$$

A matrix $\mathbf{W}$ is defined such that for any tensor $\mathbf{A}$

$$\mathbf{V}\mathbf{A}\mathbf{V} = \mathbf{W}\mathbf{A} \tag{B.43}$$

Eq. B.42 is written as:

$$-\int_{\Omega_\tau} \delta\mathbf{E}\left(\mathbf{S} + d\mathbf{S}\right) dV = -\left(\delta\mathbf{U}\right)^T \int_{\Omega_\tau} \left(\mathbf{B}\right)^T \left(\bar{\mathbf{B}}\right)^T \mathbf{W}\left(\boldsymbol{\sigma}^c + d\boldsymbol{\sigma}^c\right) J dV \tag{B.44}$$

Furthermore, matrices $\mathbf{C}_1$, $\mathbf{C}_2$, and $\mathbf{C}_3$ can be defined such that

$$\Delta\mathbf{E}\mathbf{S} + \mathbf{S}\Delta\mathbf{E} = \mathbf{C}_1\Delta\mathbf{E} \tag{B.45}$$

$$(\mathbf{V} \cdot \Delta\mathbf{E})\,\mathbf{S} = \mathbf{C}_2 \Delta\mathbf{E} \tag{B.46}$$

and

$$grad\,(\Delta\mathbf{u})\,(\mathbf{S} + d\mathbf{S}) = \mathbf{C}_3 grad\,(\Delta\mathbf{u}) \tag{B.47}$$

With the use of Eqs. B.43, B.45, B.46, and B.47 in Eqs. B.36, and B.16, the contribution to the tangent stiffness matrix can be written as:

$$\int_{\Omega_\tau} (\mathbf{B})^T \left\{ \left(\bar{\mathbf{B}}\right)^T \left[J\mathbf{W}\mathcal{D}^c\mathbf{W} + \mathbf{C}_1 + \mathbf{C}_2 \right] \bar{\mathbf{B}} + \mathbf{C}_3 \right\} \mathbf{B} dV \tag{B.48}$$

The contribution to the residual vector can be written as:

$$\int_{\Omega_\tau} (\mathbf{B})^T \left(\bar{\mathbf{B}}\right)^T \mathbf{W} \left(\boldsymbol{\sigma}^c + d\boldsymbol{\sigma}^c\right) J dV \tag{B.49}$$

Appendix C

Contact Contributions

C.1 Solid Displacements

The penetration of a slave node into the master segment and the virtual work performed by the internal (total) normal forces are given by:

$$l = \mathbf{n}^T \mathbf{H}_s \mathbf{X} \tag{C.1}$$

$$\hat{\Pi}_s^c = (\delta \mathbf{U}_s)^T \, \mathbf{H}_s^T \mathbf{n} \lambda_s \tag{C.2}$$

In incremental form, the above equations become:

$$\Delta l = \mathbf{n}^T \mathbf{H}_s \Delta \mathbf{U}^s \tag{C.3}$$

$$\Delta \hat{\Pi}_s^c = (\delta \mathbf{U}_s)^T \left[(\Delta \mathbf{H}_s)^T \, \mathbf{n} \lambda_s + \mathbf{H}_s^T \Delta \mathbf{n} \lambda_s + \mathbf{H}_s^T \mathbf{n} \Delta \lambda_s \right] \tag{C.4}$$

where:

$$\Delta\mathbf{H}_s = \frac{\partial \mathbf{H}_s}{\partial \xi}\Delta\xi = \mathbf{H}_{s,\,\xi}\Delta\xi = \mathbf{G}_s\Delta\xi \tag{C.5}$$

$$\Delta\xi = -\frac{1}{A}\Big[\|\mathbf{G}_s\mathbf{X}\|\mathbf{t}^T\mathbf{H}_s + l\mathbf{n}^T\mathbf{G}_s\Big]\Delta\mathbf{U}^s \tag{C.6}$$

$$\Delta\mathbf{n} = -\frac{1}{A}\mathbf{t}\mathbf{n}^T\Big[-\mathbf{G}_{s,\,\xi}\mathbf{X}\mathbf{t}^T\mathbf{H}_s + \|\mathbf{G}_s\mathbf{X}\|\mathbf{G}_s\Big]\Delta\mathbf{U}^s \tag{C.7}$$

$$A = \|\mathbf{G}_s\mathbf{X}\|^2 + l\mathbf{n}^T\mathbf{G}_{s,\,\xi}\mathbf{X} \tag{C.8}$$

The contribution arising from Eqs. C.3 and C.4 to the system of equations is written in matrix form as:

$$\begin{bmatrix} \mathbf{K}_{11} & \mathbf{K}_{12} \\ \mathbf{K}_{21} & 0 \end{bmatrix} \begin{Bmatrix} \Delta\mathbf{U}^s \\ \Delta\lambda_s \end{Bmatrix} = \begin{Bmatrix} \mathbf{H}_s^T\mathbf{n}\lambda_s \\ l \end{Bmatrix} \tag{C.9}$$

where:

$$\begin{aligned} \mathbf{K}_{11} = \frac{\lambda_s}{A}\Big[& -\left(\mathbf{n}^T\mathbf{G}_{s,\,\xi}\mathbf{X}\right)\mathbf{H}_s^T\mathbf{t}\mathbf{t}^T\mathbf{H}_s + l\mathbf{G}_s^T\mathbf{n}\mathbf{n}^T\mathbf{G}_s \\ & +\|\mathbf{G}_s\mathbf{X}\|\left(\mathbf{H}_s^T\mathbf{t}\mathbf{n}^T\mathbf{G}_s + \mathbf{G}_s^T\mathbf{n}\mathbf{t}^T\mathbf{H}_s\right)\Big] \end{aligned} \tag{C.10}$$

$$\mathbf{K}_{12} = -\mathbf{H}_s^T\mathbf{n} \tag{C.11}$$

$$\mathbf{K}_{21} = -\mathbf{n}^T\mathbf{H}_s \tag{C.12}$$

C.2 Darcy's Velocity

The normal component of relative Darcy's velocity and the virtual work performed by the internal normal forces due to excess pore-water pressure are given by:

$$
\begin{aligned}
l_r &= \mathbf{n}^T \mathbf{H}_r \mathbf{V}^r && \text{(C.13)} \\
\hat{\Pi}_r^c &= (\delta \mathbf{V}_r)^T \, \mathbf{H}_r^T \mathbf{n} \lambda_r && \text{(C.14)}
\end{aligned}
$$

In incremental form, the above equations become:

$$
\begin{aligned}
\Delta l_r &= \Delta \mathbf{n}^T \mathbf{H}_r \mathbf{V}^r + \mathbf{n}^T \Delta \mathbf{H}_r \mathbf{V}^r + \mathbf{n}^T \mathbf{H}_r \Delta \mathbf{V}^r && \text{(C.15)} \\
\Delta \hat{\Pi}_r^c &= (\delta \mathbf{V}_r)^T \left[(\Delta \mathbf{H}_r)^T \, \mathbf{n} \lambda_r + \mathbf{H}_r^T \Delta \mathbf{n} \lambda_r + \mathbf{H}_r^T \mathbf{n} \Delta \lambda_r \right] && \text{(C.16)}
\end{aligned}
$$

where:

$$
\Delta \mathbf{H}_r = \frac{\partial \mathbf{H}_r}{\partial \xi} \Delta \xi = \mathbf{H}_{r,\,\xi} \Delta \xi = \mathbf{G}_r \Delta \xi \qquad \text{(C.17)}
$$

The contribution arising from Eqs. C.15 and C.16 to the system of equations is written in matrix form as:

$$
\begin{bmatrix} \mathbf{0} & \mathbf{0} & \mathbf{0} \\ \mathbf{K}_{21} & \mathbf{0} & \mathbf{K}_{23} \\ \mathbf{K}_{31} & \mathbf{K}_{32} & 0 \end{bmatrix} \left\{ \begin{array}{c} \Delta \mathbf{U}^s \\ \Delta \mathbf{V}^r \\ \Delta \lambda_r \end{array} \right\} = \left\{ \begin{array}{c} \mathbf{0} \\ \mathbf{H}_r^T \mathbf{n} \lambda_r \\ l_r \end{array} \right\} \qquad \text{(C.18)}
$$

where:

$$\begin{aligned}
\mathbf{K}_{21} &= \frac{\lambda_r}{A}\Big[-\left(\mathbf{n}^T\mathbf{G}_{s,\,\xi}\mathbf{X}\right)\mathbf{H}_r^T\mathbf{t}\mathbf{t}^T\mathbf{H}_s + l\mathbf{G}_r^T\mathbf{n}\mathbf{n}^T\mathbf{G}_s \\
&\quad + \|\mathbf{G}_s\mathbf{X}\|\left(\mathbf{H}_r^T\mathbf{t}\mathbf{n}^T\mathbf{G}_s + \mathbf{G}_r^T\mathbf{n}\mathbf{t}^T\mathbf{H}_s\right)\Big] \qquad (C.19)\\
\mathbf{K}_{23} &= -\mathbf{H}_r^T\mathbf{n} \qquad (C.20)\\
\mathbf{K}_{31} &= \frac{1}{A}\Big\{\Big[-\left(\mathbf{t}^T\mathbf{H}_r\mathbf{V}^r\right)\left(\mathbf{n}^T\mathbf{G}_{s,\,\xi}\mathbf{X}\right) \\
&\quad + \left(\mathbf{n}^T\mathbf{G}_r\mathbf{V}^r\right)\|\mathbf{G}_s\mathbf{X}\|\Big]\mathbf{t}^T\mathbf{H}_s \\
&\quad + \Big[\left(\mathbf{t}^T\mathbf{H}_r\mathbf{V}^r\right)\|\mathbf{G}_s\mathbf{X}\| + l\left(\mathbf{n}^T\mathbf{G}_r\mathbf{V}^r\right)\Big]\mathbf{n}^T\mathbf{G}_s\Big\} \qquad (C.21)\\
\mathbf{K}_{32} &= -\mathbf{n}^T\mathbf{H}_r \qquad (C.22)
\end{aligned}$$

C.3 Excess Pore-Water Pressure

The difference in the excess pore-water pressure and the virtual work performed by the flux are given by:

$$\begin{aligned}
l_p &= \mathbf{H}_p\bar{\mathbf{P}}^w \qquad (C.23)\\
\hat{\Pi}_p^c &= \left(\delta\bar{\mathbf{P}}_w\right)^T\mathbf{H}_p^T\lambda_p \qquad (C.24)
\end{aligned}$$

In incremental form, the above equations become:

$$\begin{aligned}
\Delta l_p &= \Delta\mathbf{H}_p\bar{\mathbf{P}}^w + \mathbf{H}_p\Delta\bar{\mathbf{P}}^w \qquad (C.25)\\
\Delta\hat{\Pi}_p^c &= \left(\delta\bar{\mathbf{P}}_w\right)^T\left[\left(\Delta\mathbf{H}_p\right)^T\lambda_p + \mathbf{H}_p^T\Delta\lambda_p\right] \qquad (C.26)
\end{aligned}$$

where:

$$\Delta\mathbf{H}_p = \frac{\partial\mathbf{H}_p}{\partial\xi}\Delta\xi = \mathbf{H}_{p,\,\xi}\Delta\xi = \mathbf{G}_p\Delta\xi \qquad (C.27)$$

The contribution arising from Eqs. C.25 and C.26 to the system of equations is written in matrix form as:

$$\begin{bmatrix} \mathbf{0} & \mathbf{0} & \mathbf{0} \\ \mathbf{K}_{21} & \mathbf{0} & \mathbf{K}_{23} \\ \mathbf{K}_{31} & \mathbf{K}_{32} & 0 \end{bmatrix} \begin{Bmatrix} \Delta\mathbf{U}^s \\ \Delta\bar{\mathbf{P}}^w \\ \Delta\lambda_p \end{Bmatrix} = \begin{Bmatrix} \mathbf{0} \\ \mathbf{H}_p^T\lambda_p \\ l_p \end{Bmatrix} \tag{C.28}$$

where:

$$\mathbf{K}_{21} = \frac{\lambda_p}{A}\left[\|\mathbf{G}_s\mathbf{X}\|\mathbf{G}_p^T\mathbf{t}^T\mathbf{H}_s + l\mathbf{G}_p^T\mathbf{n}^T\mathbf{G}_s\right] \tag{C.29}$$

$$\mathbf{K}_{23} = -\mathbf{H}_p^T \tag{C.30}$$

$$\mathbf{K}_{31} = \frac{\mathbf{G}_p\bar{\mathbf{P}}^w}{A}\left[\|\mathbf{G}_s\mathbf{X}\|\mathbf{t}^T\mathbf{H}_s + l\mathbf{n}^T\mathbf{G}_s\right] \tag{C.31}$$

$$\mathbf{K}_{32} = -\mathbf{H}_p \tag{C.32}$$

C.4 Interface Friction

C.4.1 Stick Condition

The relative tangential (solid) velocity and the virtual work performed by the internal frictional force are given by:

$$m = \mathbf{t}^T\mathbf{H}_s\mathbf{V}^s \tag{C.33}$$

$$\hat{\Pi}^c_{F,\,\mathtt{Stick}} = (\delta\mathbf{U}_s)^T\,\mathbf{H}_s^T\mathbf{t}\lambda_f \tag{C.34}$$

In incremental form, the above equations become:

$$
\begin{aligned}
\Delta m &= (\Delta \mathbf{t})^T \mathbf{H}_s \mathbf{V}^s + \mathbf{t}^T \Delta \mathbf{H}_s \mathbf{V}^s + \mathbf{t}^T \mathbf{H}_s \Delta \mathbf{V}^s && \text{(C.35)} \\
\Delta \hat{\Pi}^c_{F,\,\texttt{Stick}} &= (\delta \mathbf{U}_s)^T \Big[(\Delta \mathbf{H}_s)^T \mathbf{t} \lambda_f + \mathbf{H}_s^T \Delta \mathbf{t} \lambda_f + \mathbf{H}_s^T \mathbf{t} \Delta \lambda_f \Big] && \text{(C.36)}
\end{aligned}
$$

where:

$$
\Delta \mathbf{t} = \frac{1}{A} \mathbf{n}\mathbf{n}^T \Big[- \mathbf{G}_{s,\,\xi} \mathbf{X} \mathbf{t}^T \mathbf{H}_s + \|\mathbf{G}_s \mathbf{X}\| \mathbf{G}_s \Big] \Delta \mathbf{U}^s \tag{C.37}
$$

The contribution arising from Eqs. C.35 and C.36 to the system of equations is written in matrix form as:

$$
\begin{bmatrix} \mathbf{K}_{11} & \mathbf{K}_{12} \\ \mathbf{K}_{21} & 0 \end{bmatrix} \begin{Bmatrix} \Delta \mathbf{U}^s \\ \Delta \lambda_f \end{Bmatrix} = \begin{Bmatrix} \mathbf{H}_s^T \mathbf{t} \lambda_f \\ m \end{Bmatrix} \tag{C.38}
$$

where:

$$
\begin{aligned}
\mathbf{K}_{11} &= \frac{\lambda_f}{A} \Big[\left(\mathbf{n}^T \mathbf{G}_{s,\,\xi} \mathbf{X} \right) \mathbf{H}_s^T \mathbf{n} \mathbf{t}^T \mathbf{H}_s + l \mathbf{G}_s^T \mathbf{t} \mathbf{n}^T \mathbf{G}_s \\
&\quad + \|\mathbf{G}_s \mathbf{X}\| \left(-\mathbf{H}_s^T \mathbf{n}\mathbf{n}^T \mathbf{G}_s + \mathbf{G}_s^T \mathbf{t}\mathbf{t}^T \mathbf{H}_s \right) \Big] && \text{(C.39)} \\
\mathbf{K}_{12} &= -\mathbf{H}_s^T \mathbf{t} && \text{(C.40)} \\
\mathbf{K}_{21} &= \frac{1}{A} \Big\{ \Big[\left(\mathbf{n}^T \mathbf{H}_s \mathbf{V}^s \right) \left(\mathbf{n}^T \mathbf{G}_{s,\,\xi} \mathbf{X} \right) \\
&\quad + \left(\mathbf{t}^T \mathbf{G}_s \mathbf{V}^s \right) \|\mathbf{G}_s \mathbf{X}\| \Big] \mathbf{t}^T \mathbf{H}_s \\
&\quad + \Big[- \left(\mathbf{n}^T \mathbf{H}_s \mathbf{V}^s \right) \|\mathbf{G}_s \mathbf{X}\| + l \left(\mathbf{t}^T \mathbf{G}_s \mathbf{V}^s \right) \Big] \mathbf{n}^T \mathbf{G}_s \Big\} \\
&\quad - \frac{1}{\alpha} \mathbf{t}^T \mathbf{H}_s && \text{(C.41)}
\end{aligned}
$$

C.4.2 Slip Condition

The virtual work performed by the Coulomb frictional force acting along the interface is given by:

$$\hat{\Pi}^{c}_{F,\,\texttt{Slip}} = -\left(\delta \mathbf{U}_s\right)^T \mathbf{H}_s^T \mathbf{t} F_f = \left(\delta \mathbf{U}_s\right)^T \mathbf{H}_s^T \mathbf{t} \mu \left(\lambda_s - \lambda_r\right) f\left(m\right) \tag{C.42}$$

In incremental form, the above equations become:

$$\begin{aligned}\Delta\hat{\Pi}^{c}_{F,\,\texttt{Slip}} \quad = \quad & \left(\delta \mathbf{U}_s\right)^T \Big[\left(\Delta \mathbf{H}_s\right)^T \mathbf{t} \mu \left(\lambda_s - \lambda_r\right) f\left(m\right) \\ & + \mathbf{H}_s^T \Delta \mathbf{t} \mu \left(\lambda_s - \lambda_r\right) f\left(m\right) \\ & + \mathbf{H}_s^T \mathbf{t} \mu \left(\Delta\lambda_s - \Delta\lambda_r\right) f\left(m\right) \\ & + \mathbf{H}_s^T \mathbf{t} \mu \left(\lambda_s - \lambda_r\right) \Delta f\left(m\right) \Big]\end{aligned} \tag{C.43}$$

where:

$$\Delta f\left(m\right) = \frac{\partial f\left(m\right)}{\partial m} \Delta m = f\left(m\right)_{,\,m} \Delta m \tag{C.44}$$

The contribution arising from Eq. C.43 to the system of equations is written in matrix form as:

$$\begin{bmatrix} \mathbf{K}_{11} & \mathbf{K}_{12} & \mathbf{K}_{13} \\ \mathbf{0} & 0 & 0 \\ \mathbf{0} & 0 & 0 \end{bmatrix} \begin{Bmatrix} \Delta \mathbf{U}^s \\ \Delta\lambda_s \\ \Delta\lambda_r \end{Bmatrix} = \begin{Bmatrix} -\mathbf{H}_s^T \mathbf{t} F_f \\ 0 \\ 0 \end{Bmatrix} \tag{C.45}$$

where:

$$
\begin{aligned}
\mathbf{K}_{11} &= -\frac{F_f}{A}\Big[\left(\mathbf{n}^T\mathbf{G}_{s,\,\xi}\mathbf{X}\right)\mathbf{H}_s^T\mathbf{n}\mathbf{t}^T\mathbf{H}_s + l\mathbf{G}_s^T\mathbf{t}\mathbf{n}^T\mathbf{G}_s \\
&\quad +\|\mathbf{G}_s\mathbf{X}\|\left(-\mathbf{H}_s^T\mathbf{n}\mathbf{n}^T\mathbf{G}_s + \mathbf{G}_s^T\mathbf{t}\mathbf{t}^T\mathbf{H}_s\right)\Big] \\
&\quad -\frac{\mu F_s f\,(m)_{,\,m}}{A}\Big\{\Big[\left(\mathbf{n}^T\mathbf{H}_s\mathbf{V}^s\right)\left(\mathbf{n}^T\mathbf{G}_{s,\,\xi}\mathbf{X}\right) \\
&\quad +\left(\mathbf{t}^T\mathbf{G}_s\mathbf{V}^s\right)\|\mathbf{G}_s\mathbf{X}\| - \frac{1}{\alpha}A\Big]\mathbf{H}_s^T\mathbf{t}\mathbf{t}^T\mathbf{H}_s \\
&\quad +\Big[-\left(\mathbf{n}^T\mathbf{H}_s\mathbf{V}^s\right)\|\mathbf{G}_s\mathbf{X}\| + l\left(\mathbf{t}^T\mathbf{G}_s\mathbf{V}^s\right)\Big]\mathbf{H}_s^T\mathbf{t}\mathbf{n}^T\mathbf{G}_s\Big\} \qquad \text{(C.46)} \\
\mathbf{K}_{12} &= -\mu f\,(m)\,\mathbf{H}_s^T\mathbf{t} \qquad \text{(C.47)} \\
\mathbf{K}_{13} &= \mu f\,(m)\,\mathbf{H}_s^T\mathbf{t} \qquad \text{(C.48)}
\end{aligned}
$$

C.5 Release Condition

The virtual work of the normal forces due to pore-water pressure acting on the interface in the release (open-gap) condition is given by:

$$\hat{\Pi}_R^c = \left(\delta\mathbf{U}_s\right)^T\mathbf{H}_s^T\mathbf{n}\lambda_r \qquad \text{(C.49)}$$

In incremental form, the above equations become:

$$\Delta\hat{\Pi}_R^c = \left(\delta\mathbf{U}_s\right)^T\Big[\left(\Delta\mathbf{H}_s\right)^T\mathbf{n}\lambda_r + \mathbf{H}_s^T\Delta\mathbf{n}\lambda_r + \mathbf{H}_s^T\mathbf{n}\Delta\lambda_r\Big] \qquad \text{(C.50)}$$

The contribution arising from Eq. C.50 to the system of equations is written in matrix form as:

$$\begin{bmatrix} \mathbf{K}_{11} & \mathbf{0} & \mathbf{K}_{13} \\ \mathbf{0} & 0 & 0 \\ \mathbf{0} & 0 & 0 \end{bmatrix} \begin{Bmatrix} \Delta\mathbf{U}^s \\ \Delta\lambda_s \\ \Delta\lambda_r \end{Bmatrix} = \begin{Bmatrix} \mathbf{H}_s^T\mathbf{n}\lambda_r \\ 0 \\ 0 \end{Bmatrix} \qquad \text{(C.51)}$$

where:

$$\begin{aligned}
\mathbf{K}_{11} &= \frac{\lambda_r}{A}\Big[-\big(\mathbf{n}^T\mathbf{G}_{s,\,\xi}\mathbf{X}\big)\,\mathbf{H}_s^T\mathbf{t}\mathbf{t}^T\mathbf{H}_s + l\mathbf{G}_s^T\mathbf{n}\mathbf{n}^T\mathbf{G}_s \\
&\quad +\|\mathbf{G}_s\mathbf{X}\|\,\big(\mathbf{H}_s^T\mathbf{t}\mathbf{n}^T\mathbf{G}_s + \mathbf{G}_s^T\mathbf{n}\mathbf{t}^T\mathbf{H}_s\big)\Big] \qquad \text{(C.52)} \\
\mathbf{K}_{13} &= -\mathbf{H}_s^T\mathbf{n} \qquad \text{(C.53)}
\end{aligned}$$

Bibliography

[1] Albert, L.F., Holtz, R.D., and Magris, E. (1987). "The superpile system: A feasible alternate foundation for TLP in deep water," *Proceedings of the 19th annual Offshore Technology Conference*, Houston, Texas, OTC 5392, pp 307-314.

[2] Andersen, K.H., Dyvik, R., Lauritzsen, R., Heien, D., Harvik, L., and Amundsen, T. (1989). "Model tests of gravity platforms. II: Interpretation," *Journal Geotechnical Engineering*, Vol. 115, No. 11, pp 1550-1568.

[3] Andersen, K.H., Dyvik, R., Shrøder, K., Hansteen, O.E., and Bysveen, S. (1993). "Fiels tests of anchors in clay. II: Predictions and interpretations," *Journal of Geotechnical Engineering*, Vol. 119, No. 10, pp 1532-1549.

[4] Andersen, K.H, Jeanjean, P., Luger, D., and Jostad, H.P. (2003). "Centrifuge tests on installation of suction anchors in soft clay," In *Deepwater Mooring Systems: Concepts, Design, Analysis, and Materials*, Edited by J. Zhang and R.S. Mercier, Houston, Texas, pp 13-27.

[5] Atkinson, J.H. (1993). *An Introduction to the Mechanics of Soils and Foundations: Through Critical State Soil Mechanics*, McGraw-Hill Book Co., New York.

[6] Aubeny, C.P., Han, S.W., and Murff, J.D., (2003a). "Inclined load capacity of suction caissons," *International Journal for Numerical and Analytical Methods in Geomechanics*, Vol. 27, pp 1235-1254.

[7] Aubeny, C.P., Han, S.W., and Murff, J.D. (2003b). "Refined model for inclined load capacity of suction caissons," *Proceedings of 22nd International Conference on Offshore Mechanics and Arctic Engineering*, Cancun, Mexico, OMAE2003-37502.

[8] Audibert, J.M.E., Clukey, E.C., and Huang, J. (2003). "Suction caisson installation at Horn Mountain - A case history," *Proceedings of the 13th International Offshore and Polar Engineering Conference*, Honolulu, Hawaii, pp 762-769.

[9] Baerheim, M. (1994). "Structural and installation design of plate foundations for jackets," *Proceedings of the 26th annual Offshore Technology Conference*, Houston, Texas, OTC 7452, pp 313-322.

[10] Bang, S., and Cho, Y. (1999). "Analytical performance study of suction piles in sand," *Proceedings of the ninth International Offshore and Polar Engineering Conference*, Brest, France.

[11] Bang, S., Preber, T., Cho, Y., Thomsan, J., Karnoski, S.R, and Taylor, R.J. (2000). "Suction piles for mooring of mobile offshore bases," *Journal of Marine Structures*, Vol. 13, pp 367-882.

[12] Biot, M.A. (1941). "General theory of three dimensional consolidation," *Journal of Applied Physics*, Vol. 26, pp 155-164.

[13] Borja, R.I., and Alarcón, E. (1995). “A mathematical framework for finite strain elasoplastic consolidation Part 1: Balance laws, variational formulation, and linearization,” *Computer methods in Applied Mechanics and Engineering*, Vol. 122, pp 145-171.

[14] Brown, G.A., and Nacci, V.A., (1971). “Performance of hydrostatic anchors in granular soils,” *Proceedings of the 3rd annual Offshore Technology Conference*, Houston, Texas, OTC 1472, pp II 533-542.

[15] Burgess, I.W., and Hird, C.C. (1983). “Stability of installation of marine caisson anchors in clay,” *Canadian Geotechnical Journal*, Vol. 20, pp 385-393.

[16] Byrne, B.W. (2000). “Investigations of suction caissons in dense sand,” PhD Dissertation, Magdalen College, Oxford.

[17] Byrne, B.W., and Houlsby, G.T. (2000). “Experimental investigation of the cyclic response of suction caissons in sand,” *2000 Offshore Technology Conference*, Houston, Texas, OTC 12194, pp 787-795.

[18] Byrne, B.W., and Houlsby, G.T. (2002a). “Experimental investigation of response of suction caissons to transient vertical loading,” *Journal of Geotechnical and Geoenvironmental Engineering*, Vol. 128, No. 11, pp 926-939.

[19] Byrne, B.W., Houlsby, G.T., Martin, C., and Fish, P. (2002b). “Suction caisson foundation for offshore wind turbines,” *Wind Engineering*, Vol. 26, No. 3, pp 145-155.

[20] Cao, J., Phillips, R., and Popescu, R. (2001). "Physical and numerical modelling on suction caissons in clay," *Proceedings of the 18th Canadian Congress of Applied Mechanics*, Memorial University of Newfoundland, St. John's, Canada, pp 217-218.

[21] Cao, J., Phillips, R., Popescu, R., Al-Khafaji, Z., and Audibert, J.M.E. (2002a). "Penetration resistance of suction caissons in clay," *Proceedings of the 12th International Offshore and Polar Engineering Conference*, Kitakyushu, May 26-31, pp 800-806.

[22] Cao, J., Phillips, R., Audibert, J.M.E., and Al-Khafazi, Z. (2002b). "Numerical analysis of the behavior of suction caissons in clay," *Proceedings of the 12th International Offshore and Polar Engineering Conference*, Kitakyushu, Japan, May 26-31, pp 795-799.

[23] Cao, J., Phillips, R., Popescu, R., Audibert, J.M.E., and Al-Khafaji, Z. (2003). "Numerical analysis of the behavior of suction caissons in clay," *International Journal of Offshore and Polar Engineering*, Vol. 13, No. 2, pp 154-159.

[24] Carey, G.F. (1997). *Computational Grids: Generation, Adaptation, and Solution Strategies*, Taylor and Francis, Washington, USA.

[25] Carter, J.P., and Balaam, N.P. (2001). "AFENA - Technical Reference Manual Version 6.0," Center for Geotechnical Research, The University of Sydney, Australia.

[26] Cauble, D.F., (1996). "An experimental investigation of the behavior of a

model suction caisson in a cohesive soil," PhD Dissertation, Massachusetts Institute of Technology.

[27] Cho, Y., Lee, T.H., Park, J.B., Kwag, D.J., Chung, E.S., and Bang, S. (2002). "Field tests on suction pile installation in sand," *Proceedings of 21st International Conference on Offshore Mechanics and Artic Engineering*, Oslo, Norway, OMAE2002-28179, pp 765-771.

[28] Clukey, E.C., and Morrison, M.J., (1993). "A centrifuge and analytical study to evaluate suction caissons for TLP applications in the Gulf of Mexico," In *Design and performance of deep foundations: Piles and piers in soil and soft rock*, Edited by P.P. Nelson, T.D. Smith and E.C. Clukey, ASCE Geotechnical Special Publication No. 38, pp 141-156.

[29] Clukey, E.C., Morrison, M.J., Gariner, J., and Corte, J.F. (1995). "The response of suction caisson in normally consolidated clays to cyclic TLP loading conditions," *Proceedings of the 27th annual Offshore Technology Conference*, Houston, Texas, OTC 7796, pp 909-918.

[30] Clukey, E.C., Banon, H., and Kulhawy, F.H., (2000). "Reliability assessment of deepwater suction caissons," *2000 Offshore Technology Conference*, Houston, Texas, OTC 12192, pp 777-785.

[31] Clukey, E.C. (2001). "Suction caisson design issues," *Proceedings of the OTRC 2001 International Conference*, April 26-27, Houston, Texas.

[32] Clukey, E.C., and Phillips, R. (2002). "Centrifuge model tests to verify suction caisson capacities for taut and semi-taut legged mooring systems,"

14th Annual Deep Offshore Technology: International Conference and Exhibition, New Orleans, Louisiana.

[33] Clukey, E.C., Aubeny, C.P., and Murff, J.D. (2003). “Comparison of analytical and centrifuge model tests for suction caisson subjected to combined loads,” *Proceedings of 22nd International Conference on Offshore Mechanics and Arctic Engineering*, Cancun, Mexico, OMAE2003-37503.

[34] Coffman, R.A. (2003). “Horizontal capacity of suction caissons in normally consolidated kaolinit,” M.Sc. Thesis, The University of Texas at Austin.

[35] Coffman, R.A., El-Sherbiny, R.M., Rauch, A.F., and Olson, R.E. (2004). “Measured horizontal capacity of suction caissons,” *Proceedings of the annual Offshore Technology Conference*, Houston, Texas, OTC 16161.

[36] Colliat, J-L., Boisard, P., Andersen, K, and Schroeder, K. (1995). “Caisson foundation as alternative anchors for permanent mooring of a process barge offshore Congo,” *Proceedings of the 27th annual Offshore Technology Conference*, Houston, Texas, OTC 7797, pp 919-929.

[37] Colliat, J-L., Boisard, P., Gramet, J-C., and Sparrevik, P. (1996). “Design and installation of suction anchor piles at a soft clay site in the Gulf of Gunea,” *Proceedings of the 28th annual Offshore Technology Conference*, Houston, Texas, OTC 8150, pp 325-337.

[38] Colliat, J-L., Boisard, P, Sparrevik, P., and Gramet, J-C. (1998). “Design and installation of suction anchor piles at soft clay site,” *Journal of Waterway, Port, Coastal, and Ocean Engineering*, July-August, pp 179-188.

[39] Coussy, O. (1995). *Mechanics of Porous Continua*, John Wiley & Sons, Chichester, UK.

[40] Dafalias, Y.F., and Popov, E.P. (1975). “A model of nonlinearly hardening materials for complex loading,” *Acta Mechanica*, Vol. 21, pp 173-192.

[41] Dafalias, Y.F., and Hermann, L.R. (1982a). *Bounding surface formulation in soil plasticity*, Chapter 10 in Soil mechanics - Transient and cyclic loads, Edited by G.N. Pande and O.C. Zienkiewicz, John Wiley & Sons Ltd., New York.

[42] Dafalias, Y.F. (1982b). “Bounding surface elastoplasticity-viscoplasticity for particulate cohesive media,” *International Union of Theoretical and Applied Mechanics (IUTAM) Symposium on Deformation and Failure of Granular Materials*, Edited by P.A. Vermeer and H.J. Luger, A.A. Balkema, Rotterdam, pp 97-107.

[43] Dafalias, Y. F. (1986). “Bounding surface plasticity I: Mathematical foundation and hypoplasticity,” *Journal of Engineering Mechanics*, ASCE, Vol. 112, No. 9, pp. 966-987.

[44] Dafalias, Y. F., and Herrmann, L. R. (1986). “Bounding surface plasticity II: Application to isotropic cohesive soils,” *Journal of Engineering Mechanics*, ASCE, Vol. 112, No. 12, pp. 1263-1291.

[45] Datta, M., and Kumar, P. (1996). “Suction beneath cylindrical anchors in soft clay,” *Proceedings of the sixth International Offshore and Polar Engineering Conference*, Los Angeles, California, pp 544-548.

[46] de Boer, R. (2000). *Theory of Porous Media: Highlights in the Historical Development and Current State*, Springer Verlag, Berlin.

[47] Deng, W., and Carter, J.P. (1999a). "Predictions of the vertical pullout capacity of suction caissons in fine-grained soils," Research Report No. R797, Center for Geotechnical Research, The university of Sydney, Australia.

[48] Deng, W., and Carter, J.P. (1999b). "Analysis of suction caissons in uniform soils subjected to inclined uplift loading," Research Report No. R798, Center for Geotechnical Research, The university of Sydney, Australia.

[49] Deng, W., and Carter, J.P. (2000a). "Inclined uplift capacity of suction caissons in sand," *2000 Offshore Technology Conference*, Houston, Texas, OTC 12196, pp 809-820.

[50] Deng, W., and Carter, J.P. (2000b). "A theoretical study of the vertical uplift capacity of suction caissons," *Proceedings of the tenth International Offshore and polar Engineering Conference*, Seattle, USA, pp 342-349.

[51] Deng. W., and Carter, J.P. (2002). "A theoretical study of the vertical uplift capacity of suction caissons," *International Journal of Offshore and Polar Engineering*, Vol. 12, No. 2, pp 89-97.

[52] Dyvik, R., Andersen, K.H., Madshus, C., and Amundsen, T. (1989). "Model tests on gravity platforms. I: Description," *Journal of Geotechnical Engineering*, Vol. 115, No. 11, pp 1532-1549.

[53] Dyvik, R., Anderson, K.H., Hansen, S.B., and Christophersen, H.P.,

(1993). "Field tests on anchors in clay. I: Description," *Journal of Geotechnical Engineering*, Vol. 119, No. 10, pp 1515-1531.

[54] El-Gharbawy, S.L. (1998). "The pullout capacity of suction caisson foundations," Ph.D. Dissertation, The University of Texas at Austin.

[55] El-Gharbawy, S.L., and Olson, R.E. (2000). "Modeling of suction caisson foundations," *Proceedings of the 10th International Offshore and Polar Engineering Conference*, Seattle, USA.

[56] El-Sherbiny, R.M. (2004). Personal communication.

[57] Erbrich, C.T., (1994). "Modeling of a novel foundation for offshore structures," *Proceedings of the 9th UK ABAQUS User's Conference*, Oxford, England, pp 235-251.

[58] Feld, T., Rasmussen, J.L., and Sorensen, P.H. (1999). "Structural and economic optimization of offshore wind turbine support structure and foundation," *Proceedings of 18th International Conference on Offshore Mechanics and Arctic Engineering*, St. Johns, Newfoundland, Canada, OMAE99/OFT-4201, pp 415-423.

[59] Gambino, S.J., and Gilbert, R.B. (1999). "Modeling spatial variability in pile capacity for reliability-based design," *Analysis, Design, Construction, and Testing of Deep Foundations*, Edited by J.M. Roesset, ASCE Geotechnical Special Publication No. 88, pp 135-149.

[60] Gilbert, R.B., Gambino, S.J., and Dupin, R.M. (1999). "Reliability-Based approach for foundation design without site-specific soil borings," *1999 Offshore Technology Conference*, Houston, Texas, pp 631-640.

[61] Gilbert, R.B., and Murff, J.D. (2001). "Identifying uncertainties in the design of suction caisson foundations," *Proceedings of the International Conference on Geotechnical, Geological and Geophysical Properties of Deepwater Sediments Honoring Wayne A. Dunlap*, OTRC, Houston, Texas, pp 231-242.

[62] Goodman, L.J., Lee, C.N., and Walker, F.J., (1961). "The feasibility of vacuum anchorage in soil," *Geotechnique*, Vol. 1, No. 4, pp 356-359.

[63] Hallquist, J.O., Goudreau, G.L., and Benson, D.J. (1985). "Sliding interfaces with contact-impact in large-scale Lagrangian computations," *Computer Methods in Applied Mechanics and Engineering*, Vol. 51, pp 107-137.

[64] Handayanu, Swamidas, A.S.J., and Booton, M. (1999). "Behavior of tension foundation for offshore structures under extreme pull-out loads," *Proceedings of 18th International Conference on Offshore Mechanics and Arctic Engineering*, St. Johns, Newfoundland, Canada, OMAE99/OFT-4204, pp 635-641.

[65] Handayanu, Swamidas, A.S.J., and Booten, M. (2000). "Ultimate strength of offshore tension foundations under vertical and inclined loads," *Proceedings of ETCE/OMAE2000 Joint Conference*, New Orleans, Louisiana, OMAE2000/OSU OFT-4032, pp 95-100.

[66] Helfrich, S.C., Brazill, R.L., and Richards, A.F., (1976). "Pullout characteristics of a suction anchor in sand," *Proceedings of the 8th annual Offshore Technology Conference*, Houston, Texas, OTC 2469, pp 501-506.

[67] Herrmann, L.R., Kaliakin, V.N., Shen, C.K., Mish, K.D., and Zhu, Z.-Y.

(1987). "Numerical implementation of plasticity model for cohesive soils," *Journal of Engineering Mechanics*, Vol. 113, No. 3, pp 500-519.

[68] Hinton, E., and Campbell, J.S. (1974). "Local and global smoothening of discontinuous finite element functions using a least squares method," *International Journal for Numerical Methods in Engineering*, Vol. 8, pp 461-480.

[69] HKS, Inc., (1998). "ABAQUS theory manual - Version 5.8."

[70] HKS, Inc., (2000). "ABAQUS/Standard user's manual - Version 6.1."

[71] Hogervorst, J.R. (1980). "Field trails with large diameter suction piles," *Proceedings of the 12th annual Offshore Technology Conference*, Houston, Texas, OTC 3817, pp 217-224.

[72] Houlsby, G.T., and Byrne, B.W. (2000). "Suction caisson foundations for offshore wind turbines and anemometer masts," *Wind Engineering*, Vol. 24, No. 4, pp 249-255.

[73] House, A.R. (2000). "The response of suction caissons to catenary loading," *4th ANZ Young GeoTechnical Professional Conference*, ACT, Australian Geomechanics Society, Vol. 35, No. 3, pp 13-22.

[74] Huang, J., Cao, J., and Audibert, J.M.E. (2003). "Geotechnical design of suction caisson in clay," *Proceedings of the 13th International Offshore and Polar Engineering Conference*, Honolulu, Hawaii, pp 770-779.

[75] Hughes, T.J.R. (1977). "Unconditionally stable algorithms for nonlinear heat conduction," *Computer Methods in Applied Mechanics and Engineering*, Vol. 10, pp 135-139.

[76] Hughes, T.J.R. (2000). *The Finite Element Method: Linear Static and Dynamic Finite Element Analysis*, Dover Publications, Inc., Mineola, New York.

[77] Jaky, J. (1944). "The coefficient of earth pressure at rest," *Journal for Society of Hungarian Architects and Engineers*, Vol. 7, pp 355-358.

[78] Kaliakin, V.N., and Herrmann, L.R. (1991). *Guidelines for implementing the elastoplastic-viscoplastic bounding surface model*, Technical Report, Department of Civil Engineering, University of California, Davis.

[79] Kaliakin, V.N. (2000). Personal communication.

[80] Keaveny, J.M., Hansen, S.B., Madshus, C., and Dyvik, R. (1994). "Horizontal capacity of large-scale model anchors," *Proceedings of the 13th International Conference on Soil Mechanics and Foundation Engineering*, New Delhi, India, pp 677-680.

[81] Ko, H.Y. (1988). "Summary of the state-of-the-art in centrifuge model testing," In *Centrifuges in Soil Mechanics*, Edited by W.H. Craig and A.N. Scholfield, pp 11-18.

[82] Krause, R., and Rank, E. (1996). "A fast algorithm for point-location in a finite element mesh," *Computing*, Vol. 57, pp 46-92.

[83] Krieg, R.D. (1975). "A practical two surface plasticity theory," *Journal of Applied Mechanics*, Vol. 42, pp 641-646.

[84] Larsen, P. (1989). "Suction anchors as an anchoring system for floating offshore constructions," *Proceedings of the 21st annual Offshore Technology Conference*, Houston, Texas, OTC 6029, pp 535-540.

[85] Luke, A.M. (2002). “Axial capacity of suction caissons in normally consolidated kaolinite,” M.Sc. Thesis, The University of Texas at Austin.

[86] Maniar, D.R., Vásquez Chicate, L.F.G., and Tassoulas, J.L. (2003). “Installation and pullout of suction caissons: Finite-element simulation,” *Proceedings of the 22nd International Conference on Offshore Mechanics and Arctic Engineering*, June 8-13, Cancun, Mexico, Paper No. OMAE2003-37501.

[87] Matlock, H. (1970). “Correlations for design of laterally loaded piles in soft clay,” *Offshore Technology Conference*, Houston, Texas, OTC 1204.

[88] Mecham, E.C. (2001). “A laboratory for measuring the axial and lateral load capacity of model suction caissons,” M.Sc. Thesis, The University of Texas at Austin.

[89] Mercier, R.S. (2003). “Experience with fixed and floating platforms for the oil and gas industry,” *PowerPoint Presentation on CD-ROM of the Workshop on Deep Water Offshore Wind Energy Systems*, Washington, D.C., October 15-16.

[90] Mesri, G. and Olson, R.E. (1971). “Mechanisms controlling the permeability of clays,” *Clays and Clay Minerals* Vol. 19, pp 151-158.

[91] Mitchell, J.K. (1986). “Practical problems from surprising soil behavior,” *Journal of Geotechnical Engineering*, Vol. 112, No. 3, pp 259-289.

[92] Murff, J.D., and Hamilton, J.M. (1993). “P-ultimate for undrained analysis of laterally loaded piles,” *Journal of Geotechnical Engineering*, Vol. 119, No. 1, pp 91-107.

[93] Murti, V., and Valliappan, S. (1986). "Numerical inverse isoparametric mapping in remeshing and nodal quantity contouring," *Computers & Structures*, Vol. 22, No. 6, pp 1011-1021.

[94] Nagtegaal, J.C. (1982). "On the implementation of inelastic constitutive equations with special reference to large deformation problems," *Computer Methods in Applied Mechanics and Engineering* Vol. 33, pp 469-484.

[95] Olson, R.E., Rauch, A.F., Gilbert,R.B., Tassoulas, J.L., Aubeny, C.P., and Murff, J.D. (2001). "Toward the design of new technologies for deepwater anchorages," *Proceedings of the Eleventh International Offshore and Polar Engineering Conference*, June 17-22, Stvanget, Noway.

[96] Olson, R. E., Rauch, A. F., Mecham, E. C., and Luke, A. M. (2003). "Self-weight consolidation of large laboratory deposits of clay," *Proceedings of the 12th Pan-American Conference on Soil Mechanics and Geotechnical Engineering*, Cambridge, Massachusetts.

[97] Pedersen, R.C. (2001). "Model offshore soil deposit: Design, preparation, and characterization," M.Sc. Thesis, The University of Texas at Austin.

[98] Pedersen, R.C., Olson, R.E., and Rauch, A.F. (2003). "Shear and interface strength of clay at very low effective stress," *Geotechnical Testing Journal*, Vol. 26, Mo. 1, pp 71-78.

[99] Phillips, R., Clark, J.I., Paulin, M.J., Meaney, R., Millan, D.E.L., and Tuff, K. (1994). "Canadian national centrifuge center with cold regions capabilities," *Centrifuge 94*, pp 57-61.

[100] Pinna, R., Martin, C.M., and Ronalds, B.F. (2001). "Guidance for design of suction caissons against buckling during installation in clay soils," *Proceedings of the 11th International Offshore and Polar Engineering Conference*, Stavanger, Norway, pp 662-668.

[101] Potts, D.M., and Zdravkovic, L. (1999). *Finite Element Analysis in Geotechnical Engineering : Theory*, Thomas Telford, London.

[102] Prévost, J.H. (1980). "Mechanics of continuous porous media," *International Journal of Engineering Science*, Vol. 18, pp 787-800.

[103] Randolph, M.F., and Houlsby, G.T. (1984). "The limiting pressure on a circular pile loaded laterally in cohesive soil," *Geotechnique*, Vol. 34, No. 4, pp 613-623.

[104] Randolph, M.F., O'Neill, M.P., and Stewart, D.P. (1998). "Performance of suction anchors in fine-grained calcareous soils," *1998 Offshore Technology Conference*, Houston, Texas, OTC 8831, pp 521-529.

[105] Rao, S.N, Ravi, R., and Ganapathy, C. (1997a). "Behavior of suction anchors in marine clays under TLP loading," *Proceedings of the 16th International Conference on Offshore Mechanics and Arctic Engineering*, Yokohama, Japan, Vol. 1-B, pp 151-155.

[106] Rao, S.N., Ravi, R., and Ganapathy, C. (1997b). "Pullout behavior of model suction anchors in soft marine clays," *Proceedings of the seventh International Offshore and Polar Engineering Conference*, Honolulu, pp 740-744.

[107] Rauch, A.F. (2004). “Personal communication on reverse end bearing capacity.”

[108] Schmertmann, J.H. (1991). “The mechanical aging of soils,” *Journal of Geotechnical Engineering*, Vol. 119, No. 9, pp 1288-1330.

[109] Senpere, D., and Auvergne, G.A. (1982). “Suction anchor piles - A proven alternative to driving or drilling,” *Proceedings of the 14th annual Offshore Technology Conference*, Houston, Texas, OTC 4206, pp 483-493.

[110] Singh, B., Datta, M., and Gulhati, S.K. (1996). “Pullout behavior of superpile anchors in soft clay under static loading,” *Marine Georesources and Geotechnology*, Vol. 14, pp 217-236.

[111] Sparrevik, P. (2001). “Suction pile technology and installation in deep waters,” *Proceedings of OTRC 2001 International Conference Honoring Professor Wayne A. Dunlap*, Geotechnical, Geological, and Geophysical Properties of Deepwater Sediments, Houston, pp 182-197.

[112] Steensen-Bach, J.O. (1992). “Recent model tests with suction piles in clay and sand,” *Proceedings of the 24th annual Offshore Technology Conference*, Houston, Texas, OTC 6844, pp II 323-330.

[113] Sukumaran, B., McCarron, W.O., Jeanjean, P., and Abouseeda, H., (1999a). “Efficient finite element techniques for limit analysis of suction caissons under lateral loads,” *Computers and Geotechnics*, Vol. 24, pp 89-107.

[114] Sukumaran, B., and McCarron, W.O., (1999b). “Total and effective stress analysis of suction caissons for Gulf of Mexico conditions,” In *Anal-*

ysis, Design, Construction and Testing of Deep Foundations, Edited by J.M. Roesset, Proceedings of the OTRC'99 Conference, Geotechnical special publication No. 88, pp 247-260.

[115] Taiebat, H.A., and Carter, J.P. (2001). "A semi-analytical finite element method for three-dimensional consolidation analysis," *Computers and Geotechnics*, Vol. 28, pp 55-78.

[116] Terzaghi, K. (1923). *Theoretical soil mechanics*, Third edition, John Wiley and Sons, Inc., New York, N.Y.

[117] Tjelta, T.I., Guttormsen, T.R., and Hermstad, J. (1986). "Large-scale penetration test at a deepwater site, *Proceedings of the 18th annual Offshore Technology Conference*, Houston, Texas, OTC 5103, pp 201-212.

[118] Tjelta, T.I. (1994). "Geotechnical aspects of bucket foundation replacing piles for Europipe 16/11-E jacket," *Proceedings of the 26th annual Offshore Technology Conference*, Houston, Texas, OTC 7379, pp 73-82.

[119] Truesdell, C., and Touppin, R.A. (1960). *The classical field theories*, In Handbuch der Physic Bd III/I, Edited by S. Flugge, Springer Verlag, Berlin.

[120] Vásquez Chicata, L.F.G. (2000). "Computational procedure for the estimation of pile capacity including simulation of the installation process," Ph.D. Dissertation, The University of Texas at Austin.

[121] Wang, M.C., Nacci, V.A., and Demars, K.R., (1975). "Behavior of underwater suction anchor in soil," *Ocean Engineering*, Vol. 3, pp 47-62.

[122] Wang, M.C., Demars, K.R., and Nacci, V.A., (1977). "Breakout capacity of model suction anchors in soil," *Canadian Geotechnical Journal*, Vol. 14, pp 246-257.

[123] Wang, M.C., Demars, K.R., and Nacci, V.A. (1978). "Applications of suction anchors in offshore technology," *Proceedings of the 10th annual Offshore Technology Conference*, Houston, Texas, OTC 3203, pp 1311-1320.

[124] Whittle, A.J., and Kavvadas, M.J., (1994). "Formulation of MIT-E3 constitutive model for overconsolidated calys," *Journal of Geotechnical Engineering*, Vol. 120, No. 1, pp 173-198.

[125] Wood, D.M. (1990). *Soil Behavior and Critical State Soil Mechanics*, Cambridge University Press, Cambridge.

[126] Wriggers, P., and Simo, J.C. (1985). "A note on tangent for fully nonlinear contact problems," *Communications in Applied Numerical Methods*, Vol. 1, pp 199-203.

[127] Zdravkovic, L., Potts, D.M., and Jardine, R.J. (2001). "A parametric study of the pull-out capacity of bucket foundations in soft clay," *Geotechnique*, Vol. 51, No. 1, pp 55-67.

[128] Zhong, Z.-H. (1993). *Finite Element Procedure for Contact-Impact Problems*, Oxford University Press Inc., New York.

[129] Zienkiewicz, O.C., and Shiomi, T. (1984). "Dynamic behavior of saturated porous media; The generalized Biot formulation and its numerical

solution," *International Journal for Numerical and Analytical Methods in Geomechanics*, Vol. 8, pp 71-96.

[130] Zienkiewicz, O.C., and Taylor, R.L. (1991). *The Finite Element Method*, McGraw-Hill, United Kingdom.

Vita

Dilip Rugnathbhai Maniar was born on August 17, 1973 in Bombay (India) to Heeragauri and Rugnathbhai Narsidas Maniar. He is youngest of six children of his parents.

Dilip attended Smt. J. B. Khot High School and completed his secondary school in May of 1988. He entered Victoria Jubilee Technical Institute (VJTI) and in May of 1992 he obtained his Diploma of Licentiate Civil and Sanitary Engineering in first class with distinction. Dilip continued at VJTI to obtain his Bachelors degree in Civil Engineering. He graduated in May of 1995 with Bachelor of Engineering (Civil Engineering) with highest honors from the University of Bombay. His outstanding academic excellence at the University of Bombay was recognized by presenting him three gold medals, one silver medal, two bronze medals, two silver trophies, and numerous other prizes. Form August of 1995 to July of 1997, Dilip worked in India with Tata Consulting Engineers and Tata Consultancy Services. Before coming to USA, he also worked briefly as a structural consultant with Maniar Construction.

Dilip came to USA in August of 1997 to enroll into graduate program at The University of Texas at Austin. In August of 2000 Dilip obtained Master of Science in Structural Engineering under the supervision of professor Michael

D. Engelhardt. Dilip stayed to pursue doctoral studies at The University of Texas at Austin. After receiving his Ph.D., Dilip will work as an Analyst with Stress Engineering Services, Inc. (Houston).

Permanent Address: B/3, Sajag Apartments,
Shimpoli Road,
Borivali (West),
Mumbai - 400 092.
India.

This dissertation was typeset with LaTeX 2ε[1] by the author.

---

[1] LaTeX 2ε is an extension of LaTeX. LaTeX is a collection of macros for TeX. TeX is a trademark of the American Mathematical Society. The macros used in formatting this dissertation were written by Dinesh Das, Department of Computer Sciences, The University of Texas at Austin, and extended by Bert Kay and James A. Bednar.